DISSERTATION

RE-MODELLING OF MITOCHONDRIAL RESPIRATION IN ARABIDOPSIS DURING DROUGHT

zur Erlangung des Doktorgrades (Dr. rer. nat.) an der
Mathematisch-Naturwissenschaftlichen Fakultät der
Rheinischen Friedrich-Wilhelms-Universität Bonn

vorgelegt von

PHILIPPE FUCHS

geboren in Schaffhausen, Schweiz

eingereicht am
24. September 2018
Bonn

THIS THESIS HAS BEEN CONDUCTED UNDER THE SUPERVISION OF:

Prof. Dr. Markus Schwarzländer
Plant Energy Biology
Institut für Nutzpflanzenwissenschaften und Ressourcenschutz
Universität Bonn
Friedrich-Ebert-Allee 144
D-53113 Bonn

Current address:
Institut für Biologie und Biotechnologie der Pflanzen
Universität Münster
Schlossplatz 8
D-48143 Münster

FIRST EXAMINER:

Prof. Dr. Andreas Meyer
Chemical Signalling
Institut für Nutzpflanzenwissenschaften und Ressourcenschutz
Universität Bonn
Friedrich-Ebert-Allee 144
D-53113 Bonn

SECOND EXAMINER:

Prof. Dr. Dorothea Bartels
Molekulare Physiologie
Institut für Zelluläre & Molekulare Botanik
Universität Bonn
Kirschallee 1
D-53115 Bonn

DATE OF ORAL EXAMINATION

07. February 2019

YEAR OF PUBLICATION

2019

"Science enhances the moral value of life, because it furthers a love of truth and reverence — love of truth displaying itself in the constant endeavor to arrive at a more exact knowledge of the world of mind and matter around us, and reverence, because every advance in knowledge brings us face to face with the mystery of our own being."

MAX PLANCK, WHERE IS SCIENCE GOING? (1933)

ACKNOWLEDGMENT

Arriving close to the end of my PhD, I am looking back to an extremely exciting and wonderful time. Yes, I would immediately take again the opportunity to conduct this PhD study. The most important reason I enjoyed it so much was for the people who were part of it and supported me throughout my studies.

Foremost, I want to express my heartfelt gratefulness and appreciation to my supervisor, **Markus S.** The three years of my PhD were a fascinating and exciting adventure, which I was privileged to full heartedly engage myself into. Thank you for your trust and enormous support, your guidance and inspiration throughout this time, and for providing this amazing scientific atmosphere. The time was a perfect blend of scientific freedom and creativity, constant intellectual and very enjoyable challenges and importantly being a part of a small but absolutely fantastic group. I would also like to extend my sincerest gratefulness to my 'second first' supervisor **Andreas J. M.**: Thank you for all your support in front and behind the scenes, for the scientific discussions and your words of motivation. Your scientific enthusiasm and joy constituted an essential component to the pleasure and self-realisation which I have enjoyed so much during my work.

I am further grateful to **D. Bartels** who kindly offered to co-supervise and, together with **P. Dörmann** and **G. Bendas**, kindly offered to examine my thesis.

A very special thanks goes to **Stephan W.**, for being my personal superhero, as a scientific supervisor and colleague, and even more so as a friend to talk to, to run together in the Kottenforst or to celebrate the highlights in life. I'm deeply honoured; thank you so much for the amazing time and support.

My sincerest gratitude also goes to my close lab-friends and previous flat members, **Zonia V.**, **Krisztina B.**, **Sajid B.** and **Stefan H.** Thank you, my dear friends, for supporting me in life and in the lab, and for bravely tolerating even my grumpiest moods. What an amazing time: two (!) weddings, exhausting bike rides, delighting and enriching conversations and international delicious food, thank you!

Valentina D.C. and **José U.**, thank you so much for everything, in particular for the wonderful trips together, the many hours rehearsing my talks (even via Skype from another continent) and for the profound and often philosophical conversations in the lab

or over a beer. I cannot emphasise enough how much I appreciate all your help throughout this time and how glad I am to have you!

My admiration and deep gratefulness also go to **Berivan M.** for being a such a loyal, fantastic student and friend in the lab. Despite my sometimes admittedly chaotic nature, in particular during the time of writing my thesis, you always covered my back. I wish you the very best for your future — and please count me in whenever I can be of help!

I am also very grateful to all the 'old' and 'new' members of the PEB group. I truly enjoyed being part of the (A)team, whether it was working together in lab, having intense 'fresh-of-the-bench' meetings & talk rehearsals, or whether it was attending the ICPMB 2017 in China, the lab retreat to the Austrian mountains or the numerous cheerful dinners — thank you everyone for this amazing time. In particular, I would like to thank **Marlene E.**, for the support at various ends during my doctoral studies, and most importantly for sharing the frustration over setbacks & joy over accomplishments in the lab, and for the plentiful serious or amusing conversations at the sterile bench or during a train ride to or from Münster. Thank you, **Thomas N.**, for being the unperturbed constant in the lab, for introducing me to the secrets of mitochondria and fluorimetry, and for always being available to help in the lab. I also would like to sincerely thank **Janina S.**, **Cristina R. and Bettina R.** for the very pleasant and welcoming time in Münster. Even though we only met during the finishing phase of my doctoral studies, your support was amazing and I am looking forward to hanging out with you in Münster.

I would also like to extend my gratitude to the other members of the Chemical Signalling and Crop Genomics teams in Bonn: **Alina O.**, **Anna M.**, **Anna-Lena F.**, **Caro M.**, **David S.**, **Felix F.**, **Frank H.**, **Jutta B.**, **Marcel B.**, **Lara O.**, **Peng Y.**, **Søren S.** and **Stefanie M.S.** Thank you guys on various accounts, in particular for the very entertaining lunch breaks, the on and off scientific discussions, and for breathing life into our big building. I enjoyed every day coming to the lab and being part of the crew. I wish you all the very best! Further, I would also like to express my gratitude to all the members of the **GRK 2064** graduate school for the scientific discussions, the organisations of GRK events and the very vivid and cheerful BBQs.

Another person I would like to thank is **Mark F.** Thank you, Mark, for tutoring me during my microscopy stay in Oxford, for your contagious enthusiasm and scientific

curiosity and for the inspiring discussions about mitochondria; it made the stay a highlight of my PhD study.

I would also like to thank our secretaries, **C. Jessen** and **S. Skamel**. Although I have not been working at so many places yet, this is by far the most efficient and supporting office I have experienced. Thank you so much for mastering all the bureaucratic challenges and for always assisting with kind and supportive words.

Ein ganz besonderer Dank gebührt meinen engen, nicht-wissenschaftlich aktiven Freunden in der Heimat: **Anja, Claudio, Michi** und **Emilia, Paty & Marco**. Danke für Eure Unterstützung aus der Ferne, für die Verankerung mit dem Leben außerhalb der Wissenschaft und die unbezahlbar guten Zeiten zusammen. Ihr seid großartig!

Von tiefstem Herzen möchte ich mich bei meinen Familien Zuhause und in Deutschland bedanken. Danke **Conny** & **Michi** für Euren unerschütterlichen Rückhalt auf jeglicher Ebene, Euer Enthusiasmus und Euer Vertrauen in mich. Danke, dass ich mich immer auf Euch verlassen kann. Meine Eltern, **Marlise** & **Michael**, und meine Geschwister **David**, **Florian** (& **Nina**) und **Milena** (& **Lorenz**) – Euch kann ich nicht genug danken für Euren wortwörtlich grenzenlosen Support. Ich bin extrem stolz einer von Euch Füchsen zu sein. Ich könnte mir wirklich keine besseren Familien vorstellen, und das beinhaltet ganz besonders meine **Patti**. Danke, dass Du die ganze Zeit über fest an meiner Seite stehst und mit mir die Tiefschläge durchlitten, die Höhepunkte gefeiert und mich bei jedem erdenklichen Belangen meiner Promotion unterstützt hast. Du hast einen besonders wichtigen Teil zu dieser Arbeit beigetragen!

TABLE OF CONTENTS

SUMMARY

Drought can severely limit growth and productivity of plants. To limit water loss by transpiration, plant leaves respond by reducing stomatal aperture. This simultaneously impairs CO_2 uptake and can reduce carbon assimilation. Sustained irradiance in the absence of sufficient CO_2 risks over-reduction of the photosynthetic and metabolic redox systems with potentially detrimental effects for the cell. In that situation, chloroplasts need to safely dissipate reductant for which several different mechanisms inside and outside the chloroplast have evolved. Mitochondrial electron transport can act as such an electron sink by reducing oxygen to water. The required capacity and flexibility to dissipate reductant are thought to be provided by uncoupling the electron flux to oxygen from the phosphorylation of ADP to ATP. Yet, our understanding of the significance, regulation and integration of the different uncoupling strategies in plant mitochondria is still limited. To investigate how (un-)coupling impacts drought acclimation, I have manipulated mitochondrial uncoupling capacity by combining mutants of *Uncoupling Protein* (*UCP*) and *Alternative Oxidase* (*AOX1a*). Phenotyping revealed slightly decreased drought tolerance and reduced leaf rosette areas of plants restricted in uncoupling, but differences were minor compared to published mutant phenotypes. Previous reports indicated altered cellular energy physiology in response to drought-related stresses. I sought to refine our understanding of the changes at subcellular level by monitoring selected key parameters in response to drought and related stresses using fluorescent protein biosensors. Despite consistent increases of ATP levels and more oxidised NAD in response to drought, subsequent monitoring of uncoupling mutants did not reveal differences between genotypes under any of the conditions tested. Surprisingly, dithiothreitol (DTT), a widely used chemical to induce reductive ER stress, strongly impaired root growth of *aox1a* and *ucp1* uncoupling mutants. A connection between thiol-based reductive stress and mitochondrial electron transport flexibility has not been reported before, and was further investigated in isolated mitochondria. Measurements of oxygen consumption revealed increased respiration in response to DTT. Multiwell-based fluorimetric assays to monitor the proton motive force, pH gradient and membrane potential, and substrate depletion rates demonstrated that small thiol molecules can feed electrons into the electron transport

chain. Based on the *in planta* and *in organello* insights, a refined model is proposed in which the mitochondria act as flexible cellular safe-guards against stress-induced cellular over-reduction not only by photosynthesis, but also by thiol-mediated reductive stress that may affect protein folding in the ER.

Considering the critical interplay between plant respiratory physiology and mitochondrial architecture in stress responses, the final section of this thesis investigates intramitochondrial pH compartmentation. The successful establishment of lines targeting the cpYFP pH biosensor to different mitochondrial compartments enabled *in vivo* measurements of pH gradients between plant mitochondrial subcompartments, suggesting a pH gradient of 0.4 units across the inner mitochondrial membrane.

ZUSAMMENFASSUNG

Trockenheit kann das Wachstum und die Produktivität von Pflanzen stark einschränken. Pflanzen können den Wasserverlust durch Transpiration über die Spaltöffnungen in den Blättern regulieren und somit minimieren. Dies wiederum beeinträchtigt die CO_2-Aufnahme und -Assimilation. Anhaltende Sonnenlichtexposition in Abwesenheit von ausreichend CO_2 birgt das Risiko einer Überreduktion der photosynthetischen und metabolischen Redoxsysteme mit potentiell schädlichen Auswirkungen auf die Zelle. In dieser Situation müssen Reduktionsäquivalente gezielt aus dem Chloroplasten abgeleitet werden, wofür verschiedene Mechanismen innerhalb und außerhalb des Chloroplasten bestehen. Der mitochondriale Elektronentransport kann durch die Reduktion von Sauerstoff zu Wasser als Akzeptor für überschüssige Reduktionsäquivalente dienen. Es wird angenommen, dass die erforderliche Kapazität und Flexibilität durch die Entkopplung des Elektronenflusses von der Phosphorylierung von ADP zu ATP bereitgestellt wird. Das Verständnis von der Bedeutung, Regulation und Integration der verschiedenen Entkopplungsstrategien in Pflanzenmitochondrien ist jedoch limitiert. Um die Auswirkungen der (Ent-) Kopplung auf die Akklimatisation der Pflanze an Trockenstress zu untersuchen, wurde die Entkopplungskapazität genetisch via *Uncoupling Protein* (*UCP*) und *Alternative Oxidase* (*AOX1a*) manipuliert. Die Phänotypisierung zeigte eine leicht verminderte Trockenstresstoleranz und verringerte Blattrosettenflächen bei Pflanzen mit eingeschränkter Entkopplung, wobei die Unterschiede im Vergleich zu veröffentlichten Phänotypen gering ausfielen. Frühere Berichte zeigten eine Veränderung der zellulären Energiephysiologie infolge von Trockenstress. Ich habe diese Veränderungen auf subzellulärer Ebene eingehender untersucht, indem ich ausgewählte Schlüsselparameter und deren Reaktion auf Trockenstress mithilfe fluoreszenter Proteinbiosensoren ausgelesen habe. Zwar bewirkte Trockenstress eine konstante Erhöhung der ATP-Konzentrationen und der Oxidationsraten von NAD im Wildtypen, die anschließenden parallelen Messungen mit den Entkopplungsmutanten zeigten unter den getesteten Bedingungen aber keine Unterschiede zwischen den Genotypen. Überraschenderweise schränkte Dithiothreitol (DTT), ein verbreitetes Reagenz zur Induktion von reduktivem ER-Stress, das Wurzelwachstum der Entkopplungsmutanten

aox1a und *ucp1* stark ein. Ein Zusammenhang zwischen Thiol-basiertem reduktivem Stress und der Flexibilität des mitochondrialen Elektronentransportes wurde bisher nicht beschrieben und daher im Rahmen dieser Arbeit in isolierten Mitochondrien weiter untersucht. Messungen des Sauerstoffverbrauchs wiesen auf eine erhöhte Atmung nach Zugabe von DTT hin. Multiwell-basierte Fluorimetrie zur Aufzeichnung des pH-Gradienten und des Membranpotentials, den beiden Komponenten der protonenmotorischen Kraft, sowie die Messungen der mitochondrialen Atmungsraten zeigten, dass kleine Thiolmoleküle Elektronen in die Elektronentransportkette einspeisen können. Basierend auf den *in planta* und *in organello* Erkenntnissen wird ein neues Modell vorgeschlagen, in welchem die Mitochondrien als flexible Sicherheitsventile gegen stressinduzierte zelluläre Überreduktion fungieren. Somit bewahren Mitochondrien die Redox-Homöostase und damit vermutlich die Integrität des Photosynthese-Apparates und der oxidativen Proteinfaltung im ER.

Der letzte Abschnitt dieser Arbeit widmet sich der intramitochondrialen pH-Kompartimentierung, welche sich in Stresssituationen abhängig von der Atmungsphysiologie der Pflanzen und der mitochondrialen Architektur verändert. Die erfolgreiche Etablierung von Pflanzenlinien, die den cpYFP pH-Biosensor in unterschiedlichen mitochondrialen Kompartimenten exprimieren, ermöglichte *in vivo* Messungen von pH-Gradienten zwischen mitochondrialen Kompartimenten der Pflanzen und deutet auf einen pH-Gradienten von 0,4 Einheiten über die innere mitochondriale Membran hin.

1 INTRODUCTION

1.1 Drought from a plant perspective

Water constitutes the most abundant molecule on our planet's surface. Yet, plants find themselves frequently exposed to restricted water availability. The condition of restricted water availability for plants — drought — results in a water deficit, due to transpiration exceeding water uptake. If the loss is continuously higher than what is replaced, drought impact on plants can have severe consequences, eventually leading to plant death. Drought was estimated to reduce yields of cereals by about 10% on average at a global scale and imposed, together with heat, the strongest constraints on crop production (Lesk et al., 2016). The forecasted increase of drought frequency and severity due to climate change further underlines the relevance of this stressor for terrestrial plant production (Dai, 2013).

A wealth of studies advanced the understanding of the mechanisms by which plants monitor their water status, painting a complex and sophisticated picture encompassing morphological, physiological and biochemical changes. Plants integrate signals from a multi-layered sensor system to control their water status. While increase of water uptake by osmotic adjustments or enhanced root growth constitutes a mid- to long-term strategy, reduction of stomatal conductance represents a rapid response to water deficit. The guard cells of a stoma function as a hydraulic valve and, in the absence of a water deficit, provide a low-resistance pathway for diffusional gas exchange between the leaf internal air space and ambient air (Boyer, 2015). Consequently, control over stomatal conductance provides an efficient means to rapidly limit water loss by transpiration. The stress hormone abscisic acid (ABA) has been identified as a major regulator in the perception of drought and the induction of downstream responses. Decreasing soil water potentials lead to a decline in the leaf water status, which triggers an ABA accumulation in the shoots due to enhanced foliar synthesis (McAdam et al., 2016). This can result in an up to 50-fold accumulation of ABA in the leaves within a few hours (Beardsell and Cohen, 1975), where ABA induces the reduction of stomatal aperture by triggering a cascade of reactions that reduces the turgor pressure of guard cells, *e.g.* efflux of potassium and anions, and the export or conversion of organic osmotic compounds (Munemasa et al., 2015; Santelia and Lawson, 2016).

Alongside ABA, signalling intermediates, such as H_2O_2 (Zhang et al., 2001), coinciding pH changes (Wilkinson and Davies, 1997) and crosstalk with other signalling pathways have been described to contribute to the fine-tuning of stomatal closure during the occurrence of drought (Munemasa et al., 2015; Santelia and Lawson, 2016).

1.2 Organellar cooperation to prevent over-reduction and photoinhibition of the photosynthetic apparatus

Photosynthesis and cell expansion are amongst the early processes affected by water deficit. The dramatic effect of drought on photosynthesis is the result of the need to acquire CO_2 which is linked to water loss. For an herbaceous C_3 plant, measurements of the photosynthetic water-use efficiency, the ratio between carbon assimilated in photosynthesis and transpirational water loss, suggested that 200–500 molecules of H_2O are lost for every CO_2 molecule fixed by photosynthesis (Lambers et al., 2008). Since the exchange rates of CO_2:H_2O are largely fixed, any measure by the plant to reduce transpirational water loss inevitably gives rise to a reduced CO_2 uptake. Reduced stomatal aperture decreases carbon assimilation rate; either directly caused by diffusion limitations of CO_2 through the stomata and the mesophyll (Figure 1A) (Dietz and Heber, 1983; Quick et al., 1992; Flexas et al., 2004) or by alterations of carbon assimilation metabolism (Tezara et al., 1999; Lawlor and Cornic, 2002).

In photosynthesis the incoming light energy needs to be carefully matched by the regulation of the photochemical reactions to avoid over-reduction and damage to photosynthetic machinery (Andersson and Aro, 2001; Takahashi and Badger, 2011; Roach and Krieger-Liszkay, 2014). A reduced demand of metabolic reductant due to restricted carbon assimilation combined with sustained irradiance requires rapid and effective adjustments. The importance of maintaining the balance between reducing and oxidising (redox) processes is reflected by the comprehensive set of sophisticated mechanisms dedicated to ensure the integrity of the photosynthetic machinery, *e.g.* dissipation of absorbed light energy as thermal energy, Mehler peroxidase reaction or non-photochemical quenching (Murchie and Niyogi, 2011; Takahashi and Badger, 2011; Roach and Krieger-Liszkay, 2014). Additional processes to maintain photosynthesis under physiologically and metabolically non-favourable conditions include photorespiration and

reductant shuttling via the malate valve, which link the photosynthetic metabolism and redox balance of the chloroplast with cellular redox and energy homeostasis.

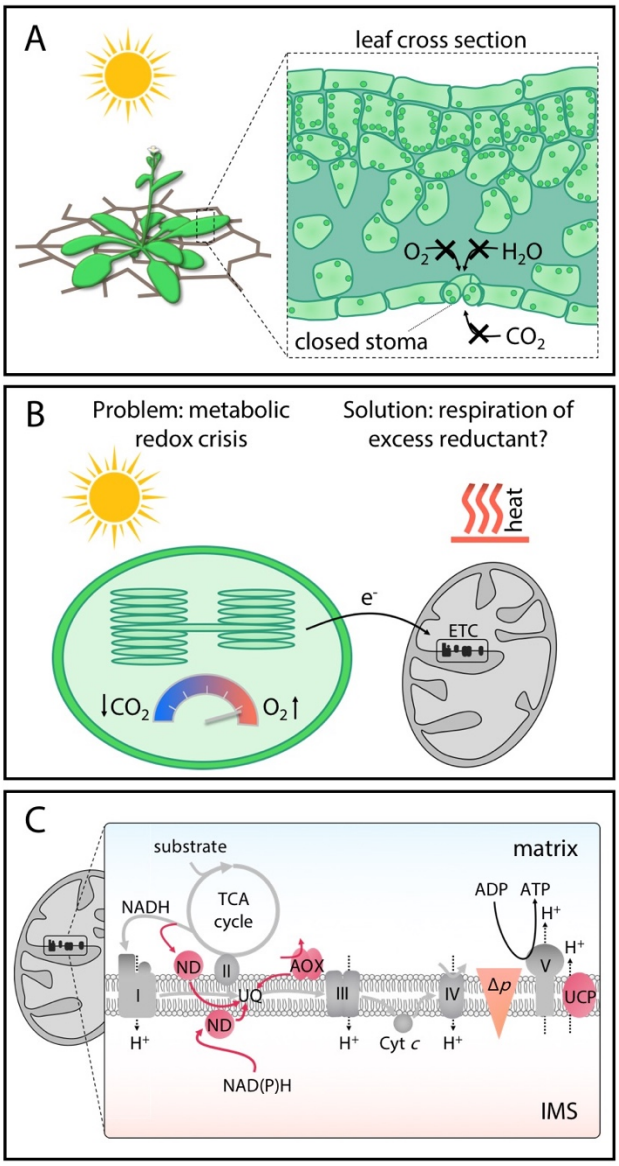

Figure 1: Mitochondrial uncoupling protects plants from metabolic over-reduction during drought.
(**A**) Plants exposed to water shortage reduce their stomatal aperture to efficiently cut water loss at the cost of diffusional gas exchange between leaf internal spaces and ambient air. (**B**) Continuous O_2 release and CO_2 depletion by photosynthesis change leaf internal gas composition, raising the risk of photoinhibition and over-reduction of the photosynthetic electron transport chain. One mechanism to counteract photoinhibition is net export of electrons from chloroplasts to mitochondria. The mitochondrial electron transport chain (ETC) serves as an electron sink (Atkin and Macherel, 2009). The energy released may be partly conserved by phosphorylation of ADP or fully dissipated as heat. (**C**) The mitochondrial ETC of plants is composed of complexes I-IV (grey) generating the protonmotive force (Δp) between mitochondrial matrix and intermembrane space (IMS). Δp is harnessed by the F_0F_1 ATP synthase (complex V; grey) to phosphorylate ADP. The plant mitochondrial ETC includes non-energy-conserving bypasses comprising NAD(P)H-Dehydrogenases (ND; red) and Alternative Oxidases (AOX; red). Uncoupling Proteins (UCP; red) act downstream of the ETC and reduce energy-conservation by dissipating Δp. The carefully concerted activity of the non-energy-conserving components allows flexible adjustments of respiratory coupling and dissipation of excess reductant, *e.g.* under drought stress. Arrows in grey and red indicate electron flow along the redox gradient. Arrows in black indicate proton translocation (dashed) or ADP phosphorylation (solid). Cyt *c* = Cytochrome *c*, UQ = Ubiquinone, TCA = tricarboxylic acid.

Photorespiration represents the downstream salvage pathway of the oxygenase activity of ribulose-1,5-bisphosphate carboxylase/oxygenase (Rubisco) and is essential to protect the photosynthetic machinery against photoinhibition (Wu et al., 1991; Heber et al., 1996; Kozaki and Takeba, 1996). The oxygenation activity of Rubisco is commonly understood as an unwanted side reaction and can be explained by the evolution of Rubisco about 3 billion years ago during a time when atmospheric oxygen concentrations were negligible (Nisbet et al., 2007). Importantly, oxygenase activity results in the production of the dead-end metabolite 2-phosphoglycolate (2PG). 2PG accumulation is prevented and its carbon partially salvaged by the photorespiratory pathway, which involves a succession of enzymatic reactions in chloroplasts, the mitochondria and the peroxisomes. Organellar cooperation enables the recovery of phosphate and 75% of the carbon originally lost as 2PG. Indeed, the repair function of the photorespiratory pathway is essential; impairments inhibit photosynthetic carbon assimilation due to the lack of Calvin-Benson cycle intermediates and accumulation of photorespiratory pathway intermediates inhibiting the Calvin-Benson cycle (Bauwe et al., 2010). The operation of the pathway requires the provision of ATP and reducing equivalents. While these costs are conceivably disadvantageous under optimal growth conditions, reducing equivalent oxidation and ATP hydrolysis may be beneficial under conditions of limited CO_2 supply to sustain photosynthetic electron transport and to avoid photoinhibition (Wu et al., 1991; Kozaki and Takeba, 1996; Cornic and Fresneau, 2002). Under standard growth conditions, it was estimated that in about one out of three reactions Rubisco binds oxygen (oxygenation) instead of carbon dioxide (carboxylation) (Sharkey, 1988). Drought-induced changes of the gas homeostasis in the inner leaf space in the light result from stomatal closure and ongoing carbon assimilation. Decrease of CO_2 and increase of O_2 further favour the oxygenation over the carboxylase reaction (Wingler et al., 1999). The oxygenation proportion is additionally favoured by elevated temperatures, often coinciding with drought as an environmental factor and as a consequence of reduced transpirational cooling (Urban et al., 2017; Peterhänsel et al., 2010).

The malate valves represent another carbon flux-based mechanism of the chloroplast to link the optimisation of photosynthesis to other subcellular locations. Specifically, reductant is shuttled between the chloroplast and other cellular compartments to maintain metabolic redox balance (Scheibe, 2004; Scheibe and Dietz, 2012). In the

chloroplast, active photosynthetic electron transfer can, via the ferredoxin-thioredoxin system, redox-activate the NADP-dependent malate dehydrogenase, which uses excess NADPH to convert oxaloacetate to malate (Scheibe and Beck, 1979; Carr et al., 1999). The regeneration of the electron acceptor $NADP^+$ allows the maintenance of photosynthetic ATP synthesis. Simultaneously, the export of malate to the cytosol, and to other compartments, via malate-oxaloacetate shuttles maintains the gradient between the chloroplasts and the cytosol (Scheibe, 2004). Disrupting the operation of the malate valve by disrupting the shuttling through genetic interference with the oxaloacetate transporter pOMT1 leads to an increased accumulation of reducing equivalents in the chloroplast stroma and photoinhibition under higher light intensities (Kinoshita et al., 2011). Disrupting the oxaloacetate–malate conversion in chloroplasts through the genetic interference with NADP-MDH on the contrary revealed no phenotypic impairment, even under high-light conditions, but showed adjustments of the photorespiratory pathway and indications of increased reductant export to mitochondria (Hebbelmann et al., 2012). These findings exemplify the importance of extra-plastidial cellular compartments to prevent over-reduction and photoinhibition of the photosynthetic apparatus (Figure 1B).

1.3 The role of mitochondria during drought

Photosynthesis provides all substrate for mitochondrial metabolism, either directly, or indirectly via the cellular metabolic network. Well-watered plants release 30–70% of the CO_2 fixed per day by photosynthesis back into the atmosphere by respiration (Atkin and Macherel, 2009). While the dependence of respiration on photosynthesis has always been evident from a thermodynamic perspective, the converse dependence of mitochondrial respiration on photosynthesis has been appreciated only later (Raghavendra et al., 1994; Raghavendra and Padmasree, 2003; Atkin and Macherel, 2009; Bailleul et al., 2015; Araújo et al., 2014). For instance, chemical or genetic inhibition at different sites of the mitochondrial electron transport chain (ETC) was shown to decrease photosynthetic carbon assimilation rates. Under favourable growth conditions, the decrease was proposed to be caused by a lack of mitochondrial ATP supply to optimise carbon assimilation in the chloroplast (Krömer and Heldt, 1991; Raghavendra et al., 1994; Gandin et al., 2012; Bailleul et al., 2015). Conversely, under adverse environmental conditions, such as drought or high light, the inhibition of photosynthesis appears dominated by a failure of the mitochondria

to sustain photorespiratory carbon fluxes and/or photosynthetic redox balance. In situations of increased photorespiratory carbon flux, glycine oxidation becomes a major reductant source to mitochondrial respiration (Wingler et al., 1999; Igamberdiev et al., 2001; Bykova et al., 2005). Additional reductant is exported to mitochondria via other pathways, such as malate valves (Yoshida et al., 2007). As a result, interference with the mitochondrial ETC restricts the capacity to dissipate excess reducing power. Since photosynthesis, including photorespiration, can be a major source of electron flux mitochondrial respiratory chain capacity can be a major constraint to photosynthesis (Figure 1B) (Sweetlove et al., 2006; Giraud et al., 2008; Strodtkötter et al., 2009; Vishwakarma et al., 2015).

Reduced rates of carbon assimilation rates and the operation of mitochondrial metabolism as an electron sink involves changes in the broader redox and energy homeostasis of the cell. Rapid fractionation of cytosol, chloroplast and mitochondria from barley protoplasts revealed that photorespiratory conditions induce a pronounced increase of the cellular NADH/NAD^+ and ATP/ADP ratios (Wigge et al., 1993; Igamberdiev et al., 2001). Comparison of the NADH/NAD^+ and ATP/ADP ratios from the three cell compartments under photorespiratory conditions revealed that mitochondria were most affected; exhibiting a three-fold increase of NADH/NAD^+ and a two-fold increase of the ATP/ADP ratio, whereas changes in chloroplasts were less pronounced (Wigge et al., 1993; Igamberdiev et al., 1997). Notably, the ratios of NADPH/$NADP^+$ remained stable between the treatments (Wigge et al., 1993), suggesting efficient acclimation, including reductant export from the chloroplast particularly to the mitochondrion (Figure 1B).

The need to rapidly change function in response to cellular and environmental conditions makes respiratory flexibility a key feature of plant mitochondria. Under normal water status and carbon assimilation, efficient provision of energy by mitochondria in the form of phosphorylation supports most cellular functions, which potentially even includes carbon assimilation in chloroplasts (Krömer and Heldt, 1991; Gandin et al., 2012; Bailleul et al., 2015). Under adverse growth conditions, mitochondria serve as a reductant sink and buffer cellular energy and redox homeostasis, at the cost of energy efficiency (Giraud et al., 2008; Vishwakarma et al., 2015; Barreto et al., 2017). The mechanistic centrepiece to enable such a degree of flexibility, is a particularly sophisticated mitochondrial electron transport chain in plants (Figure 1C).

1.4 Architecture of mitochondria in higher plants

Although photosynthetic carbon fixation in the chloroplasts is the ultimate source of organic building blocks, plants rely on mitochondria for carbon metabolism and provision of cellular phosphorylation potential, particular in the absence of active photosynthesis. There are notable differences between mitochondria of plants and animals, but the basic principles of their structure and function, such as double-membrane architecture or mechanisms of energy transformation, are highly conserved.

1.4.1 The outer mitochondrial membrane: a selective sieve

Mitochondria consist of two membranes; the outer mitochondrial and the inner mitochondrial membrane (OMM and IMM). The OMM is permeable to molecules with a molecular weight below ~5,000 Da (Werkheiser and Bartley, 1957; Colombini, 1980). The permeability is thought to be mainly mediated by porins (also called Voltage-Dependent Anion Channels, VDACs), which occur in the OMM at very high abundance (Figure 2). We recently employed quantitative proteomics on purified mitochondria from heterotrophic *Arabidopsis thaliana* (*At*) cell cultures and estimated 82,000 VDAC protein copies per individual Arabidopsis mitochondrion on average (Braun et al., in preparation), which is in line with previous calculations for mung bean and potato mitochondria based on electron micrographs and X-ray diffraction studies (Mannella and Bonner, 1975). Under the assumption that *At*VDACs are similar to the crystal structure of human VDAC (Bayrhuber et al., 2008), 35% of the OMM area are estimated to consist of VDAC protein (Figure 3). Considering the adjustable regulation of VDAC permeability evidenced by several groups (Moran et al., 1992; Bera and Ghosh, 2001; Zizi et al., 1994; Hodge and Colombini, 1997; Mlayeh et al., 2010), the OMM may constitute a conditional micro-sieve with presumably direct regulatory roles in organelle metabolism and physiology.

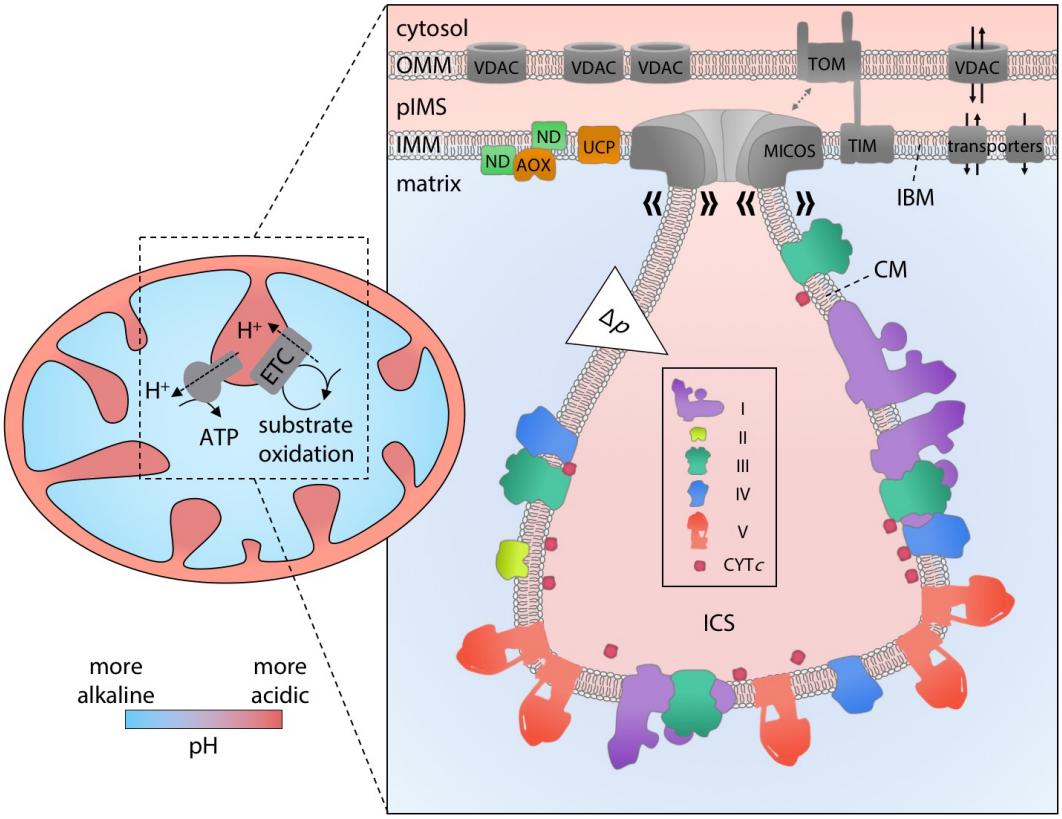

Figure 2: Hypothetical concept of how spatial and functional separation of the inner mitochondrial membrane (IMM) may be organised in plants.

Modified from Schwarzländer and Fuchs, 2017.

Saccular cristae as frequently observed in plant mitochondria maintain a comparatively large intracristal space (ICS) volume, which is connected to the peripheral intermembrane space (pIMS) by a cristal junction of a small diameter. Junction properties may be dynamically adjusted to modulate exchange between ICS and pIMS, potentially involving regulation by the ring-like oligomers of the mitochondrial contact site and cristae organising system (MICOS). Such diffusion restrictions could generate microcompartments within mitochondrial subcompartments, *e.g.* 'hyper'-acidic pIMS, potentially supported by the preferential localisation of respiratory complexes and supercomplexes of the classical pathway (I–V, and CYT*c*: Cytochrome *c*) to the cristal membrane (CM) and of the alternative pathway (internal and external alternative NAD(P)H Dehydrogenases: ND and Alternative Oxidase: AOX) to the inner boundary membrane (IBM) of the inner mitochondrial membrane (IMM). Uncoupling Protein (UCP) and IMM transporters for the exchange of solutes with the cytosol are shown in the peripheral section of the IMM to allow for efficient solute transport across both membrane systems. OMM: outer mitochondrial membrane, VDAC: Voltage-Dependent Anion Channel, TOM: Translocase of the Outer mitochondrial Membrane, TIM: Translocase of the Inner mitochondrial Membrane, Δ*p*: proton motive force. Blue and red areas: relative alkaline and relative acidic environments, respectively.

1.4.2 The inner mitochondrial membrane: oxidative phosphorylation at high capacity

The IMM has received far more attention than the OMM, mainly because it hosts the oxidative phosphorylation machinery. Oxidative phosphorylation is composed of (1) the oxidation of metabolic reductant by the ETC and (2) the phosphorylation of ADP to ATP by the F_0F_1 ATP synthase. The identification of the link between the two processes represented a major challenge to the fields of biochemistry and biology (Gautheron, 1984). In 1961, P. D. Mitchell postulated the, at that time, polarising and controversial chemiosmotic hypothesis, *i.e.* the connection of the two processes by an electrochemical gradient across a proton-impermeable membrane (Mitchell, 1961, 2011). Despite the meticulous and comprehensive elaboration of the chemiosmotic hypothesis, the scientific community was not easily convinced (Slater, 1967) and it took several years before it was fully accepted.

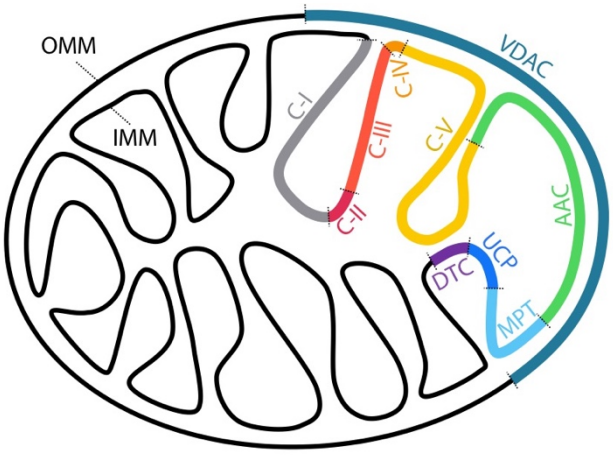

Protein family/complex	area of OMM
VDAC	35.0%
Protein family/complex	**area of IMM**
Complex I (C-I)	5.0%
Complex II (C-II)	0.7%
Complex III (C-III)	3.0%
Complex IV (C-IV)	0.3%
Complex V (C-V)	8.4%
AAC	6.6%
MPT	2.5%
UCP	1.0%
DTC	0.8%
remaining	< 1%

Figure 3: Proportions of mitochondrial membrane areas constituted by individual protein families.
Modified from Braun et al., in preparation.
Left: Schematic representation of the outer mitochondrial membrane (OMM) and the inner mitochondrial membrane (IMM) of a typical plant mitochondrion in a 1:3 ratio (membrane area represented as lines). Colour-coded membrane segments represent the proportional constitution of OMM or IMM by the most abundant protein families and protein complexes in % of total membrane area occupied as shown in table (right) as calculated from a quantitative proteome from Arabidopsis cell culture mitochondria (Braun et al., in preparation). VDAC (Voltage-Dependent Anion Channel), C-I (NADH:Ubiquinone Oxidoreductase), C-II (Succinate Dehydrogenase), C-III (Cytochrome bc_1 complex), C-IV (Cytochrome *c* Oxidase), C-V (F_0F_1 ATP synthase), AAC (ADP/ATP Carrier), MPT (Mitochondrial Phosphate Transporter), UCP (Uncoupling Protein), DTC (Dicarboxylate/Tricarboxylate Carrier).

Reducing equivalents from diverse sources, *e.g.* the TCA cycle or photorespiratory glycine conversion, can be oxidised by the mitochondrial ETC, which is composed of a series of functionally separated multiprotein complexes I-IV. The conveyance of electrons along the ETC onto the final electron acceptor oxygen is coupled to the proton translocations across the IMM. The resulting chemiosmotic potential, the proton motive (Δp) force, is then used by the F_0F_1 ATP synthase (complex V) to phosphorylate ADP to ATP (Figure 1C, Figure 2).

Although mitochondria fulfil many functions, *e.g.* iron-sulfur cluster assembly or amino acids metabolism, oxidative phosphorylation is dominating by far at the level of protein abundance. 17% of the IMM surface of a typical Arabidopsis cell culture mitochondrion is composed of ETC complexes I–V (Figure 3) (Braun et al., in preparation), which is consistent with reports from rat liver mitochondria (Gupte et al., 1984). For the high abundance of ETC complexes to be functional, effective provision of substrates is required, which is mirrored by the high copy numbers of several transporters. Using the same proteomic approach as for VDAC and ETC complexes, it was estimated that the transporters for adenylate, phosphate, di- and tricarboxylate supply of the mitochondrial matrix amount to 11% of the IMM area (Figure 3) (Braun et al., in preparation). In total, the ETC complexes and carriers make up ~28% of the IMM area of a typical Arabidopsis mitochondrion, which is consistent with observations in *Neurospora crassa* mitochondria where the IMM is predominantly composed of proteins (77% of IMM weight) and to a far lesser extent by lipids (Hallermayer and Neupert, 1974).

Cells make use of oxidative phosphorylation to maintain a high phosphorylation potential by strongly displacing the observed mass action ratio of ATP/ATP from equilibrium. This renders the phosphorylation of ADP to ATP thermodynamically unfavourable and a considerable amount of energy (Gibbs energy; ΔG) is required to uphold the high ATP/ADP mass action ratio. The ΔG required to synthesise ATP, requires a high protonmotive force, which is dominated by the electrical component in mitochondria. The electrical field across the IMM typically amounts to > 300,000 V cm^{-1}, which is within the range of that of a bolt of lightning. Operating bioenergetic membrane processes under such conditions necessitates strict regulatory mechanisms and energy dissipation systems to prevent damage by over-reduction of the ETC redox centres, and excessive release of reactive oxygen species (primarily superoxide), in turn. Drought stress

provides a challenge to the organellar redox and energy transformation systems in particular (section 1.2, section 1.3).

1.4.3 The intimate relationship between mitochondrial function and architecture

Apart from keeping the phosphorylation potential of the adenylate pool high, oxidative phosphorylation inevitably separates the mitochondrial intermembrane space (IMS) and matrix into subcompartments of distinct protein inventories and chemical properties (Figure 2). In human HeLa cells, the mitochondrial matrix pH was observed *in vivo* to be 0.45–0.5 units higher, *i.e.* more alkaline, than in the IMS (Llopis et al., 1998; Poburko et al., 2011). Slightly smaller pH gradients across the IMM were estimated for plants. Isolated plant mitochondria of mung bean and of arum spadices supplemented with respiratory substrates to simulate active respiration, revealed a ΔpH of 0.40 and 0.35, respectively (Moore et al., 1978). Recent studies suggest that the mitochondrial subcompartments can accommodate distinct microcompartments (Strauss et al., 2008; Rieger et al., 2014). The microcompartmentation is thought to originate from heterogenous protein compositions within the IMM in combination with specific spatial IMM arrangements. For instance, immunogold labelling revealed that ETC complexes predominantly localise to the cristal membrane part of the IMM (Gilkerson et al., 2003). Furthermore, locally enriched F_0F_1 ATP synthase dimers were detected at the cristal rims of the IMM (Davies et al., 2012). In combination with the IMM cristal fold, the enriched F_0F_1 ATP synthase dimers were modelled to constitute a proton trap (Strauss et al., 2008; Davies et al., 2012). Despite the central and intimate link of pH gradients to oxidative phosphorylation, *in vivo* insights of the local proton concentrations have until recently been hampered by the lack of suitable sensing methods.

The development of genetically encoded pH biosensors (section 1.6) provided an approach to measure *in vivo* pH gradients between and within mitochondrial compartments. In human HeLa cells, the combination of a genetically encoded pH biosensor targeted to the mitochondrial matrix side-by-side with a pH-sensitive dye in the cytosol indicated pH values of 7.6 and 7.15, respectively (Poburko et al., 2011). Under the assumption that the OMM poses no diffusional barrier to protons and pH is uniform within a given compartment, the cytosol–matrix pH difference reflects the pH gradient across the IMM. In conflict with those assumptions, measurements in human ECV304 cells

with EYFP as pH sensor revealed pH values of 7.8, 6.9 and 7.6 for the mitochondrial matrix, IMS and cytosol, respectively (Porcelli et al., 2005). The difference of 0.7 pH units between the cytosol and IMS might indicate microcompartmentation of pH within the organellar subcompartments. In support of this, a recent study reported lateral IMS pH gradients between functional complexes of the ETC in mitochondria of HeLa cells (Rieger et al., 2014). Using fusions of the pH biosensor sEcpH to subunits of complex IV (Cytochrome *c* Oxidase) and complex V (F_0F_1 ATP synthase), the authors determined a lateral pH gradient of 0.3 units in the IMS, which was absent when mitochondrial respiration was inhibited. Empirical data on the sub- or microcompartmentation of any physiological parameter in plant mitochondria are scarce, and, if available, they are typically based on *in vitro* experiments with purified mitochondria.

1.5 The uncoupling systems of plant mitochondria

The oxidative phosphorylation machinery of plants is particularly sophisticated and contains, in addition to the core energy-conserving ETC complexes, several additional components: alternative NAD(P)H Dehydrogenases (ND), Alternative Oxidases (AOX) and Uncoupling Proteins (UCP) (Figure 1C) (Vanlerberghe and Ordog, 2002; Vercesi et al., 2006; Rasmusson et al., 2008). Their combined activity and regulation give rise to remarkable respirational flexibility and represents the mechanistic basis to flexibly tune respiratory activity between the extremes of efficient provision of phosphorylation potential and reductant dissipation without energy conservation.

1.5.1 The alternative NAD(P)H dehydrogenase family

Plants possess several NDs (7 in *Arabidopsis thaliana*; Rasmusson et al., 2008) that differ in evolutionary origin and function, and can be sub-grouped into A- and B-type NDs with regard to the localisation at the inner mitochondrial membrane IMM, either exposed to the mitochondrial matrix (NDA) or the IMS (NDB) side (Figure 1C) (Rasmusson et al., 1999). Additionally, plants including Arabidopsis, possess a to date little investigated C-type ND, which presumable originated from the chloroplast progenitor (Michalecka et al., 2003). Apart from plants, NDs were identified in fungi, protists and bacteria, but not in animals (Friedrich et al., 1995; Joseph-Horne et al., 2001; Rasmusson et al., 2008). NDs represent a non-energy-conserving by-pass to complex I of the ETC. Depending on the

isoform, the enzyme catalyses the oxidation of NADH and/or NADPH from the mitochondrial matrix or the cytosol coupled to the reduction of ubiquinone as a central component of the classical ETC, but does not contribute to proton-translocation (Rasmusson et al., 2008). The *in vivo* regulation of ND activity is not fully clear and likely differs between the isoforms; pH and Ca^{2+}-dependent activation of Arabidopsis and potato NDB1, and kinetic control via different K_m have been reported (Rasmusson and Møller, 1991; Geisler et al., 2007; Hao et al., 2015).

1.5.2 The alternative oxidase family

AOX proteins reside at the matrix exposed IMM side and can be found in algae (Weger et al., 1990), fungi (Minagawa et al., 1992; Yukioka et al., 1998), and protists (Clarkson et al., 1989), but are most widespread present in higher plants, where they include several isoforms sub-grouped into AOX1 and AOX2 proteins (Figure 4) (Costa et al., 2014; Pennisi et al., 2016). AOX1 isoforms are found in mono- and dicotyledons, whereas AOX2 isoforms are absent from the genomes of monocotyledons (Considine et al., 2002; Costa et al., 2014). Arabidopsis possesses 5 AOX isoforms, which separate into two major groups based on the amino acid sequence similarities, consisting of AOX2 and AOX1a, AOX1b, AOX1c and AOX1d. Notably, AOX1d can be further distinguished from AOX1a–AOX1c as a small separate subgroup (Figure 4C) (Costa et al., 2014; Clifton et al., 2006). In Arabidopsis, *AOX1a* is the most highly expressed isoform throughout most developmental stages and tissues (Figure 5B) and is highly stress-inducible. In fact, *AOX1a* and *AOX1d* are amongst the most stress-responsive nuclear genes encoding mitochondrial proteins (Clifton et al., 2006).

Functionally, AOX couples ubiquinol oxidation to the reduction of molecular oxygen to water. As such it provides a by-pass to the complexes III and IV and that differs from the classical electron path by lack of any proton translocation. Two main mechanisms of biochemical regulation of AOX are well established, depending on the redox and carbon status of the mitochondrion. Specifically, AOX is present as dimer either non-covalently or covalently linked by a disulfide bond formed between two highly conserved cysteine residues in the N-terminal part of the protein. The reduced state of the dimer was found to be the catalytically active one (Rhoads et al., 1998; Umbach et al., 2006). Activity of reduced AOX can be further enhanced by different TCA cycle metabolites, most notably pyruvate

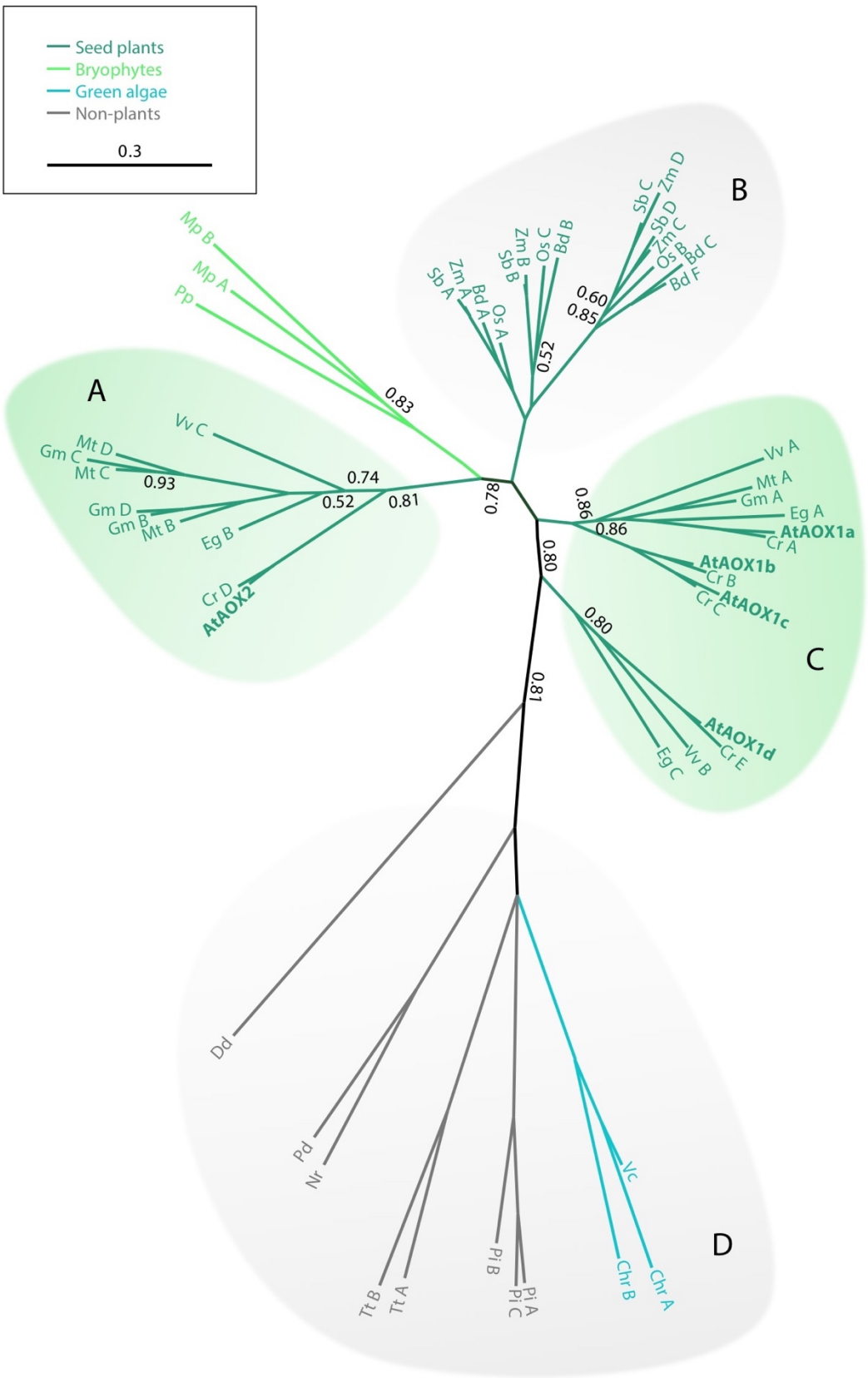
Seed plants
Bryophytes
Green algae
Non-plants
0.3
A
B
C
D
Mp B
Mp A
Pp
Vv C
Mt D
Gm C
Mt C
Gm D
Gm B
Mt B
Eg B
Cr D
AtAOX2
Sb A
Zm A
Bd A
Os A
Sb B
Zm B
Os C
Bd B
Sb C
Zm D
Sb D
Zm C
Os B
Bd C
Bd F
Vv A
Mt A
Gm A
Eg A
AtAOX1a
Cr A
AtAOX1b
Cr B
Cr C
AtAOX1c
AtAOX1d
Vv B
Cr E
Eg C
Dd
Pd
Nr
Tt B
Tt A
Pi B
Pi A
Pi C
Vc
Chr B
Chr A
0.83
0.74
0.93
0.52
0.81
0.78
0.52
0.60
0.85
0.86
0.80
0.80
0.81

Figure 4: Phylogenetic tree of Arabidopsis AOX1a and its homologs from representative non-plant and plant species.
Amino acid sequences of representative species were retrieved from NCBI blasted against *Arabidopsis thaliana* Alternative Oxidase 1a (AOX1a) and shown as unrooted tree calculated with MrBayes. Scale bar represents 30 substitutions per 100 amino acids. Numerical values along the tree represent bootstrap values of respective branching (only values < 0.95 indicated). (**A**), (**B**) (**C**) and (**D**) refer to distinct clusters within phylogenetic tree. At: *Arabidopsis thaliana*, Bd: *Brachypodium distachyon*, Cr: *Capsella rubella*, Chr: *Chlamydomonas reinhardtii*, Dd: *Dictyoselium discoideum*, Eg: *Erythranthe guttata*, Gm: *Glycine max*, Mp: *Marchantia polymorpha*, Mt: *Medicago truncatula*, Os: *Oryza sativa*, Pa: *Podospora anserina*, Pi: *Phytophthora infestans*, Pp: *Physcomitrella patens*, Sb: *Sorghum bicolor*, Tt: *Tetrahymena thermophila*, Vv: *Vitis vinifera*, Vc: *Volvox carteri*, Zm: *Zea mays*.

for AOX1a, by thiohemiacetal formation (Millar et al., 1993; Umbach and Siedow, 1993; Rhoads et al., 1998; Selinski et al., 2018). Differential preferences towards different TCA cycle metabolites by the isoforms might explain why *AOX1a* knock-out mutants are not functionally complemented by the remaining isoenzymes (amino acid sequences similarities of *At*AOX isoforms between 55–82%), even though *AOX1d* expression was found upregulated (Strodtkötter et al., 2009; Vishwakarma et al., 2015; Kühn et al., 2015).

1.5.3 The uncoupling protein family

UCP function is best studied in brown adipose tissue in animals, where UCP1 was initially discovered and described to mediate non-shivering thermogenesis (Bouillaud et al., 1986; Enerbäck et al., 1997; Matthias et al., 2000; Golozoubova et al., 2001; Nedergaard et al., 2001). The later identified animal isoforms UCP2–5 appear to fulfil more diverse functions, including lipid metabolism, glucose-stimulated insulin secretion or dampening of mitochondrial reactive oxygen species (ROS) production (Weigle et al., 1998; Arsenijevic et al., 2000; Krauss et al., 2002; Affourtit and Brand, 2008; Kwok et al., 2010). UCPs were initially thought to only occur in animals, but homologs were subsequently also found in potato tubers and later confirmed to be conserved in plant genomes (Vercesi et al., 1995; Laloi et al., 1997). Apart from animals and plants, UCP can also be found in some lower Eukarya groups such as Unikonts (Luévano-Martínez, 2012). UCP belongs to the mitochondrial carrier family, consisting of 58 protein members in Arabidopsis, and is an integral IMM protein (Palmieri et al., 2011; Haferkamp and Schmitz-Esser, 2012). After the discovery of *At*UCP1 (Maia et al., 1998) and *At*UCP2 (Watanabe et al., 1999), six Arabidopsis *UCP* isogenes were identified and re-named *Plant Uncoupling Mitochondrial Protein* (*PUMP*) *1–6* (Borecký et al., 2006). Subsequent studies, however, revealed that

PUMP4–6 exhibit biochemical properties typical of the phylogenetically closely related Dicarboxylate Carrier (DIC) known from yeast and animals (Palmieri et al., 2008). Accordingly, PUMPs were re-grouped into UCP1–UCP3 and non-uncoupling proteins DIC1–DIC3. Notably, *At*UCP1 and *At*UCP2 are highly similar and share 72% identical

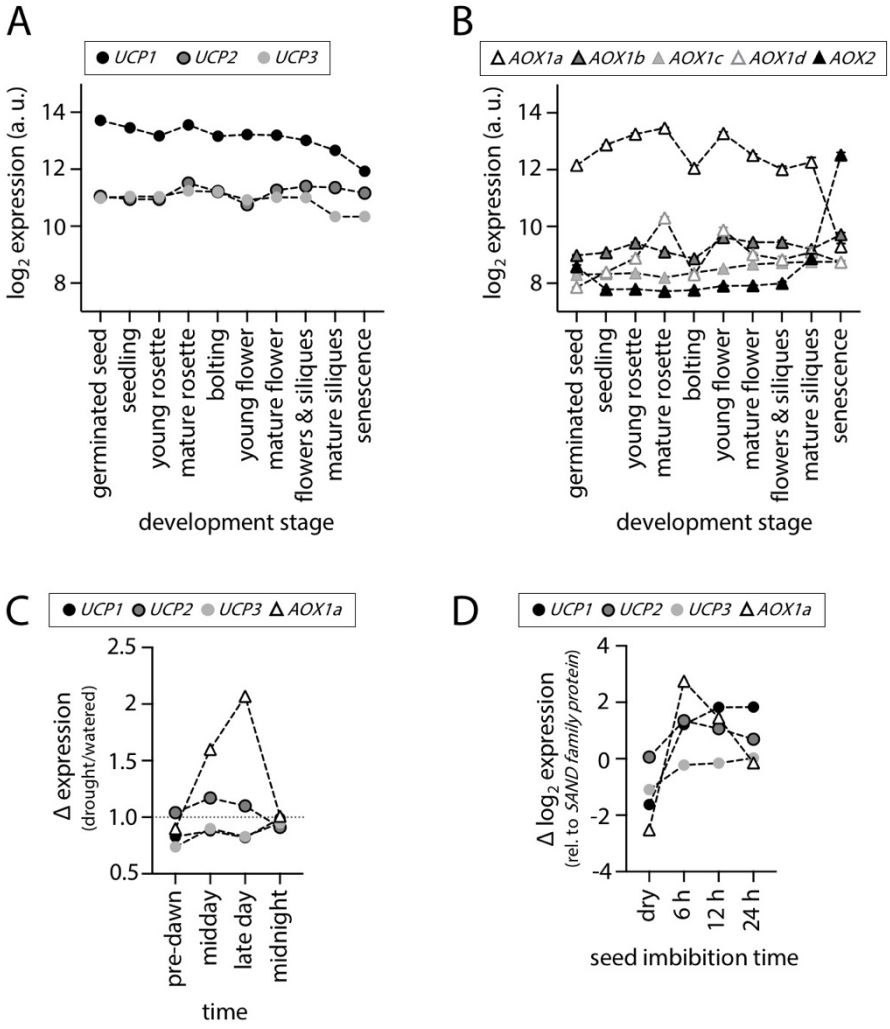

Figure 5: Gene expression of *AOX* and *UCP* isoforms during plant development and drought stress in Arabidopsis.

(**A**) and (**B**) represent whole plant average expression levels of *Alternative Oxidase* (*AOX*) and *Uncoupling Protein* (*UCP*) isoforms, respectively, at different time points during plant development. Y-axes: Log_2 expression values (a.u.) from ATH1 Genechips. Data retrieved via Genevestigator v3 (Hruz et al., 2008). (**C**) Comparison of expression level changes from *UCP* isoforms and *AOX1a* in rosette leaves of 32-d-old plants in response to drought. Y-axis: Ratio of expression levels measured under drought compared to well-watered conditions. Data from Wilkins et al., 2010. (**D**) Comparison of expression levels from *UCP* isoforms and *AOX1a* in seeds during seed imbibition relative to *SAND family protein*. Data from Nakabayashi et al., 2005. Expression data in (C) and (D) were retrieved via eFP Browser (Winter et al., 2007).

amino acids, whereas *At*UCP3 only shares 35% and 37% in similarity with *At*UCP1 and *At*UCP2, respectively (Figure 6) (Monné et al., 2018). Given the dissimilarity of UCP3 and the fact that empirical characterisations almost exclusively relied on *At*UCP1, the exact number of *UCP*-like genes in Arabidopsis is still debated but mostly considered to encompass *UCP1–UCP3* (Nogueira et al., 2011; Haferkamp and Schmitz-Esser, 2012).

The most highly expressed isoform in Arabidopsis is *UCP1*, but in contrast to some of the *ND* and *AOX* isoforms, expression of *UCP*s in general is relatively stable under most stress-treatments and throughout development (Figure 5A, C) (Clifton et al., 2005; Nogueira et al., 2011). Nonetheless, there are exceptions, such as low temperatures or seed germination leading to an increased expression of *AtUCPs* (Figure 5D) (Clifton et al., 2005; Nogueira et al., 2011). The absence of pronounced changes in expression suggest that regulation primarily occurs at the post-transcriptional levels. Supporting evidence for this comes from functional characterisations of plant UCP. Employing purified coupled mitochondria or functional reconstitution experiments confirmed *bona fide* proton gradient uncoupling activity of UCP (Borecký et al., 2001; Smith et al., 2004; Considine et al., 2003). Analogously to their mammalian counterparts, plant UCP proton conductance is activated by superoxide and aldehyde products of lipid peroxidation and inactivated by purine nucleotides (Ježek et al., 1996; Jarmuszkiewicz et al., 1998; Borecký et al., 2001; Considine et al., 2003; Smith et al., 2004; Sweetlove et al., 2006). Interestingly, the proton gradient-uncoupling activity of UCP as suggested by several independent studies was challenged very recently based on the *in vitro* reconstitution of *At*UCP1 and *At*UCP2 in phospholipid vesicles (Monné et al., 2018). Electroneutral transport function for organic and amino acids was suggested instead. Transport function is conceivable in principle, considering that the uncoupling mechanism of mammalian UCPs likely relies on fatty acid shuttling (Berardi and Chou, 2014; Crichton et al., 2017) and UCPs belong to mitochondrial carrier family (Palmieri et al., 2011; Haferkamp and Schmitz-Esser, 2012). Nevertheless, the interpretations by Monné et al. (2018) deserve experimental follow up since the lack of a membrane potential and absence of biochemical UCP activators render any deduction of UCP function in functional mitochondria or full *in vivo* conditions highly speculative.

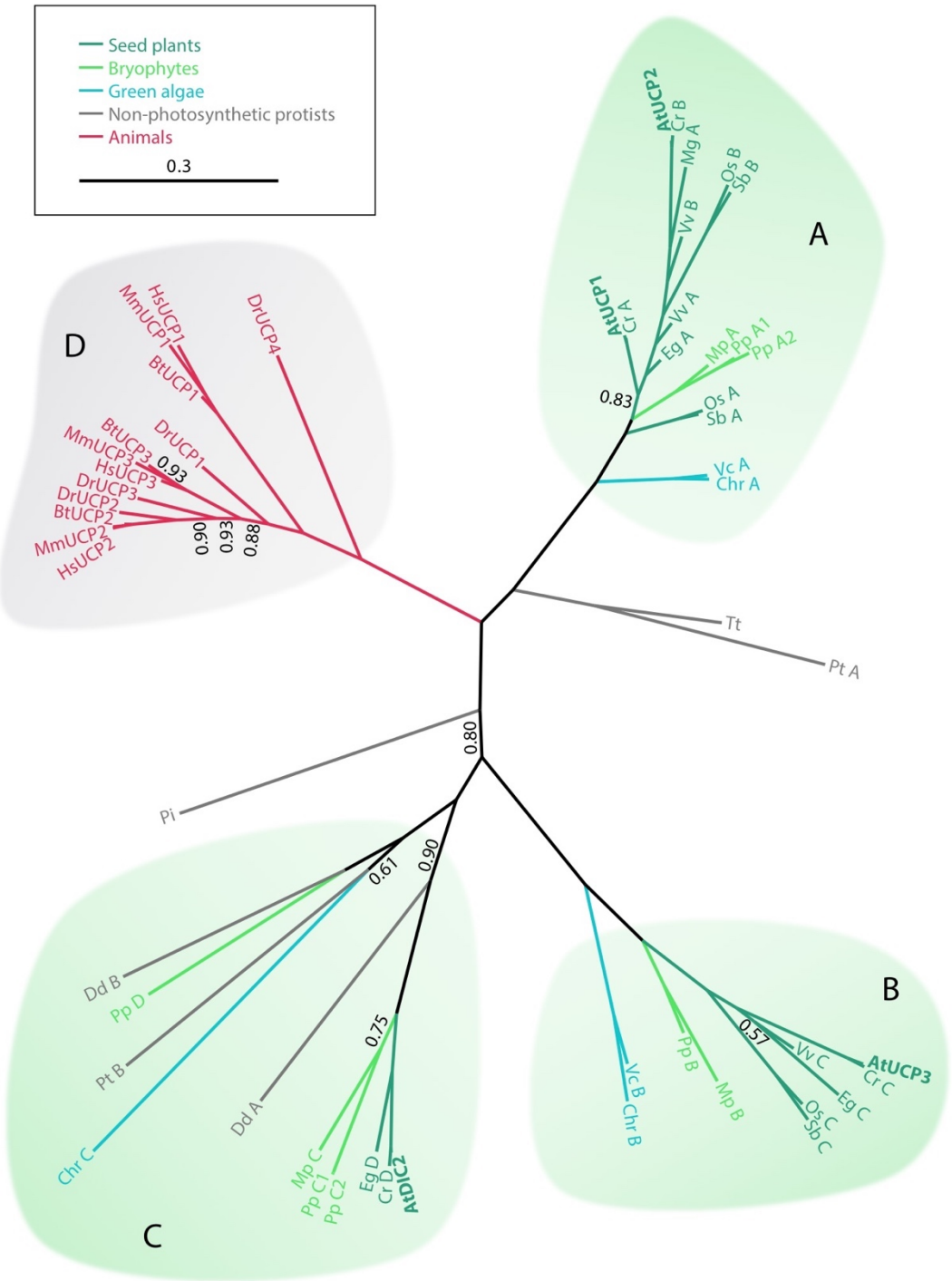
Seed plants
Bryophytes
Green algae
Non-photosynthetic protists
Animals
0.3
A
B
C
D
AtUCP2
Cr B
Mg A
Os B
Sb B
Vv B
AtUCP1
Cr A
Vv A
Eg A
Mp A
Pp A1
Pp A2
Os A
Sb A
Vc A
Chr A
0.83
HsUCP1
MmUCP1
BtUCP1
DrUCP4
BtUCP3
MmUCP3
HsUCP3
DrUCP1
DrUCP3
DrUCP2
BtUCP2
MmUCP2
HsUCP2
0.93
0.90
0.93
0.88
Tt
Pt A
0.80
Pi
0.61
0.90
Dd B
Pp D
Pt B
Chr C
Dd A
0.75
Mp C
Pp C1
Pp C2
Eg D
Cr D
AtDIC2
Vc B
Chr B
Pp B
Mp B
0.57
Vv C
AtUCP3
Cr C
Eg C
Os C
Sb C

Figure 6: Phylogenetic tree of human UCP1 and its homologs from representative protist, plant and animal species.
Amino acid sequences of representative species were retrieved from NCBI blasted against *Homo sapiens* Uncoupling Protein 1 (UCP1) and shown as unrooted tree calculated with MrBayes. Scale bar represents 30 substitutions per 100 amino acids. Numerical values along the tree represent bootstrap values of respective branching (only values < 0.95 indicated). (**A**), (**B**) (**C**) and (**D**) refer to distinct clusters within phylogenetic tree. At: *Arabidopsis thaliana*, Bt: *Bos taurus*, Cr: *Capsella rubella*, Chr: *Chlamydomonas reinhardtii*, Dr: *Danio rerio*, Dd: *Dictyoselium discoideum*, Eg: *Erythranthe guttata*, Hs: *Homo sapiens*, Mm: *Mus musculus*, Mp: *Marchantia polymorpha,* Os: *Oryza sativa*, Pi: *Phytophthora infestans*, Pp: *Physcomitrella patens*, Pt: *Paramecium tetraurelia*, Sb: *Sorghum bicolor*, Tt: *Tetrahymena thermophila*, Vv: *Vitis vinifera*, Vc: *Volvox carteri.*

1.5.4 The role of mitochondrial uncoupling in plants

From a physiological perspective, the enzymes ND, AOX and UCP (henceforth referred to as uncoupling components) act functionally redundant by mediating the uncoupling of substrate oxidation from ADP phosphorylation. The enzymes ND and AOX by-pass proton-translocating complexes and thereby uncouple at level of the ETC, UCP mediates proton flux back across the IMM and thereby uncouples at the level of chemiosmotic potential. Together, the oxidative phosphorylation and the uncoupling systems can achieve flexible stochiometric adjustment of ATP yield per reducing equivalent, *i.e.* ranging from 0 ATP molecules (complete uncoupling) to about 2.5 ATP molecules generated (complete coupling; Alberts et al., 2002) for the oxidation of one NADH molecule.

From an anthropocentric point of view, uncoupling and dissipation of energy as heat seems a wasteful process; unless the aim is thermogenesis. In fact, a small number of plants, such as several Araceae species or titan arum (*Amorphophallus titanium*), have been identified to purposely conduct mitochondrial uncoupling for heat production. The presence of mitochondrial uncoupling components in non-thermogenic plants, and interestingly also UCP in ectothermic animals (Stuart et al., 1999), points towards roles beyond thermogenesis. It has been well-established in animals and plants that mitochondrial uncoupling attenuates ROS production and protects against cellular damage (Maxwell et al., 1999; Smith et al., 2004; Brand and Esteves, 2005). The presence of a multi-layered uncoupling system suggests particular importance in plants, yet, its relevance under physiological conditions is insufficiently understood for more far-reaching conclusions.

An important consideration is that autotrophic plant cells in the light are typically not restricted in energy. Rather than optimal usage of energy resources, maintenance of homeostasis at highly variable external conditions is of key importance. Drought or high light in particular contribute to a state of cell physiology in which removal of excess reductant is of vital importance. Mitochondrial uncoupling in plants then provides a safe electron sink to maintain homeostasis of the metabolic redox pools and prevent excessive formation of ROS such as singlet oxygen, superoxide or hydrogen peroxide by the chloroplast or the mitochondrion (Giraud et al., 2008; Barreto et al., 2017). Specifically, uncoupling allows (up)regulation of metabolic fluxes 'on demand' to provide, for instance, carbon skeletons for biosynthesis, high photorespiratory flux through glycine decarboxylase or oxidation of large amounts of proline as a part of recovery from stress. The importance of uncoupling in plants for maintaining photosynthesis under abiotic stress conditions has been demonstrated by reverse genetic approaches. A T-DNA insertion mutant of *At*UCP1 revealed a specific inhibition of photorespiration. The mutant exhibited a decreased glycine-to-serine oxidation rate which manifested in a decreased carbon assimilation rate and lower shoot biomass accumulation (Sweetlove et al., 2006). In contrast, tobacco plants overexpressing *AtUCP1* were able to tolerate drought better as judged by higher photosynthesis rates, higher biomass and seed yield (Begcy et al., 2011; Barreto et al., 2017). Knock-out *aox1a* Arabidopsis plants revealed higher non-photochemical and lower photochemical quenching proportions in response to combined drought stress and moderate light. Apart from the lowered photosynthetic efficiency, superoxide production and anthocyanin accumulation were increased, indicating disturbed redox metabolism (Giraud et al., 2008). Consistent effects on photosynthesis were also detected upon treatment of wheat leaves with the AOX inhibitor salicylhydroxamic acid (SHAM) (Bartoli et al., 2005).

1.6 Live monitoring plant energy metabolism with genetically encoded biosensors

The rise of genetically encoded fluorescent biosensors has revolutionised the way how biology can be studied by providing a novel, highly versatile and specific analytical approach to *in vivo* monitor concentrations or dynamics of bioanalytes or bioactivities. Genetically encoded fluorescent biosensors typically consist of one or more fluorescent

proteins (FPs), which are functionalised to (reversibly) bind or react with a specific chemical compound. Depending on the status of the functional group, the fluorescent properties of the FPs change, which can be optically monitored. Ideally, the biosensor enables specific monitoring of a defined analyte or physical parameter at high spatiotemporal resolution with minimal perturbation of the biological system.

The ability to real-time monitor at high spatiotemporal resolution has proven particularly powerful to elucidate rapid or highly compartmentalised processes, such as neuronal circuits in animals (Knöpfel, 2012) or pH microcompartments in the mitochondrial IMS in human cells (Rieger et al., 2014). Genetically encoded biosensors have also found widespread applications in plants and enabled the generation of unprecedented insights into the dynamic nature of plant physiology. The studies focussed on paramters such as Ca^{2+}, redox conditions, pH, primary metabolites, ROS production, phytohormones or nutrients on whole plant down to on a subcellular level (Hilleary et al., 2018; Walia et al., 2018). Although the biosensors are specific for different parameters, they work according to related principles and thus the following section focusses on the biosensors applied in this study.

A well-established sensor in plants is the redox-sensitive Green Fluorescent Protein 2 (roGFP2) fused to human Glutaredoxin 1 (Grx1) to monitor the glutathione redox potential (E_{GSH}). The sensor is ratiometric by excitation and consists of a GFP molecule with two cysteine residues engineered to two juxtaposed β-sheets at the β-barrel surface, which can be oxidised to form a disulfide bridge through a specific, reversible and rapid equilibration reaction with the ambient E_{GSH} (Marty et al., 2009; Meyer and Dick, 2010; Schwarzländer et al., 2016) (Figure 7). Since their introduction, Grx1-roGFP2 and closely related variants of the biosensor have been used to investigate plant redox dynamics in several studies over the recent years (Marty et al., 2009; Aller et al., 2013; Dubreuil-Maurizi et al., 2011; Albrecht et al., 2014; Attacha et al., 2017).

The fluorescence properties of a circularly permuted Yellow Fluorescent Protein (cpYFP) variant, originally used as a core structure of the Ca^{2+} sensor Pericam (Nagai et al., 2001), are highly sensitive to pH. The circular permutation introduces a cleft into the YFP β-barrel structure and renders the chromophore, which is typically shielded by the GFP β-barrel structure, accessible to de-/protonation in dependence of the surrounding medium pH. As for roGFP2, the sensor is ratiometric by excitation (Figure 7) (Schwarzländer et al.,

2014). Applications of cpYFP in Arabidopsis have focused on mitochondria where pH changes constitute a central component of mitochondrial energy physiology (Schwarzländer et al., 2011, 2012).

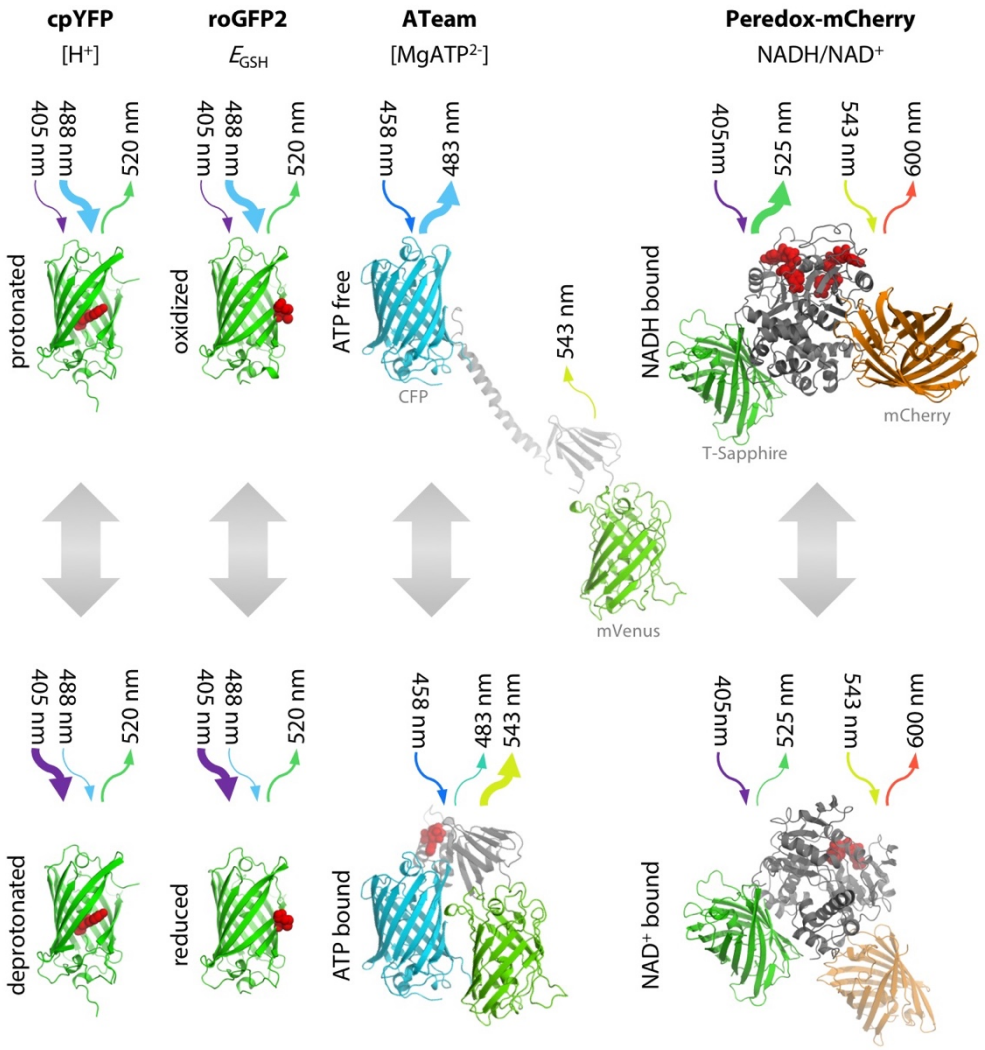

Figure 7: Spectral dynamics and conformational models of four genetically encoded fluorescent biosensors.

Figure modified from Stephan Wagner.

(left to right) CpYFP (circularly permuted Yellow Fluorescent Protein): A cleft in the protein's β-barrel allows direct de-/protonation of the chromophore (red) in dependence of the pH environment, leading to a ratiometric change in excitation efficiencies (Schwarzländer et al., 2014). RoGFP2 (redox-sensitive Green Fluorescent Protein): Oxidation/reduction of two engineered cysteine residues (highlighted in red) on the barrel's surface results in the formation/breakage of a disulfide bond in dependence of the redox environment. This small structural change leads to ratiometric changes in excitation efficiencies (Dooley et al., 2004; Hanson et al., 2004). *(continued on next page)*

(Figure 7 continued)
ATeam (Adenosine 5'-triphosphate indicator based on epsilon subunit for analytical measurements): Förster Resonance Energy Transfer (FRET)-based sensor constituted by a monomeric super-enhanced Cyan Fluorescent Protein (mseCFP; cyan) and a circularly permuted monomeric Venus (cp173-mVenus; green). $MgATP^{2-}$ (molecule highlighted in red) -binding by the connecting ε-subunit induces a conformational sensor rearrangement leading to changes of FRET efficiency between chromophores (Imamura et al., 2009; Kotera et al., 2010). Peredox-mCherry: a circularly permuted T-Sapphire (green) integrated into a bacterial NADH-binding protein, Rex. Binding of either NADH or NAD^+ (molecule highlighted in red) to the same binding pocket(s) in Rex induces a conformational change and alters the fluorescence excitation and emission of T-Sapphire. Normalisation to protein abundance is possible through fusion with mCherry (orange) that is insensitive to the NAD redox state (Hung et al., 2011; Hung and Yellen, 2014). Downward and upward arrows indicate common sensor fluorescence excitation and emission wavelengths, respectively.

The biosensor ATeam1.03-nD/nA (Adenosine 5'-Triphosphate indicator based on epsilon subunit for analytical measurements) to measure $MgATP^{2-}$ concentration was initially characterised in human HeLa cells and subsequently established for *in vivo* sensing in plants (Imamura et al., 2009; Kotera et al., 2010; De Col et al., 2017). The $MgATP^{2-}$-binding ε-subunit fragment of the ATP synthase from *Bacillus* sp. represents the sensory module, which is sandwiched by two fluorescent proteins, the Cyan Fluorescent Protein (mseCFP) and a circularly permuted monomeric Venus (mVenus). Reversible binding of $MgATP^{2-}$ leads to conformational rearrangements and thereby to altered Förster Resonance Energy Transfer (FRET) efficiencies (Figure 7). The biosensor was successfully applied in Arabidopsis to monitor changes in cytosolic $MgATP^{2-}$ concentrations in response to processes, such as wounding of leaves or low oxygen stress in seedlings (De Col et al., 2017).

The Peredox-mCherry sensor consists of a bacterial NAD(H)-sensing protein (Rex) which is directly linked to a circularly permuted GFP variant (T-Sapphire). Upon binding of either NADH or NAD^+, Rex undergoes a conformational change coupled to changes in the T-Sapphire fluorescence intensity. The expression levels are normalised via the C-terminally attached, NAD(H)-inert mCherry (Figure 7). Peredox-mCherry was initially described in mouse cells and was recently also introduced into the basidiomycete *Ustilago maydis* (Hung et al., 2011; Hung and Yellen, 2014; Hartmann et al., 2018). Application of the biosensor in plants has not been published, but comprehensive *in vitro* and *in planta* characterisations are in progress in the host lab (Negroni, 2017).

The small selection of fluorescent protein biosensors introduced here offer reasonable coverage of different parameters directly or closely related to energy physiology in plants. In combination with innovative fluorimetric monitoring methods, the biosensors appear suited to elucidate compartmentalised changes of energy metabolism in response to drought or other stress conditions *in vivo*.

1.7 Objectives of the study

The reactions of plants to drought encompass a multifaceted set of sophisticated adjustments. One of the most well-studied short-term responses is the reduction of stomatal aperture. This leads to changes in the leaf internal gas homeostasis, a repression of carbon assimilation and an increased photorespiration (Dietz and Heber, 1983). An excess of cellular reductant requires safe disposal and mitochondrial electron transport has been proposed to provide a flexible electron sink. This flexibility is supported by the ability to uncouple substrate oxidation from ADP phosphorylation. Mitochondrial uncoupling is mechanistically underpinned by proteins dissipating energy at the levels of either the ETC or the chemiosmotic potential. However, despite implicit functional overlap and some similarities in the phenotypic impairments observed for uncoupling mutants (Sweetlove et al., 2006; Giraud et al., 2008; Barreto et al., 2017), the question arises to what extent both mechanistic layers of uncoupling are able to cooperate and complement each other functionally. The two systems have not been investigated side-by-side or in combination so far. The key objective of the presented work was therefore:

1. *To establish the role of mitochondrial uncoupling in the plant response to drought and other abiotic stresses.*

This objective was further refined based on the unexpected observation of a pronounced phenotype of the uncoupling mutants to the thiol-reductant dithiothreitol:

2. *To identify the underlying mechanism by which mitochondrial uncoupling contributes to the tolerance of plants towards thiol-based reductant.*

Related to the attempt to understand the physiological significance of uncoupling, a final technical objective was:

3. *To measure pH gradients between different mitochondrial subcompartments to gain in vivo insights into plant energy physiology.*

2 MATERIALS AND METHODS

2.1 Consumables and laboratory equipment

2.1.1 Consumables

General chemicals were purchased from AppliChem (www.applichem.com/home), Sigma-Aldrich (www.sigmaaldrich.com), Duchefa (www.duchefa-biochemie.com), Merck (www.merckmillipore.de) and Roth (www.carlroth.com). General plastic ware was purchased from Sarstedt (www.sarstedt.com/home) and VWR (de.vwr.com/store). Micropore tape was purchased from 3M (www. 3mdeutschland.de).

2.1.2 Enzymes, specific materials and kits

Enzymes, specific material and kits employed for conducting described experiments are described in Table 1 and Table 2.

Table 1: Enzymes used in this study.

Enzyme	Manufacturer
BP clonase II enzyme mix	Invitrogen™, www.thermofisher.com
LR clonase II enzyme mix	Invitrogen™, www.thermofisher.com
*Avr*II endonuclease	New England Biolabs®, www.neb.com
*Bsa*I endonuclease	New England Biolabs®, www.neb.com
*Bpi*I endonuclease	New England Biolabs®, www.neb.com
*Nde*I endonuclease	New England Biolabs®, www.neb.com
*Pac*I endonuclease	New England Biolabs®, www.neb.com
Thermolysin	Sigma-Aldrich, www.sigmaaldrich.com
Proteinase K	Invitrogen™, www.thermofisher.com
Phusion® High-Fidelity DNA Polymerase	Thermo Scientific, www.thermofisher.com
Taq™ DNA Polymerase	New England Biolabs®, www.neb.com
T4 DNA Ligase	Thermo Scientific, www.thermofisher.com

Table 2: Specific materials and kits used in this study.

Material/kit designation	Manufacturer
HiTrap™ Chelating HP column	GE Healthcare Life Sciences, www.gelifesciences.com
NucleoSpin® Plasmid	Macherey-Nagel, www.mn-net.com
NucleoSpin® RNA	Macherey-Nagel, www.mn-net.com
NucleoSpin® Gel and PCR Clean-up	Macherey-Nagel, www.mn-net.com
PerfeCTa SYBR Green FastMix	Quantabio, www.quantabio.com
qScript™ cDNA Synthesis Kit	Quantabio, www.quantabio.com
RevertAid First Strand cDNA Synthesis	Thermo Scientific, www.thermofisher.com
GFP Tag Antibody	Thermo Scientific, www.thermoscientific.com
Goat anti-rabbit poly-horseradish peroxidase secondary antibody	Thermo Scientific, www.thermoscientific.com
Pierce ECL Western Blotting Substrate	Thermo Scientific, www.thermoscientific.com
Roti-Quant®	Roth, www.carlroth.com

2.1.3 Laboratory equipment

Laboratory equipment employed in this study to conduct the experiments is listed in Table 3.

Table 3: Technical equipment used in this study.

Device	Manufacturer
A1000 plant growth chamber	Conviron, www.conviron.com
Airstream® Class II Biological Safety	ESCO, www.escoglobal.com
Analytical Balance Summit SI-234	Denver Instrument, www.denverinstrument.com
ÄKTA Prime Plus chromatography	GE Healthcare, www.gelifesciences.com
ÄKTAdesign 50 mL superloop	GE Healthcare, www.gelifesciences.com
Beckman Centrifuge Avanti® J-26-XP	Beckman, www.beckmancoulter.com
Beckman Rotor JA-10	Beckman, www.beckmancoulter.com
Beckman Rotor JA-25.50	Beckman, www.beckmancoulter.com
C1000™ Thermal cycler	Bio-Rad, www.bio-rad.com
C1000™ Thermal cycler Reaction Module 48W	Bio-Rad, www.bio-rad.com
Canon CanoScanLide 700F	Canon, www.canon.de
Canon EOS 1100D EF-S digital camera	Canon, www.canon.de
CFX96™ Real-Time PCR Detection System	Bio-Rad, www.bio-rad.com
CLARIOstar® plate reader	BMG, www.bmglabtech.com
Electroporator MicroPulser™	Bio-Rad, www.bio-rad.com
Eppendorf BioPhotometer Plus	Eppendorf, www.eppendorf.de
Eppendorf Centrifuge 5424 R	Eppendorf, www.eppendorf.de
Eppendorf Centrifuge 5430	Eppendorf, www.eppendorf.de
Eppendorf Thermomixer™ Comfort	Eppendorf, www.eppendorf.de

Device	Manufacturer
Eppendorf Thermomixer™ Compact	Eppendorf, www.eppendorf.de
Gel documentation MF-ChemiBIS 2.0	DNR Bio-Imaging Systems, www.dnr-is.com
Incubators 28°C Ecotron Typ ET25-TA-RC	INFORS HT, www.infors-ht.com
Incubators 37°C Ecotron Typ ET25-TA-00	INFORS HT, www.infors-ht.com
INTAS ECL Chemostar imager	INTAS, www.intas.de
ISMATEC Peristaltic pump REGLO digita	Ismatec, www.ismatec.com
Labculture® Vertical laminar flow cabinet	ESCO, www.escoglobal.com
Leica DCF425C camera	Leica, www.leica-microsystems.com
Leica M165FC stereomicroscope	Leica, www.leica-microsystems.com
Magnetic Stirrer MR Hei-Mix L	Heidolph, www.heidolph-instruments.de
Metrohm pH-meter 827 pH lab	Metrohm, www.metrohm.com
Mini-PROTEAN® Tetra cell	Bio-Rad, www.bio-rad.com
Mini-PROTEAN® II Multi-casting chamber	Bio-Rad, www.bio-rad.com
Mini Trans-Blot® cell	Bio-Rad, www.bio-rad.com
Nanodrop™ 2000c	Thermo Scientific, www.thermoscientific.com
Orbital platform shaker Unimax 1010	Heidolph, www.heidolph-instruments.de
Oxygraph Clark-type oxygen electrode	Hansatech Instruments,
pH-Meter FE20 – FiveEasy™	Mettler Toledo, www.mt.com
Plant growth chambers	Jan Weiler GmbH, https://www.jan-weiler.de
POLARstar® Omega plate reader	BMG, www.bmglabtech.com
PowerPac Basic™ power supply	Bio-Rad, www.bio-rad.com
PowerPac™ HC power supply	Bio-Rad, www.bio-rad.com
Precision Balance TP1502	Denver Instrument, www.denverinstrument.com
S1000™ Thermal Cycler	Bio-Rad, www.bio-rad.com
S1000™ Thermal Cycler Reaction Module 96W	Bio-Rad, www.bio-rad.com
SONOPULS Ultrasonic Homogenizers HD 2200	Bandelin, www.bandelin.com
T100™ Thermal Cycler	Bio-Rad, www.bio-rad.com
TKA LabTower EDI water purification system	Thermo Electron LED, www.thermofisher.com
UV-lamp, portable	M&S, www.m-und-s-laborgeraete.de
Vacuum concentrator Savant® DNA 120	Thermo Scientific, www.thermofisher.com
Vortex mixers Scientific Industries	Scientific Industries, www.scientificindustries.com
Zeiss Axio Observer Z1 Zeiss	Zeiss, www.zeiss.de
Zeiss confocal microscope LSM780	Zeiss, www.zeiss.de
Zeiss Plan-Apochromat 63x/1.40 Oil DIC M27	Zeiss, www.zeiss.de

2.2 Plant methods

2.2.1 Plant material

Experiments were based on *Arabidopsis thaliana* ecotype Columbia-0 (Col-0) wild-type (WT) and/or on different T-DNA mutant (Table 4) plants. *ucp1* T-DNA

insertion and its complemented lines, cUCP1 #9 and #14 were kindly provided by Lee Sweetlove, Oxford. The T-DNA insertion lines for *ucp2*, *ucp3* and *aox1a* were ordered from the Nottingham Arabidopsis Stock Centre. The corresponding double and triple mutants were established by crossing in this study. The Arabidopsis sensor lines used for confocal microscopy and multiwell plate reader-based fluorimetry are listed in Table 5.

Table 4: *Arabidopsis thaliana* T-DNA insertion lines investigated or propagated to higher order mutants. Underlined references include *in vivo* characterisation of the T-DNA line. Not underlined references describe the corresponding gene/protein but T-DNA mutants have not yet been characterised. An execption to that is *ucp2* for which a characterisation was published during the course of this study (Monné et al., 2018).

Name	Locus/loci	Line	Main reference
ucp1	*AT3G54110*	SAIL 536_G01	Sweetlove et al. (2006)
cUCP1 #9	*AT3G54110*	SAIL 536_G01 complemented with p*UCP1*::*UCP1*	Sweetlove et al. (2006)
cUCP1 #14	*AT3G54110*	SAIL 536_G01 complemented with p*UCP1*::*UCP1*	Sweetlove et al. (2006)
ucp2	*AT5G58970*	SALK 080188	Parsons et al. (2012)
ucp3	*AT1G14140*	SALK 091181	Borecký et al. (2006)
aox1a	*AT3G22370*	SALK 084897	Giraud et al. (2008)
ucp1 ucp3	*AT3G54110*, *AT1G14140*	SAIL 536_G01, SALK 091181	
ucp1 aox1a	*AT3G54110*, *AT3G22370*	SAIL 536_G01, SALK 084897	
ucp3 aox1a	*AT1G14140*, *AT3G22370*	SALK 091181, SALK 084897	
ucp1 ucp3 aox1a	*AT3G54110*, *AT1G14140*, *AT3G22370*	SAIL 536_G01, SALK 091181, SALK 084897	

Table 5: *Arabidopsis thaliana* lines stably expressing different biosensors or reporter protein fusions.

Arabidopsis line	Constructed/provided by	Reference
cyt-ATeam 1.03nD/nA	M. Schwarzländer	De Col et al. (2017)
cyt-Peredox-mCherry	M. Schwarzländer	unpublished Arabidopsis line
cyt-GRX1-roGFP2	L. Marty	Marty et al. (2009)
cyt-cpYFP	M. Schwarzländer	unpublished Arabidopsis line
mts-cpYFP	M. Schwarzländer	Schwarzländer et al. (2011)
mts-GFP	D. Logan	Logan and Leaver (2000)
NMT1-GFP	D. Logan	Logan and Leaver (2000)

2.2.2 Plant growth on agar plates

Seeds were surface-sterilised by incubating for 3 min in 70% (v/v) ethanol and washing three times with sterile water prior to transfer onto 92 x 16 mm Petri dishes containing 25 mL of freshly prepared standard growth medium (half-strength Murashige and Skoog medium (MS; Murashige and Skoog, 1962), 10 mM MES pH 5.8, 0.1% (w/v)

sucrose, 1% (w/v) agar). After sealing the agar plates with Parafilm and stratification for at least 2 d in the dark at 4°C, the plates were transferred to growth cabinets and vertically grown under long-day conditions (16 h 75–100 µmol photons m^{-2} s^{-1} at 22°C, 8 h darkness at 18°C).

2.2.3 Plant growth in hydroponic cultures

Arabidopsis seedlings were grown in hydroponic pots for 16 d as described by Sweetlove et al. (2007) under long-day conditions (16 h 50–75 µmol photons m^{-2} s^{-1} at 22°C; 8 h darkness at 18°C). Sterile glass pots were filled with 50 mL liquid medium (half-strength MS medium including vitamins, 2% (w/v) sucrose, 0.04% (w/v) MES pH 5.8 with KOH and 0.1% (w/v) microagar carefully spread on top of the medium. After autoclaving, pots were moved to a laminar flow hood and ~5 mg of surface-sterilised Arabidopsis seeds (incubated in 70% (v/v) ethanol gently shaking for 5 min, subsequently in 5% (v/v) sodium hypochlorite and 0.1% (v/v) TWEEN-20 for 30 min before thoroughly washed 3–5 times with sterile water) (modified from Clough and Bent, 1998) were carefully placed on top of solidified floating agar discs. Pots were closed with transparent plastic lids and sealed with Micropore tape. After stratification for ≥ 2 d at 4°C, pots were transferred onto rotary shakers and gently agitated at ~60 rpm in the growth cabinet for 16 days.

2.2.4 Plant growth on soil

If not indicated otherwise, 3–5 seeds were placed on water-imbibed Jiffy-7 or squared pots filled with a soil mixture (Floradur B-seed, Perlite Perligran 0-6 and quartz sand in a ratio of 10:1:1, respectively) and stratified for at least 2 d in the dark at 4°C and 100% relative humidity. Plants were maintained covered with a transparent plastic dome during the first week after transfer to the growth cabinet (16 h 100–120 µmol photons m^{-2} s^{-1} at 22°C, 8 h darkness at 18°C) to ensure saturated relative humidity during germination. By the time cotyledons were fully developed, plastic domes were removed and plants were thinned out to one plant per pot. Thinning out was omitted for plants dedicated to seed propagation or floral dipping (section 2.2.10). Relative humidity was maintained at ~50% for the remaining part of plant development.

2.2.5 Seedling phenotyping on agar plates

Seedlings germinated and vertically grown for 4–5 d as described in section 2.2.2 were carefully transferred to new agar plates containing 25 mL of standard growth medium plus selected additives to induce abiotic stress. Agar plates were prepared with freshly autoclaved medium cooled down to 50°C, supplemented with sterile-filtered additives (Table 6) and immediately casted. To control for plate effects, 6 seedlings from the WT and corresponding mutant lines were placed side-by-side on the new plates. After sealing with Micropore tape, plates were photographically documented and placed back to the growth cabinet. At indicated timepoints, seedlings were subjected to follow-up photographic documentations. Increase of primary root and total root length were quantified from images with Fiji (www.fiji.sc; Schindelin et al., 2012) (Rueden et al., 2017) or RootReader2D (www.plantmineralnutrition.net/rootreader.htm) (Clark et al., 2013), respectively.

Table 6: Additives for induction of abiotic stress during seedling root phenotyping on agar plates.

Abbreviation	Full name	Solvent	Final conc.	Supplier
AA	Antimycin A from *Streptomyces*	DMSO	20 µM	Sigma-Aldrich
DTT	Dithiothreitol	H_2O	350–1000 µM	Roth
man	Mannitol	H_2O	300 mM	Roth
NAA	Naphthaleneacetic acid	KOH	75 nM	Sigma-Aldrich
NaCl	Sodium chloride	H_2O	50–150 mM	Fisher Chemical
SA	Salicylic acid	EtOH	100 µM	Roth
sorb	Sorbitol	H_2O	200 mM	Roth
TM	Tunicamycin from *Streptomyces*	DMSO	25–500 ng mL^{-1}	Sigma-Aldrich

2.2.6 Whole plant phenotyping on soil

Plants were grown at standard conditions on Jiffy-7 or squared pots as described in section 2.2.4. Plants were either maintained at standard conditions or exposed to stress-inducing conditions detailed in individual phenotyping experiments. Leaf rosette area development was documented photographically from the top perspective and analysed with a custom Leaf Lab tool (Version 1.41) described in Wagner et al. (2015a). Height of the primary inflorescence was documented with a camera from a perpendicular angle and quantified using Fiji (www.fiji.sc) (Schindelin et al., 2012; Rueden et al., 2017).

2.2.7 Dark-induced leaf senescence

The third true leaf from 3-week-old plants grown on Jiffy-7 under standard conditions (section 2.2.4) was gently cut and incubated for 5 d in a Petri dish floating on assay medium (10 mM MES pH 5.8, 5 mM KCl, 10 mM $MgCl_2$, 10 mM $CaCl_2$) (De Col et al., 2017) in the dark. Progression of senescence, referred to as greenness, was quantified based on pixel-wise division of green by red colour intensities retrieved from RGB-encoded images using Fiji (www.fiji.sc; Schindelin et al., 2012; Rueden et al., 2017).

2.2.8 Seed germination efficiency

Non-dormant, synchronised Arabidopsis seeds harvested from plants grown under standard conditions were incubated for 3 min in 70% (v/v) ethanol and washed three times with sterile water before they were transferred onto squared Petri dishes containing 50 mL of standard growth medium. To control for plate effects, seeds of WT and mutant lines were placed side-by-side on the same agar plate. After sealing with Parafilm, plates were transferred to growth cabinets without prior stratification. After 2 days, germination efficiency (radicle penetrating endosperm and testa) was evaluated at the stereomicroscope.

2.2.9 Transient transformation of *Nicotiana benthamiana* tobacco plants

Agrobacterium tumefaciens AGL-1 or C58C1 cells transformed with the designated construct were grown for 24 h at 28°C and 160 rpm in 5 mL Lysogeny broth medium (LB) containing the appropriate antibiotics. Bacteria were washed twice with sterile water, which was also used as infiltration medium. OD_{600} was adjusted to 0.5–1.0. Two–five days after infiltration, plants were subjected to confocal imaging.

2.2.10 Stable transformation of *Arabidopsis thaliana* plants

Arabidopsis plants were grown on soil under long-day conditions (section 2.2.4) and the primary inflorescence branch was removed to increase the number of inflorescence branches and numbers of flowers per plant, prior to the plant transformation following the protocol established by Clough and Bent (1998). *Agrobacterium tumefaciens* AGL-1 or C58C1 cells transformed with the designated construct were grown at 28°C and 220 rpm in 400 mL LB medium containing the appropriate antibiotics until an OD_{600} of 0.8–1.0. Cells were harvested by centrifugation at 5,000 *g* for 10 min and resuspended in dipping

medium (5% (w/v) sucrose and 0.02% (v/v) surfactant Silwet L-77) to a final OD_{600} of 1.0. After dipping the inflorescence branches for ~5 s in suspension, plants were maintained for 12–18 h in the dark at room temperature and 100% relative humidity. After the incubation, plants were returned to standard growth conditions. Seeds were harvested and selected for positively transformed plants by antibiotic/herbicide resistance or/and fluorescence as described below. Plants transformed with constructs containing the bialaphos resistance (bar) gene as selection marker were sown on soil at high density under long-day conditions. After 2 days of stratification, pots were sprayed with a 240 mg L^{-1} glufosinate ammonium solution (Basta) and transferred to growth cabinets. Spraying was repeated one week later. Plants transformed with constructs containing the hygromycin phosphotransferase resistance gene (hpt) were screened *in vitro* following a modified protocol established by Harrison et al. (2006). Seeds were surface-sterilised and grown on agar plates containing standard growth medium supplemented with 20 µg mL^{-1} hygromycin B. Plants transformed with a fluorescent reporter gene were additionally screened at the stereomicroscope employing either a GFP filter (excitation: 470 ± 20 nm, emission: 525 ± 25 nm) or a DsRed filter (excitation: 545 ± 15 nm, emission: 620 ± 30 nm), depending on the reporter protein.

2.3 Bacteriological methods

2.3.1 Bacterial strains

Bacterial *Escherichia coli* and *Agrobacterium tumefaciens* strains used in the described experiments are listed in Table 7.

Table 7: *Escherichia coli* and *Agrobacterium tumefaciens* strains used in this study.

Bacterial strain	Genotype
A. tumefaciens AGL-1	AGL-0 (C58 pTiBo542) recA::bla, T-region deleted Mop(+) Cb(R). AGL-0 background based on EHA101 with T-region deleted (Δ*aph*)(Rif^R, Amp^R) (Lazo et al., 1991)
A. tumefacines C58C1	C58 background; T$_i$-plasmid cured (Rif^R, Amp^R) (Deblaere et al., 1985)
E. coli BL21 DE3	F$^-$ *ompT gal dcm lon hsdS$_B$*($r_B^- m_B^-$) λ(DE3 [*lacI lacUV5-T7p07 ind1 sam7 nin5*]) [*malB*$^+$]$_{K-12}$(λ^S) (Studier and Moffatt, 1986)
E. coli DB3.1	F$^-$ *gyr*A462 *end*A1 Δ(*sr*1-*rec*A) *mcr*B *mrr hsd*S20(r_B^- m_B^-) *ara*-14 *gal*K2 *lac*Y1 *pro*A2 *rps*L20 (Sm^R) *xyl*5 Δ *leu mtl*1 λ$^-$ (Invitrogen)
E. coli DH5α	F$^-$ Φ80*lac*ZΔM15 Δ(*lac*ZYA-*arg*F) U169 *rec*A1 *end*A1 *hsd*R17 (r_K^-, m_K^+) *pho*A *sup*E44 *thi*-1 *gyr*A96 *rel*A1 λ$^-$ (Stratagene)
E. coli Rosetta 2 DE3	F$^-$ *ompT hsd*S$_B$(r_B^- m_B^-) *gal dcm* (DE3) pRARE2 (Cam^R) (Novagen)
E. coli TOP10	F$^-$ *mcrA* Δ(*mrr-hsd*RMS-*mcr*BC) Φ80*lac*ZΔM15 Δ*lac*X74 *rec*A1 araD139 Δ(*ara-leu*)7697 *gal*U *gal*K *rps*L (Str^R) *end*A1 *nup*G (Invitrogen)

2.3.2 Bacterial growth

Bacteria were cultivated in liquid LB medium (1% (w/v) tryptone, 0.5% (w/v) yeast extract, 1% (w/v) NaCl, pH 7 with NaOH) (Bertani, 1951) at 160 rpm and 37°C (*E. coli*) or 28°C (*A. tumefaciens*). For growth on plates with solid LB medium, 2% (w/v) agar was added before autoclaving. Appropriate amounts of the corresponding sterile-filtered antibiotics were added after autoclaving (Table 8). For glycerol stocks, 1 mL of bacterial culture with an OD_{600} of ~1 was added to 0.6 mL 80% (v/v) glycerol and stored at -86°C.

Table 8: Working concentrations of antibiotics.

Antibiotic	Abbreviation	Working concentration [µg mL^{-1}]
Ampicillin	amp	100
Carbenicillin	carb	100
Gentamycin	gent	50
Kanamycin	kan	50
Rifampicin	rif	50
Spectinomycin	spec	100
Streptomycin	str	100

2.3.3 Transformation of *A. tumefaciens* cells by electroporation

Electro-competent *A. tumefaciens* cells were transformed employing a Micropulser electroporator according to the manufacturer's protocol. Amounts of 40 µL of *A. tumefaciens* cells were thawed on ice and 1 µL plasmid added. After 10 min incubation

on ice, the cell-plasmid suspension was loaded to a pre-chilled electroporation cuvette and pulsed with 2.500 V for ~5 ms. Immediately after pulsing, 500 µL LB medium was added and the bacteria suspension was incubated at 28°C and 160 rpm for 1–2 h. To select for transformed cells, 50–200 µL of bacterial suspension was spread onto agar plate with LB medium and selective antibiotics. After growth at 28°C for ~2 d, colonies were examined via colony-PCR.

2.3.4 Transformation of *E. coli* cells by heat-shock

Chemically competent *E. coli* cells were transformed by heat-shock. Amounts of 100 µL of *E. coli* cells were thawed on ice and 1 µL plasmid added. After 10 min of incubation on ice, cells were heat-shocked at 42°C for 75 s and immediately transferred back on ice for 2 min. After the addition of 600 µL LB or SOC (2% (w/v) tryptone, 0.5% (w/v) yeast extract, 10 mM NaCl, 10 mM $MgCl_2$, 20 mM glucose, pH 7 with NaOH) (modified from Hanahan, 1983), bacterial suspension was incubated at 37°C and 160 rpm for 1 h. To select for transformed cells, bacteria were concentrated by gentle centrifugation and spread onto agar plate with LB medium and selective antibiotics. After growth at 37°C for ~12 h, colonies were tested via colony-PCR.

2.3.5 Plasmid isolation from *E. coli* cells

For plasmid extraction, 5 mL LB medium containing the selective antibiotics was inoculated with bacteria and grown overnight at 37°C and 160 rpm. Plasmid DNA was isolated with the NucleoSpin Plasmid kit following the protocol of the manufacturer (Macherey-Nagel).

2.4 Protein methods

2.4.1 Recombinant protein expression and purification

Recombinant protein purification was conducted as described in De Col et al. (2017) with minor modifications. *E. coli* Rosetta 2 (DE3) or BL21 cells harbouring the plasmid pETG10A:cpYFP and pETG10:Peredox-mCherry were received from M. Schwarzländer, Bonn (Schwarzländer et al., 2014) and Y. L. Negroni, Bonn (Negroni, 2017), respectively. A starting culture of 50 mL LB including selective antibiotics was

inoculated. After incubation overnight at 37°C and 160 rpm, 5 mL was used to inoculate the main culture of 500 mL LB containing selective antibiotics. The culture was grown in a baffled flask under the conditions described above (2.3.2) to an OD_{600} of 0.2–0.3 before being transferred to continuing growth at 21°C. After reaching an OD_{600} of 0.6, 0.2 mM isopropyl-β-D-thiogalactopyranosid was added to induce protein expression overnight. Cells were harvested by centrifugation at 4,000 *g* and 4°C (pre-chilled centrifuge) for 15 min, washed in 50 mL binding buffer (50 mM Tris-HCl pH 8.0, 250 mM NaCl, 20 mM imidazole) and centrifuged again as described before. Washed pellet was subjected to cell lysis by freezing in liquid nitrogen, thawing on ice and subsequently resuspended in 15 mL lysis buffer (50 mM Tris, 250 mM NaCl, 20 mM imidazole, 1 mg mL^{-1} lysozyme, 0.1 mg mL^{-1} DNaseI and 0.2 mM PMSF). After incubation on ice for 30 min, suspension was subjected to 4 intervals of 2 min ultrasonication (40% power output, 50% duty cycle) and 5 min incubation on ice to avoid extensive warming. Cell debris was removed by centrifugation at 40,000 *g* and 4°C for 15 min and supernatant loaded onto a Ni-NTA HiTrap column via a 50-mL-ÄKTAdesign superloop. Proteins were eluted from the column with an imidazole gradient (10–250 mM in 100 mM Tris-HCl, pH 8.0, 250 mM NaCl) using an ÄKTA Prime Plus chromatography system. Fractions with high purity and concentration of recombinant protein were pooled. After estimating protein concentration via Bradford assay (section 2.4.2), 10% (v/v) glycerol was added and aliquoted protein shock-frozen in liquid nitrogen for storage at –86°C.

2.4.2 Estimating protein concentrations

Protein concentrations from recombinant protein purifications or from isolated mitochondria were estimated using the Bradford assays based on bovine serum albumin (BSA) as standard (Bradford, 1976). The appropriately diluted protein of interest was compared with the BSA standards (0.0, 0.1, 0.2, 0.4 and 0.8 mg mL^{-1} BSA) by mixing 10 µL protein solution with 250 µL Bradford reagent (Roti-Quant), incubating for 5 min at room temperature and monitoring absorbance at 595 nm with a POLARstar Omega or a CLARIOstar microplate reader. Standard and protein samples were measure in triplicates.

2.4.3 SDS-PAGE and staining

Prior to the electrophoretic separation of proteins, samples were boiled at 95°C for 6 min in Laemmli sample buffer (2% (w/v) SDS, 50 mM Tris-HCl pH 6.8, 0.002% (w/v) bromophenol blue, 5% (v/v) β-mercaptoethanol and 10% (v/v) glycerol) (Laemmli, 1970). Protein samples were loaded onto a denaturating discontinuous polyacrylamide gel (Williams and Reisfeld, 1964), composed of a 4% stacking gel and a 12% resolving gel. Gel electrophoresis was performed in SDS-running-buffer (25 mM Tris-HCl pH 8.3, 192 mM glycine, 0.1% (w/v) SDS) for ~30 min at 80 V until the proteins entered the stacking gel and for the remaining time at 120 V until bromophenol blue front exited at the bottom of the gel. PageRuler Unstained Protein Ladder (Thermo) was added as molecular mass standard.

After gel electrophoresis, proteins were stained overnight in Colloidal Comassie (10% (w/v) citric acid, 0.08% (w/v) Coomassie Brilliant Blue G250, 8% (w/v) ammonium sulfate and 20% (v/v) methanol). Subsequently, the gel was destained (10% (v/v) acetic acid and 50% (v/v) ethanol) for several hours until the gel background was clear of dye.

2.4.4 Protein blotting and immunodetection

Proteins separated on an unstained SDS page (section 2.4.3) were wet-blotted (40 mA for 16 h at 4°C; blotting buffer: 25 mM Tris, 192 mM glycine, 20% (v/v) methanol) onto a polyvinylidene difluoride membrane (BioTrace PVDF Transfer Membrane; Pall Corporation). After blocking for 1 h in TBS-T buffer (50 mM Tris-HCl pH 7.6, 150 mM NaCl, 0.05 % (v/v) Tween 20) supplemented with 3% (w/v) BSA, the membrane was probed with polyclonal GFP Tag antibody (1:1,000; Thermo). Goat anti-rabbit poly-horseradish peroxidase secondary antibody (1:20,000; Thermo) was used for detection of chemiluminescence using the Pierce ECL Western Blotting Substrate (Thermo).

2.5 Mitochondria methods

2.5.1 Purification of intact mitochondria

Intact mitochondria from 16-d-old Arabidopsis seedlings were isolated following the protocol described by Escobar et al. (2006) with minor modifications. All steps were conducted as far as possible on ice and using pre-chilled (4°C) solutions and instruments. Amounts of ~10–20 g hydroponically grown seedlings were rinsed with cold water and

mortared in 300–350 mL extraction buffer (Table 9). Homogenate was filtered through a layer of Miracloth (Merckmillipore) and residing seedling material mortared again in the presence of ~2 g quartz sand. After repeating the filtering step, cell debris was removed by centrifugation at 1,300 *g* for 5 min. Supernatant was centrifuged at 18,000 *g* for 20 min and carefully resuspended in residual buffer using a wet fine brush before the addition of 300–350 mL wash buffer (Table 9). Both centrifugation steps including fine brush-based pellet resuspension were repeated to concentrate mitochondrial fraction in the cell extract. Resuspended pellet (~2 mL) was loaded on a 0–6% (w/v) PVP gradient (Table 9) and centrifuged at 40,000 *g* for 40 min with disengaged active-deceleration. Yellowish-brown mitochondrial fraction at the lower part of the gradient was recovered using plastic Pasteur pipettes and transferred to ~60 mL final wash medium (Table 9). After splitting into 3 fractions, suspensions were centrifuged at 23,700 *g* for 15 min and mitochondrial pellets resuspended by carefully agitating the tubes. Resuspended mitochondrial fractions were pooled in 20 mL final wash buffer and the centrifugation was step repeated. Supernatant was discarded and mitochondrial pellet resuspended in residual buffer (~500 µL) for subsequent experiments.

Table 9: Compositions of buffer media and gradients for mitochondria purification.
All buffer and gradient solutions were prepared the day before the mitochondrial purification, except for DTT and ascorbic acid, which were added freshly. Two gradient solutions containing 0 and 6% (w/v) PVP-40 were prepared to establish PVP gradient using a gradient mixer.

Buffer	Component	Concentration
Extraction buffer pH 7.4	Sucrose	250 mM
	EDTA	1.5 mM
	MOPS	15 mM
	BSA	0.4% (w/v)
	PVP-40	0.6% (w/v)
	DTT	10 mM
	Ascorbic acid	100 mM
Wash buffer pH 7.5	Sucrose	300 mM
	TES	10 mM
	BSA	0.1% (w/v)
Final wash buffer pH 7.5	Sucrose	300 mM
	TES	10 mM
Gradient solution	Sucrose	300 mM
	TES	10 mM
	BSA	0.1% (w/v)
	Percoll	32% (v/v)
	PVP-40	0–6% (w/v)

2.5.2 Oxygen consumption measurements of purified mitochondria

Respiration of purified mitochondria was analysed using a Clark-type oxygen electrode (Oxygraph, Hansatech) as previously described (Sweetlove et al., 2007; Wagner et al., 2015a). Respiration of 40 µL purified mitochondria was measured in 1 mL basic incubation medium (0.3 M sucrose, 5 mM KH_2PO_4, 10 mM TES-KOH pH 7.5, 10 mM NaCl, 2 mM $MgSO_4$, 0.1% (w/v) BSA) in response to the sequential addition of 10 mM dithiothreitol (Roth), 50 µM nigericin sodium salt (Sigma-Aldrich), 10 µM valinomycin from *Streptomyces fulvissimus* (Abcam), 50 µM antimycin A from *Streptomyces* sp. (Sigma-Aldrich) and 2 mM salicylhydroxamic acid (Sigma-Aldrich).

2.5.3 Cytochrome *c* latency assay

Respiration rates of 20–40 µL isolated mitochondria were recorded in response to sequentially added 10 mM ascorbate (r_{asc}), 50 µM Cytochrome *c* ($r_{Cyt\ c}$) and 0.1% (v/v) Triton X-100 (r_{Triton}) in the oxygen electrode chamber. The integrity of mitochondria was calculated applying following formula: $1 - \{(r_{Cyt\ c} - r_{asc}) / (r_{Triton}) - r_{asc})\}$ (Sweetlove et al., 2002).

2.5.4 Protein protease protection assay

Protease protection assas were conducted as described in Welchen et al. (2016). Outer mitochondrial membrane integrity of purified mitochondria (section 2.5.1) from hydroponically grown 16-d-old Arabidopsis seedlings (section 2.2.3) was tested via the Cytochrome *c* latency assays (section 2.5.3). Only mitochondria with outer membrane intactness > 90% were used. Mitochondria were incubated on ice for 2 h without supplementation or in the presence of thermolysin (66.7 mg g^{-1} total mitochondrial protein) and in the absence or presence of 0.1% Triton X-100 to disrupt mitochondrial membranes. Protease reactions were stopped by addition of Laemmli sample buffer (section 2.4.3) and boiling the samples at 95°C for 6 min. Total mitochondrial protein amounts of 24 µg (NMT1-GFP), 12 µg (dLDH-cpYFP) and 6 µg (mts-cpYFP or mts-GFP) were loaded onto and separated by SDS-page (section 2.4.3). Protection/degradation of the candidate proteins was detected via Western blotting and chemiluminescence (section 2.4.4).

2.6 Multiwell plate reader-based fluorimetry

2.6.1 CpYFP-based monitoring of mitochondrial matrix pH dynamics

The assay employing the monitoring of mitochondrial matrix pH dynamics to study respiratory substrate properties was developed from the work of Schwarzländer et al. (2011). Volumes of 10 µL intact, freshly isolated mitochondria (section 2.5.1) from 16-d-old Arabidopsis seedlings stably expressing mitochondrial matrix localised circularly permuted Yellow Fluorescent Protein (cpYFP) were added to 190 µL basic incubation medium (0.3 M sucrose, 5 mM KH_2PO_4, 10 mM TES-KOH pH 7.5, 10 mM NaCl, 2 mM $MgSO_4$, 0.1% (w/v) BSA) in a transparent 96-well plate (NUNC). Fluorescence of cpYFP was recorded with a CLARIOstar microplate reader at 25°C employing top optics with 3.5 mm focal height, well-multichromatic monitoring, 40 flashes per cycle and double orbital shaking at 500 rpm for 5 s before each measurement cycle. Emission was recorded at 520 ± 5 nm in two separate tracks from excitation at 400 ± 5 nm or 482 ± 8 nm. For sequential supplement addition, monitoring of fluorescence was briefly paused and appropriate volumes of reagents were pipetted to the mitochondrial suspensions. All solutions were prepared in advance, pH-adjusted to 7.5, aliquoted and frozen in liquid nitrogen for storage at –86°C.

For visualisation of traces and direct comparability between independent experiments, $\log_{10}$ ratio value (emission from excitation at 482 nm divided by emission from excitation at 400 nm) of mock treatment was subtracted from $\log_{10}$ ratio value of treatments. Measurements were conducted in tri- or quadruplicates.

2.6.2 Rhodamine 123-based monitoring of mitochondrial membrane potential

The assay to monitor mitochondrial membrane potential using multiwell plate reader fluorimetry was developed based on previous reports (Emaus et al., 1986; Nie et al., 2015). Amounts of 7.5 µL intact, freshly isolated mitochondria from 16-d-old WT Arabidopsis seedlings were added to 192.5 µL basic incubation medium supplemented with 150 nM Rhodamine 123 (ACROS Organics) and added to a transparent 96-well plate (NUNC). Fluorescence of Rhodamine 123 was recorded with a CLARIOstar microplate reader at 25°C employing the same settings as described for cpYFP-based measurements (section 2.6.1) except for the focal height set to 5.5 mm and the adjustment of the emission

and excitation. Emission from samples was recorded at 535 ± 15 nm from excitation at 487 ± 14 nm. Sequential addition of substrates and depiction of $\Delta\log_{10}$ ratio value between treatment and mock was conducted as described for cpYFP-based measurements (section 2.6.1).

2.6.3 CpYFP-based mitochondrial protein sublocalisation and topology

A similar protocol as described in section 2.6.1 was used. To account for varying cpYFP fluorescence intensities in different lines, 10–100 µL freshly isolated mitochondria from 16-d-old Arabidopsis seedlings stably expressing cpYFP fused to different mitochondrial proteins (section 2.8.13) were added per well and supplemented with basic incubation medium to a final volume of 200 µL. Differing cpYFP fluorescence intensities between the selected lines required adjusting of the emission gain. To enable the comparison between experiments, $\log_{10}$ ratio values were normalised by setting the y-value to 0 after reaching a stable baseline before the respiratory substrate addition.

2.6.4 Peredox-mCherry-based *ex situ* monitoring of mitochondrial NADH oxidation

The *ex situ* assay was developed from experiments described in De Col et al. (2017). Amounts of 10 µL intact, freshly isolated mitochondria from 16-d-old WT Arabidopsis seedlings were resuspended in basic incubation medium, 500 µM NAD^+ and 0.5 µM purified recombinant Peredox-mCherry. Solution with a total volume of 200 µL was added to a well of a transparent 96-well plate (NUNC) for fluorimetry in a CLARIOstar microplate reader. The chromophores T-Sapphire and mCherry were excited at 400 ± 10 nm and 570 ± 10 nm, and emissions were collected at 515 ± 7.5 nm and 610 ± 5 nm, respectively. Samples were imaged via top optics with a focal height of 8.0 mm, incubation temperature at 25°C, well-multichromatic monitoring, 50 flashes per cycle and double orbital shaking at 400 rpm for 10 s before each measurement cycle. Supplementation with reductant was performed after NADH-NAD^+ ratios decreased sufficiently and returned into the dynamic range of the Peredox-mCherry sensor as judged by the decrease of the sensor ratio values following the plateau phase.

2.6.5 Peredox-mCherry-based *in vivo* monitoring of NAD redox state dynamics

For *in vivo* measurements of NAD redox changes, Arabidopsis leaf discs or intact 7–10-d-old seedlings stably expressing Peredox-mCherry in the cytosol were subjected to multiwell plate reader-based fluorimetry (modified protocol from De Col et al., 2017). Plant material was submerged in 200 µL assay medium (10 mM MES pH 5.8, 5 mM KCl, 10 mM $MgCl_2$, 10 mM $CaCl_2$) in a transparent 96-well plate (NUNC). Peredox-mCherry fluorescence was recorded in a CLARIOstar microplate reader as described above (section 2.6.4). Background fluorescence of control plants without sensor expression was recorded in parallel and subtracted before analysis. Plates were pre-incubated in the dark for 60–90 min before recording to minimise after-effects of active photosynthesis.

2.7 Microscopy methods

All microscopy imaging was performed with a confocal laser scanning Zeiss LSM780 microscope and a ×10 (Plan-Apochromat, 0.3 N.A), ×40 (C-Apochromat, 1.20 N.A., water immersion) or ×63 lens (Plan-Apochromat, 1.40 N.A., oil immersion). General procedures of ratiometric *in vivo* imaging were performed as described in Wagner et al. (2015b).

2.7.1 Monitoring cytosolic ATeam, Peredox-mCherry and GRX1-roGFP2 biosensors

Seedlings from mannitol drought-mimicking experiment expressing the different biosensors were incubated in the dark for at least 30 min to minimise after-effects of active photosynthesis before they were carefully mounted in perfluorodecalin for confocal microscopy. From each seedling, images from root tip and cotyledon were recorded applying 4-fold line averaging and pinhole set to 1.5–4 Airy units. Fluorescence settings were adjusted to different spectral properties of biosensors: ATeam1.03-nD/nA was excited at 458 nm and mseCFP and cp173-mVenus emission collected at 465–500 nm and 526–561 nm, respectively. Peredox-mCherry chromophores T-Sapphire and mCherry were excited at 405 nm and 543 nm, and emission collected at 499–544 nm and 579–615 nm, respectively. GRX1-roGFP2 was sequentially excited at 405 nm and 488 nm, and emission collected at 505–530 nm. For Peredox-mCherry and GRX1-roGFP2 seedlings, 405 nm excitation-induced auto-fluorescence was collected at 430–470 nm and factored into ratio

calculation by subtraction from fluorescence intensity of the corresponding channel. Root tip and cotyledon single plane images were x,y-noise-filtered, fluorescence background and auto-fluorescence corrected and subsequently ratiometrically analysed using a custom MATLAB-based software (Fricker, 2016).

2.7.2 Submitochondrial localisation of dLDH and quantitative analysis

Imaging and analysis were conducted as described in Wagner et al. (2015a) and Welchen et al. (2016). Seedlings from different lines were vacuum-infiltrated for 20–30 min with 200 nM MitoTracker Orange (Invitrogen) before subjected to co-localisation studies at the confocal microscope. GFP and MitoTracker were excited at 488 nm and 543 nm, and emissions were collected at 495–545 nm and 570–620 nm, respectively. Chlorophyll fluorescence was recorded at 650–700 nm from excitation at 488 nm. Pinhole was maintained at 1 Airy unit. For subsequent offline quantitative analysis, pixel intensities of GFP and MitoTracker channels were measured centrally across mitochondria and extracted with the Zeiss ZEN software. To account for varying diameters of analysed mitochondria pools, intensity distributions were normalised to the average diameter of the measured mitochondria.

2.7.3 Imaging of mitochondrial proteins fused to cpYFP

Images of hypocotyl cells from 5–8-d-old Arabidopsis seedlings stably expressing cpYFP fused to a mitochondrial protein of interest were recorded by sequentially exciting cpYFP at 405 nm and 488 nm and collecting the emission at 508–535 nm. Chlorophyll fluorescence excited by 488 nm-laser and 405 nm excitation-induced auto-fluorescence were collected at 630–690 nm and 425–460 nm, respectively. Pinhole was set to 1 Airy unit. For analysis of submitochondrial pH differences, images were recorded from root tips of seedlings to ensure efficient tissue penetration during cpYFP pH calibration. Single-plane images were x,y-noise-filtered, and autofluorescence and background fluorescence corrected. Subsequently, regions of interest capturing individual mitochondria were manually set and ratiometrically analysed using the custom MATLAB-based software (Fricker, 2016). The calculated $\log_{10}$ cpYFP ratio values measured at pH 7 and pH 8 were used to fit linear trendlines and to retrieve the corresponding linear trendline equations (dLDH-cpYFP: $y = 0.612x - 4.783$; cyt-cpYFP: $y = 0.5126x - 3.6849$; mts-cpYFP:

$y = 0.6657x - 5.041$ with $y = \log_{10}$ cpYFP ratio and x = pH). Physiological pH values were calculated by inserting into the equations the cpYFP values recorded during the perfluorodecalin incubation.

2.8 Molecular biological methods

2.8.1 DNA extraction from Arabidopsis plants

Ten-d-old Arabidopsis seedlings or rosette leaves from 4-week-old plants were disrupted manually using small plastic pistils or a TissueLyser II (Qiagen) at 30 Hz twice for 10 s. DNA was extracted following the protocol from Edwards et al. (1991). Homogenised plant material was resuspended in 400 µL buffer (200 mM Tris-HCl pH 7.5, 250 mM NaCl, 25 mM EDTA and 0.5% (w/v) SDS) and centrifuged at 20,000 *g* for 10 min. Supernatant was recovered and 400 µL isopropanol was added. After inverting samples ~5 times and incubation for 1–2 min at room temperature, the centrifugation step was repeated and the pellet was washed with 700 µL 70% (v/v) ethanol. Centrifugation and washing steps were repeated and followed by air-drying of pellet and subsequent resuspension in 20–40 µL water.

2.8.2 RNA extraction from Arabidopsis plants

Seven-d-old seedlings or leaves of 3-week-old plants were collected and immediately frozen in liquid nitrogen. Frozen samples were disrupted in a TissueLyser II (Qiagen) at 30 Hz twice for 10 s using adapters pre-chilled to –86°C. RNA was isolated using the NucleoSpin RNA isolation kit (Macherey-Nagel) following the manufacturer's protocol. RNA integrity was assessed on a denaturing agarose gel by checking the integrity and the ratio between the 28S and 18S rRNA bands (Aranda et al., 2012).

2.8.3 Oligonucleotides

Lyophilised salt-free primers (Table 10–17) were ordered from Eurofins Genomics (www.eurofinsgenomics.eu). After resuspension in H_2O, primer stock solutions (100 µM) were stored at –20°C.

Table 10: Genotyping primers.

Primer	Product/gene	Sequence
P1	*AT3G54110 UCP1*	GACGAAGATGTGAAGTAGACC
P2	*AT3G54110 UCP1*	GGCTCATACATTCCAATCCTAAG
P3	SAIL T-DNA	ATGGATAAATAGCCTTGCTTCC
P4	*AT5G58970 UCP2*	ATTTACAATAGCATTCCGGGC
P5	*AT5G58970 UCP2*	TCGATCAATCACTGTCACTGG
P6	SALK T-DNA	ATTTTGCCGATTTCGGAAC
P7	*AT1G14140 UCP3*	TTCATCATCCTCGTCTTCACC
P8	*AT1G14140 UCP3*	AGATTGCGAGAAAGGAAGGAG
P9	*AT3G22370 AOX1a*	TGGCCTACCGATTTGTTCTTC
P10	*AT3G22370 AOX1a*	GCTTAAGCAGAGGTGATGATG

Table 11: qRT PCR primers.

Primer	Product/gene	Sequence
P11	*AT3G54110 UCP1*	TAGCCGTAATCGTCGTCGTC
P12	*AT3G54110 UCP1*	GGGCAAGGAAAGGTCGGATT
P13	*AT5G58970 UCP2*	GTGAGAATTTGCCCAAGTATAGAGG
P14	*AT5G58970 UCP2*	TGGCGATGAAGTCCTGCAAT
P15	*AT1G14140 UCP3*	GGCTCTCGTCGGAGGATTTT
P16	*AT1G14140 UCP3*	TCGATTGGTCCCGAGTACCT
P17	*AT3G22370 AOX1a*	TCGTTGGCCTACCGATTTGT
P18	*AT3G22370 AOX1a*	ACCATTCCAGGTACTGCTGC
P19	*AT2G28390 SAND*	CCATATTGCAAGAAGTTTGCGCGTCTG
P20	*AT2G28390 SAND*	GCAAGTCATCGGGATGGAGAGACG
P21	*AT4G34270 TIP41*	AATGCGTTTGACGCACTAGC
P22	*AT4G34270 TIP41*	GAGACGGCTTGCTCCTGAAT

Table 12: semi-qRT PCR primers.

Primer	Product/gene	Sequence
P23	*AT5G09810 ACTIN7*	ATGGCCGATGGTGAGGA
P24	*AT5G09810 ACTIN7*	GAAGCATTTCCTGTGAACAATC
P25	*AT3G54110 UCP1*	ATGGTGGCGGCTGGTAA
P26	*AT3G54110 UCP1*	CTTTTGGACGCATCGAGTTC

Table 13: CRISPR cloning oligonucleotides and verification primers.
Oligonucleotide pairs P29/30, P31/32, P33/34 and P35/36 were hybridised and cloned into sgRNA vectors. P27 and 28 were used to screen for deletions in transformed plants.

Primer	Product/gene	Sequence
P27	UCP1 exon1–2	AAACCCTAACCTCCTCTCTTTAATTC
P28	UCP1 exon1–2	TGAAAGAAGAAGAATTTGTAACCCA
P29	UCP1 exon 1 target site	ATTGGTTTTCTGGATCGAAGATGG
P30	UCP1 exon 1 target site	AAACCCATCTTCGATCCAGAAAAC
P31	UCP1 exon 1 target site	ATTGAGTGCCTTCGCTGCTTGCGT
P32	UCP1 exon 1 target site	AAACACGCAAGCAGCGAAGGCACT
P33	UCP1 exon 2 target site	ATTGGTTACTCTGCCTAAATATCG
P34	UCP1 exon 2 target site	AAACCGATATTTAGGCAGAGTAAC
P35	UCP1 exon 2 target site	ATTGGATTGGAATGTATGAGCCGG
P36	UCP1 exon 2 target site	AAACCCGGCTCATACATTCCAATC

Table 14: Primers for cpYFP constructs producing reporter lines with good signal-to-noise ratio.
CCTAGG: *Avr*II endonuclease restriction sites. Asterisks mark primers used for transcript enrichment before amplification with primers adding *att*B sites.

Primer	Product/gene	Sequence
P37	*AT5G13490 AAC2*	GGGGACAAGTTTGTACAAAAAAGCAGGCTTCATGGTTGAACAGACTCAGCAC
P38	*AT5G13490 AAC2*	GGGGACCACTTTGTACAAGAAAGCTGGGTTGGCACCTCCAGATCCATAC
P39*	*AT3G22370 AOX1a*	TGAAACAATGATGATAACTCGCG
P40*	*AT3G22370 AOX1a*	AGAAAGCCGAATCCAAGTATGG
P41	*AT3G22370 AOX1a*	GGGGACAAGTTTGTACAAAAAAGCAGGCTTCATGATGATAACTCGCGGTGGA
P42	*AT3G22370 AOX1a*	GGGGACCACTTTGTACAAGAAAGCTGGGTTATGATACCCAATTGGAGCTGGA
P43*	*AT2G19680 ATPsyn g 1*	GTATTGAAAAATGGCATCAAAATTG
P44*	*AT2G19680 ATPsyn g 1*	GTCTCAATTTCAAGGGTAGTAGCC
P45	*AT2G19680 ATPsyn g 1*	GGGGACAAGTTTGTACAAAAAAGCAGGCTTCACCATGGCATCAAAATTGGTTCAACTTC
P46	*AT2G19680 ATPsyn g 1*	GGGGACCACTTTGTACAAGAAAGCTGGGTTAGGGTAGTAGCCGGTGAAAG
P47*	*AT4G26210 ATPsyn g 2*	TTAAGAGATGGCATCAAAGTTGC
P48*	*AT4G26210 ATPsyn g 2*	TTGCTTTCTTTCTTCAAGGGTAG
P49	*AT4G26210 ATPsyn g 2*	GGGGACAAGTTTGTACAAAAAAGCAGGCTTCACCATGGCATCAAAGTTGCTACAATTG
P50	*AT4G26210 ATPsyn g 2*	GGGGACCACTTTGTACAAGAAAGCTGGGTTAGGGTAGTAGCCGGTGAAAG
P51*	*AT4G29480 ATPsyn g 3*	TGTGAAGATGGCATCGAAG
P53*	*AT4G29480 ATPsyn g 3*	ACTCTCCTTCATGGGTAATAGCC
P54	*AT4G29480 ATPsyn g 3*	GGGGACAAGTTTGTACAAAAAAGCAGGCTTCACCATGGCATCGAAGTTGATACAAGTTC
P55	*AT4G29480 ATPsyn g 3*	GGGGACCACTTTGTACAAGAAAGCTGGGTTTGGGTAATAGCCTGTGAAGGTG
P56	*AT2G27730 CI P2*	GGGGACAAGTTTGTACAAAAAAGCAGGCTTCATGGCAACAAGAAATGCTTTGAGA
P57	*AT2G27730 CI P2*	GGGGACCACTTTGTACAAGAAAGCTGGGTTCTCTTGGACCTCTGGCTGC
P58	*AT4G04870 CLS1*	GGGGACAAGTTTGTACAAAAAAGCAGGCTTCATGGCGATTTACAGATCTCTAAGA
P59	*AT4G04870 CLS1*	GGGGACCACTTTGTACAAGAAAGCTGGGTTTGATCTCTTAATCATAGATATAGGTC
P60	*AT2G22500 DIC1*	GGGGACAAGTTTGTACAAAAAAGCAGGCTTCATGGGTCTAAAGGGTTTTGCTG
P61	*AT2G22500 DIC1*	GGGGACCACTTTGTACAAGAAAGCTGGGTTAAAGTCATAGTCCTTGAACAACTTC
P62	*AT4G24570 DIC2*	GGGGACAAGTTTGTACAAAAAAGCAGGCTTCATGGGAGTCAAAAGTTTCGTTGA
P63	*AT4G24570 DIC2*	GGGGACCACTTTGTACAAGAAAGCTGGGTTAAAATCTCGAAGCAGCTTCCTAA
P64*	*AT5G06580 dLDH*	TCTCCTACGTTGTGAAATCCAC
P65*	*AT5G06580 dLDH*	AGAAACAGTATGAGGCCAAACG
P66	*AT5G06580 dLDH*	GGGGACAAGTTTGTACAAAAAAGCAGGCTTCATGGCTTTCGCTTCAAAATTCGC
P67	*AT5G06580 dLDH*	GGGGACCACTTTGTACAAGAAAGCTGGGTTGAAACATACATGAGGAGGAATTAAC
P68*	*AT2G47510 FUM1*	CTGTCAGGTAGAAGAATCCATG
P69*	*AT2G47510 FUM1*	CTCCAAAAACAACTATCAATCGG
P70	*AT2G47510 FUM1*	GGGGACAAGTTTGTACAAAAAAGCAGGCTTCATGTCGATTTACGTCGCGTCG
P71	*AT2G47510 FUM1*	GGGGACCACTTTGTACAAGAAAGCTGGGTTATCGGAGGGACCAATCATCTT
P72*	*AT3G15660 GRXS15*	ATTTAGAGATGGCGGCTTCTTTAT
P73*	*AT3G15660 GRXS15*	CACTCGTCAGCATAACTTCCA
P74	*AT3G15660 GRXS15*	GGGGACAAGTTTGTACAAAAAAGCAGGCTTCATGGCGGCTTCTTTATCGAGC
P75	*AT3G15660 GRXS15*	GGGGACCACTTTGTACAAGAAAGCTGGGTTATCTTGGTTTCCGGAGACGTC
P76	*AT1G09575 MCU1*	GGGGACAAGTTTGTACAAAAAAGCAGGCTTCATGTGGTCAATGGGTTTGATAAG
P77	*AT1G09575 MCU1*	GGGGACCACTTTGTACAAGAAAGCTGGGTTGTCCCTGCGACTCTGCAA
P78	*AT1G22520 MIC10*	GGGGACAAGTTTGTACAAAAAAGCAGGCTTCATGGAAACGACGAAGAGTAACAG
P79	*AT1G22520 MIC10*	GGGGACCACTTTGTACAAGAAAGCTGGGTTAAACCTGTAACTTAGTCGATATGTGA
P80	*AT1G22520 MIC10*	GGGGACCACTTTGTACAAGAAAGCTGGGTTCTCTTCTGCTGCCTGAGATACA
P81	*AT5G14040 MPT3*	GGGGACAAGTTTGTACAAAAAAGCAGGCTTCATGGAATCTCCGAAGAATTCTCT
P82	*AT5G14040 MPT3*	GGGGACCACTTTGTACAAGAAAGCTGGGTTGGCTTTGGCTTCAGTAGCTG
P83	*AT5G22350 NMT1*	GGGGACAAGTTTGTACAAAAAAGCAGGCTTCATGAGGCCAATCCTATTGCCG
P84	*AT5G22350 NMT1*	GGGGACCACTTTGTACAAGAAAGCTGGGTTAGACCGTAAACTCCATCCACG
P85*	*AT4G37930 SHMT1*	TAGAGAGAGGTTTAGCGAAAAATG
P86*	*AT4G37930 SHMT1*	GAAAACACTTGTGGGGTGAAAC
P87	*AT4G37930 SHMT1*	GGGGACAAGTTTGTACAAAAAAGCAGGCTTCATGGCGATGGCCATGGCTC
P88	*AT4G37930 SHMT1*	GGGGACCACTTTGTACAAGAAAGCTGGGTTGTTCTTGTACTTCATGGTTTCTTTC
P89	*AT1G18480 SLP2*	GGGGACAAGTTTGTACAAAAAAGCAGGCTTCATGTCAAGCAGAGAAAACCCTA
P90	*AT1G18480 SLP2*	GGGGACCACTTTGTACAAGAAAGCTGGGTTAGCTTTGACTTCAACTTGCTTAGG
P91*	*AT5G11690 TIM17-3*	AGCATTGTCAGGAACATGGACA
P92*	*AT5G11690 TIM17-3*	ATGACATTCTCATCAAAGACAACC

Primer	Product/gene	Sequence
P93	*AT5G11690 TIM17-3*	GGGGACAAGTTTGTACAAAAAAGCAGGCTTCATGGACACTAAGAAGAAATCTAAGG
P94	*AT5G11690 TIM17-3*	GGGGACCACTTTGTACAAGAAAGCTGGGTTCTTGCTCCCGAACGGAGG
P95*	*AT1G17530 TIM23-1*	TCTCCCGTCTTCTTCTAATGG
P96*	*AT1G17530 TIM23-1*	TCACTCCGGTTCTTCATATGTG
P97	*AT1G17530 TIM23-1*	GGGGACAAGTTTGTACAAAAAAGCAGGCTTCATGGCGATCAATCGTAGCTCC
P98	*AT1G17530 TIM23-1*	GGGGACCACTTTGTACAAGAAAGCTGGGTTTATGTGAGCATACCGCTTGAAAA
P99*	*AT1G27390 TOM20-2*	CACCTGAATCTGAAGATGGAGT
P100*	*AT1G27390 TOM20-2*	ATGGCTTTAGGCTTTATCTGGC
P101	*AT1G27390 TOM20-2*	GGGGACAAGTTTGTACAAAAAAGCAGGCTTCATGGAGTTCTCTACCGCCG
P102	*AT1G27390 TOM20-2*	GGGGACCACTTTGTACAAGAAAGCTGGGTTTTATCTGGCAGGAGGTGGAG
P103	*AT1G64220 TOM7-2*	GATCCCTAGGATGGCGGCTAAAAGTACGTTG
P104	*AT1G64220 TOM7-2*	GGGGACCACTTTGTACAAGAAAGCTGGGTTTTAAACGGGAGAGAGGAGGTG
P105	*AT1G31020 TRX-o2*	GGGGACAAGTTTGTACAAAAAAGCAGGCTTCACCATGAAGAGTCAATGGTCTAATTTTC
P106	*AT1G31020 TRX-o2*	GGGGACCACTTTGTACAAGAAAGCTGGGTTCTTGTAGAGTTGTTCCATGACACT
P107*	*AT3G54110 UCP1*	CGTTTTCTGGATCGAAGATGGT
P108*	*AT3G54110 UCP1*	CTCTGCTTAAAACTATGTGTCTC
P109	*AT3G54110 UCP1*	GGGGACAAGTTTGTACAAAAAAGCAGGCTTCATGGTGGCGGCTGGTAAATC
P110	*AT3G54110 UCP1*	GGGGACCACTTTGTACAAGAAAGCTGGGTTGTTTCTTTTGGACGCATCGAGT
P111	cpYFP	GGGGACAAGTTTGTACAAAAAAGCAGGCTTCATGTACAACAGCGACAACGTCT
P112	cpYFP	GATCCCTAGGGGTACCGTTGTACTCCAGC

Table 15: Primers for cpYFP fusion constructs producing reporter lines with low signal-to-noise ratio.
CCTAGG: *Avr*II endonuclease restriction sites. Asterisks mark primers used for transcript enrichment before amplification with primers adding *att*B sites.

Primer	Product/gene	Sequence
P113*	*AT3G08580 AAC1*	GATCTGTAAGAGTTCAAAATGGTTG
P114*	*AT3G08580 AAC1*	AGCAATGCTTAGGCACCTCC
P115	*AT3G08580 AAC1*	GGGGACAAGTTTGTACAAAAAAGCAGGCTTCATGGTTGATCAAGTTCAGCACC
P116	*AT3G08580 AAC1*	GGGGACCACTTTGTACAAGAAAGCTGGGTTGGCACCTCCTGATCCGTAC
P117*	*AT5G63400 AK1*	TAGATCAGCTATGGCGACCG
P118*	*AT5G63400 AK1*	CTTGAGGAGTCTTTGATCATGAC
P119	*AT5G63400 AK1*	GGGGACAAGTTTGTACAAAAAAGCAGGCTTCATGGCGACCGGTGGTGCT
P120	*AT5G63400 AK1*	GGGGACCACTTTGTACAAGAAAGCTGGGTTTGACAATGCTTTTTTAACCTCTGAT
P121	*AT2G19680 ATPsyn g 1*	GATCCCTAGGATGGCATCAAAATTGGTTCAACTTC
P122	*AT2G19680 ATPsyn g 1*	GGGGACCACTTTGTACAAGAAAGCTGGGTTAGGGTAGTAGCCGGTGAAAG
P123	*AT4G26210 ATPsyn g 2*	GATCCCTAGGATGGCATCAAAGTTGCTACAATTG
P124	*AT4G26210 ATPsyn g 2*	GGGGACCACTTTGTACAAGAAAGCTGGGTTAGGGTAGTAGCCGGTGAAAG
P125	*AT4G29480 ATPsyn g 3*	GATCCCTAGGATGGCATCGAAGTTGATACAAGTTC
P126	*AT4G29480 ATPsyn g 3*	GGGGACCACTTTGTACAAGAAAGCTGGGTTTGGGTAATAGCCTGTGAAGGTG
P127	*AT2G15680 CML30*	GGGGACAAGTTTGTACAAAAAAGCAGGCTTCATGTCAAACGTGAGTTTTCTTGAG
P128	*AT2G15680 CML30*	GGGGACCACTTTGTACAAGAAAGCTGGGTTGACATTGTTGGAAGACATCATTTTG
P129	*AT4G23290 CRK21*	GGGGACAAGTTTGTACAAAAAAGCAGGCTTCATGCAAAAGAACAAAATGGTCGACT
P130	*AT4G23290 CRK21*	GGGGACCACTTTGTACAAGAAAGCTGGGTTACGAGGTCTAACACTCGTGAT
P131*	*AT1G22840 CYTC1*	GTTCCTGATCGCGTAGCTCA
P132*	*AT1G22840 CYTC1*	CACCATCAGATTCACTTAGGC
P133	*AT1G22840 CYTC1*	GGGGACAAGTTTGTACAAAAAAGCAGGCTTCATGGCGTCGTTTGATGAAGCA
P134	*AT1G22840 CYTC1*	GGGGACCACTTTGTACAAGAAAGCTGGGTTCTTAGGCGCAGTAGATTCCTT
P135	*AT4G10040 CYTC2*	GGGGACAAGTTTGTACAAAAAAGCAGGCTTCATGGCGTCGTTCGACGAAG
P136	*AT4G10040 CYTC2*	GGGGACCACTTTGTACAAGAAAGCTGGGTTAGCAGTACCTTCCTTCAAATAAG
P137*	*AT1G49880 ERV1*	GCATTGTCTAATTTCTCGAGTGA
P138*	*AT1G49880 ERV1*	TAGTTAATAAATGGGTCTAAAAGTCC
P139	*AT1G49880 ERV1*	GGGGACAAGTTTGTACAAAAAAGCAGGCTTCATGGGTGAGAAGCCATGGCA
P140	*AT1G49880 ERV1*	GGGGACCACTTTGTACAAGAAAGCTGGGTTAAAGTCCATAGAAGTTCCATGGA
P141	*AT5G27540 MIRO1*	GATCCCTAGGATGGCGAGATACGCTGCT
P142	*AT5G27540 MIRO1*	GGGGACCACTTTGTACAAGAAAGCTGGGTTTCAGGCAGACGAGCTCTTTC
P143	*AT4G28220 NDB1*	GGGGACAAGTTTGTACAAAAAAGCAGGCTTCATGACATTACTTTCCTCTCTCG
P144	*AT4G28220 NDB1*	GATCCATATGCTTTTTGTTAGCTTCTTCGTTAGC
P145	*AT4G28220 NDB1*	GATCCATATGGGAGGTTCAGGAGGCAGCTACAACAGCGACAACGTCTATAT

Primer	Product/gene	Sequence
P146	*AT4G28220 NDB1*	GATCCCTAGGTCCACCTGATCCGCCGCTGGTACCGTTGTACTCCAGC
P147	*AT4G28220 NDB1*	GATCCCTAGGGAGGAGCATAAGAAGAAGAAAGTAG
P148	*AT4G28220 NDB1*	GGGGACCACTTTGTACAAGAAAGCTGGGTTTCAGATGCGGCTTGAATC
P149	*AT4G28220 NDB1*	GGGGACAAGTTTGTACAAAAAAGCAGGCTTCATGACATTACTTTCCTCTCTCG
P150	*AT4G28220 NDB1*	GATCCATATGACTTGATTTGACTTTCACTGTGATAT
P151	*AT4G28220 NDB1*	GATCCATATGGGAGGTTCAGGAGGCAGCTACAACAGCGACAACGTCTATAT
P152	*AT4G28220 NDB1*	GATCCCTAGGTCCACCTGATCCGCCGCTGGTACCGTTGTACTCCAGC
P153	*AT4G28220 NDB1*	GATCCCTAGGGGAGAACTCGTAAGTATTCCTC
P154	*AT4G28220 NDB1*	GGGGACCACTTTGTACAAGAAAGCTGGGTTTCAGATGCGGCTTGAATC
P155*	*AT4G28220 NDB1*	ATGACATTACTTTCCTCTCTCG
P156*	*AT4G28220 NDB1*	TCAGATGCGGCTTGAATC
P157	*AT4G28220 NDB1*	GGGGACAAGTTTGTACAAAAAAGCAGGCTTCATGACATTACTTTCCTCTCTCG
P158	*AT4G28220 NDB1*	GGGGACCACTTTGTACAAGAAAGCTGGGTTTCAGATGCGGCTTGAATC
P159	*AT4G11010 NDPK3*	GGGGACAAGTTTGTACAAAAAAGCAGGCTTCATGAGCTCTCAAATCTGCAGATC
P160	*AT4G11010 NDPK3*	GGGGACCACTTTGTACAAGAAAGCTGGGTTGTTGTCACCATAGAGCCACTT
P161*	*AT3G46560 TIM9*	TAGTCGAAAGAAAAGAGTTGGGA
P162*	*AT3G46560 TIM9*	CTATATCAGTCTTGGGTTGGTG
P163	*AT3G46560 TIM9*	GGGGACAAGTTTGTACAAAAAAGCAGGCTTCATGGACGCAAGCATGATGGC
P164	*AT3G46560 TIM9*	GGGGACCACTTTGTACAAGAAAGCTGGGTTGTCTTGGGTTGGTGCGTTC
P165*	*AT3G20000 TOM40*	AAAGGATATTCAAAAGCGGTAGAG
P166*	*AT3G20000 TOM40*	TGCCGGTTTTTATTCGGTCTTTTAACCAA
P167	*AT3G20000 TOM40*	GGGGACAAGTTTGTACAAAAAAGCAGGCTTCATGGCGGATCTTTTACCACCTCTTA
P168	*AT3G20000 TOM40*	GGGGACCACTTTGTACAAGAAAGCTGGGTTACCAACTGTTAATCCGAAACCAAA
P169	*AT5G39950 TRX-h2*	GGGGACAAGTTTGTACAAAAAAGCAGGCTTCACCATGGGAGGAGCTTTATCAACTG
P170	*AT5G39950 TRX-h2*	GGGGACCACTTTGTACAAGAAAGCTGGGTTTGCTCTGAGTTTGCTAACTTTCTTCTC
P171*	*AT5G58970 UCP2*	GTTCCTATAGCATAACAATGGCG
P172*	*AT5G58970 UCP2*	CGACTAGGGATCTGAGAATCAA
P173	*AT5G58970 UCP2*	GGGGACAAGTTTGTACAAAAAAGCAGGCTTCATGGCGGATTTCAAACCAAGGA
P174	*AT5G58970 UCP2*	GGGGACCACTTTGTACAAGAAAGCTGGGTTATCGTACAAGACTTCTCTTAGAAAC
P175*	*AT1G14140 UCP3*	ATCCGGTGAAAATGGAGCGG
P176*	*AT1G14140 UCP3*	GTAAGAACTAAAGAACACAAATCTCAA
P177	*AT1G14140 UCP3*	GGGGACAAGTTTGTACAAAAAAGCAGGCTTCATGGAGCGGAGCCGAGTG
P178	*AT1G14140 UCP3*	GGGGACCACTTTGTACAAGAAAGCTGGGTTGAAGGAAGAGATTCCTGCCAG
P179*	*AT3G01280 VDAC1*	TCAGATAAGCAACAATGGTGAAAG
P180*	*AT3G01280 VDAC1*	CTTCCATCTCAGTTTCAAGGCT
P181	*AT3G01280 VDAC1*	GGGGACAAGTTTGTACAAAAAAGCAGGCTTCATGGTGAAAGGTCCCGGTC
P182	*AT3G01280 VDAC1*	GGGGACCACTTTGTACAAGAAAGCTGGGTTAGGCTTGAGTGCGAGAGCC
P183*	*AT5G15090 VDAC3*	GAGGCAATCATGGTTAAAGGTC
P184*	*AT5G15090 VDAC3*	GGTGGTATCTTCTCAGGGCT
P185	*AT5G15090 VDAC3*	GGGGACAAGTTTGTACAAAAAAGCAGGCTTCATGGTTAAAGGTCCAGGACTCT
P186	*AT5G15090 VDAC3*	GGGGACCACTTTGTACAAGAAAGCTGGGTTGGGCTTGAGAGCGAGAGC

Table 16: Primers for modification of pSS01 vector backbone.

CCTAGG: *Avr*II endonuclease restriction sites. TTAATTAA: *Pac*I endonuclease restriction sites.

Primer	Product/gene	Sequence
P187	cpYFP	TGCCTAGGTACAACAGCGACAACGTCTATATC
P188	cpYFP	TCTTAATTAATTAGGTACCGTTGTACTCCAGCT
P189	EGFP	TTGCCTAGGATGGTGAGCAAGGGCGA
P190	EGFP	TCTTAATTAATTACTTGTACAGCTCGTCCATGC

Table 17: Primers for DNA sequencing.

Primer	Product/gene	Sequence
P191	pDONR207 vector	TCGCGTTAACGCTAGCATGGATCTC
P192	pDONR207 vector	GTAACATCAGAGATTTTGAGACAC
P193	pSS01 vector	CGCACAATCCCACTATCCTT
P194	pSS01 vector	GCTGAACTTGTGGCCGTTTA
P195	sgRNA vectors (M13)	GTAAAACGACGGCCAGT

2.8.4 Polymerase chain reaction

Polymerase chain reactions (PCRs) were conducted with the Phusion high fidelity DNA polymerase (New England Biolabs) and the *Taq* DNA polymerase (Thermo) following the manufacturers' protocol. Phusion high fidelity DNA polymerase was used for cloning amplification reactions to minimise error rates. *Taq* DNA polymerase was used for verification experiments, such as genotyping or colony PCRs. For genotyping PCR, 1 µL of resuspended DNA was added as amplification template. Colony PCR was based on 1 µL of bacterial suspension prepared from a bacterial colony picked from a selected plate and suspended in 50 µL water. To ensure efficient cell lysis and bacterial DNA release, the initial heating step was prolonged to 5 min.

2.8.5 DNA agarose gel electrophoresis and PCR fragment purification

PCR products were separated and analysed via agarose gel electrophoresis. PCR reaction mix was supplemented with loading buffer (final conc.: 0.05% (w/v) bromophenol blue, 0.05% (w/v) xylene cyanole and 8% (v/v) glycerol) and loaded onto agarose gel. Gel was prepared with half-strength TBE buffer (45 mM boric acid, 45 mM Tris-HCl pH 8.0, 1 mM EDTA), 1–2% (w/v) agarose depending on expected size of DNA fragments and supplemented with 40 µL L^{-1} HDGreen Plus (Intas). GeneRuler DNA Ladder Mix (Thermo) served as base pair length standard. Electrophoresis was performed at 80–120 V for 30–60 min in custom chambers floated with half-strength TBE buffer. Gels were documented in a MF-ChemiBIS 2.0 (DNR Bio-Imaging System) or INTAS ECL Chemostar (Intas) imaging system.

For purification of PCR fragments, bands of interest were excised from agarose gel and recovered using the NucleoSpin Gel and PCR clean-up kit (Macherey-Nagel).

2.8.6 Quantification of RNA and DNA concentration

Concentrations of purified RNA, plasmid DNA, genomic DNA or of PCR-amplified DNA were quantified with a Nanodrop spectrophotometer.

2.8.7 Genotyping of Arabidopsis mutants

Genomic DNA from Arabidopsis plants was isolated as described in section 2.8.1. Amounts of 1 µL gDNA were used as template for PCRs using primers binding to native gene sequence (WT allele) or combination of T-DNA left border-binding primer together with native gene sequence-binding primer (see Figure 8A for primer combinations). Primer sequences used for genotyping are listed in Table 10.

2.8.8 Complementary DNA synthesis

RNA was transcribed reversely to complementary DNA (cDNA) using two different protocols depending on intended downstream analyses. For quantitative RealTime (qRT) PCR, 2 µg RNA was reverse transcribed employing the qScript cDNA Synthesis kit (Quantabio). After reverse transcription following the supplier's protocol, cDNA (20 µL) was diluted by adding 40 µL water. cDNA dedicated for semi-quantitative RT-PCR or cloning was reverse transcribed from 1 µL RNA using the RevertAid First Strand cDNA Synthesis kit (Thermo) with Oligo(dT)$_{18}$ primers. After reverse transcription following the supplier's protocol, cDNA (20 µL) was diluted adding 20 µL water.

2.8.9 Quantitative and semi-quantitative real-time PCR

Primer pairs for assessment of transcript abundances in qRT and semi-qRT PCRs were designed following the recommendations of Udvardi et al. (2008) (see Table 11 and Table 12 for primers). For qRT PCRs, PCR efficiency for each primer pair was assessed by conducting calibration dilution curves (1:1 dilution series in factor two steps up to 1:128) in each quantification experiment. PCR efficiency was calculated as described in Bustin et al. (2009); $10^{-1/\text{slope}}-1$. Primer efficiencies were between 93% and 106%, $R^2 > 0.98$. Amounts of 1 µL cDNA served as template for qRT PCRs performed with PerfeCTa SYBR Green FastMix (Quanta) in a 384-well plate using a CFX96 Real-Time PCR Detection System. Experiments were conducted following the manufacturer's protocol except for downscaling single reactions to a total volume of 4 µL. All qRT PCR quantifications were based on 3–4 technical replicates and 3 biological replicates unless stated otherwise. Expression levels were calculated relative to the *SAND family protein* (*AT2G28390*) previously described as a suitable reference gene for transcript normalisation in Arabidopsis (Czechowski et al., 2005).

Semi-qRT PCR was based on full-length reverse transcribed cDNA (section 2.8.8). Amounts of 1 µL cDNA served as template for standard Phusion high fidelity DNA polymerase-based PCR reactions (section 2.8.4) in 20 µL single reaction volumes. PCR consisted of 20–30 amplification cycles. Volumes of 4 µL were loaded on a 1% agarose gel and separated by gel electrophoresis (section 2.8.5).

2.8.10 DNA sequencing

DNA sequencing by Eurofins (www.eurofinsgenomics.eu) was employed to determine locations of T-DNA insertion and to verify the correct assembly of vectors. pDONR207 vectors were tested with primer P191 and/or P192, pSS01 vectors with P193 and/or 194, CRISPR sgRNA vector with primer P195 (Table 17).

2.8.11 Vectors used for recombination, transformation or as cloning template

Vectors used for Gateway recombination, DNA sequence template or for stable transformation of Arabidopsis plants are listed in Table 18.

Table 18: Vectors used for recombination, transformation or as cloning template.

Vector	Resistance	Constructed/provided	Reference	Purpose in this study
pH2GW7:mts-cpYFP	$Spec^R$, (Hyg^R in plants)	M. Schwarzländer, Münster	Schwarzländer et al., 2011	cpYFP sequence template
pUBC-EGFP-Dest	$Spec^R$, ($Basta^R$ in plants)	C. Grefen, Bochum	Grefen et al., 2010	EGFP sequence template
pSS02:cyt-Peredox-mCherry	Kan^R, (Hyg^R in plants)	M. Schwarzländer, Münster	Unpublished	Transformation of plants
pSS01	Kan^R, ($Basta^R$ in plants)	A. Meyer, Bonn	Brach et al., 2009	Destination vector, modified in this study
pDONR207	$Gent^R$	Invitrogen	www.thermofisher.com	Gateway recombination

2.8.12 CRISPR-Cas9 cloning

Attempted CRISPR-Cas9-based genome editing was performed with the editing toolkit described in Ordon et al. (2017). Targeting sequences for single-guide RNAs were selected to have a GC-content between 40–60%, low self-complementarity and low off-target likelihood using the online tool ChopChop (www.chopchop.cbu.uib.no). Four targeting sequences were chosen in total, designed to pairwise induce a deletion in the first and second exon of *UCP1* (see Table 13 for primers, see Supplemental Figure 1 for selected editing sites). Following the protocol, targeting sequences were ordered as oligonucleotides, hybridised and *Bpi*I cut/ligated into corresponding sgRNA shuttle vectors. After

verification by DNA sequencing (M13; Table 17), sgRNA shuttle vectors were *Bsa*I cut/ligated into the multiplex genome editing vector pDGE4. Assembled pDGE4 vector ($UBI_{promoter}$ for plant expression) was used to transform Arabidopsis plants via Agrobacteria (AGL-1)-mediated floral dipping (section 2.2.10). BASTA-resistant transformants were propagated to second generation and screened for genomic deletions. Screening was based on PCR/gel electrophoresis using the primer pair combination P27/P28 (Table 13, Supplemental Figure 1).

2.8.13 Cloning of the mitochondrial proteins fused to cpYFP or EGFP

Gene transcripts encoding selected mitochondrial proteins were enriched using primers binding in UTRs (P* in Table 14 and Table 15) to serve as template for second PCR adding *att*B Gateway recombination sites. Alternatively, transcript sequences were directly amplified with *att*B adding primers. Amplified DNA fragments were purified and BP-recombined into the pDONR207 Gateway donor vector (Invitrogen) (pDONR207:gene). For DNA sequences intended to be fused to the C-terminus of cpYFP, sequences were amplified including the STOP codon and via *Avr*II cut/ligated to cpYFP prior the recombination into the donor vector (pDONR207:cpYFP-*Avr*II-gene with STOP). Accuracy of the inserted sequence and assembly was confirmed by DNA sequencing (section 2.8.10). Verified recombined pDONR207 vectors were LR-recombined with modified pSS01 destination vectors. The roGFP2 (in frame behind the Gateway cassette) of the pSS01 vector was replaced with cpYFP or EGFP using *Avr*II and *Pac*I cut/ligation. The vectors pH2GW7:mts-cpYFP and pUBC-EGFP-Dest were used as DNA templates for PCR amplification of cpYFP and EGFP, respectively (see Table 16 and Table 19 for primers and vectors). After recombination of the pSS01 destination with the recombined pDONR207 vectors, the expression clones were verified by colony PCR after the transformation into *E.coli* DH5α or TOP10 cells. Subsequently, Agrobacteria (C58C1 or AGL-1) were transformed for floral dipping of Arabidopsis plants (section 2.2.10). A selection of established clones was transiently expressed in *N. benthamiana* plants to verify operability (section 2.2.9).

NDB1 was, in addition to the fusion with the N-terminus of cpYFP (NDB1-cpYFP), also amplified with cpYFP inserted into alpha helices at 44K–45E (position 1) or at 307S–308G (position 2). The N-terminal parts of NDB1 were amplified to include *Nde*I

restriction sites and the C-terminal NDB1 parts to include *Avr*II restriction sites. cpYFP was amplified flanked with 6-amino acid-long linker sequences (GGSGGS) at either end plus corresponding *Nde*I and *Avr*II restriction sites. After restriction and purification, fragments were joined by ligation yielding NDB1-*Nde*I-GGSGGS-cpYFP-SGGSGG-*Avr*II-NDB1(with STOP) constructs. After verification via DNA sequencing, constructs were LR recombined with pSS01 as described above.

Primers used to amplify gene sequences for BP recombination with pDONR207 are listed in Table 14 and Table 15. Primers to amplify cpYFP and GFP with restriction sites for cloning into pSS01 destination vector are listed in Table 16. Corresponding plasmids and stably transformed Arabidopsis lines generated in this work are indicated below in Table 19. The vectors pDONR207:GET3c (C. Grefen; Xing et al., 2017), pDONR207:MICU and pDONR207:NMT1 (both from S. Wagner; Wagner et al., 2015a) were kind gifts.

Table 19: Plasmids and stably transformed *Arabidopsis thaliana* lines generated in this study for the expression of mitochondrial candidate proteins fused to different reporter proteins.
pDONR207: entry clones carrying gene coding sequences for mitochondrial targeted protein. cpYFP-gene denotes fusion of gene sequence to C-terminus of cpYFP via *Avr*II cut/ligation. pSS01: expression clones created by LR recombination of entry clones with destination vector carrying either cpYFP or EGFP in frame behind the Gateway cassette. Note that cpYFP-gene fusions were amplified with Stop codon at C-terminus to avoid translation with additional cpYFP at C-terminal end. All pSS01 vectors have been stably transformed into Arabidopsis.

pDONR207	pSS01: cpYFP	pSS01:EGFP
AAC1	*AAC1-cpYFP*	
AAC2	*AAC2-cpYFP*	
AK1	*AK1-cpYFP*	
AOX1a	*AOX1a-cpYFP*	*AOX1a-EGFP*
ATPsyn g 1	*ATPsyn g 1-cpYFP*	
cpYFP-ATPsyn g 1	*cpYFP-ATPsyn g 1*	
ATPsyn g 2	*ATPsyn g 2-cpYFP*	
cpYFP-ATPsyn g 2	*cpYFP-ATPsyn g 2*	
ATPsyn g 3	*ATPsyn g 3-cpYFP*	
cpYFP-ATPsyn g 2	*cpYFP-ATPsyn g 2*	
ATPsyn g 3	*ATPsyn g 3-cpYFP*	
CI P2	*CI P2-cpYFP*	
CLS1	*CLS1-cpYFP*	
CRK21-1	*CRK21-1-cpYFP*	
CYTC1	*CYTC1-cpYFP*	
CYTC2	*CYTC2-cpYFP*	
DIC1	*DIC1-cpYFP*	
DIC2	*DIC2-cpYFP*	
dLDH1	*dLDH1-cpYFP*	
ERV1	*ERV1-cpYFP*	
FUM1	*FUM1-cpYFP*	
–	*GET3c-cpYFP*	

pDONR207	pSS01: cpYFP	pSS01:EGFP
GRXS15	*GRXS15-cpYFP*	
MCU1	*MCU1-cpYFP*	
MIC10	*MIC10-cpYFP*	
–	*MICU-cpYFP*	
cpYFP-MIRO1	*cpYFP-MIRO1*	
MPT3	*MPT3-cpYFP*	
NDB1	*NDB1-cpYFP*	
NDB1-cpYFP position 1	*NDB1-cpYFP* position 1	
NDB1-cpYFP position 2	*NDB1-cpYFP* position 2	
NDPK3	*NDPK3-cpYFP*	
–	*NMT1-cpYFP*	
SHMT1	*SHMT1-cpYFP*	
SLP2	*SLP2-cpYFP*	
TIM9	*TIM9-cpYFP*	
TIM17-3	*TIM17-3-cpYFP*	
TIM23	*TIM23-cpYFP*	
cpYFP-TOM7-2	*cpYFP-TOM7-2*	
cpYFP-TOM20-2	*cpYFP-TOM20-2*	
TOM40-1	*TOM40-1-cpYFP*	
TRX-h2	*TRX-h2-cpYFP*	
TRX-o2	*TRX-o2-cpYFP*	
UCP1	*UCP1-cpYFP*	*UCP1-EGFP*
UCP2	*UCP2-cpYFP*	*UCP2-EGFP*
UCP3	*UCP3-cpYFP*	*UCP3-EGFP*
VDAC1	*VDAC1-cpYFP*	
VDAC3	*VDAC3-cpYFP*	

2.9 Phylogenetic analyses

Protein sequences of representative species were retrieved from NCBI Standard Protein Blast using human UCP1 or Arabidopsis AOX1a (UniProt identifier P25874 and Q39219) as query sequences. After manual curation, sequences were aligned with MUSCLE (Edgar, 2004) in MEGA 6 (Tamura et al., 2013) using default parameters. An unrooted tree was calculated using MrBayes with split frequencies < 0.01 after 2,000,000 generations with a mixed amino acid model (Huelsenbeck and Ronquist, 2001).

2.10 Statistical analyses and data plotting

Data were statistically analysed with R studio (www.rstudio.com) or GraphPad Prism 7.0a (www.graphpad.com). Data plotting was conducted with GraphPad Prism 7.0a.

3 RESULTS

3.1 Genetic interference with respiratory uncoupling

3.1.1 Introduction

In plants, mitochondrial uncoupling has predominantly been perceived as a means to reduce mitochondrial ROS production, to maintain cellular energy homeostasis and to support photosynthesis, with particular importance under abiotic stress conditions (C; section 1.3) (Trono et al., 2004; Sweetlove et al., 2006; Giraud et al., 2008; Smith et al., 2009; Barreto et al., 2017; Zhang et al., 2017). For instance, *aox1a* Arabidopsis mutants were found more susceptible to the combination of drought and moderate light stress than wild-type (WT) plants (Giraud et al., 2008). Arabidopsis *ucp1* mutants revealed a photorespiratory phenotype under increased light intensities (Sweetlove et al., 2006), whereas plants overexpressing *UCP* were more drought tolerant (Barreto et al., 2017). Despite the relatively mild phenotypes and likely functional redundancy of gene isoforms and uncoupling systems, characterisations of higher order mutants comprising members from the same or from the different enzyme families have not been reported so far. To address the issue of functional redundancy a first aim of this work was to generate higher order mutants. To that end I aimed for a rational approach of combining selected mutants of *AOX* and *UCP* to overcome potential physiological redundancy.

3.1.2 Selection of candidate mutants and transcript quantification

To study the importance and putative redundancy between UCP and AOX *in vivo*, T-DNA insertion lines were obtained and corresponding transcript abundances were analysed. For *AOX*, the isoform with the highest expression, *AOX1a* (*AT3G22370*), was selected (Figure 5) (Clifton et al., 2005; Vanlerberghe et al., 2009). For *UCP*, all isoforms, *UCP1* (*AT3G54110*), *UCP2* (*AT5G58970*) and *UCP3* (*AT1G14140*), were included (Figure 8A) (Nogueira et al., 2011). The two previously characterised T-DNA insertion lines *aox1a-1* (Giraud et al., 2008; referred to as *aox1a*) and *ucp1-1* (Sweetlove et al., 2006; referred to as *ucp1*), and T-DNA insertions for *UCP2* and *UCP3* were analysed. Both *UCP2* and *UCP3* were uncharacterised when this work was started, but an *ucp2* mutant was

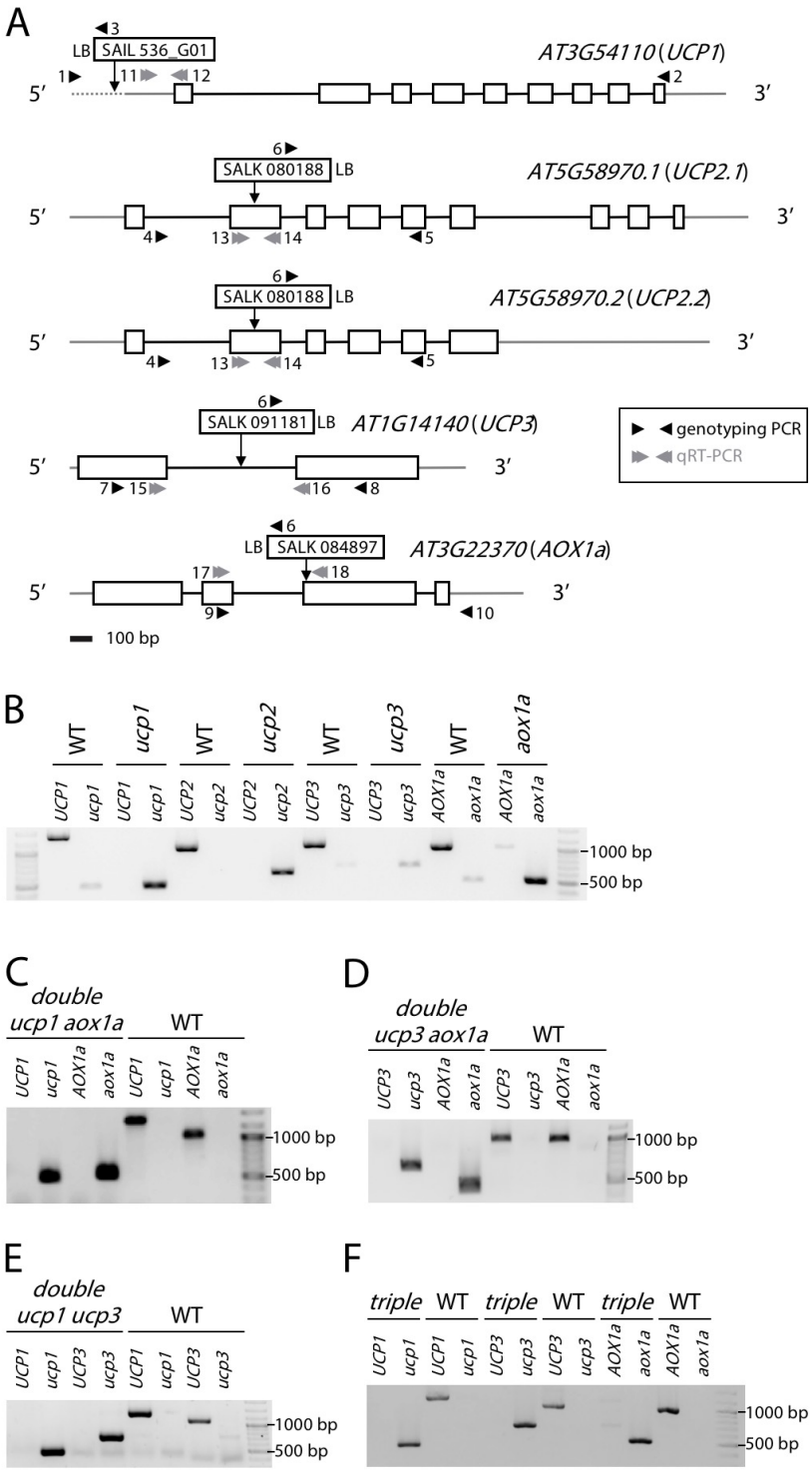
A
LB SAIL 536_G01
AT3G54110 (UCP1)
SALK 080188 LB
AT5G58970.1 (UCP2.1)
AT5G58970.2 (UCP2.2)
SALK 091181 LB
AT1G14140 (UCP3)
genotyping PCR
qRT-PCR
LB SALK 084897
AT3G22370 (AOX1a)
5′
3′
100 bp
B
WT
ucp1
ucp2
ucp3
aox1a
UCP1
ucp1
UCP2
ucp2
UCP3
ucp3
AOX1a
aox1a
1000 bp
500 bp
C
double ucp1 aox1a
WT
D
double ucp3 aox1a
WT
E
double ucp1 ucp3
WT
F
triple
WT

Figure 8: Gene models and genotyping of candidate uncoupling mutant lines.
(**A**) Gene models of Arabidopsis *Uncoupling Proteins* (*UCP1*, *UCP2*, *UCP3*) and *Alternative Oxidase 1a* (*AOX1a*). *UCP2.1* and *UCP2.2*: predicted splice variants, black boxes: exons, black lines in-between: introns, grey lines at 5' and 3' end: UTRs, dotted grey line: un-transcribed sequence, black arrow heads: genotyping PCR primers (Table 10), grey double arrow heads: qRT-PCR primers (Table 11) used in Figure 9. Name and orientation of T-DNA insertions are indicated on top of corresponding genes. (**B**) Agarose gels of genotyping PCR products on corresponding T-DNA lines depicted in (A). Agarose gels of genotyping PCR products on T-DNA insertions in double mutants *ucp1 aox1a* (**C**), *ucp3 aox1a* (**D**), and *ucp1 ucp3* (E). (**F**) Agarose gel of genotyping PCR products on T-DNA insertions in *ucp1 ucp3 aox1a* mutant (*triple*).

recently published (Monné et al. 2018). PCR genotyping confirmed homozygous T-DNA insertion for *ucp1* (SAIL 536_G01), *ucp2* (SALK 080188), *ucp3* (SALK 091181) and *aox1a* (SALK 084897) (Figure 8B). DNA sequencing from the left border T-DNA sequence verified the T-DNA insertions and determined the insertion positions 571 bp (*ucp2*), 690 bp (*ucp3*) or 913 bp (*aox1a*) downstream of the corresponding start codon (Figure 8A). Unexpectedly, *ucp1* T-DNA insertion was located 230 ± 2 bp upstream of the start codon. This was in contrast with a previous characterisation of the same line, which localised the insertion in the first intron of *UCP1* (Sweetlove et al., 2006). The unexpected insertion position was compared to the T-DNA flanking sequence deposited on TAIR (www.arabidopsis.org), which also indicated an insertion position 230 ± 2 bp upstream of the start codon. Together, this argues for a T-DNA insertion in the promotor, but not within the transcribed gene sequence.

The impact of the different insertions on transcript expression was analysed via qRT PCR. Residual *UCP1* transcript was detected, albeit at significantly reduced levels (12% compared to WT; Figure 9A). Transcript levels of *UCP2*, *UCP3* and *AOX1a* were below the detection limit (Figure 9A). To investigate whether residual expression levels in *ucp1* represent full-length transcripts, a semi-qRT PCR was performed in an independent follow-up experiment (Figure 9D). Quantification of the PCR bands from the agarose gel confirmed the knock-down in *ucp1* (~20% of WT expression; Figure 9E). Western-blot results from a previous report, which showed a nearly complete loss of UCP1 protein (-95% relative to WT), hypothesised to originate from antibody cross-reactions with other UCP isoforms (Sweetlove et al., 2006), may now be interpreted as residual UCP1 protein. These data imply that a knock-down of *ucp1* by 80–95% results in the reported photorespiratory phenotype (Sweetlove et al., 2006). Together these data confirmed *ucp2*, *ucp3* and *aox1a* as

full knock-outs, whereas *ucp1* represented a knockdown with approximately 13–20% of residual *UCP1* transcript relative to WT.

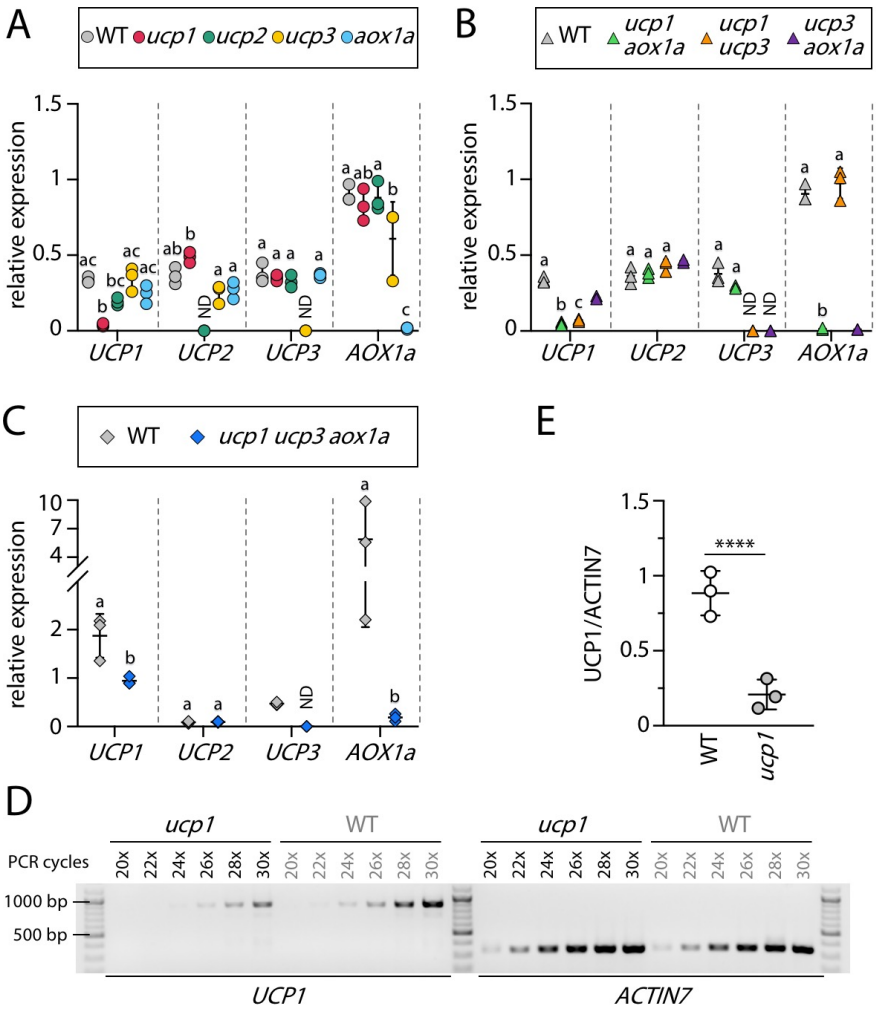

Figure 9: Transcript quantification in wild-type and uncoupling mutant plants.
(**A**) Transcript quantification in single mutants by qRT PCR on cDNA reversely transcribed from RNA isolated from leaves of 3-week-old Arabidopsis plants grown on soil under standard conditions. Reference gene: *SAND FAMILY PROTEIN*. $n = 3$ biological replicates. Different letters indicate significant differences according to two-way ANOVA with Tukey's multiple comparisons test ($P < 0.01$). ND: not detectable. (**B**) Transcript quantification in double mutants as described in (A). Note that *ucp3 aox1a* was excluded from statistical analysis since $n = 2$. (**C**) Transcript quantification in triple mutant as described in (A) on cDNA reverse transcribed from RNA isolated from pooled 8-d-old seedlings. (**D**) Agarose gel image of semi-qRT PCR with primers (Table 12) amplifying full-length gene transcripts from cDNA reverse transcribed from RNA isolated from pooled 7-d-old seedlings. (**E**) Quantification of *UCP1* and *ACTIN7* bands from semi-qRT PCR shown in (D). Y-axis: Measured band intensities shown as ratio from $UCP1_{26x}/ACTIN7_{20x}$, $UCP1_{28x}/ACTIN7_{22x}$ and $UCP1_{30x}/ACTIN7_{24x}$. Significant difference between genotypes according to two-sided t-test (****$P < 0.0001$).

In the absence of an alternative T-DNA insertion in *UCP1*, genome editing via CRISPR-Cas9 multiplex genome editing (Ordon et al., 2017) was attempted to establish a knock-out *ucp1* mutant. Despite the recovery of stably transformed Arabidopsis plants (inferred from the selection marker mediated resistance to glufosinate ammonium), no genome editing events (Supplemental Figure 1) were detected. This was presumably due to a problem with the published destination vectors, as similar issues were observed systematically by different researchers (personal communication with J. Stuttmann, Halle (GER), 2018). Since the issue was only discovered late during this work, the CRISPR-Cas9 approach could not be followed up any further.

3.1.3 All candidate proteins, except UCP2, localised to mitochondria

In most instances, a physical pre-requisite for proteins to act redundantly lies in co-localisation to the same cell compartment. Notably, UCP2, in contrast to UCP1, UCP3 and AOX1a, has so far not been detected in the Arabidopsis mitochondria proteome, but was reported to be part of the Golgi protein inventory (Parsons et al., 2012). To independently investigate the localisation of the candidate proteins, enhanced GFP (EGFP) was fused to the C-termini of their coding sequences under the control of the cauliflower mosaic virus 35S (CaMV35S) promotor and stably transformed into an Arabidopsis line stably expressing mCherry targeted to the mitochondrial matrix (mts-mCherry; El Zawily et al., 2014). Confocal microscopy of hypocotyl cells from seedlings revealed a perfect co-localisation of UCP1-EGFP and AOX1A-EGFP, respectively, with the mCherry-labelled mitochondria (Figure 10A). Although no EGFP fluorescence was detected in UCP3-EGFP transformants, which may be due to silencing, mitochondrial localisation appears likely with regard to the repeated detection of UCP3 in mitochondrial proteomes (Klodmann et al., 2011; Wagner et al., 2015a; Senkler et al., 2017). In contrast, EGFP signal from the fusion with UCP2 revealed fluorescent structures of regular, globular shape, but did not co-localise with neither mts-mCherry nor chlorophyll (Figure 10A). The shape of the UCP2-EGFP labelled structures appeared comparable to the findings from transient co-overexpression of UCP2-YFP and a Golgi marker construct in onion epidermal cells (Parsons et al., 2012). The absence of co-localisation with Cherry-labelled mitochondria was further validated by images recorded from guard cells (Figure 10B) and time course observations in hypocotyl cells (Figure 10C). Guard cells displayed in addition to the

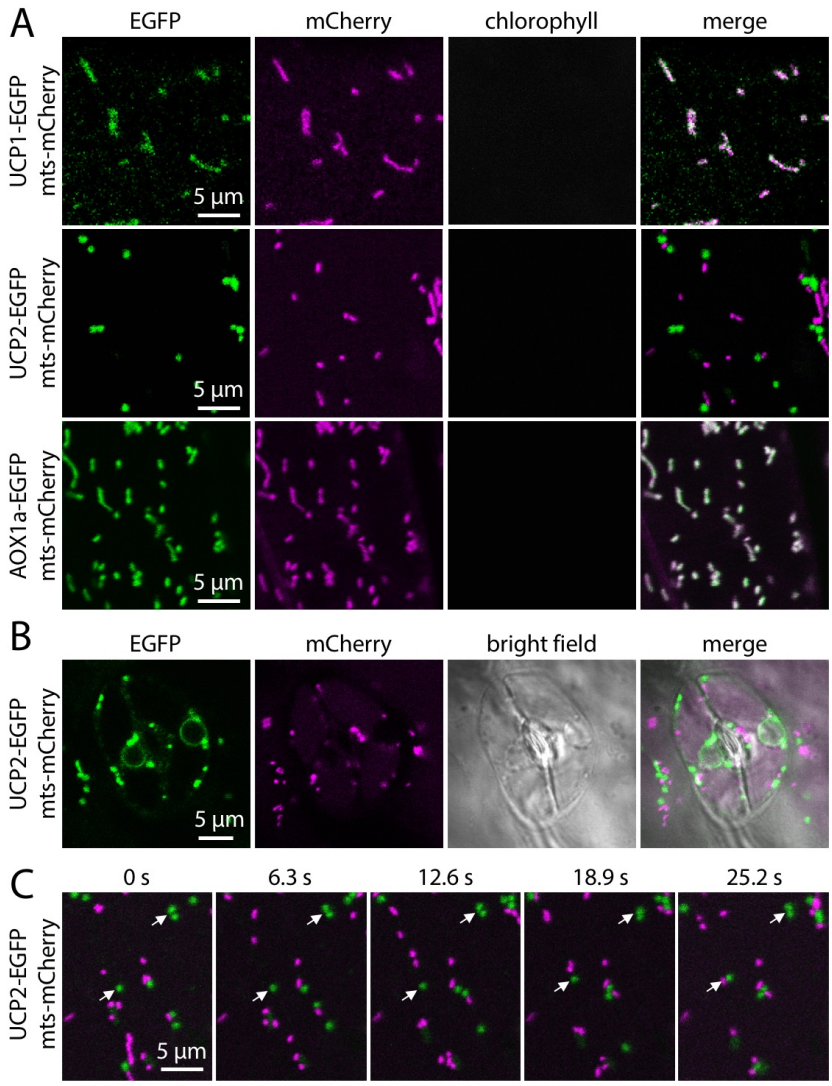

Figure 10: Representative CLSM images of Arabidopsis seedlings stably co-expressing mCherry in the mitochondrial matrix and candidate proteins fused to EGFP.

CLSM images recorded from Arabidopsis seedlings expressing mitochondrial matrix targeted mCherry (mts-mCherry) and different candidate proteins fused to enhanced Green Fluorescent Protein (EGFP) under the control of the cauliflower mosaic virus 35S promotor. EGFP fluorescence: green, mCherry fluorescence: magenta, chlorophyll fluorescence: white. (**A**) CLSM images recorded from hypocotyl cells of 5-d-old Arabidopsis seedlings expressing mts-mCherry and UCP1-EGFP (upper panel), UCP2-EGFP (middle panel) or AOX1a-EGFP (lower panel). (**B**) CLSM images of two guard cells at the abaxial epidermis of cotyledon of a seedling expressing mts-mCherry and UCP2-EGFP. (**C**) CLSM time course of a hypocotyl cell of a seedling expressing mts-mCherry and UCP2-EGFP. Individual images represent merged channels of EGFP and mCherry. White arrows indicate static EGFP-labelled structures relative to dynamic mCherry-labelled mitochondria.

aforementioned structures a large ring of EGFP fluorescence. The perfect overlap of these rings with the nuclear envelopes recorded in the bright field channel might indicate partial localisation of UCP2-EGFP to the nuclear envelope which is continuous with of the ER; similar nuclear envelope-fluorescent structures were reported for the overexpression of Golgi-localised proteins such as Synaptotagmin 2 fused to GFP (Zhang et al., 2011). Observations from time series further indicate differences in the motility. EGFP-labelled spherical structures appeared relatively static compared to mitochondria (Figure 10C). This is concordant to the note that the intracellular velocity of mitochondria is approximately twice as high than of Golgi vesicles or peroxisomes, which are of similar size to mitochondria (Stefano et al., 2014). In summary, the recorded confocal microscopy images in combination with previous proteomic studies suggest mitochondrial localisation for UCP1, UCP3 and AOX1a. In contrast, UCP2 appears not to localise to mitochondria to any extent within the sensitivity range of the method and was therefore excluded from the generation of higher order mutant lines.

3.1.4 Generation of higher order mutants to reduce mitochondrial uncoupling capacity

Previous characterisations of single knock-out mutants of UCP or AOX under stress revealed only mild phenotypic impairments (*e.g.* Sweetlove et al., 2006; Giraud et al., 2008). To investigate whether this might be attributed to functional redundancy among the proteins, the isolated T-DNA insertion lines were crossed to generate higher order mutants. Based on the protein sublocalisation data (section 3.1.3, Figure 10), UCP2 was excluded from the crossings. The single mutant lines were crossed and the double mutants *ucp1 aox1a*, *ucp1 ucp3* and *ucp3 aox1a*, were confirmed to be homozygous in both loci by genotyping PCR (Figure 8C–E). As for single mutants, transcript abundances were quantified by qRT PCR (Figure 9B). The analogous procedure was applied to the triple mutant *ucp1 ucp3 aox1a*, including verification by genotyping PCR (Figure 8F) and transcript quantification (Figure 9C) (see Table 4 for a complete list of acquired and generated uncoupling mutants). In line with the previous observation, the *UCP1* transcript abundance was clearly reduced but residual transcript levels were detectable in *ucp1 aox1a* (15% relative to WT), *ucp1 ucp3* (21% relative to WT) and *ucp1 ucp3 aox1a* (50% relative to WT) mutants.

3.1.5 Discussion

3.1.5.1 Expression of the Uncoupling Genes in the WT and T-DNA Mutants

The relative transcript abundances of *UCP1*, *UCP2*, *UCP3* and *AOX1a* (Figure 9) matched data retrieved from the bioinformatics resources Genevestigator (Hruz et al., 2008) and eFP browser (Winter et al., 2007) overall (Figure 5). The different expression levels of *UCP1* and *AOX1a* between the samples isolated from rosette leaves and seedlings might be accounted for by different growth conditions. Furthermore, data retrieved from Genevestigator also suggest developmental regulation of expression (Figure 5A, B).

For genes of the same family (or of functional redundancy), interference with one gene may trigger increased expression of the remaining isoforms as a compensatory response. The uncoupling mutants displayed no systematic change in the expression of the non-mutated genes, which is consistent with the Arabidopsis *aox1a* transcriptome from Giraud et al. (2008).

3.1.5.2 Sublocalisation of the candidate proteins

The absence of UCP2-EGFP from mitochondria (Figure 10) is in line with previous findings reporting UCP2 as a component of the Golgi proteome, which was further verified by a reporter protein fusion (Parsons et al., 2012). However, a recent reporter protein study using transient transformation of tobacco protoplasts suggested mitochondrial localisation for UCP2 (Monné et al., 2018). The contractionary results might be explained by the different expression systems used. The influence of the expression system on the localisation outcome has recently been highlighted for the proteins Glutathione Peroxidase-like 4 and 5, revealing different sublocalisations in Arabidopsis than in tobacco (Attacha et al., 2017). Apart from the expression system, the process of GFP-tagging can also interfere with the targeting of the protein of interest, for instance by masking the targeting signal(s) or by impairing the integration into a protein complex or membrane (*e.g.* UCP into IMM) (Millar et al., 2009). Although a mitochondrial localisation of UCP2 cannot be fully excluded, the absence of the protein from any published mitochondrial proteome (in contrast to UCP1 and UCP3; *e.g.*, Klodmann et al., 2011; Wagner et al., 2015a; Senkler et al., 2017) renders a notable UCP2 abundance unlikely.

The fact that UCP2 could be excluded from the generation of higher order mutant lines greatly facilitated the crossing regime and allowed to deplete UCP in mitochondria already in the double mutant. Although the AOX family in Arabidopsis includes 5 members, AOX1a is the dominant isoform which cannot be complemented for by the other AOX isoforms (Strodtkötter et al., 2009; Selinski et al., 2018). Accordingly, it was reasoned that the generation of the triple mutant by crossing *aox1a* with *ucp1 ucp3* should give rise to plants with strongly restricted uncoupling capacity and increased stress sensitivity, for instance to drought as previously noted for the *aox1a* and *ucp1* single mutants (Giraud et al., 2008; Smith et al., 2009; Barreto et al., 2017). The lines established in this section provide the foundation for the following *in vivo* studies to dissect the role of mitochondrial uncoupling during drought stress and other related stresses.

3.2 Analysis of the role of uncoupling in drought stress tolerance

3.2.1 Introduction

Previous reports suggested UCP and AOX proteins play an important role in plants to withstand drought and related abiotic stress conditions (and section 1.5.4) (Sweetlove et al., 2006; Giraud et al., 2008; Begcy et al., 2011; Barreto et al., 2014, 2017). The two enzyme families have also been linked to cold stress (Maia et al., 1998; Fiorani et al., 2005; Watanabe et al., 2008; Grabelnych et al., 2014) and developmental processes, such as germination and leaf senescence (Begcy et al., 2011; Chrobok et al., 2016). The involvement in identical physiological processes indicates redundancy, which is supported by the similar functions of the proteins, *i.e.* reducing the degree of coupling between electron transport and ATP synthesis (section 1.5) (Borecký and Vercesi, 2005; Rasmusson et al., 2008; Nogueira et al., 2011). The following section aims to test the hypothesis that the process of mitochondrial uncoupling via UCP and AOX contributes to drought tolerance, as well as to tolerance to related abiotic stress conditions. Using a genetic approach to interfere with the uncoupling capacity, a focus was set on overcoming potential functional redundancy.

3.2.2 Inability to reproduce reported phenotypes while testing single and double uncoupling mutants

To find out if the T-DNA insertions in the different lines give rise to phenotypic differences at the whole plant level in the absence of a particular stress, plants were grown under standard conditions and assessed for differences in their growth and development. A previous characterisation of *ucp1* plants grown on soil revealed a significantly decreased shoot dry mass compared to WT (reduction ~13%). Analysing the leaf rosette area, *ucp1* and *ucp3* revealed small but significantly reduced leaf rosette areas compared to WT plants (Figure 11A, B). The small difference between *ucp1* and WT is in line with a reported reduction of *ucp1* shoot dry mass (Sweetlove et al., 2006). No analogous reports on *ucp3* were found. Interestingly, the independently assayed double mutant *ucp1 ucp3* did not demonstrate any difference to the WT in leaf rosette area, neither did the *ucp1 aox1a* double mutant (Figure 11D, E).

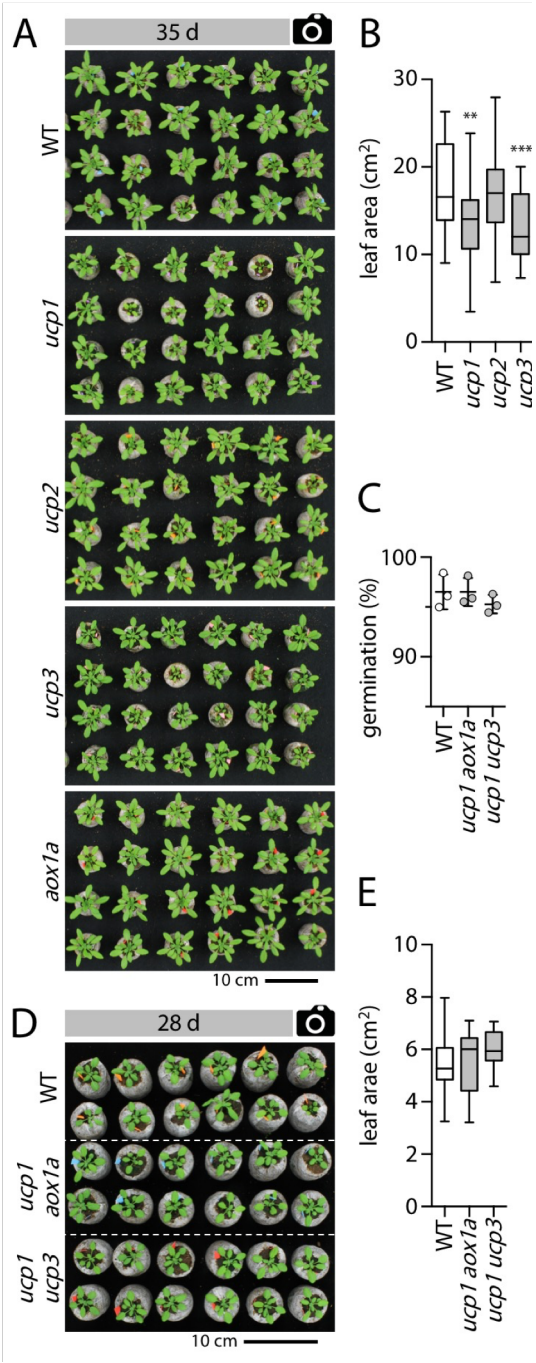

Figure 11: Analysis of Arabidopsis leaf rosette development and germination rate in lines impaired in mitochondrial uncoupling under standard growth conditions.

(**A**) Images of 35-d-old wild-type (WT) and single mutant plants grown under standard conditions in Jiffy pots. (**B**) Quantification of leaf rosette area of 35-d-old plants as shown in (A). $n \geq 28$ plants. Significant differences between WT and mutants according to one-way ANOVA with Bonferroni's multiple comparisons test ($^{**}P < 0.01$, $^{***}P < 0.001$). Boxes: 1st and 3rd quartiles with median and Tukey whiskers. (**C**) Proportion of seeds germinated 2 d after start of imbibition. $n = 3$ agar plates with 100 seeds each. No significant differences between WT and double mutants according to one-way ANOVA with Bonferroni's multiple comparisons test ($P \geq 0.05$). (**D**) Image of 28-d-old WT and double mutant plants grown as described in (A). (**E**) Quantification of leaf rosette area of 28-d-old plants shown in (D) $n \geq 11$ plants. Boxes: 1st and 3rd quartiles with median and Tukey whiskers. No significant differences according to one-way ANOVA with Bonferroni's multiple comparisons test ($P \geq 0.05$).

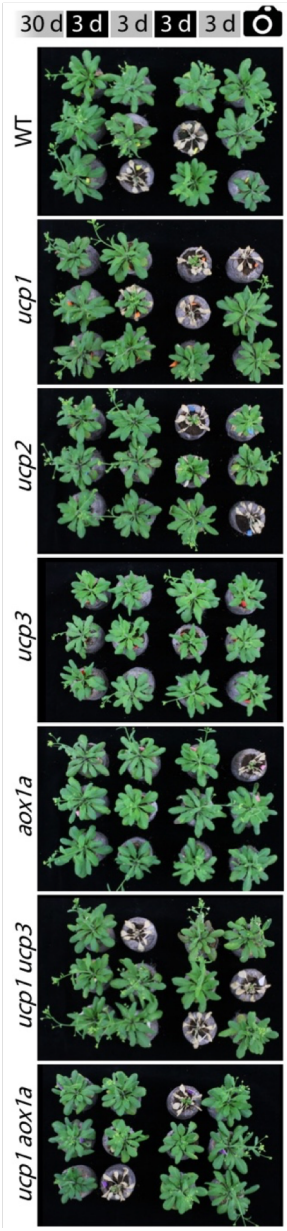

Figure 12: Leaf rosette area analysis under drought and increased light of Arabidopsis lines impaired in mitochondrial uncoupling.
Images of 42-d-old wild-type (WT) and mutant plants after exposure to recurring drought and subsequent re-watering treatments. Plants were grown for 30 d under standard conditions before exposed twice to drought and increased light intensity for 3 d each (black boxes in scheme; arrested watering and increased irradiance 450 µmol m^{-2} s^{-1}) followed by re-watering and standard light intensities (grey boxes; regular watering and 100–120 µmol m^{-2} s^{-1}).

Apart from affecting shoot development, overexpression of *AtUCP1* in tobacco plants was reported to lead to an earlier seed germination, particularly under salt-stress conditions (Begcy et al., 2011). Consistently, *UCP1* and *AOX1a* transcript levels were found upregulated during seed germination (Figure 5). The potential connection was investigated in a seed germination assay by comparing double mutants and WT germination rates within 48 h after start of imbibition. No significant difference in germination rates were found between the double mutant and WT lines under standard conditions (Figure 11C). Absence of an obvious phenotypic difference between WT and mutant plants might be accounted for by a mainly stress-alleviating function of UCP and AOX. Hence, plant performance under stress conditions was investigated next. Drought, especially in combination with increased light intensities, had been reported to lead to increased anthocyanin accumulation and lower survival rates for *aox1a* plants relative to WT plants (Giraud et al., 2008). Arabidopsis *ucp1* plants showed decreased photorespiratory capacity (Sweetlove et al., 2006), and given that photorespiration is generally induced under drought, increased drought sensitivity was expected (see also Figure 1). Single and double mutant plants

were grown under standard conditions for 30 days before the plants were exposed to gradually imposed drought combined with increased light intensities. Even though the treatment was severe as judged by the lack of recovery of individual plants, neither single nor double mutants appeared to be notably more impaired than WT plants (Figure 12). Subtle differences can naturally not be excluded, considering the limited replicate numbers (n = 12–14 plants). Nevertheless, the absence of a consistent and obvious phenotypic difference appears in conflict with previous reports. It might likewise indicate the requirement of specific environmental conditions accentuating the requirement of UCP- and AOX-mediated uncoupling.

3.2.3 Exposure to drought-related stressor exhibits no phenotypic differences between uncoupling mutants and WT seedlings

To test a broader range of specific drought-related stressors in a more controlled manner than on soil, seedling phenotyping assays on agar plates were conducted. Seedlings were grown on standard agar plates for 4 days before being transferred onto plates containing stress-inducing additives. After an additional 4 days on the stress-inducing plates, primary root growth of the seedlings was measured. In the control treatment, seedlings were transferred onto new plates without stress-inducing additives, in which the mutant seedlings were phenotypically indistinguishable from WT seedlings (Figure 13Figure 13A, D). Exposing seedlings to 300 mM mannitol led to a pronounced reduction of the primary root growth, but no difference was observed in this response between the genotypes (Figure 13B, E). To verify the phenotyping method, plants were exposed to antimycin A, which inhibits the mitochondrial electron transport chain at complex III, leading to an almost complete arrest of seedling root growth in plants lacking *AOX1a* (Figure 13C, F, G). The strong impairment of *aox1a* by Antimycin A supports the importance of the *AOX1a* isoform, which cannot be compensated for by other AOX isoforms (Strodtkötter et al., 2009; Selinski et al., 2018). This is in agreement with the role of AOX to act as a bypass when the capacity of the mitochondrial Cytochrome *c* Oxidase pathway is limiting (Maxwell et al., 1999; Vishwakarma et al., 2015). In contrast to the *aox1a* line, lines lacking *UCP1*, *UCP2* or *UCP3* appeared unaffected by the inhibition of complex III.

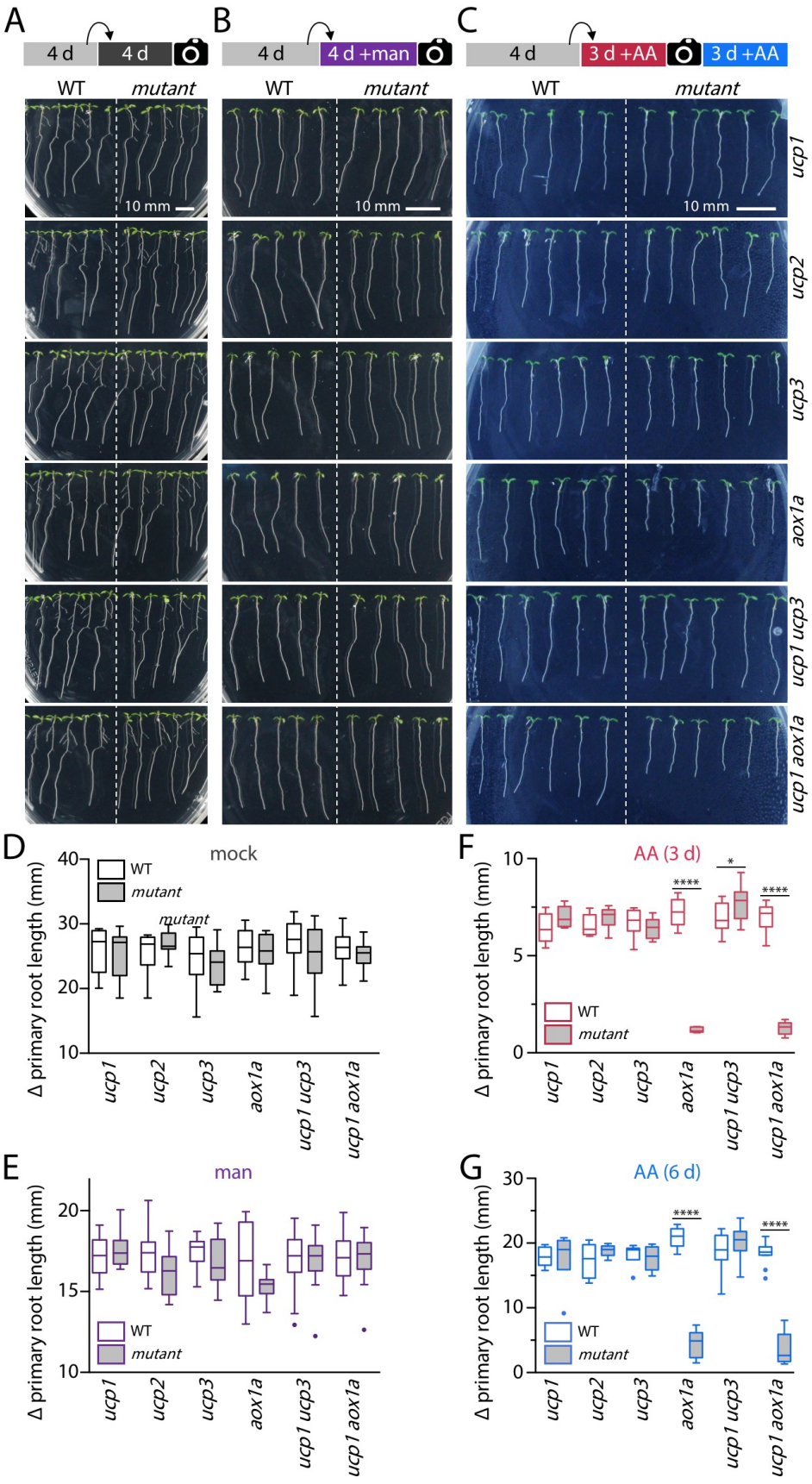
A
4 d
4 d
B
4 d
4 d +man
C
4 d
3 d +AA
3 d +AA
WT
mutant
10 mm
ucp1
ucp2
ucp3
aox1a
ucp1 ucp3
ucp1 aox1a
D
mock
Δ primary root length (mm)
WT
mutant
E
man
F
AA (3 d)
G
AA (6 d)
****
*

Figure 13: Root development of Arabidopsis wild-type, single and double mutant seedlings under abiotic stress.
(**A**) Eight-d-old Arabidopsis wild-type (WT) and mutant seedlings were germinated and vertically grown 4 d on standard agar plates before they were transferred onto new plates with identical composition and grown for additional 4 days. (**B**) As in (A) except that seedlings were transferred onto new plates supplemented with 300 mM mannitol (man). (**C**) As in (A) except that seedlings were transferred onto new plates supplemented with 20 µM antimycin A (AA). Seedlings were documented and primary root growth quantified 3 d (shown) and 6 d after transfer. (**D**), (**E**), (**F**) and (**G**) Quantification of primary root growth after transfer onto new agar plates. $n \geq 10$, $n \geq 11$, $n \geq 5$, $n \geq 5$, respectively. Significant differences between WT and mutants in (F) and (G), but not in (D) and (E), according to one-way ANOVA with Bonferroni's multiple comparisons test (*$P < 0.05$, ****$P < 0.0001$). Boxes: 1st and 3rd quartiles with median and Tukey whiskers.

Cold represents another, abiotic stress reportedly involving both UCP and AOX1a (Maia et al., 1998; Fiorani et al., 2005; Watanabe et al., 2008; Grabelnych et al., 2014). Arabidopsis plants grown at 4°C have been found to significantly upregulate *UCP* expression and UCP protein levels (Maia et al., 1998). Furthermore, AOX1a appears important to mediate cold acclimation. Anti-sense lines reduced in AOX grown at moderate cold and light intensities (12°C and 400 µmol m^{-2} s^{-1}) accumulated slightly but significantly less shoot biomass, whereas the opposite was observed for plants overexpressing mutated, constitutively active AOX1a (Fiorani et al., 2005). To mimic similar conditions, seedlings were transferred onto control agar plates and exposed to moderate temperatures (12°C) and light intensities (400 µmol m^{-2} s^{-1}). The transfer of the seedlings led to a visible accumulation of anthocyanin, but largely reversed after 12–15 days (Figure 14A). Quantification of the primary root growth within 9 days after transfer revealed a minor but significant reduction for *ucp1 ucp3*, whereas detectable phenotypic differences between *ucp1 aox1a* and WT seedlings remained absent (Figure 14B).

3.2.4 Triple uncoupling mutant reveals small phenotypic differences to WT plants

The absence of any stronger impairment of the uncoupling mutants may be accounted for by a functional backup, for which the remaining gene homologues are the obvious candidates. A phenotypic comparison of the *ucp1 ucp3 aox1a* triple mutant (see section 3.1.4 for generation of mutant) was undertaken to investigate this possibility. It was reasoned that AOX1a is the limiting isoform for *in vivo* AOX capacity (see *aox1a* root growth at antimycin A in Figure 13) and UCP1 and UCP3 are the only UCP proteins localised in the mitochondria (section 3.1.3). As such the two major known mitochondrial

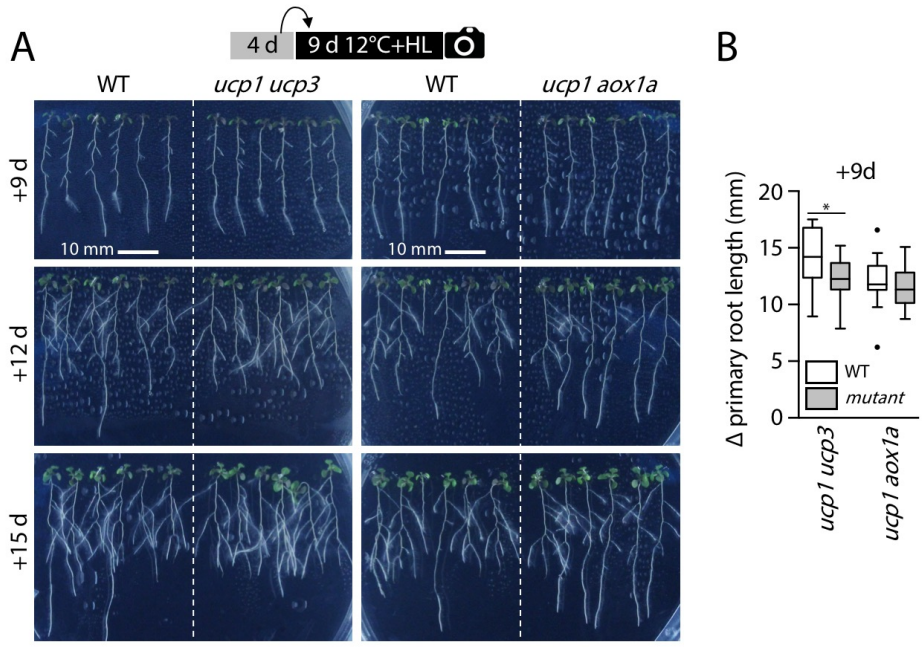

Figure 14: Root development of Arabidopsis wild-type and uncoupling mutant seedlings under moderate cold and light-stress.

(**A**) Thirteen-d-old Arabidopsis wild-type (WT) and mutant seedlings germinated and vertically grown 4 d on standard agar plates before they were transferred onto freshly prepared plates with identical composition but subjected to 12°C and 400 µmol m^{-2} s^{-1}. (**B**) Quantification of primary root growth 9 d after transfer. $n \geq 18$. Boxes: 1st and 3rd quartiles with median and Tukey whiskers. Significant differences between WT and mutants according to one-way ANOVA with Bonferroni's multiple comparisons test (*$P < 0.05$).

uncoupling mechanisms are functionally abolished in the triple mutant. Germination and growth for 5 days on standard agar plates did not show any differences between WT and mutant seedlings (Figure 15A). This was confirmed by measurements of the primary root length (Figure 15B). Gross plant development on soil was followed by standardised photographs and analysis of the leaf rosette area. Notably, from 36 days on, which was roughly the time of transition from vegetative to reproductive growth, the triple mutant plants exhibited a smaller leaf rosette area compared to the WT (reduced by 13%, 14% and 10% at day 36, 40 and 43, respectively; Figure 15C, D). Independent of the leaf rosette area, primary inflorescence appearance and height were similar for both lines (Figure 15E, F).

To investigate if the small differences observed between the lines might increase under stress, plants were exposed to drought and dark-induced leaf senescence. The drought treatment followed the experimental conditions described in Giraud et al. (2008), under which *aox1a* Arabidopsis plants showed pronounced sensitivity to combined

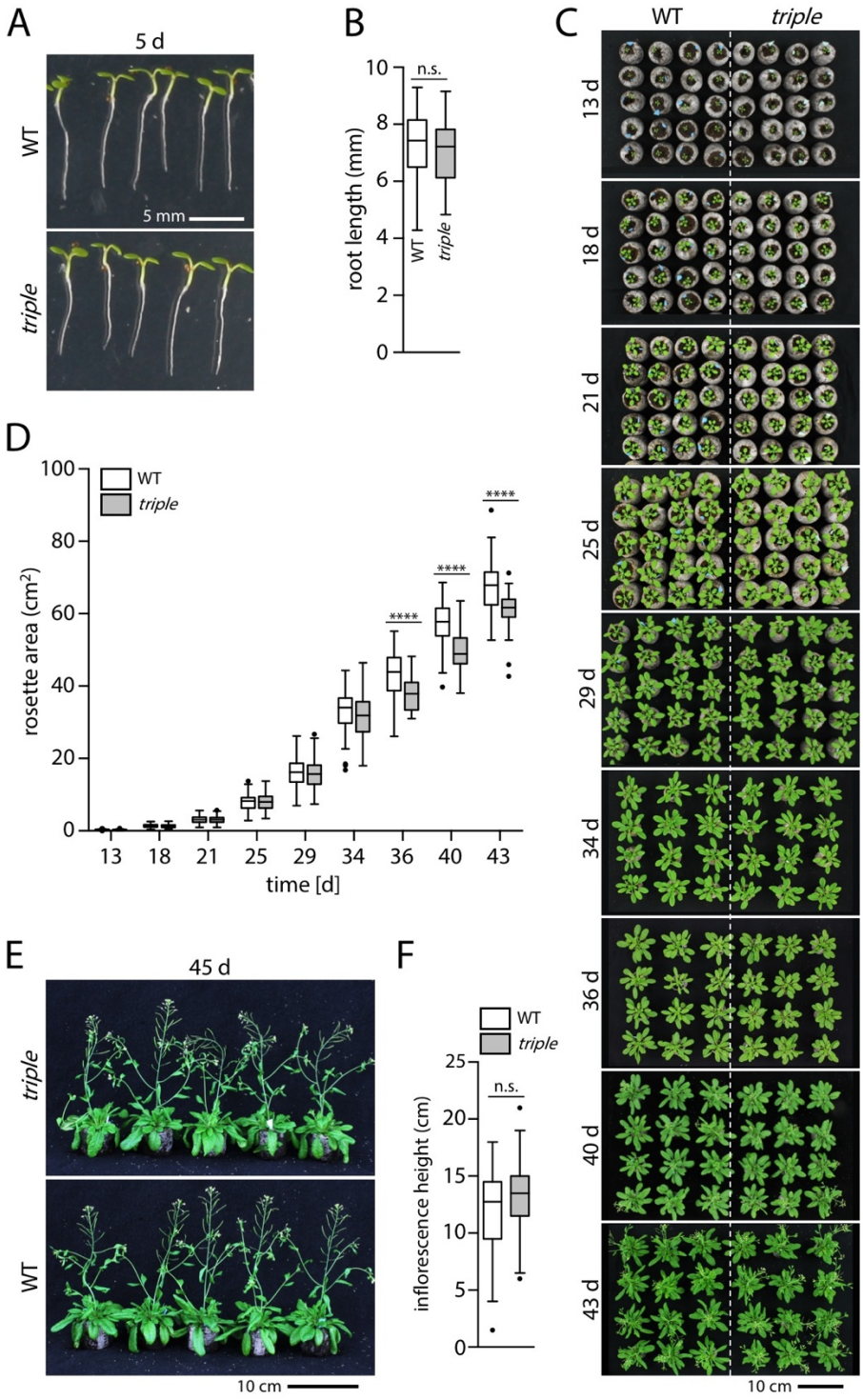

Figure 15: Comparison of primary root length, leaf rosette area and inflorescence height of Arabidopsis wild-type and *ucp1 ucp3 aox1*a mutant plants under standard growth conditions.

(**A**) Representative images of wild-type (WT) and *ucp1 ucp3 aox1a* (*triple*) seedlings germinated and vertically grown on agar plates under standard conditions for 5 d. (**B**) Primary root length of 5-d-old Arabidopsis seedlings as shown in (A). $n \geq 63$. Boxes: 1st and 3rd quartiles with median and Tukey whiskers. Not significantly different according to two-sided t-test ($P > 0.05$). *(continued on next page)*

(Figure 15 continued)
(**C**) Representative images of WT and mutant plants during course of phenotyping experiment grown under standard conditions (16 h light, 100–120 µmol m^{-2} s^{-1}, at 22°C and 8 h dark at 18°C). (**D**) Leaf rosette area during development of plants as shown in (C). $n \geq 48$. Boxes: 1st and 3rd quartiles with median and Tukey whiskers. Significant differences between genotypes according to two-way ANOVA with Bonferroni's multiple comparisons test (****$P < 0.0001$). (**E**) Representative images of 45-d-old WT and *triple* mutant plants grown on Jiffy pellets. (**F**) Inflorescence height quantification of 45-d-old plants as shown in (E). $n = 48$. Boxes: 1st and 3rd quartiles with median and Tukey whiskers. Not significantly different according to two-sided t-test ($P > 0.05$).

drought and light stress. After 10 days of treatment, watering and standard light intensities were resumed allowing the plants to recover. WT plants appeared to cope slightly better with the treatment as judged by the survival rates (WT: 9 out of 9, triple: 6 out of 9) (Figure 16A). The drought treatment with standard light intensities, however, did not reveal such tendencies.

It was reasoned that under energy-limiting conditions, such as dark-induced senescence, restricted uncoupling capacity might provide an advantage. In agreement with this concept, transcript data from senescing plants indicated a repression of *UCP* isoforms and *AOX1a* (Chrobok et al., 2016). Detached leaves from 3-week-old plants were incubated for 5 days in darkness. WT and triple mutant lines showed senescence as indicated by a decrease in green colour, but the WT leaves remained slightly greener indicating a slower chlorophyll degradation (16B, C).

Treatment with antimycin A, as applied by spraying, was used as a control. Spraying plants with 50 µM antimycin A strongly inhibited the increase of the leaf rosette area of triple mutants as compared to the WT plants (reduced by 29%, 42%, 47% and 45% at day 34, 36, 40 and 43, respectively; Figure 16D, E), which was hardly affected by the treatment (WT leaf rosette areas were comparable to plants depicted in Figure 15). The antimycin A control validates the functional importance of AOX1a when the capacity of the mitochondrial ETC is limiting. Under the applied regimes of drought stress and dark-induced senescence, the triple mutant showed different behaviour to the WT, although those changes appeared modest, especially when compared to previous reports on *aox1a* and *ucp1* single mutants (Giraud et al., 2008; Sweetlove et al., 2006).

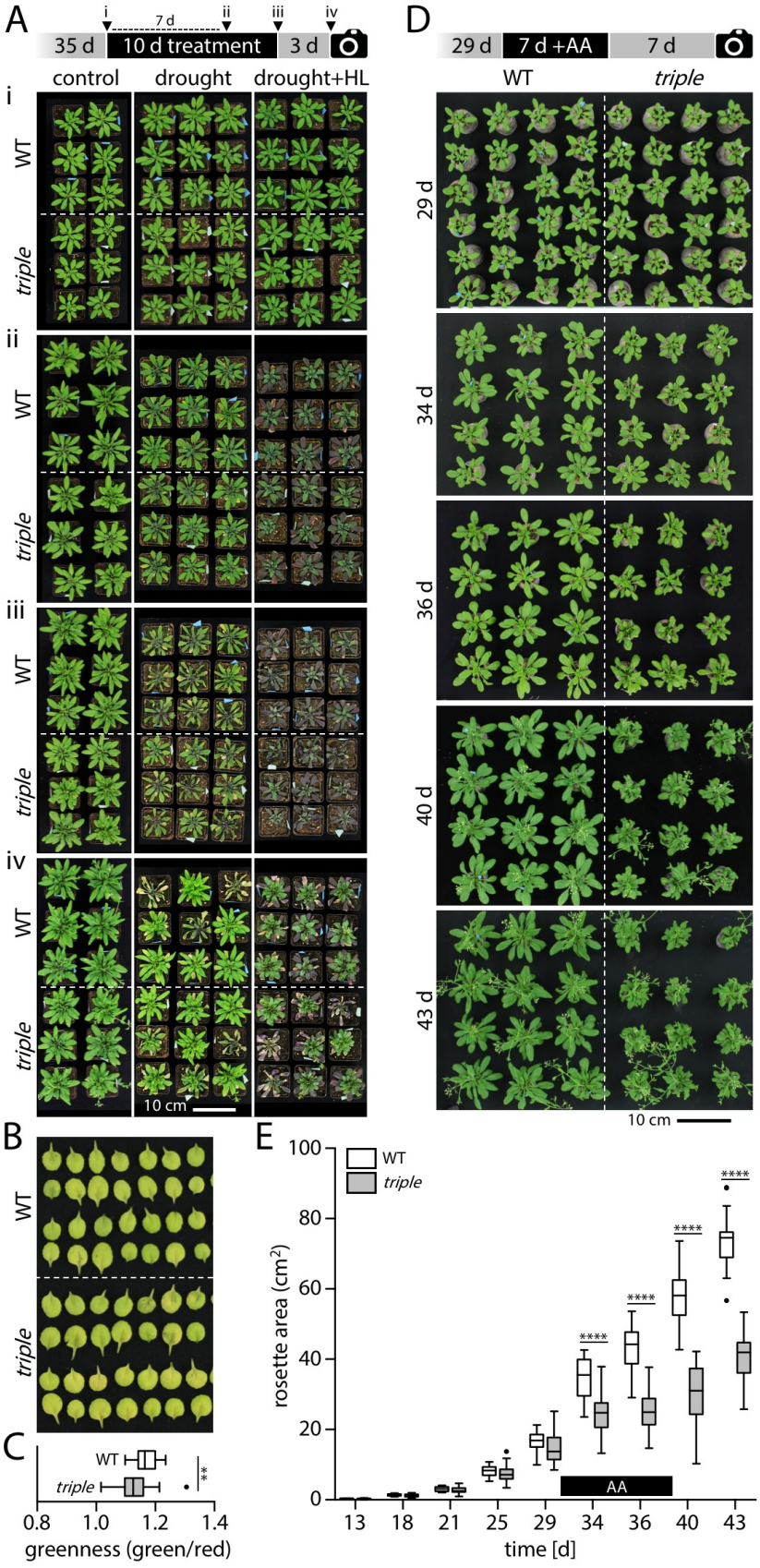
A
i
7 d
ii
iii
iv
35 d
10 d treatment
3 d
control
drought
drought+HL
WT
triple
10 cm
B
C
WT
triple
**
0.8
1.0
1.2
1.4
greenness (green/red)
D
29 d
7 d +AA
7 d
WT
triple
34 d
36 d
40 d
43 d
10 cm
E
WT
triple
rosette area (cm²)
100
80
60
40
20
0
****
AA
13
18
21
25
29
34
36
40
43
time [d]

Figure 16: Comparison of leaf rosette area and germination rate of Arabidopsis wild-type and *ucp1 ucp3 aox1a* mutant plants under challenging conditions.
(**A**) Representative images of wild-type (WT) and *ucp1 ucp3 aox1a* (*triple*) plants during the phenotyping experiment. At the age of 35 d (i), plants were either maintained at standard condition (control; regular watering and 100–120 µmol m^{-2} s^{-1}) or subjected to drought by withholding water with or without a high-light treatment (HL; 400 µmol m^{-2} s^{-1}). After 10 d of treatment (iii), plants were returned to initial conditions and the recovery was monitored (iv). (**B**) Dark-induced senescence in leaves floated for 5 d in complete darkness on assay medium. Leaves harvested from 3-week-old plants (independent from (A)) grown under standard conditions in Jiffy pellets were assayed. (**C**) Quantification of progression of dark-induced senescence in leaves shown in (B). Greenness: green divided by red pixel intensity retrieved from RGB-encoded image. $n = 30$ leaves from different plants. Boxes: 1st and 3rd quartiles with median and Tukey whiskers. Significant differences between genotypes according to two-sided t-test (**$P < 0.01$). (**D**) Representative images of WT and mutant plants during course of phenotyping experiment from age of 29 d to 43 d. Top (29 d): plants before spraying with 50 µM antimycin A (AA). 34 d, 36 d and 40 d: plants following 1st, 2nd or 3rd AA spraying, respectively. Bottom (43 d): plants 7 d after last AA spraying. (**E**) Plant leaf rosette area quantification following growth of plants as shown in (D). $n = 24$. Boxes: 1st and 3rd quartiles with median and Tukey whiskers. Significant differences between genotypes according to two-way ANOVA with Bonferroni's multiple comparisons test (****$P < 0.0001$).

3.2.5 Discussion

The comparisons of the single, double and triple uncoupling mutants against WT plants revealed several differences, *e.g.* decreased tolerance to the combination of drought and light stress (Figure 16A) or lower leaf rosette areas under standard growth conditions (Figure 15). But, all differences were minor in absolute degree. The absence of strong phenotypic differences combined with the inability to reproduce previously reported phenotypes (*e.g.* Giraud et al., 2008; Sweetlove et al., 2006) suggests that specific conditions need to be fulfilled to require mitochondrial energy uncoupling.

3.2.5.1 Mitochondrial ETC capacity was not limiting under the applied conditions

The prerequisite of specific conditions to necessitate mitochondrial energy uncoupling is indirectly supported by the strong phenotype observed for *aox1a* mutant plants in the presence of the mitochondrial ETC inhibitor antimycin A (Figure 13, Figure 15Figure 15). This observation implies two important considerations. Firstly, the strong phenotype of *aox1a* demonstrates a central and non-interchangeable role of AOX1a amongst its isoforms. Although AOX1d was shown to be induced in response to *aox1a* antimycin A-treatments, increased AOX1d protein levels failed to phenotypical rescue the mutant (Strodtkötter et al., 2009). Secondly, it verifies the important role of the alternative electron pathway under restricted mitochondrial ETC capacities. The fact that the other

applied conditions did not elicit pronounced phenotypic differences between the uncoupling mutants and WT suggests that the mitochondrial ETC capacity was not constituting a major flux bottleneck, *i.e.* the treatments did not trigger a situation of excess reductant which required dissipation by respiratory uncoupling via UCP and/or AOX.

3.2.5.2 Uncoupling might be required for the tolerance of other stress conditions

The absence of pronounced phenotypic differences is also unexpected regarding the degree of evolutionary conservation of UCP and AOX. Both proteins are phylogenetically well-conserved and are present in multiple isoforms (Figure 4, Figure 6). Yet, uncoupling mutant plants with mitochondria nearly devoid of UCP and lacking the major AOX isoform AOX1a, were largely indistinguishable from WT plants. It is tempting to speculate that the two enzyme families could fulfil other functions than those addressed in this study by the applied treatments.

3.3 Monitoring *in vivo* cellular energy physiology changes in response to drought and in uncoupling mutants

3.3.1 Introduction

Drought is a major environmental stress factor to plants, for which they have evolved complex responses. One of the best studied responses is the regulation of stomatal conductance (Figure 1). Attempting to reduce water loss, plants close their stomata but at the cost of impaired gas exchange. This leads to a rapid arrest of photosynthesis and triggers increased rates of photorespiration due to depleted leaf internal CO_2 and increased O_2 levels (Dietz and Heber, 1983; Quick et al., 1992; Flexas et al., 2004). The switching between the pathways involves a fundamental re-programming of (sub)cellular energy homeostasis (Wigge et al., 1993; Igamberdiev et al., 2001), whereby the photorespiratory pathway can become a major reductant source to mitochondria (Bykova et al., 2005; Igamberdiev et al., 2001).

To date, comparisons of subcellular energy parameters relied mostly on destructive methods with no or minimal spatiotemporal resolution. To compensate for these technical limitations, assays based on genetically encoded biosensors were developed to monitor energy parameters in intact Arabidopsis plants. *In vivo* monitoring techniques were adopted to assess the consequences of drought and other abiotic stresses at the cell physiological level and moreover, to investigate energy physiology homeostasis in the uncoupling mutants under stress conditions.

3.3.2 Drought affects cellular energy physiology in WT plants

Arguably, two of the most central pillars of cellular energy physiology are ATP and NAD. Glutathione redox potential (E_{GSH}) represent an additional parameter directly related to energy physiology and was reported to be affected by drought (Jubany-Mari et al., 2010; Brossa et al., 2013). Despite the central role of these three parameters, little is known about their *in vivo* spatiotemporal changes in response to drought stress. To gain a better understanding, measurements of $MgATP^{2-}$, NAD redox status and E_{GSH} in living plants using the ATeam 1.03-nD/nA, Peredox-mCherry and GRX1-roGFP2 biosensors (section 1.6, Figure 7), respectively, were conducted (Dooley et al., 2004; Marty et al., 2009; Hung et al., 2011; Hung and Yellen, 2014; De Col et al., 2017). The seedlings with the

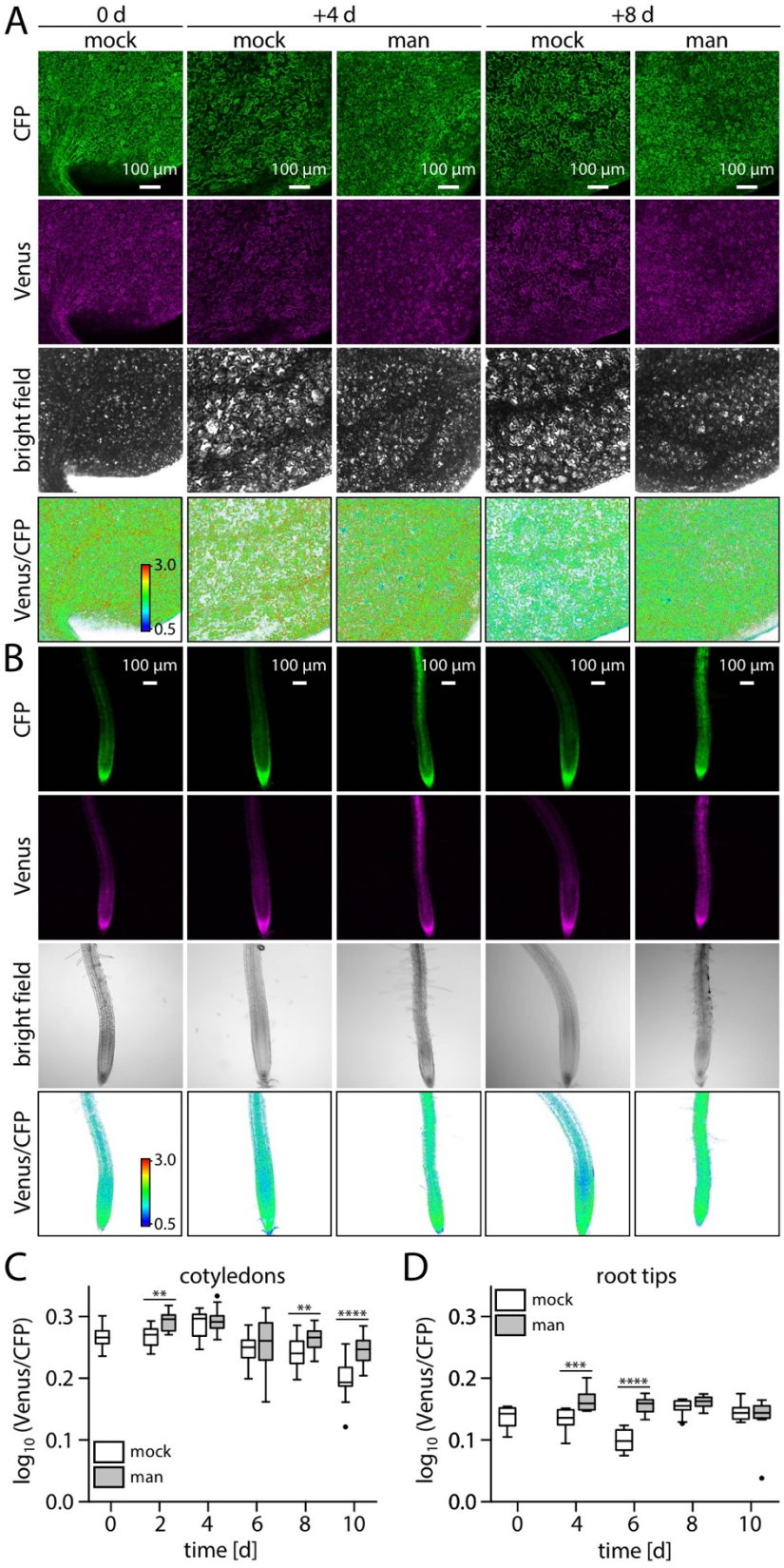
A
0 d
+4 d
+8 d
mock
mock
man
mock
man
CFP
Venus
bright field
Venus/CFP
100 µm
3.0
0.5
B
C
cotyledons
log10 (Venus/CFP)
time [d]
mock
man
D
root tips

Figure 17: *In vivo* measurements of cytosolic $MgATP^{2-}$ levels in Arabidopsis wild-type seedlings under control and drought conditions.

Four days after germination and growth on standard vertical agar plates, Col-0 wild-type seedlings stably expressing cytosolic ATeam 1.03-nD/nA were transferred onto new agar plates without (mock) or with 300 mM mannitol (man). Seedlings subjected to CLSM for $MgATP^{2-}$ level analyses at indicated time points. ATeam was excited at 458 nm the fluorescence emission of mseCFP (CFP, green) and cp173-mVenus (Venus, magenta) was collected at 465–500 nm and 526–561 nm, respectively. False-colour images (Venus/CFP) depict the emission intensity ratio. High Venus/CFP ratios indicate high $MgATP^{2-}$ levels and are shown in red, whereas low levels are shown in blue. (**A**) Representative CLSM images of cotyledons of ATeam 1.03-nD/nA seedlings. (**B**) Representative CLSM images of root tips of ATeam 1.03-nD/nA seedlings. (**C**) Quantified relative changes of $MgATP^{2-}$ for cotyledons ($n \geq 19$). Y-axis: $\log_{10}$ ratio values of Venus and CFP fluorescence intensities (higher values indicate higher $MgATP^{2-}$ levels). Boxes: 1st and 3rd quartiles with median and Tukey whiskers. Significant differences between treatments according to two-way ANOVA with Bonferroni's multiple comparisons test (**$P < 0.01$, ***$P < 0.001$, ****$P < 0.001$). (**D**) Quantified relative changes of $MgATP^{2-}$ for root tips ($n \geq 11$) as described in (C).

biosensors were germinated and grown for 4 days at standard conditions before being either transferred onto control agar plates or plates supplemented with mannitol. At selected time points (0–10 days after transfer), intact seedlings were analysed by confocal microscopy and treatments compared.

For plants expressing cytosolic ATeam 1.03-nD/nA, small but significant differences between the treatments were observed (Figure 17, Figure 18). Specifically, plants exposed to mannitol showed higher cytosolic $MgATP^{2-}$ concentrations than their counterparts growing on standard plates in all three independent experiments. In contrast to the relatively minor treatment effect, comparison of root tips with cotyledons revealed a consistent tissue effect, *i.e.* higher $MgATP^{2-}$ levels in cotyledons than in root tips. The observed tissue heterogeneity is in agreement with the $MgATP^{2-}$ tissue gradients reported in a recent study (partially resulting from this work) employing the same Arabidopsis sensor line (De Col et al., 2017).

Cytosolic NAD redox state also showed significant differences between treatments. A significant oxidation in the cotyledons was observed (Figure 19), which was observed in all three independent experiments despite the spatial heterogeneity within the tissues (Figure 19, Figure 20). Moreover, the NAD redox analysis revealed pronounced tissue effects between cotyledons and root tips. The increased oxidation in the cotyledons was concordant to previous observations based on the same sensor (Negroni, 2017).

Analyses of cytosolic E_{GSH} revealed remarkably stable redox potentials (Figure 21). The transfer and growth of the seedlings on mannitol revealed no consistent effect on E_{GSH}. This is in contradiction to previous observations based on cytosolic roGFP1 (Jubany-Mari et al., 2010; Brossa et al., 2013), and might be explained by different experimental settings and growth conditions.

Considering the results from the biosensor measurements, the energy and metabolic redox status in the cytosol of WT plants was clearly shifted correlating with the root growth phenotype, *i.e.* the formation of long root hairs in root tip proximity and a smaller root tip diameter in response to mannitol exposure (*e.g.* Figure 19). NAD oxidation in response to drought appears counterintuitive, considering the conceptual framework of photoinhibition leading to a reduction of the NAD(P) pools. Yet, since confocal imaging took place in the dark (except for the laser illumination) and the reductive impact of photoinhibition can only be expected in the light, the observed oxidation might be a result of an acclimatisation response, which might also contribute to the observed higher $MgATP^{2-}$ concentrations.

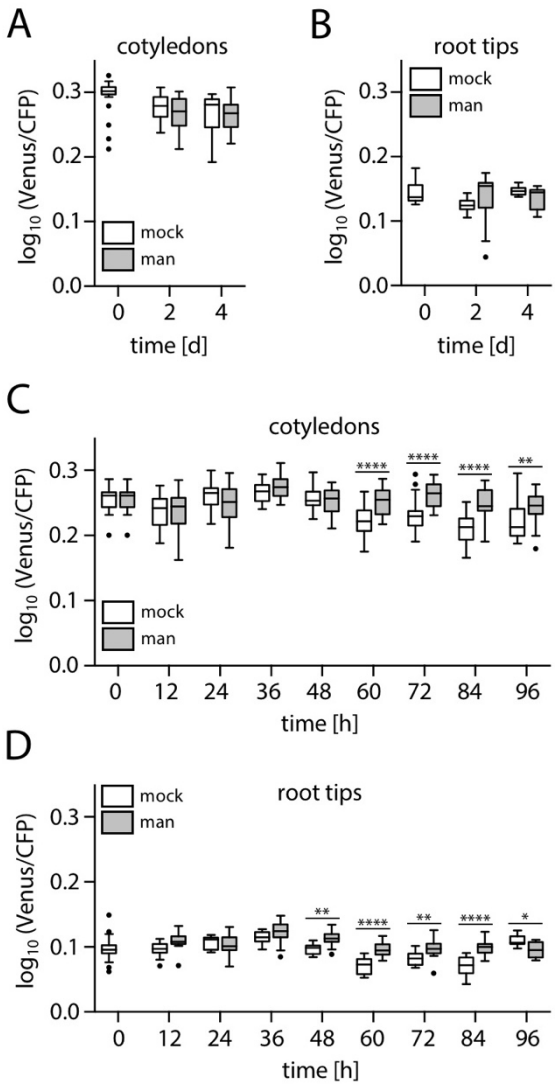

Figure 18: Experimental replicates of *in vivo* cytosolic $MgATP^{2-}$ level measurements under control and drought conditions.

Experiment performed as described in **Figure 17** except for time intervals between CLSM recordings. Y-axis: log_{10} ratio values of mseCFP (CFP) and cp173-mVenus (Venus) fluorescence intensities (high Venus/CFP ratios indicate high $MgATP^{2-}$ levels). Boxes: 1st and 3rd quartiles with median and Tukey whiskers. Significant differences between treatments according to two-way ANOVA with Bonferroni's multiple comparisons test (*$P < 0.05$, **$P < 0.01$, ****$P < 0.0001$). (**A**) Quantified relative changes of $MgATP^{2-}$ for cotyledons ($n \geq 24$). (**B**) Quantified relative changes of $MgATP^{2-}$ for root tips ($n \geq 14$). (**C**) Quantified relative changes of $MgATP^{2-}$ for cotyledons ($n \geq 22$). (**D**) Quantified relative changes of $MgATP^{2-}$ for root tips ($n \geq 14$).

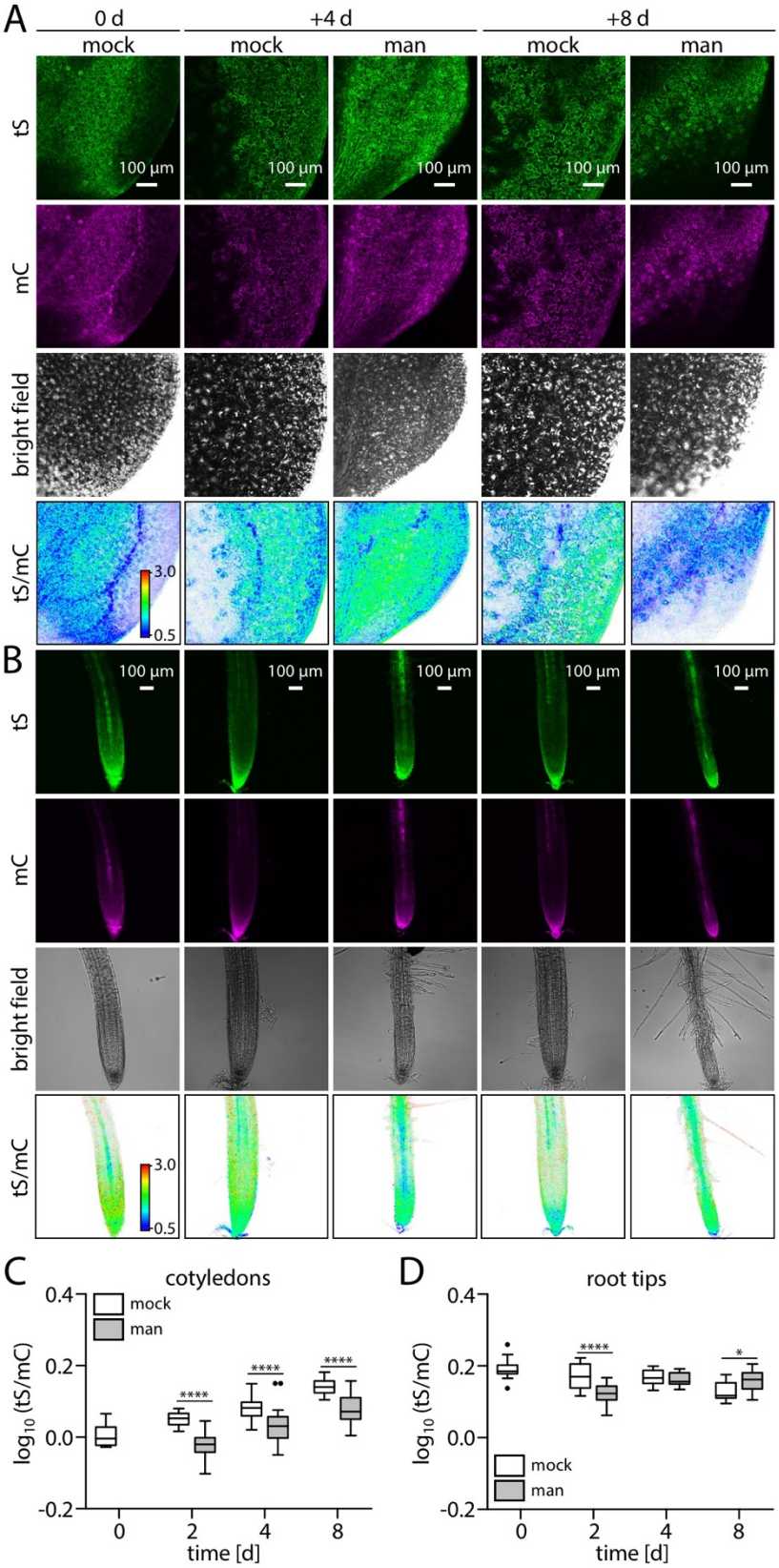
A
0 d
+4 d
+8 d
mock
mock
man
mock
man
tS
mC
bright field
tS/mC
100 µm
3.0
0.5
B
C
cotyledons
D
root tips
mock
man
log10 (tS/mC)
time [d]
****
*

Figure 19: *In vivo* measurements of NAD redox state in Arabidopsis wild-type seedlings under control and drought conditions.

Four days after germination and growth on standard vertical agar plates, Col-0 wild-type seedlings stably expressing cytosolic Peredox-mCherry (Hung et al., 2011) were transferred onto new agar plates without (mock) or with 300 mM mannitol (man). Seedlings were subjected to CLSM for NAD redox state analyses at indicated time points. Peredox-mCherry was excited at 405 nm (T-Sapphire (tS), green) and 543 nm (mCherry (mC), magenta) whereas the emission was collected at 499–544 nm and 579–615 nm, respectively. Additionally, 405 nm excitation-induced auto-fluorescence collected at 430–450 nm (not shown) and factored in the ratio calculation. False-colour images (tS/mC) depict the emission intensity ratio. High tS/mC ratios indicate a more reduced NAD pool and are shown in red, whereas blue colours indicate a less reduced NAD pool. (**A**) Representative CLSM images of cotyledons of Peredox-mCherry seedlings. (**B**) Representative CLSM images of root tips of Peredox-mCherry seedlings. (**C**) Quantified relative changes of NAD redox state for cotyledons ($n \geq 18$). Y-axis: $\log_{10}$ ratio values of tS and mC fluorescence intensities (higher values indicate a more reduced NAD pool). Boxes: 1st and 3rd quartiles with median and Tukey whiskers. Significant differences between treatments according to two-way ANOVA with Bonferroni's multiple comparisons test (*$P < 0.05$, ****$P < 0.0001$). (**D**) Quantified relative changes of NAD redox state for root tips ($n \geq 12$) as described in (C).

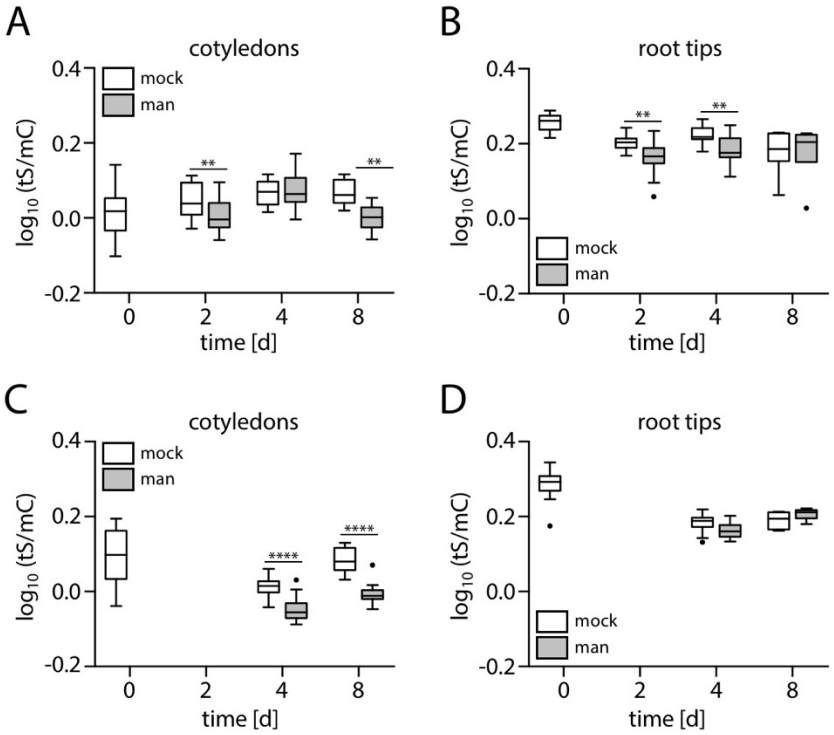

Figure 20: Experimental replicates of cytosolic NAD redox state *in vivo* measurements under control and drought conditions.

Experiment performed as described in Figure 19 except for time intervals between CLSM recordings. Y-axis: $\log_{10}$ ratio values of t-Sapphire (tS) and mCherry (mC) fluorescence intensities (large number: NAD more reduced, small number: NAD more oxidised). Boxes: 1st and 3rd quartiles with median and Tukey whiskers. Significant differences between treatments according to two-way ANOVA with Bonferroni's multiple comparisons test (**$P < 0.01$, ****$P < 0.0001$). (**A**) Quantified relative changes of NAD redox state for cotyledons ($n \geq 8$). (**B**) Quantified relative changes of NAD redox state for root tips ($n \geq 6$). (**C**) Quantified relative changes of NAD redox state for cotyledons ($n \geq 12$). (**D**) Quantified relative changes of NAD redox state for root tips ($n \geq 6$).

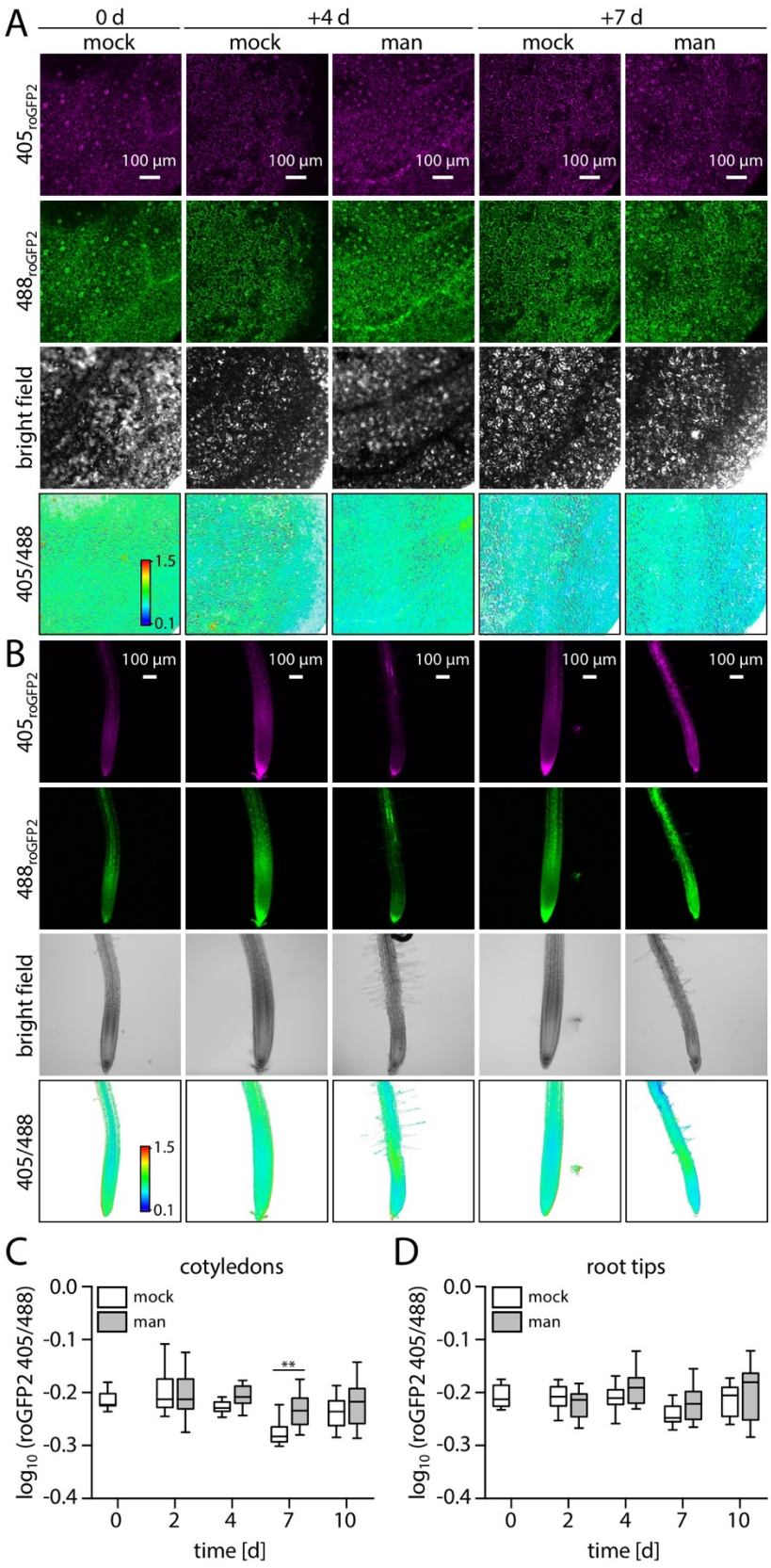
A
0 d
+4 d
+7 d
mock
mock
man
mock
man
405roGFP2
488roGFP2
bright field
405/488
100 µm
1.5
0.1
B
C
cotyledons
D
root tips
mock
man
log10 (roGFP2 405/488)
0.0
-0.1
-0.2
-0.3
-0.4
**
0
2
4
7
10
time [d]

Figure 21: *In vivo* measurements of glutathione redox potential (E_{GSH}) in Arabidopsis wild-type seedlings under control and drought conditions.
Four days after germination and growth on standard vertical agar plates, Col-0 wild-type seedlings stably expressing cytosolic GRX1-roGFP2 (Marty et al., 2009) were transferred onto new agar plates without (mock) or with 300 mM mannitol (man). Seedlings were subjected to CLSM for E_{GSH} analyses at indicated time points. GRX1-roGFP2 was sequentially excited at 405 nm (405_{roGFP2}, magenta) and 488 nm (488_{roGFP2}, green) whereas the emission was collected at 505–530 nm. Additionally, 405 nm excitation-induced auto-fluorescence was collected at 430–450 nm (not shown) and factored in the ratio calculation. False-colour images (405/488) depict the emission intensity ratio for the two excitation wavelengths. High 405/488 ratios indicate a more oxidised glutathione pool and are shown in red, whereas blue colours indicate a more reduced glutathione pool. (**A**) Representative CLSM images of cotyledons of GRX1-roGFP2 seedlings. (**B**) Representative CLSM images of root tips of GRX1-roGFP2 seedlings. (**C**) Quantified relative changes of E_{GSH} for cotyledons ($n \geq 7$). Y-axis: $\log_{10}$ ratio values of roGPF2 fluorescence intensities (high values indicate a more oxidised glutathione). Boxes: 1st and 3rd quartiles with median and Tukey whiskers. Significant differences between treatments according to two-way ANOVA with Bonferroni's multiple comparisons test (**$P < 0.01$). (**D**) Quantified relative changes of E_{GSH} for root tips ($n \geq 7$) as described in (C).

3.3.3 Establishing multiwell-based fluorimetry to measure cytosolic NAD redox dynamics

As described above, the cytosolic NAD measurements using Peredox-mCherry revealed a shift in redox status in response to osmotic stress exposure (Figure 19, Figure 20). Yet, the approach that was established in this study remains constraint by the necessity of consecutively sampling large numbers of individual images by confocal microscopy. To enable dynamic measurements in an increased throughput setting and to allow the in-depth characterisation of NAD redox dynamics in plants, a new method with increased sampling capacity and executability of parallel treatments was developed. Intact Arabidopsis seedlings expressing cytosolic Peredox-mCherry were subjected to multiwell plate reader-based fluorimetry. Recordings of spectral emission scans in response to excitation at 400 nm and at 550 nm, wavelengths commonly used for the chromophores T-Sapphire and mCherry, revealed distinctly different emission spectra for plants with or without expression of Peredox-mCherry (Figure 22A). The clear spectral difference, *i.e.* the high signal-to-noise ratio of 10:1 and 41:1 for emission collected 515 ± 7.5 nm (T-Sapphire) and 610 ± 5 nm (mCherry), suggested multiwell plate reader-based fluorimetry to be suitable to monitor cytosolic NAD redox dynamics *in vivo*. The applicability of the system to measure physiological NAD redox changes was validated by the reducing effect of photosynthetic electron transport on the NAD pool (Heber, 1974). Seedlings incubated in assay medium with or without supplementation of 3-(3,4-dichlorophenyl)-1,1-

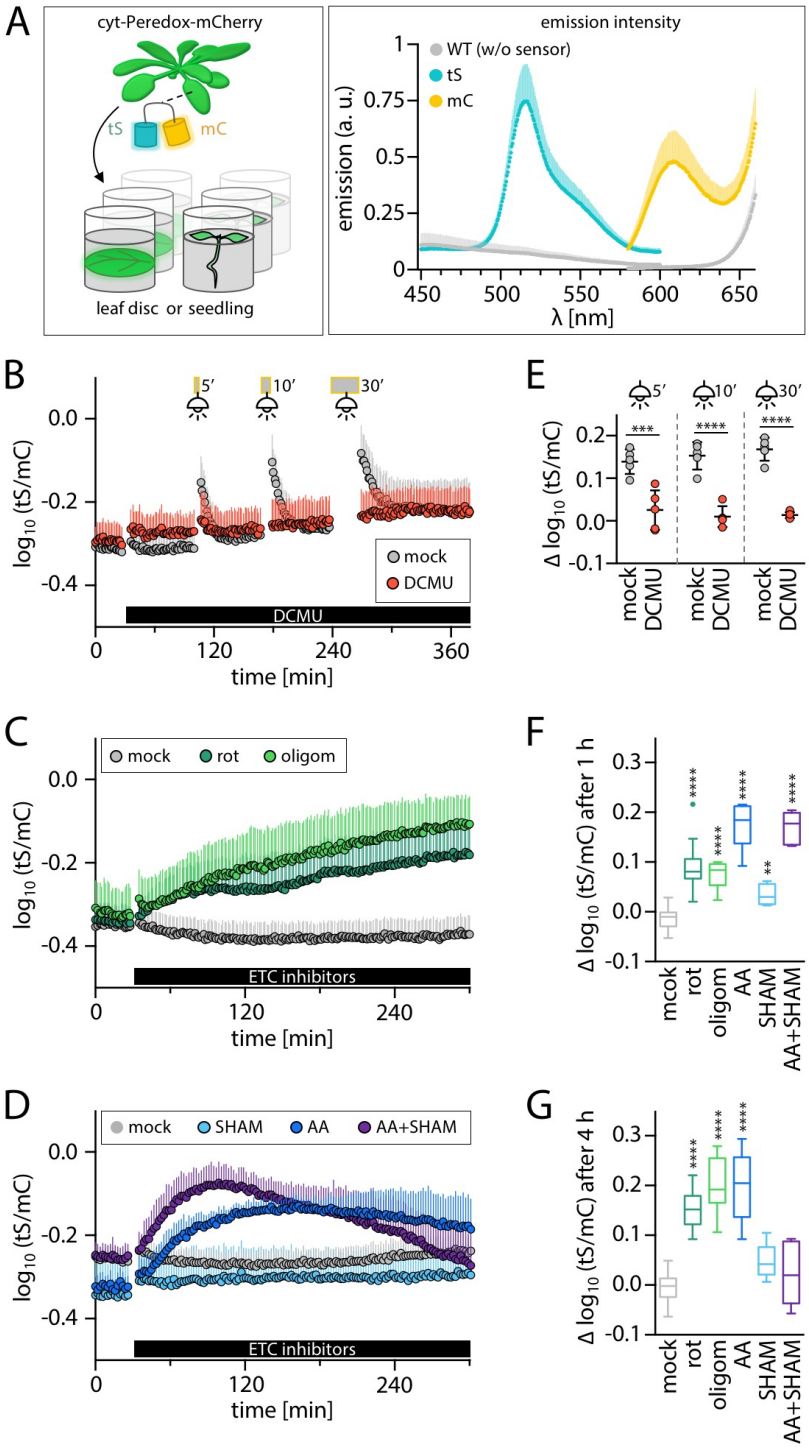

Figure 22: *In vivo* monitoring of the NAD redox state in Arabidopsis wild-type seedlings in response to actinic light and inhibitors.

(**A**) Graphical representation of the experimental approach. **Left**: Arabidopsis seedlings or leaf discs stably expressing cytosolic Peredox-mCherry were submerged in wells of a 96-well plate prefilled with assay medium. After ~90 min of incubation in the dark, time courses of fluorescence intensities were recorded in the plate reader. *(continued on next page)*

(Figure 22 continued)
Right: spectral properties of Col-0 wild-type (WT) plants with (cyan/light orange) or without (grey) expression of cytosolic Peredox-mCherry. T-Sapphire (tS; cyan) emission scan with excitation at 400 ± 7.5 nm and emission collected at 0.5 nm-intervals. mCherry (mC; light orange) emission scan with excitation at 550 ± 7.5 nm and emission collected at 0.5 nm-intervals. $n \geq 4$, mean + SD. (**B**), (**C**) and (**D**) Peredox-mCherry ratio (tS/mC) of 8-d-old WT seedlings in response to different treatments. Black bars at the bottom of graphs indicate the addition of inhibitor or mock. tS was excited at 400 ± 10 nm and emission was collected at 515 ± 7.5 nm, mC was excited at 570 ± 10 nm and emission was collected at 610 ± 5 nm. High tS/mC ratios indicate a more reduced NAD pool. (B) addition of 10 µM 3-(3,4-dichlorophenyl)-1,1-dimethylurea (DMCU; inhibitor of PSII) and exposure to actinic light. Grey bars on top of the graph indicate illuminations (400 µmol m^{-2} s^{-1} for 5, 10 or 30 min, respectively). $n = 5$, mean + SD. (C) Addition of 50 µM rotenone (rot; ETC complex I inhibitor) or 100 µM oligomycin (oligom; ATP synthase inhibitor). $n \geq 8$, mean + SD. (D) Addition of 2 mM salicylhydroxamic acid (SHAM; AOX inhibitor), 20 µM antimycin A (AA; inhibitor of complex III) or combination of both. $n \geq 5$, mean + SD. (**E**) Box plot of Peredox-mCherry ratio changes between value directly after illumination and subsequent plateau phase (60 min after illumination end). Boxes: 1st and 3rd quartiles with median and Tukey whiskers. $n = 5$. Statistical differences between treatments according to one-way ANOVA with Bonferroni's multiple comparisons test (***$P < 0.001$, ****$P < 0.0001$). (**F**) and (**G**) Box plots of Peredox-mCherry ratio changes in response to 1 h or 4 h treatment described in (C) and (D) compared to ratio directly before treatment. $n \geq 5$. Boxes: 1st and 3rd quartiles with median and Tukey whiskers. Statistical differences between mock and inhibitor treatments according to one-way ANOVA with Dunnett's multiple comparisons test (**$P < 0.01$, ****$P < 0.0001$).

dimethylurea (DCMU), a photosystem II inhibitor, were exposed to actinic light (Figure 22B). Measurements were not feasible in the light, but were performed before and after light exposure. In the absence of DCMU, seedlings showed a pronounced increase of the Peredox-mCherry sensor ratio by 0.14, 0.15 and 0.17 $\log_{10}$ units in response to 5, 10 or 15 min of actinic light, respectively (Figure 22E), indicating a reduction of the NAD pool in response to light. The absence of light led to a decreasing of the sensor ratio value, indicating a re-oxidation of the NAD pool (Figure 22B). Conversely, seedlings exposed to DCMU failed to reveal similar kinetics and remained largely unresponsive to light as judged by the Peredox-mCherry ratio changes being reduced to 18%, 7% and 8%, respectively, compared to mock treatment (Figure 22B, E); demonstrating that the cytosolic NAD reduction was directly linked to active photosynthetic electron transport. To further test if this new methodology could allow to prove the direct impact of mitochondrial respiratory activity on cytosolic NAD redox status, seedlings were supplemented with different inhibitors to block the mitochondrial ETC at complex I (rotenone; Figure 22C), complex III (antimycin A; Figure 22D) or complex V/ATP synthase (oligomycin; Figure 22C). Strikingly, each inhibitor triggered an almost instantaneous increase of the sensor ratios in all the experiments (Figure 22F, G). In contrast, only minor changes were

observed in response to the addition of salicylhydroxamic acid (SHAM) to inhibit AOX (Figure 22D, F, G). These results suggest that the multiwell-based fluorimetry using the cytosolic Peredox-mCherry sensor in intact seedlings was sufficiently sensitive to monitor NAD redox dynamics in response to changes in organelle function and paved the way for further measurements in mitochondrial uncoupling mutants under stress conditions.

3.3.4 Uncoupling mutant plants maintain WT-like NAD redox dynamics

The maintenance of cellular redox homeostasis is a widely accepted key function of mitochondrial uncoupling, which separates the phosphorylation status of the adenylate pools from the metabolic redox status, with the NAD pool as the central cofactor. Yet, this role has been largely based on indirect evidence and NAD redox measurements directly in the cytosol have been lacking (Sweetlove et al., 2006; Giraud et al., 2008; Barreto et al., 2017). To investigate the impact of mitochondrial uncoupling on cytosolic NAD homeostasis by *in vivo* sensing, the double mutant *ucp1 aox1a* was selected as a representative uncoupling mutant, lacking the dominant isoform of both gene families (Clifton et al., 2005; Vanlerberghe et al., 2009). Accordingly, *ucp1 aox1a* was stably transformed with the cytosolic Peredox-mCherry biosensor. Leaf discs from 4-week-old plants were then assayed by multiwell plate reader-based fluorimetry as described above (Figure 22). Recordings of Peredox-mCherry baselines for both genotypes WT and *ucp1 aox1a* suggested the absence of an obviously different NAD redox state under non-challenged conditions (compare traces during initial 60 min in Figure 23A). The addition of antimycin A (Figure 23A) or oligomycin (Figure 23B) to inhibit the mitochondrial ETC complex III or V, respectively, produced a fast increase of the sensor ratio in both backgrounds, which were similar between the double mutant and the WT, however. In the following, combinations of actinic light with either the ETC inhibitor antimycin A or the addition of sucrose were employed to modify cytosolic NAD status. It was reasoned that the interruption of the mitochondrial electron transport combined with a photosynthetic activation may enhance the reductive shift. The remaining capacity to oxidise NADH might largely relay on mitochondrial uncoupling. Sucrose was previously found to increase the reduction of the cytosolic NAD pool (Negroni, 2017), although the exact mechanism remains speculative. Both experimental regimes triggered a strong increase of the sensor ratio (Figure 23C, D). Additional illumination of the samples treated with antimycin A showed little impact

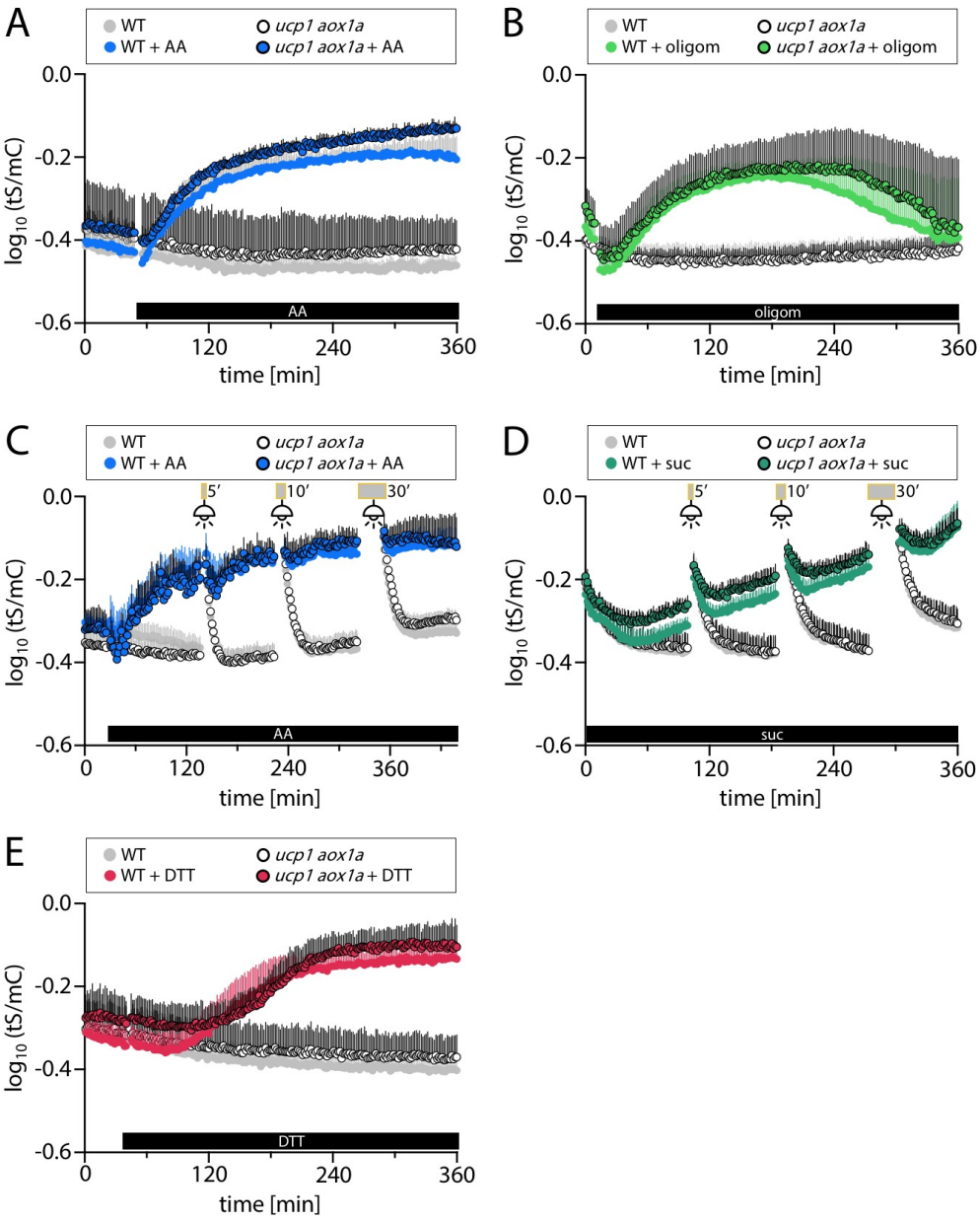

Figure 23: *In vivo* comparison of NAD redox state in leaves of Arabidopsis wild-type and double mutants. Plate reader-based fluorimetric measurements employing the approach described in Figure 22. Ratio of T-Sapphire (tS)/mCherry (mC) of leaf discs from 4-week-old Arabidopsis plants stably expressing cytosolic Peredox-mCherry were monitored in response to different treatments (for experimental approach details see Figure 22A). Black bars at the bottom of graphs indicate addition of inhibitor or mock to wells. tS was excited at 400 ± 10 nm and the emission collected at 515 ± 7.5 nm, mC was excited at 570 ± 10 nm and the emission collected at 610 ± 5 nm. High tS/mC ratios indicate a more reduced NAD pool. (**A**) Addition of 20 µM antimycin A (AA) or mock. $n \geq 4$, mean + SD. (**B**) Addition of 100 µM oligomycin (oligom) or mock. $n \geq 11$, mean + SD. (**C**) Addition of 20 µM antimycin A (AA) or mock. Additionally, actinic light 400 µmol m^{-2} s^{-1} for 5, 10 or 30 min, respectively, indicated by grey boxes on top of the graph. $n \geq 9$, mean + SD. (**D**) Analogous to (C) except for the replacement of the inhibitor treatment with the addition of 5% (w/v) sucrose prior to the start of the assay. $n = 10$, mean + SD. (**E**) Addition of 10 mM dithiothreitol (DTT) or mock. $n \geq 4$, mean + SD.

on the sensor ratio. Notably, antimycin A abolished the re-reduction of the NAD pool after light-to-dark transition (Figure 23C), indicating that this reduction is linked to mitochondrial ETC activity. Sucrose addition resulted in a slower increase of the Peredox-mCherry ratio compared to antimycin A, and additional NAD reduction from the illumination was observed (Figure 23D). A similar response was recorded upon the addition of dithiothreitol (DTT), that acts as an unspecific reductant for oxidised thiols and as an activator of AOX (Millar et al., 1993; Umbach and Siedow, 1993; Rhoads et al., 1998). Addition of 10 mM DTT elicited a marked reduction of the NAD pool by a yet unknown mechanism, but did not reveal obvious differences between the genotypes (Figure 23E). Despite the clear responses to the treatments, which demonstrated the flexibility of the cytosolic NAD redox status, the genotypes performed similarly. This suggest that uncoupling did not have a strong impact on NAD redox dynamics, even under reductive challenges.

3.3.5 Discussion

The application of genetically encoded biosensors proved to be a powerful tool to monitor *in vivo* subcellular changes of central parameters of energy metabolism. The complementation of CLSM analysis with plate reader-based measurements allowed to apply treatments in parallel at an increased throughput rate.

3.3.5.1 Cytosolic NAD redox status is flexible and regulated by respiratory and photosynthetic electron transport activity

Plate reader-based measurements confirmed the flexibility of NAD redox states in the cytosol and enabled to verify the direct influence of photosynthetic and respirational electron transport chain activities. This is concordant to early studies based on cell cultures or reconstituted *in vitro* systems, which reported an export of metabolic reductant from the chloroplast during photosynthesis (Heber, 1974). Reductant export can take place via different pathways, such as the malate valves which are constituted by a combination of malate-oxaloacetate shuttles and malate dehydrogenases using NAD(P) as a cofactor (Scheibe, 2004). In the chloroplast, photosynthetic electron transfer redox-activates NADP-dependent malate dehydrogenase to convert oxaloacetate into malate (Scheibe and Beck, 1979; Carr et al., 1999), which can be exported by malate-oxaloacetate shuttles to the

cytosol, mitochondria and peroxisomes (Scheibe, 2004). The note of reductant export is supported by the plate reader data revealing an increased reduction of the cytosolic NAD pool upon exposure to actinic light (Figure 22B). The combined application of actinic light and mitochondrial ETC inhibitor (Figure 23C) furthermore indicates a photosynthetic electron transfer-dependent export of reductant to mitochondria. In untreated plants, the cytosolic NAD pool is rapidly re-oxidised in the dark (Figure 22B), but not in the presence of mitochondrial ETC inhibition (Figure 23C).

Uncoupling appeared not to play a major role during cytosolic NAD homeostasis as demonstrated by the *ucp1 aox1a* NAD redox dynamics (Figure 23) and the absence of an obvious effect in response to AOX inhibition (Figure 22). This was unexpected considering the severe growth impairment of *aox1a* plants when treated with antimycin A on agar plates (Figure 13C, F, G) or on soil (Figure 16D, E). The reason for this discrepancy remains to be investigated, but might be explained by the different time spans of the approaches (hours *versus* days). Antimycin A is well-known to strongly enhance *AOX1a* expression and capacity (Vanlerberghe and McLntosh, 1996; Saisho et al., 1997; Vishwakarma et al., 2015), providing alleviation to the restricted mitochondrial ETC capacity while still allowing to uphold Δp-driven ATP synthesis (via complex I). The electron flow via AOX was also reported to be relevant to maintain efficient photosynthesis. While indifferent under standard conditions, antimycin A-treated *aox1a* Arabidopsis plants revealed a disrupted photosynthetic electron transport (F_V/F_M reduced by ~57% relative to WT) and strongly altered photorespiratory carbon fluxes (glycine/serine ratio increased by ~760%) (Strodtkötter et al., 2009). These data confirm the emerging picture of mitochondria directly supporting chloroplast metabolism, particularly photosynthesis (Sweetlove et al., 2006; Bailleul et al., 2015; Larosa et al., 2018). Thus, in the presence of complex III inhibition, AOX provides not only an alternative pathway to allow maintenance of mitochondrial ATP synthesis but in addition a pathway to support photosynthesis. It is conceivable that ramping up the necessary uncoupling capacity and metabolic adjustments in response to a sudden antimycin A exposure requires a certain acclimation time. This might explain the similar NAD reduction among WT and uncoupling mutant plants (Figure 23A). On a more long-term scale, WT plants appeared to cope relatively well as judged by the root growth (Figure 13). Conversely, *aox1a* plants were most likely unable to sustain mitochondrial ATP synthesis and efficient

photosynthesis (Strodtkötter et al., 2009; Vishwakarma et al., 2015), leading to an abolished root growth in the presence of antimycin A. It will be interesting to compare the NAD redox state under prolonged antimycin A exposure to investigate whether the manifestation of the root phenotype of *aox1a* is accompanied with a perturbated NAD redox homeostasis.

3.3.5.2 Plate-reader based fluorimetry offers a powerful approach to dissect *in vivo* NAD physiology in response to different treatments

The NAD redox state changes upon addition of sucrose or DTT demonstrated the potential of the plate reader-based fluorimetry approach to generate live-insights into cell physiology in response to different stimuli (Figure 23D, E). The uptake and import of sucrose into the cytosol, which can be catabolised by the sucrose synthase and the sucrose invertase to enter the secondary carbon metabolism (Bieniawska et al., 2007; Barratt et al., 2009), might explain the observed NAD reduction upon sucrose addition. Further investigations will be needed to determine the exact mechanism leading to this increased NAD reduction. Incubation of leaf discs with 5 mM DTT was previously observed to change central metabolic pathways (Kolbe et al., 2006). These changes were assumed to originate from DTT-mediated alterations of redox-modulated enzyme activities, but a mechanistic model explaining the metabolic modifications has not been proposed (Kolbe et al., 2006). Thus, the pathways by which exogenous sucrose or DTT led to the observed reduction of the NAD pool remain to be addressed in detail.

In addition to fluorimetric measurements based on Peredox-mCherry, the assays are virtually extendable to assess any cellular parameter for which a biosensor has been generated (for an overview see Sanford and Palmer, 2017; Walia et al., 2018). Based on the drought-induced changes of $MgATP^{2-}$ levels (Figure 17), additional fluorimetric measurements with the ATeam biosensor would be a reasonable next experimental step. The recently developed ATeam assays to monitor *in vivo* wounding or hypoxia responses independently underline the potential of the biosensor approaches (De Col et al., 2017), offering a tool to further investigate the effects of restricted uncoupling and different stress treatments on cellular energy physiology.

3.4 Uncoupling mutants' capacity to withstand reductive stress

3.4.1 Introduction

Contrary to expectations, WT and higher order uncoupling mutant plants displayed only minor phenotypic differences under drought stress conditions (section 3.2). It was therefore reasoned that uncoupling may be more important under other stress-inducing conditions. To test a broader variety of different conditions in a higher throughput manner, the previously applied agar plate-based phenotyping methodology was employed (section 3.2.3).

3.4.2 Reducing stress triggers root growth impairment in triple uncoupling mutant

Salicylic acid (SA) was reported to act dose-dependently either as mitochondrial inhibitor or uncoupler. Higher SA concentrations were shown to inhibit respiration whereas lower concentrations (≤ 100 µM) increased respiration in tobacco cell cultures and isolated mitochondria despite the absence of ADP, indicating increased uncoupling (Norman et al., 2004). Consistent with an enhanced mitochondrial oxygen consumption, Norman et al. (2004) observed increased AOX transcript and protein levels in salicylic acid-treated tobacco cell suspensions. WT and *ucp1 ucp3 aox1a* mutant seedlings transferred to agar plates supplemented with 100 µM salicylic acid showed a reduction of primary root growth compared to the seedlings transferred onto control agar plates (-65%). However, the genotypes remained phenotypically indistinguishable (Figure 24A, B). In contradiction to previous observations (Figure 15B), triple mutants showed a slightly but significantly higher primary root growth than WT on control plates (+10%) or on plates without sucrose (+12%) (Figure 24A, B). This was presumably caused by different seed batches and the consequent different germination vigour.

Next, seedling primary root growth was compared under naphthaleneacetic acid, sorbitol, sodium chloride, DTT and antimycin A. Naphthaleneacetic acid is a synthetic auxin analogue and has been shown to negatively interfere with retrograde signalling by repressing *AOX1a* expression (Ivanova et al., 2014). Sorbitol has been suggested recently to serve as a better osmotic stress agent than mannitol, since mannitol was found to induce osmotic stress and also biotic stress in Arabidopsis plants (Claeys et al., 2014). Tolerance to sodium chloride salt stress was previously linked to *AOX1a* capacity. Hydroponically

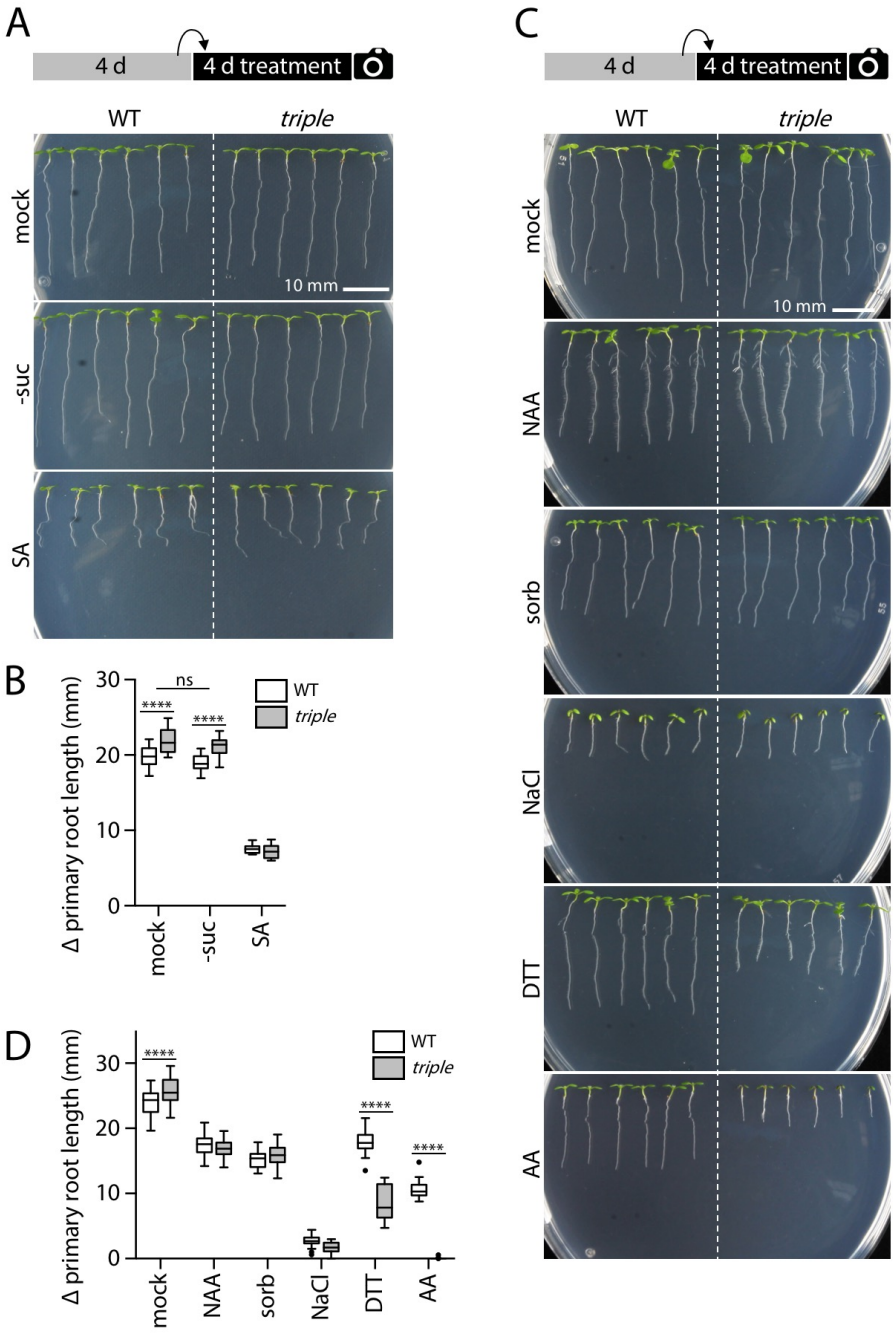

Figure 24: Root growth analysis of Arabidopsis wild-type and *ucp1 ucp3 aox1a* mutant seedlings on agar plates supplemented with and without stress-inducing chemicals.

Comparison of primary root growth of wild-type (WT) and triple (*ucp1 ucp3 aox1a*) mutant seedlings grown side-by-side. Plants were germinated and vertically grown for 4 d on standard agar plates before they were transferred onto new plates with and without stress-inducing additives. Boxes in plots represent 1st and 3rd quartiles with median and Tukey whiskers. Differences between genotypes were tested using a two-way ANOVA with Bonferroni's multiple comparisons test (****$P < 0.0001$). *(continued on next page)*

(Figure 24 continued)
(**A**) Representative images of 8-d-old Arabidopsis WT and triple mutant seedlings 4 d after transfer onto new agar plates with identical composition (mock), without sucrose (-suc) or supplemented with 100 µM salicylic acid (SA). (**B**) Primary root growth within 4 d from seedlings described in (A). $n \geq 12$. (**C**) Representative images of 8-d-old WT and triple mutant Arabidopsis seedlings 4 d after transfer onto new plates with identical composition (mock) or supplemented with 75 nM naphthaleneacetic acid (NAA), 200 mM sorbitol (sorb), 150 mM sodium chloride (NaCl), 750 µM dithiothreitol (DTT) or 20 µM antimycin A (AA). (**D**) Primary root growth within 4 d from seedlings described in (C). $n \geq 30$.

grown Arabidopsis plants overexpressing *AtAOX1a* exhibited 30–40% higher growth rates compared to WT plants under 100 mM sodium chloride (Smith et al., 2009). DTT, an unspecific reductant for oxidised thiols, triggers a perturbation of cellular metabolic fluxes (Kolbe et al., 2006; section 3.4.5) and an increase of the NADH/NAD^+ ratio in the cytosol (Figure 23E). Antimycin A was used as a control to verify the phenotyping method (section 3.2.3). Compared to the mock treatment, naphthaleneacetic acid (-31%), sorbitol (-37%) and sodium chloride (-91%) all resulted in a decreased primary root growth (Figure 24C, D), however, the genotypes remained indistinguishable. Since sodium chloride inhibited seedling root growth nearly completely, its impact was examined in detail in a dilution series experiment (Figure 25A). Intermediate sodium chloride concentrations of 50 and 100 mM also impaired primary root growth, but significantly more in the triple mutants (-13% and -9% relative to WT, respectively; Figure 25B). The increased sensitivity towards salt stress is in line with the previously described enhanced salt tolerance of *AtAOX1a* overexpression lines (Smith et al., 2009). Surprisingly, growth on DTT-supplemented agar plates reduced primary root growth of triple mutants much stronger (-67%) than of WT seedlings (-26%) (Figure 24C, D). The control treatment with antimycin A strongly impaired triple mutant root growth (Figure 24C, D), as observed before (Figure 13). Taken together, the triple mutants maintained a WT-like root growth under most conditions but exhibited a strong impairment when grown on plates supplemented with DTT and antimycin A.

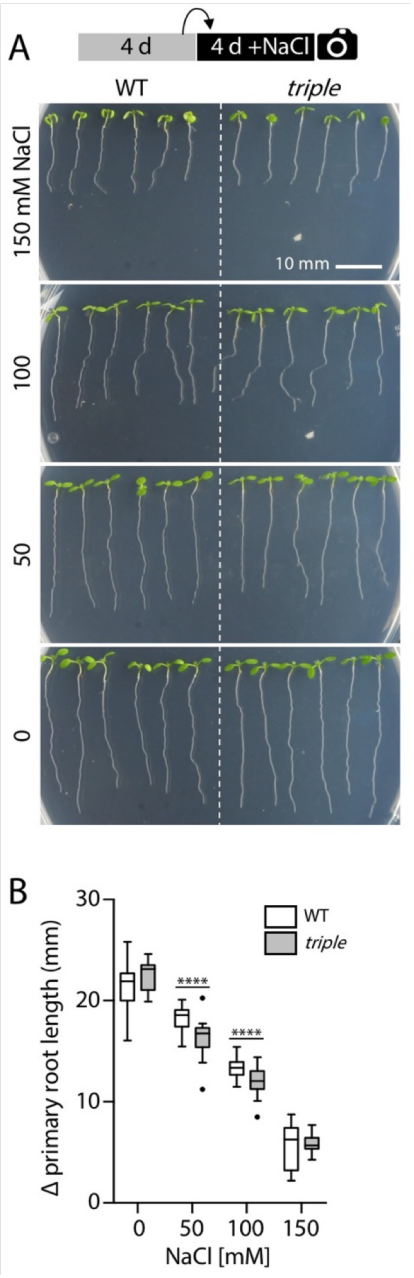

Figure 25: Root growth analysis of Arabidopsis wild-type and *ucp1 ucp3 aox1a* seedlings on agar plates supplemented with sodium chloride.
(**A**) Representative images of 8-d-old wild-type (WT) and *ucp1 ucp3 aox1a* (*triple*) Arabidopsis seedlings grown for 4 d on standard agar plates before transfer onto new plates supplemented with 0–150 mM NaCl and grown for 4 d. (**B**) Primary root growth within 4 d from seedlings described in (A). $n \geq 17$. Boxes: 1st and 3rd quartiles with median and Tukey whiskers. Significant differences between genotypes according to two-way ANOVA with Bonferroni's multiple comparisons test (****$P < 0.0001$).

3.4.3 *Ucp1* and *aox1a* reveal increased sensitivity towards reductive stress

The phenotypic impairment of the uncoupling mutants under DTT was unexpected since a connection between DTT and mitochondrial respiration or uncoupling has not been reported before. To identify the gene(s) responsible for the phenotypic impairment, seedlings from the triple mutant *ucp1 ucp3 aox1a* were assayed together with

the individual single mutants *ucp1*, *ucp3* and *aox1a* using the experimental regime described above (section 3.4.2). Consistent with the previous experiment, the root growth was significantly lower in the triple mutant than in the WT (-32%) (Figure 26). Root growth was also significantly reduced in *aox1a* (-28%) and even stronger in *ucp1* (-84%). *ucp3* was indistinguishably from WT seedlings (Figure 26B).

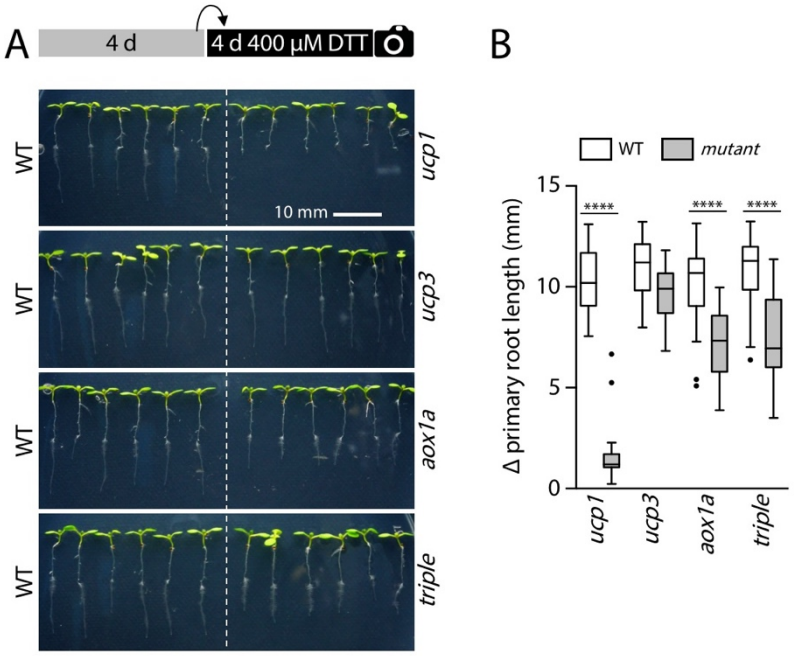

Figure 26: Root growth analysis of Arabidopsis wild-type, single and triple mutant seedlings on agar plates supplemented with DTT.

(**A**) Representative images of 8-d-old Arabidopsis seedlings germinated and vertically grown for 4 d on standard agar plates (half-strength MS, 10 mM MES pH 5.8, 0.1% (w/v) sucrose, 1% (w/v) agar) before transfer onto new plates supplemented with 400 µM dithiothreitol (DTT) and grown for 4 d. (**B**) Primary root growth within 4 d from seedlings described in (A). $n \geq 22$. Boxes: 1st and 3rd quartiles with median and Tukey whiskers. Significant differences between genotypes according to one-way ANOVA with Bonferroni's multiple comparisons test (****$P < 0.0001$).

Unexpectedly, root growth of *ucp1* was more inhibited than of *aox1a* or of the triple mutant *ucp1 ucp3 aox1a*. To verify that *ucp1* is the cause of the strong phenotype, the experiment was repeated and two *ucp1*-complemented lines — referred to as *cUCP* (Sweetlove et al., 2006) — were included. In addition, also *ucp2* and the double mutant *ucp1 aox1a* were investigated. Root growth of *ucp1*, *aox1a* and of the triple mutant was decreased under DTT in accordance to the previous observations (Figure 24, Figure 26). However, the difference between *aox1a* and WT (18%) was smaller than observed before

(-28%; Figure 28), probably due to a lower DTT efficacy as judged by the higher root growth of the WT seedlings. Notably, primary root growth was recovered in the complemented mutant lines *cUCP1 #9* and *#14*, confirming *UCP1* as the phenotype-responsible locus. Double mutant seedlings *ucp1 aox1a* (-88%) revealed a pronounced reduction in primary root growth similar to *ucp1* (-92%). *ucp2* and *ucp3* were phenotypically indistinguishable from WT (Figure 27). Taken together, both *UCP1* and *AOX1a* were required to maintain WT-like root growth in the presence of 400 mM DTT, although the former appeared more important as judged by the root phenotype.

As *ucp1* was most pronounced inhibited in root growth, it was reasoned that UCP1 might be generally more important than AOX1a to tolerate DTT. To test this, phenotyping experiments were repeated with seedlings transferred onto agar plates supplemented with a decreased (350 µM) or increased (750 µM) DTT concentration. Lower DTT concentration had a smaller inhibitory effect on primary root growth for all lines (Figure 28A, B; compare with Figure 27). Nevertheless, *ucp1* (-33%), *ucp1 aox1a* (-8%) and the triple mutant *ucp1 ucp3 aox1a* (-18%) revealed significantly decreased root growth relative to WT seedlings. Transfer of the seedlings to agar plates supplemented with 750 µM DTT let to a complete arrest of primary root growth irrespective of the genotype. Three days after transfer, lateral roots started to emerge. After an additional 3 days, total root length per seedling was quantified (Figure 28C, D). In contrast to the low DTT concentrations, *ucp1* seedlings were phenotypically indistinguishable from WT seedlings. The mutants *ucp2* and ucp3 were also phenotypically indistinguishable from WT. In striking contrast, all *aox1a* lines (*aox1a*, *ucp1 aox1a* and triple mutant) completely lacked formation of lateral roots (Figure 28C). Overall, the phenotypic data show that UCP1 and AOX1a are required to maintain root growth under DTT-induced stress. The relative importance of UCP1 and AOX1a changes in a dose-dependent manner. The two other UCP isoforms, UCP2 and UCP3, seem not to be involved to mediate growth tolerance under the tested conditions to any major extent.

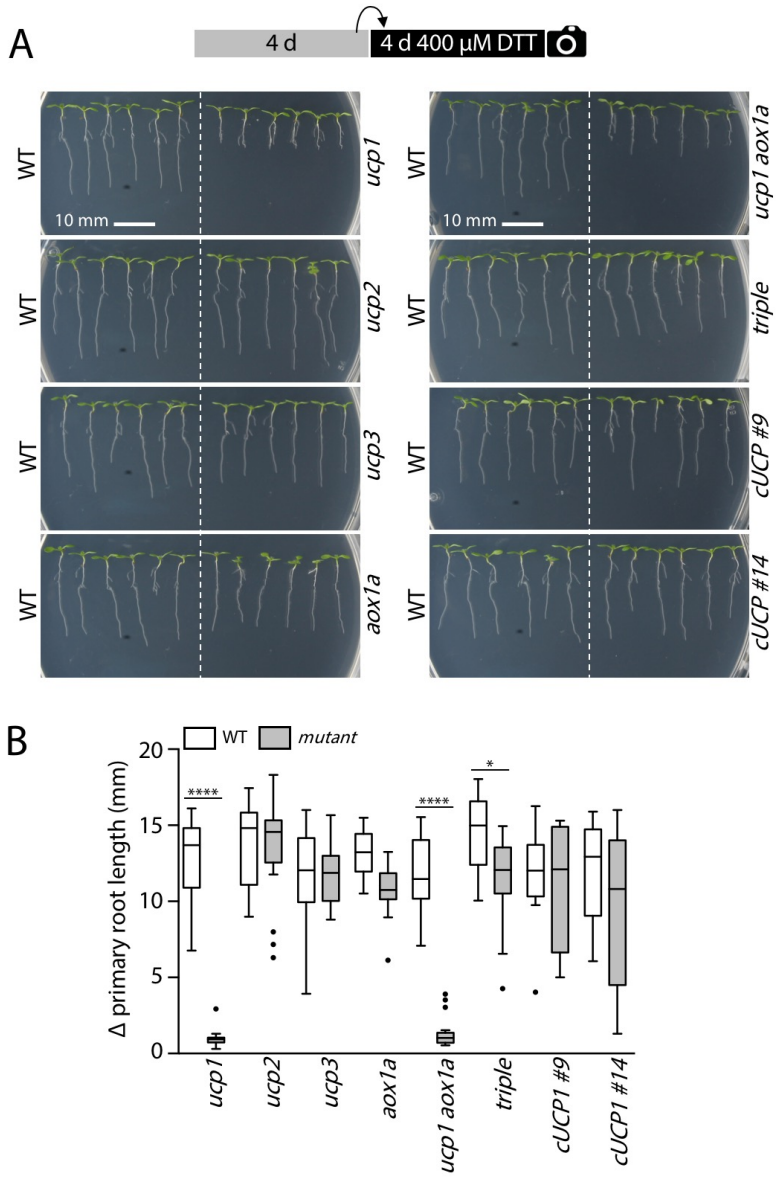

Figure 27: Extended root growth analysis of Arabidopsis wild-type and uncoupling mutant seedlings on agar plates supplemented with DTT.

(**A**) Representative images of 8-d-old Arabidopsis seedlings germinated and vertically grown for 4 d on standard agar plates before transferred onto new agar plates supplemented with 400 µM dithiothreitol (DTT) and grown for 4 d. (**B**) Primary root growth within 4 d from seedlings described in (A). $n \geq 11$. Boxes: 1st and 3rd quartiles with median and Tukey whiskers. Significant differences between genotypes according to one-way ANOVA with Bonferroni's multiple comparisons test (*$P < 0.05$, ****$P < 0.0001$).

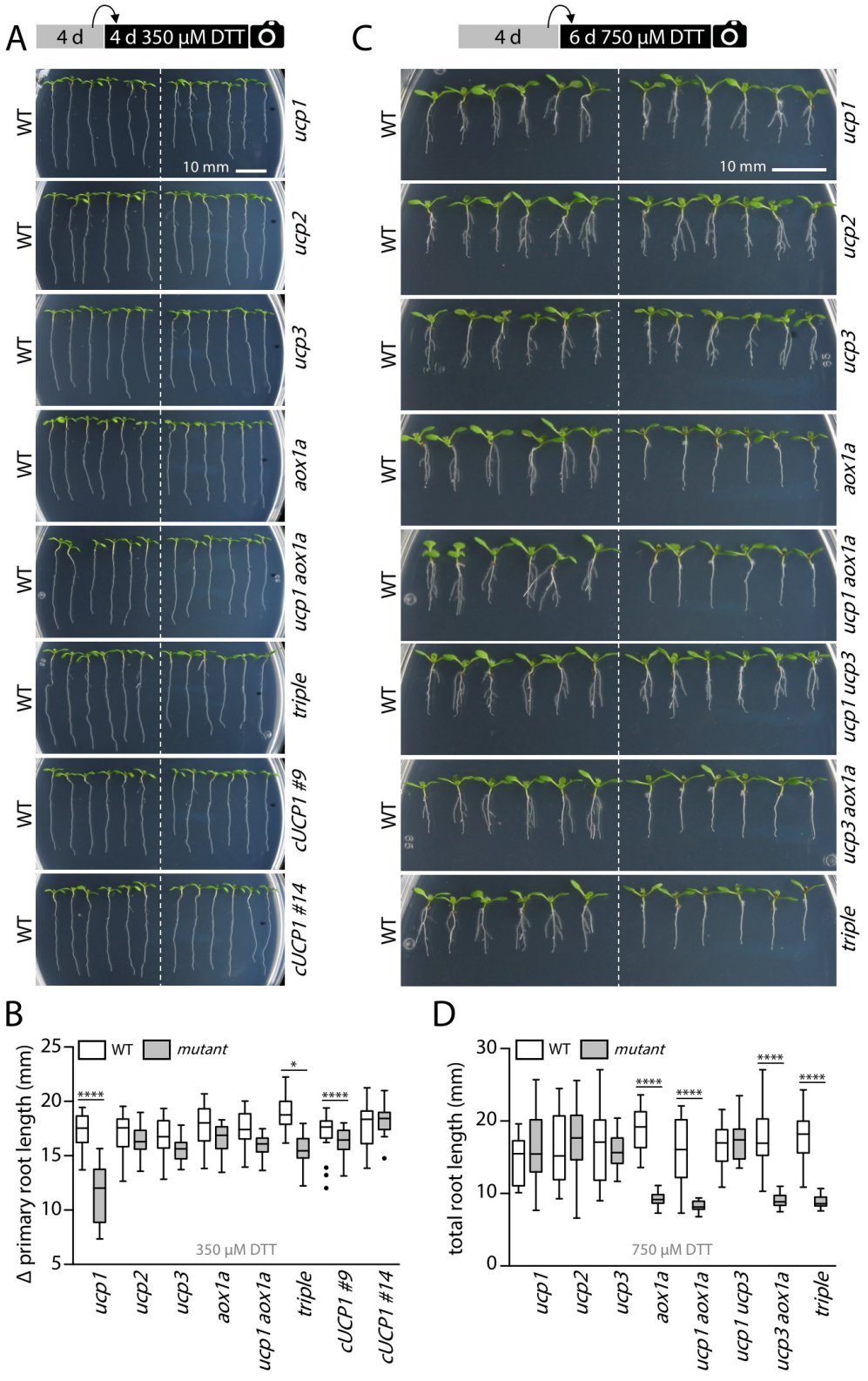

Figure 28: Root growth analysis of Arabidopsis wild-type and mutant seedlings on agar plates supplemented with different DTT concentrations. *(continued on next page)*

(Figure 28 continued)
(**A**) Representative images of 8-d-old Arabidopsis seedlings germinated and vertically grown for 4 d on standard agar plates before they were transferred onto new agar plates supplemented with 350 µM dithiothreitol (DTT) and grown for 4 d. (**B**) Increase of primary root length within 4 d after transfer onto new agar plates from seedlings described in (A). $n \geq 21$. Boxes: 1st and 3rd quartiles with median and Tukey whiskers. Significant differences between genotypes according to one-way ANOVA with Bonferroni's multiple comparisons test (*$P < 0.05$, ****$P < 0.0001$). (**C**) As in (A), except that seedlings were transferred onto new agar plates supplemented with 750 µM DTT and grown for 6 d. (**D**) Quantification of total root length from 10-d-old seedlings described in (C). $n = 18$. Boxes: 1st and 3rd quartiles with median and Tukey whiskers. Significant differences between genotypes according to one-way ANOVA with Bonferroni's multiple comparisons test (****$P < 0.0001$).

3.4.4 Loss of *UCP1* and *AOX1a* does not alter tolerance to tunicamycin induced ER-stress

DTT is a well-established reductive ER-stress-inducing agent and is often used to interfere with protein maturation in the ER and to trigger the unfolded protein response pathway (Martínez and Chrispeels, 2003; Liu et al., 2007; Iwata et al., 2008). Tunicamycin, an alternative commonly used ER-stress-inducing agent, acts redox-independently and disturbs protein maturation in the ER by inhibiting N-linked glycosylation. Treatment of Arabidopsis with tunicamycin induces a downstream transcriptomic response that overlaps with the one triggered by DTT (Martínez and Chrispeels, 2003). To test whether the sensitivity of uncoupling mutants to DTT might be caused by ER-stress in general, seedling root growth was monitored under different concentrations of tunicamycin (0–500 ng mL^{-1}). Despite the pronounced growth inhibition after transfer onto tunicamycin plates, the uncoupling mutants were indistinguishable from WT plants (Figure 29, Supplemental Figure 2). This indicates that mitochondrial uncoupling plays a role to withstand the reductive-stress component of DTT rather than general ER-stress-inducing conditions.

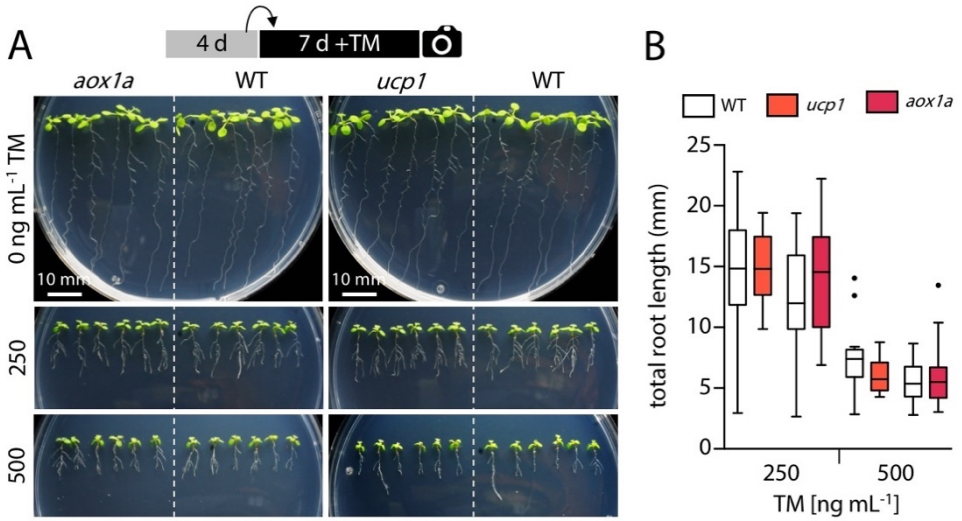

Figure 29: Root growth analysis of Arabidopsis wild-type and uncoupling mutant seedlings on agar plates supplemented with different tunicamycin concentrations.
(A) Representative images of 11-d-old Arabidopsis seedlings germinated and vertically grown for 4 d on standard agar plates before they were transferred and grown for 7 d on new plates supplemented with 0–500 ng mL^{-1} tunicamycin (TM). (**B**) Quantification of total root length from 11-d-old seedlings described in (C). $n = 17$. Boxes: 1st and 3rd quartiles with median and Tukey whiskers. No significant differences between genotypes according to one-way ANOVA with Bonferroni's multiple comparisons test ($^{ns}P > 0.05$).

3.4.5 Discussion

Dissecting the phenotypic differences in root growth, initially discovered in the triple mutant compared to the WT, revealed that both UCP1 and AOX1a play a pivotal role to withstand DTT-mediated reductive stress. Notably, UCP1 seems primarily required to maintain primary root growth at low to moderate DTT concentrations, whereas AOX1a appears more important under moderate to high DTT concentrations.

3.4.5.1 UCP1 and AOX1a, but not UCP2 and UCP3, are required to tolerate DTT-mediated reductive stress

The *ucp1* single mutant revealed a higher sensitivity than the triple mutant towards moderate DTT concentrations (Figure 26–Figure 28). Given that *aox1a* also revealed a reduced primary root growth at moderate DTT concentrations, an equal or stronger impairment would have been expected. However, qRT PCR analyses suggested a stronger knock-down in *ucp1* than in the triple mutant (Figure 9), which might explain the reduced DTT-sensitivity of the double and triple mutants. The findings constitute an additional

reason to reinforce the efforts in genome editing approaches (section 3.1.2; Supplemental Figure 1) to generate independent *ucp1* mutant lines. This will be crucial to address whether the loss of UCP1 and AOX1a has additive effects on the root growth impairment.

The uncoupling mutants responded similar to antimycin A and to DTT as judged by the drastically impaired root growth impairments of *ucp1* at 400 mM DTT (Figure 27) or *aox1a* at 750 mM DTT (Figure 28). The similar phenotypes suggest that dissipation of excess reductant becomes a major task in the presence of DTT. This is supported by the increased reduction of the NAD pool in response to the addition of DTT similar to antimycin A (Figure 23). The DTT-inhibition of *ucp1* and *aox1a* represents the most pronounced phenotypes described to date for uncoupling mutants (Fiorani et al., 2005; Sweetlove et al., 2006; Giraud et al., 2008; Watanabe et al., 2008; Smith et al., 2009; Barreto et al., 2017), which is in agreement with the idea of substantial uncoupling in the presence of DTT.

In contrast to UCP1, the other two isoforms UCP2 and UCP3 appeared dispensable under the tested conditions. This is in line with the note that UCP2 is likely a component of the Golgi apparatus and not part of mitochondria to any measurable extent (Figure 10) (Parsons et al., 2012). Although UCP3 has been repeatedly detected in mitochondrial proteomes (Klodmann et al., 2011; Wagner et al., 2015a; Senkler et al., 2017), its abundance is considerably lower than that of UCP1. In mitochondria isolated from 2-week-old Arabidopsis seedlings or from cell cultures, UCP3 protein levels were on average 50-times lower than those of UCP1 (Wagner et al., 2015a; Braun et al., in preparation). Apart from the abundance, UCP3 might also functionally differ from UCP1. Phylogenetic analyses revealed a higher amino acid sequence similarity to the dicarboxylate carrier 2 (DIC2) than to UCP1 or UCP2 (Figure 6), a fact recently mentioned as well by Monné et al. (2018).

Depending on the applied DTT concentration, reductive stress tolerance appears predominantly mediated by either UCP1 or AOX1a as judged by the seedling root growth. At moderate DTT concentrations, primarily UCP1 but also AOX1a was required to maintain normal primary root growth (Figure 27, Figure 28), whereas at higher concentrations, only AOX1a but not UCP1 seemed involved in lateral root formation (Figure 28). The tissue-dependent dominance of either protein might be based on differing protein abundances between the tissues. Indeed, the removal of apical auxin dominance to

induce lateral root formation upregulates expression of AOX1a (4.2-fold) stronger than of UCP1 (1.7-fold) (De Smet et al., 2008).

3.4.5.2 The missing link between DTT and mitochondrial uncoupling

The connection of mitochondrial energy physiology to DTT-mediated reductive stress represents a fascinating topic, yet its underlying mechanism remains speculative. Tunicamycin treatments (Figure 29) suggest a role of mitochondrial uncoupling under specifically reductive, rather than under general ER-stress-inducing conditions. According to the working model (Figure 1), drought causes reductive stress in plants, which is dissipated by mitochondrial uncoupling. The DTT treatment represents the isolation and controlled application of the 'reductant excess' component. The validity of this analogy is supported on the transcriptomic level. DTT-treated WT leaves exhibited a highly similar gene expression pattern to that observed for *aox1a* leaves exposed to drought and moderate-light stress (Kolbe et al., 2006; Giraud et al., 2008, 2012).

Under drought, it was reasoned that mechanisms such as photorespiration and malate valves mediate reductant export from chloroplasts to mitochondria, where flexible uncoupling allows reductant dissipation (section 1.3). In contrast, how and by which mechanism DTT-mediated reductive stress might give rise to a need of mitochondrial uncoupling is unknown. Hypothetically, DTT could interfere with mitochondria and mitochondrial energy metabolism in different ways. (1) Studies primarily conducted on bovine and mouse heart mitochondria, but also in plants, have demonstrated redox modifications of a number of mitochondrial proteins. Redox-active disulfide groups were identified for enzymes of the TCA cycle, such as citrate synthase, succinate dehydrogenase, fumarase or malic enzyme (Balmer et al., 2004; Dixon et al., 2005; Schmidtmann et al., 2014; Nietzel, 2017) or of the ETC (Balmer et al., 2004; Nietzel, 2017). The addition of DTT is expected to maintain the redox regulated proteins in the reduced state, which can lead to an increased or decreased activity depending on the enzyme (Hurd et al., 2012; Schmidtmann et al., 2014; Daloso et al., 2015). Uncontrolled redox-activation might lead to an accumulation of metabolic reductant, which then could require dissipation via uncoupling. In line with that, AOX is well-known to be redox-activated by DTT and could be involved in the dissipation of excess metabolic reductant (Umbach and Siedow, 1993; Rhoads et al., 1998). (2) Similar to the ER lumen, the mitochondrial intermembrane space

(IMS) mediates oxidative protein-folding (Mesecke et al., 2005). DTT might disturb the redox relay of the IMS protein folding machinery by re-reducing proteins that were oxidised by the machinery. This potentially limits the supply of the ETC components which are inserted via the IMS. Consequentially arising restrictions in the mitochondrial ETC capacities might then be compensated for by the uncoupling components. (3) Electrons from DTT might be relayed via an unknown pathway into the mitochondrial ETC, increasing the reductant pressure on the ETC. Uncoupling would then contribute to respire off reductant and avoid otherwise DTT-induced damage form cellular over-reduction. *In vitro* experiments with purified *At*ERV1, a sulfhydryl oxidase of the IMS, showed that DTT can efficiently reduce ERV1, which then passes the electrons to Cytochrome *c* of the mitochondrial ETC (Peleh et al., 2017). It remains to be determined whether such redox relay systems can supply electrons *in vivo* to a notable amount from DTT into the mitochondrial ETC.

Taken together, it is not known by which mean mitochondrial uncoupling renders plants more tolerant to DTT-imposed, unspecific reductive stress. Yet, several independent observations, NAD redox changes (Figure 23), transcriptomic changes (Kolbe et al., 2006; Giraud et al., 2008, 2012), root growth phenotypes of *ucp1* and *aox1a* (Figure 26–Figure 28), conclusively suggest that the net outcome of the DTT treatment is excess reductant, which is dissipated via mitochondrial uncoupling.

3.5 The role of mitochondria to maintain cellular redox and NAD homeostasis

3.5.1 Introduction

A link between DTT-mediated reductive stress and mitochondrial respiration and uncoupling, as suggested by impaired root growth, has been an unexpected observation. There have been no previous reports indicating an impact of DTT on mitochondria; instead DTT-toxicity has been primarily associated with reductive ER-stress (Iwata et al., 2008; Howell, 2013). The following section aims to shed light on the nature of the connection between DTT-mediated reducing stress and the impaired root growth of uncoupling mutants.

Isolated mitochondria are frequently assayed in the presence of DTT. For instance, buffers used to purify mitochondria frequently contain DTT in a range of 5–10 mM as a reductant to preserve cysteine residues and iron-sulfur clusters of mitochondrial proteins from oxidation during the isolation process (Escobar et al., 2006; Sweetlove et al., 2007). Measurements of the AOX activity in isolated mitochondria generally also involve DTT addition in a range of 5–10 mM to reduce the disulfide bond of the enzyme dimer, which is essential for its full activity (section 1.5.2) (Vanlerberghe et al., 1999; Escobar et al., 2006). Negative impacts of DTT on mitochondrial structure and function have not been reported.

3.5.2 Addition of DTT increases oxygen consumption of isolated mitochondria

One of the hypothesised scenarios addressing the link between DTT and the need of increased mitochondrial uncoupling was that DTT might pass electrons into the ETC and thereby cause a bottleneck to the mitochondrial ETC capacity (see section 3.4.5 for details). No report about the presence or absence of such an effect was reported in literature. It was hypothesised that if electrons from DTT can be passed to the mitochondrial ETC, this should result in a respiratory oxygen consumption. To test this, intact mitochondria from 16-d-old Arabidopsis WT seedlings were purified and oxygen consumption was recorded in a Clark-type oxygen electrode chamber. The addition of 10 mM DTT elicited an instantaneously increased oxygen consumption rate, even though *bona fide* mitochondrial substrates were absent (Figure 30A). The oxygen consumption rate decreased again in response to ETC inhibition by antimycin A (complex III) and SHAM (AOX) (Figure 30B, C). Notably, DTT also increased the oxygen consumption rate

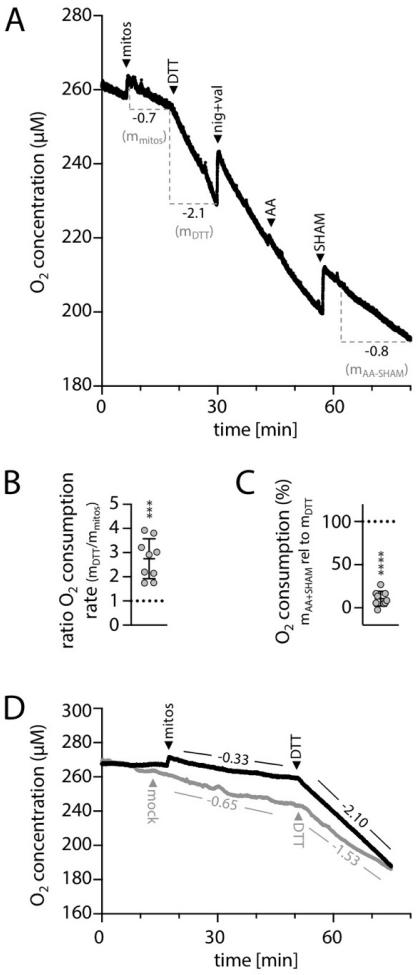

Figure 30: Oxygen consumption of isolated mitochondria from wild-type Arabidopsis seedlings in response to DTT addition.

(**A**) Representative polarographic trace from an oxygen consumption assay conducted on purified mitochondria isolated from 16-d-old wild-type (WT) Arabidopsis seedlings. Arrow heads with labels indicate addition of mitochondria (mitos), 10 mM dithiothreitol (DTT), 50 µM nigericin + 10 µM valinomycin (nig+val), 50 µM antimycin A (AA), 2 mM salicylhydroxamic acid (SHAM). Values below the trace represent oxygen consumption rates (m_{mitos}, m_{DTT}, $m_{AA\text{-}SHAM}$) calculated for time span indicated by grey dashed lines. (**B**) Scatter dot plot of ratio between oxygen consumption rates after (m_{DTT}) and before (m_{mitos}) addition of DTT. Dotted line at Y = 1 represents the expected ratio if addition of DTT had no impact on O_2 consumption. Values below or above dotted line represent decline or increase of respiration in response to DTT addition, respectively. $n = 9$ independent measurements (grey circles) derived from 3 independent mitochondria purifications. Black lines: mean ± SD. Ratios were significantly different to 1 (unchanged O_2 consumption) according to one-sample t-test (***$P < 0.001$). (**C**) Scatter dot plot depicting proportion of oxygen consumption rates after inhibition ($m_{AA\text{-}SHAM}$) relative to rates after addition of DTT (m_{DTT}). Dotted line at Y = 100 represents expected condition if addition of AA and SHAM had no effect on oxygen consumption. $n = 9$ independent measurements (grey circles) derived from 3 independent mitochondria purifications. Black lines: mean ± SD. Ratios were significantly different to 100% (unchanged respiration) according to one-sample t-test (****$P < 0.0001$). (**D**) Polarographic traces representing oxygen consumption from two assays conducted in parallel. Black trace: with purified mitochondria isolated from 16-d-old WT Arabidopsis seedlings, grey trace: mock without mitochondria. Arrow heads with labels indicate additions of mitochondria (mitos) or mock, and of 10 mM DTT. Numbers above (black) or below (grey) traces indicate oxygen consumption before and after addition of DTT for corresponding trace.

in the absence of mitochondria. DTT addition increased oxygen consumption in both electrode chambers with and without mitochondria, running in parallel, but to an almost 3-fold higher extent in the presence of mitochondria (+636%) than in the absence of mitochondria (+235%; Figure 30D). Neither of the effects have been reported in literature before and it remains unclear how DTT affects oxygen consumption and/or recording by the electrode. The higher DTT-induced increase of oxygen consumption in mitochondria

versus the control medium, and the reversibility of the DTT-triggered oxygen consumption by the inhibitors suggest, however, that a component of the increase represents genuine mitochondrial ETC-mediated oxygen consumption.

3.5.3 Thiol-based reductant trigger ETC-dependent mitochondrial matrix pH dynamics

The reproducible increase of mitochondrial ETC-dependent oxygen consumption by the addition of DTT was unexpected. Despite extensive investigation of mitochondrial respiration by Clark-type electrode-based measurements over decades and across species (Hackenbrock, 1966; Estabrook, 1967), this effect appears to not have been reported. To control for a potential artefact, orthogonal experiments were required. As an independent approach mitochondrial proton motive force (Δp) measurements were devised. To examine the pH component of the Δp, isolated mitochondria expressing the pH biosensor cpYFP (Figure 7) in the matrix were assayed using a multiwell plate reader-based fluorimetry setup (Figure 31A). This approach was previously introduced to characterise the sensor protein cpYFP and to study mitochondrial matrix pH dynamics in response to different respiratory substrates (Schwarzländer et al., 2011). Mitochondria were isolated from Arabidopsis seedlings stably expressing the cpYFP pH sensor targeted to the mitochondrial matrix. The purified mitochondria were re-suspended and added to a 96-well plate for fluorimetric analyses of the cpYFP emission ratios in response to sequential excitation at 400 and 482 nm (Figure 31A).

The control substrates pyruvate and malate induced a rapid increase of the cpYFP ratio, which indicated matrix alkalinisation in agreement with the establishment of a pH gradient across the IMM by proton export. Subsequent addition of mitochondrial ETC inhibitors or uncouplers reversed the cpYFP ratio back to baseline, which indicated a re-acidification by passive (inhibitors) or active (uncouplers) degradation of the pH gradient (Figure 31B).

Applying the same experimental procedure to test the ability of DTT to support the generation of a pH gradient resulted in a similar response of the sensor (Figure 31B). Addition of DTT triggered a mitochondrial matrix alkalinisation, which was reversed by the addition of ETC inhibitors. To test the concentration dependence of the response, 1 mM and 10 mM DTT were assayed in parallel. The addition of 1 mM DTT induced

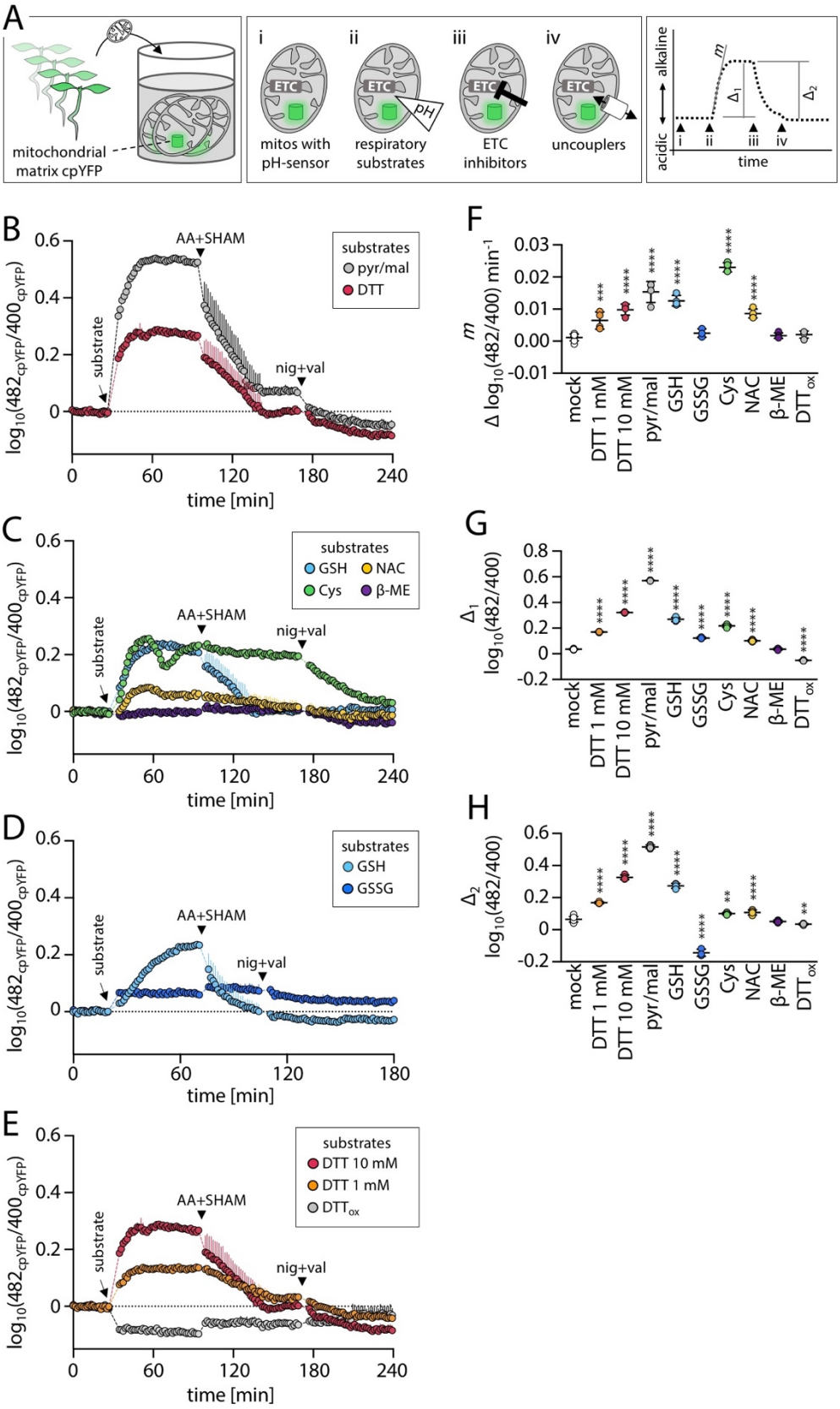
A
mitochondrial matrix cpYFP
i
ii
iii
iv
ETC
pH
mitos with pH-sensor
respiratory substrates
ETC inhibitors
uncouplers
alkaline
acidic
time
B
substrates
pyr/mal
DTT
substrate
AA+SHAM
nig+val
time [min]
C
substrates
GSH
NAC
Cys
β-ME
D
substrates
GSH
GSSG
E
substrates
DTT 10 mM
DTT 1 mM
DTT ox
F
G
H
mock
DTT 1 mM
DTT 10 mM
pyr/mal
GSH
GSSG
Cys
NAC
β-ME
DTT ox

Figure 31: *In organello* monitoring of mitochondrial matrix pH dynamics in response to different additives.
(**A**) Schematic representation of the plate reader-based experimental approach to monitor pH dynamics in the mitochondrial matrix. **Left box**: purification of intact mitochondria from 16-d-old Arabidopsis seedlings stably expressing the mitochondrial matrix localised circularly permuted Yellow Fluorescent Protein (cpYFP). Isolated mitochondria were re-suspended in basic incubation buffer and added to wells of a 96-well plate. cpYFP emission was recorded at 520 ± 5 nm in two separate tracks with excitation at 400 ± 5 nm and 482 ± 8 nm using a plate reader. **Centre box**: manipulations during running assay. i: re-suspended, respiratory-inactive mitochondria. ii: addition of substrates, *e.g.* TCA-cycle intermediates, to restore electron transport chain (ETC) activity and establish a pH gradient (ΔpH) across the inner mitochondrial membrane. iii: addition of inhibitors to arrest ETC activity and passively dissipate ΔpH via proton leakage. iv: addition of uncouplers to ensure full degradation of ΔpH. **Right box**: pH dynamics in the mitochondrial matrix in response to manipulations i–iv. Scheme additionally indicates parameters extracted from traces for statistical analyses. *m*: slope of initial linear phase in response to substrate addition. Δ_1: substrate-induced pH difference (difference between plateau after and directly before substrate addition). Δ_2: ETC inhibitor-induced pH difference (difference between plateau after substrate addition and value before uncoupler addition). (**B**), (**C**), (**D**) and (**E**) pH dynamics in the mitochondrial matrix in response to different substrates recorded via cpYFP as described in (A). Y-axes: ratio of cpYFP fluorescence excited at 400 or 482 nm shown as difference to mean of mock treatment (dotted line at Y = 0). Increase or decrease of ratio indicates more alkaline or more acidic pH, respectively. $n \geq 3$, mean + SD. Arrow heads mark addition of substrates (β-ME: 10 mM β-mercaptoethanol, Cys: 10 mM cysteine, DTT: 10 mM dithiothreitol, DTT_{ox}: 10 mM dithiane, GSH: 10 mM glutathione, GSSG: 5 mM oxidised glutathione, NAC: 10 mM N-acetyl-cysteine, pyr/mal: 10 mM pyruvate + 10 mM malate + 0.3 mM NAD + 0.1 mM thiamine pyrophosphate), ETC inhibitors (AA: 20 µM antimycin A, SHAM: 2 mM salicylhydroxamic acid) and uncouplers (nig: 50 µM nigericin, val: 10 µM valinomycin). Note that DTT trace in (B) is identical to 10 mM DTT trace in (E). (**F**), (**G**) and (**H**) Dot plots depicting quantification of *m* (slope), Δ_1 (substrate-induced pH difference) and Δ_2 (ETC inhibitor-induced pH difference) from (B–E) as described in (A). $n \geq 3$, black lines: mean ± SD. Significant differences between mock and substrate treatments according to one-way ANOVA with Dunnett's multiple comparisons test (**$P < 0.01$, ***$P < 0.001$, ****$P < 0.0001$).

qualitatively similar changes, yet at smaller amplitudes than 10 mM DTT (-53%; Figure 31E). The findings are in line with the oxygen consumption data (Figure 30) and indicate a transfer of electrons from DTT to oxygen via the mitochondrial ETC resulting in active proton pumping.

To elucidate whether this is a general feature of thiol-based reducing agents, mitochondria were supplemented with reduced glutathione (GSH), cysteine (Cys), N-acetyl-cysteine (NAC) or β-mercaptoethanol (β-ME) in parallel assays. The additions increased cpYFP ratios similarly to DTT, although the amplitude varied among the reducing agents (GSH 81%, Cys 63% and NAC 23% relative to DTT-induced cpYFP ratio increases; Figure 31C). An exception was β-ME, which failed to induce cpYFP ratio changes, suggesting that β-ME did not trigger notable proton translocation at the mitochondrial ETC. Addition of mitochondrial ETC inhibitors to GSH supplemented

mitochondria decreased cpYFP ratios back to the baseline. Mitochondria supplemented with Cys or NAC, in contrast, revealed only minor cpYFP changes upon inhibitor additions (Figure 31G, H).

Reversible matrix alkalinisation suggests that electrons from thiol-based reductant can be passed to the mitochondrial ETC and drive proton translocation. Oxidation of the thiol group, rather than the backbone, is a likely mechanism. It was therefore reasoned that the oxidised forms of the respective substrates should not be able to support matrix alkalinisation. This was tested by replacing GSH and DTT with their oxidised versions, GSSG and dithiane. No increase in matrix pH was detected, suggesting the absence of ETC activity (Figure 31D, F). In summary, the cpYFP dynamics propose that specific — but not all — small thiol molecules can act as electron source for the mitochondrial ETC.

3.5.4 Thiol-based reductant generates ETC-dependent mitochondrial membrane potential

Respiratory electron transport at the mitochondrial ETC generates the Δp, which is composed of the pH gradient across the IMM (ΔpH) and the mitochondrial membrane potential ($\Delta\Psi$). Given that the addition reducing agents led to matrix alkalinisations indicating the establishment of ΔpH, it was reasoned that that $\Delta\Psi$ should be established simultaneously. To examine this, mitochondria were isolated from Arabidopsis WT seedlings (without expression of any sensor) and resuspended together with the $\Delta\Psi$-sensitive, cationic dye rhodamine 123 (Rho123). Activity of the ETC induces a build-up of $\Delta\Psi$, which leads to the Nernstian accumulation of Rho123 in the mitochondria and quenching of its fluorescence (Figure 32A) (Baracca et al., 2003). The experimental settings were kept as described for the matrix pH measurements, except for an adjustment of the dye-specific fluorescence parameters (Figure 31).

The pyruvate/malate control led to a rapid Rho123 fluorescence quenching, indicating the generation of $\Delta\Psi$, in line with previous reports (Baracca et al., 2003). Subsequent addition of mitochondrial ETC inhibitors and membrane uncouplers restored fluorescence back to the baseline (Figure 32B). Analogous to pyruvate/malate, supplementation of mitochondria with DTT also resulted in a distinct quenching of Rho123 fluorescence (42% relative to quenching for pyruvate/malate); addition of inhibitors and membrane uncouplers restored fluorescence intensity (Figure 32B).

Addition of Cys triggered an even steeper rate of Rho123 fluorescence quenching than DTT (182% relative to DTT quenching rate; Figure 32C, D). While fluorescence was only restored upon addition of mitochondrial ETC inhibitors when mitochondria were treated with pyruvate/malate, Cys-treated mitochondria restored fluorescence without the addition of inhibitors or uncouplers (Figure 32E, F). The addition of GSH, NAC or β-ME failed to significantly alter Rho123 fluorescence relative to the mock treatment (Figure 32C–F). Taken together, the Rho123 measurements also indicate an ETC activity in response to the addition of specific thiol-based reducing agents, and provides independent confirmation that electrons from thiols can be transferred to the mitochondrial ETC.

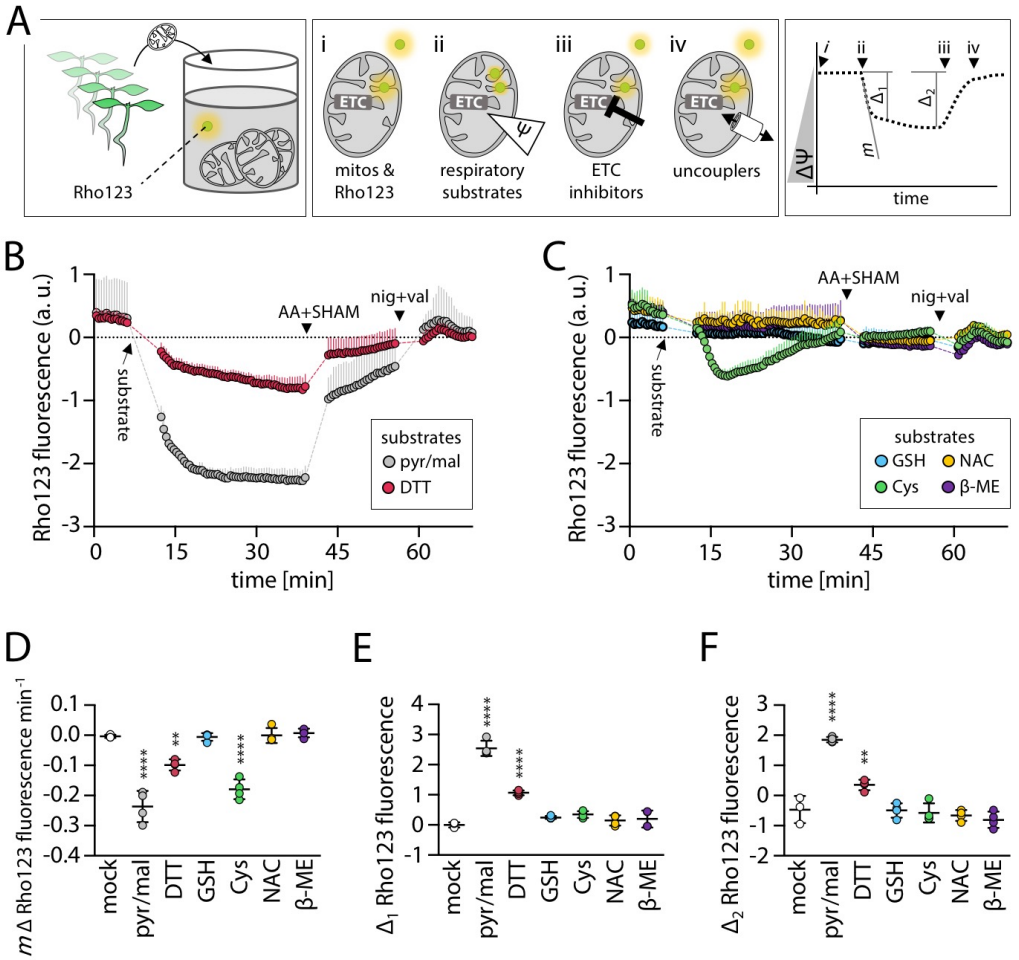

Figure 32: *In organello* monitoring of mitochondrial membrane potential in response to different additives.

(**A**) Schematic representation of the plate reader-based experimental approach to monitor dynamics of mitochondrial membrane potential (ΔΨ). *(continued on next page)*

(Figure 32 continued)
Left box: purification of intact mitochondria from 16-d-old wild-type Arabidopsis seedlings, re-suspended in basic incubation buffer with membrane-sensitive dye Rhodamine 123 (Rho123) and added to wells of 96-well plate. Rho123 emission was collected at 535 ± 15 nm while excited at 487 ± 7.5 nm using a plate reader. **Centre box**: manipulations during running assay. i: re-suspended, respiratory-inactive mitochondria. ii: addition of substrates, *e.g.* TCA-cycle intermediates, to restore electron transport chain (ETC) activity and establish ΔΨ. iii: addition of inhibitors to arrest ETC activity and passively dissipate ΔΨ via proton leakage. iv: addition of uncouplers to ensure full dissipation of ΔΨ. **Right box**: ΔΨ dynamics in response to manipulations i–iv described in centre box. Increase of ΔΨ leads to quenching-based reduction of Rho123 fluorescence. Scheme additionally indicates parameters extracted from traces for statistical analyses. *m*: slope of initial linear phase in response to substrate addition. Δ_1: substrate-induced ΔΨ difference (difference between plateau after and before substrate addition). Δ_2: ETC inhibitor-induced ΔΨ difference (difference between plateau after substrate addition and value before uncoupler addition). (**B**) and (**C**) ΔΨ dynamics of mitochondria in response to different substrates recorded via Rho123 fluorescence as described in (A). Y-axes: Rho123 fluorescence intensity shown as difference to the mean of mock treatment (dotted line at Y = 0). Increase or decrease of fluorescence intensity indicates lower or higher ΔΨ, respectively. $n \geq 3$, mean + SD. Arrow heads mark addition of substrates (β-ME: 10 mM β-mercaptoethanol, Cys: 10 mM cysteine, DTT: 10 mM dithiothreitol, GSH: 10 mM glutathione, NAC: 10 mM N-acetyl-cysteine, pyr/mal: 10 mM pyruvate + 10 mM malate + 0.3 mM NAD + 0.1 mM thiamine pyrophosphate), ETC inhibitors (AA: 20 µM antimycin A, SHAM: 2 mM salicylhydroxamic acid) and uncouplers (nig: 50 µM nigericin, val: 10 µM valinomycin). (**D**), (**E**) and (**F**) Dot plots depicting quantification of *m* (slope), Δ_1 (substrate-induced ΔΨ difference) and Δ_2 (ETC inhibitor-induced ΔΨ difference) from (B) and (C) as described in (A). $n \geq 3$, black lines: mean ± SD. Significant differences between mock and substrate treatments according to one-way ANOVA with Dunnett's multiple comparisons test (**$P < 0.01$, ****$P < 0.0001$).

Plant UCP1, similar to the mammalian UCP1, has been described to mediate dissipation of the chemiosmotic potential by translocating protons across the IMM (Ježek et al., 1996; Borecký et al., 2001; Smith et al., 2004). However, the uncoupling function of UCPs has recently been challenged by *in vitro* reconstitution in phospholipid vesicles, suggesting instead a transport function for organic and amino acids (Monné et al., 2018). The assay described in Figure 31 to monitor mitochondrial matrix pH changes might be suitable to test uncoupling abilities of UCP, since it is able to assess the impact of UCP activity in intact mitochondria rather than artificial phospholipid vesicles. Isolated mitochondria from Arabidopsis seedlings expressing cpYFP in the matrix were assayed as described in section 3.5.3. Prior to recordings, mitochondrial suspensions were supplemented with activators (4-hydroxynonenal; increased uncoupling) and inhibitors of UCP (fatty-acid-free bovine serum albumin (BSA) and ATP; reduced uncoupling) (Ježek et al., 1996; Borecký et al., 2001; Smith et al., 2004; Sweetlove et al., 2006). The addition of DTT to the pre-treated mitochondria induced a matrix alkalisation rate (0.014 cpYFP $\log_{10}$

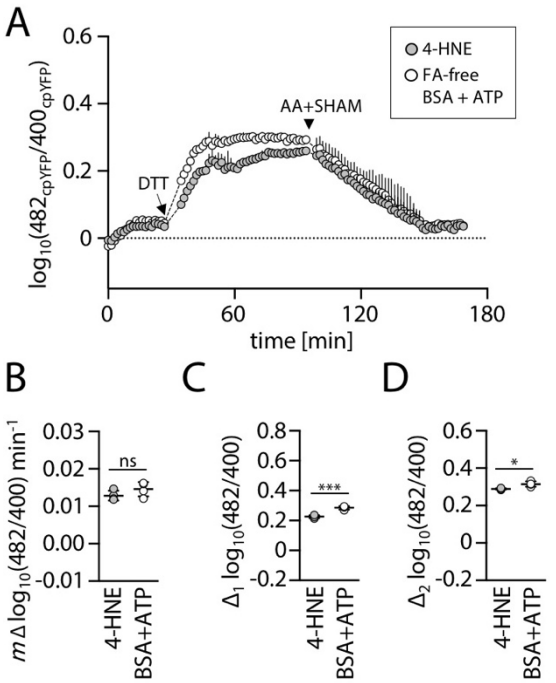

Figure 33: *In organello* examination of UCP-mediated uncoupling by mitochondrial matrix pH monitoring.

(**A**) Dynamics of mitochondrial matrix pH in response to different treatments monitored via pH biosensor cpYFP (see Figure 31A for experimental details). Y-axis: ratio of cpYFP fluorescence excited at 400 or 482 nm shown as difference to mean of mock treatment (dotted line at Y = 0). An increase or decrease of ratio indicates a more alkaline or more acidic pH, respectively. $n = 4$, mean + SD. Prior start, 30 µM 4-hydroxynonenal (4-HNE) or 0.25% (w/v) fatty acid-free bovine serine albumin (FA-free BSA) + 2 mM ATP were added to activate or inhibit uncoupling activity of mitochondrial UCP, respectively. Arrow heads mark addition of 10 mM dithiothreitol (DTT) and of ETC inhibitors 20 µM antimycin A + 2 mM salicylhydroxamic acid (AA+SHAM). (**B**), (**C**) and (**D**) Dot plots depicting quantification of m (slope), Δ_1 (substrate-induced pH difference) and Δ_2 (ETC inhibitor-induced pH difference) from traces in (A) (see Figure 31A for details on parameter calculation). $n = 4$, black lines: mean ± SD. Significant differences between treatments according to two-sided t-test ($^*P < 0.05$, $^{***}P < 0.001$).

ratio units; Figure 33A, B) comparable to previous observations (0.010 cpYFP $\log_{10}$ ratio units; Figure 31B). Yet, the mitochondrial absolute matrix alkalinisation was significantly lower in mitochondria pre-treated with 4-hydroxynonenal (-24% relative to treatment with BSA and ATP; Figure 33C), which was also reflected by the larger cpYFP ratio decrease in response to the addition of ETC-inhibitors (+12% relative to treatment with BSA and ATP; Figure 33C), pointing towards a reduced coupling upon the addition of UCP activators. The findings suggest that Arabidopsis mitochondria, presumably via UCP, can regulate non-energy-conserving proton translocation across the IMM. The different proton

gradients across the IMM induced by the activation or inhibition of UCP are in line with the reports from UCP activity studies in isolated potato and Arabidopsis mitochondria, in which measurements of ΔΨ also revealed differences in mitochondrial coupling (Smith et al., 2004; Sweetlove et al., 2006).

3.5.5 Thiol-based reductant competes with NADH oxidation by isolated mitochondria

Taken together, the recordings of oxygen consumption rates (Figure 30), the mitochondrial matrix pH (Figure 31) and ΔΨ dynamics (Figure 32) suggest that thiol-based reducing agents can supply electrons to the mitochondrial ETC and drive the establishment of a proton motive force. Based on that it was reasoned that the supplementation of reducing agents to mitochondria respiring from a set pool of TCA cycle intermediates should increase the total pool of metabolic reductant available for respiration. Accordingly, substrate depletion, as indicated by a breakdown of the proton motive force, should be delayed.

To test this hypothesis, the recombinantly purified NAD redox state biosensor (Peredox-mCherry; Figure 7) was added to suspensions of isolated WT mitochondria for *ex situ* fluorimetric monitoring of the NAD redox state (Figure 34A). In a first step, different concentrations of malate were added to the mitochondrial suspensions, which resulted in a dose-dependent reduction of the NAD pool as indicated by the Peredox-mCherry $\log_{10}$ ratio values increases of 0.10, 0.26 and 0.31 upon the addition of 0.5, 1.5 and 10 mM malate, respectively (Figure 34B). Malate can be imported and metabolised by plant mitochondria (*e.g.* Zoglowek et al., 1988; Pastore et al., 2003), however, any efficient export of NADH is unlikely for plant mitochondria. Thus, the observed *ex situ* NAD reduction is most likely explained by mitochondrial enzymes released from ruptured mitochondria; which amount to 5–10% of the total mitochondria as judged by Cytochrome *c* latency assays (section 2.5.3). The released enzymes can oxidise malate linked to the reduction of NAD^+ to NADH. Over time, the Peredox-mCherry ratio decreased again, indicating a re-oxidation of the NAD pool by the NADH-dehydrogenases of the mitochondrial ETC. The re-oxidation was significantly delayed by the additional supplementation with DTT, GSH, Cys and NAC (Figure 34C–F). Surprisingly, the addition of DTT, GSH and Cys triggered a transient increase of the Peredox-mCherry ratio (Figure 34H), which indicates that a part

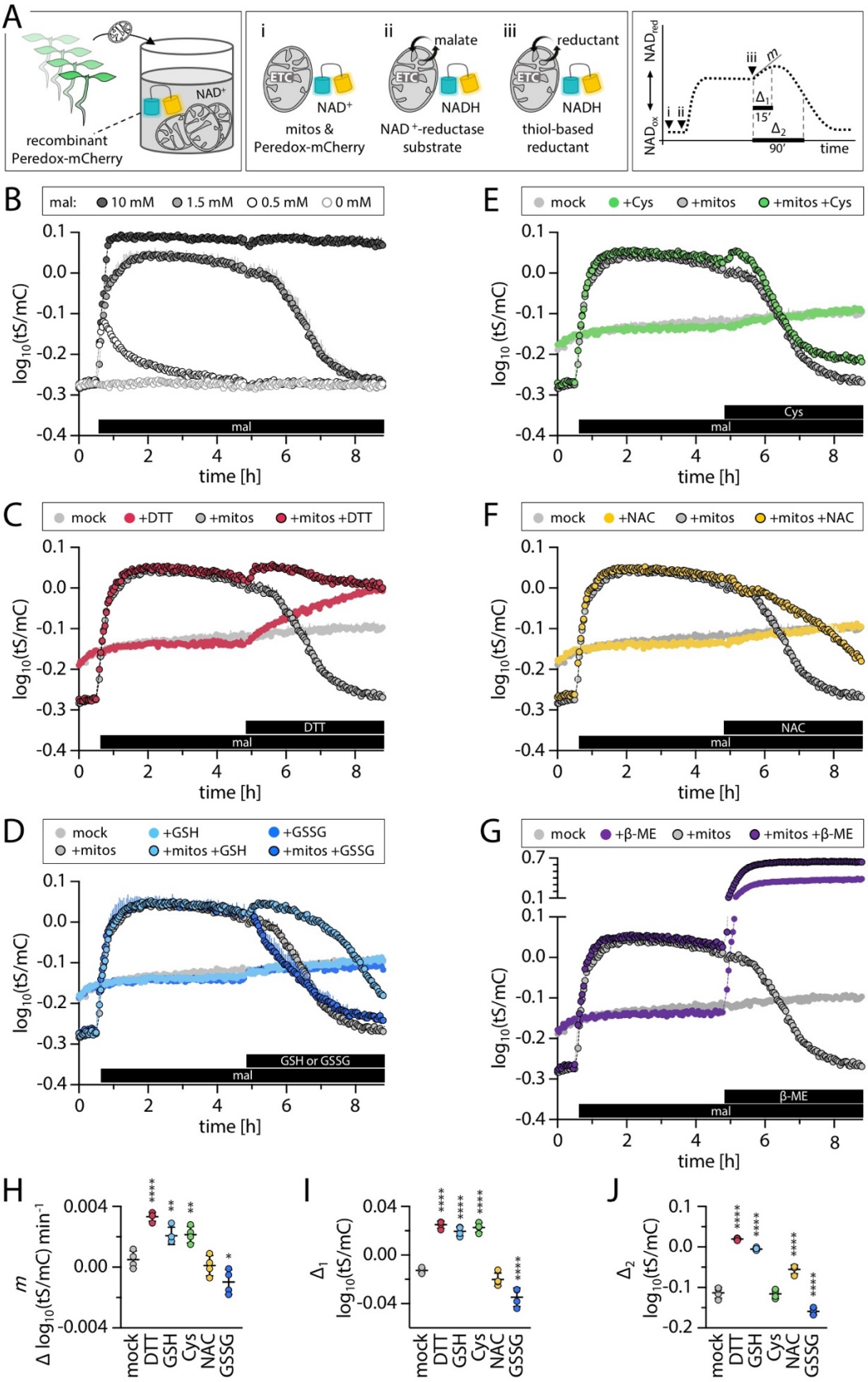
A
recombinant Peredox-mCherry
NAD+
i
ii
malate
iii
reductant
ETC
NAD+
NADH
NADH
mitos & Peredox-mCherry
NAD+-reductase substrate
thiol-based reductant
NADred
NADox
Δ1
15'
Δ2
90'
time
B
mal: 10 mM 1.5 mM 0.5 mM 0 mM
mal
time [h]
C
mock +DTT +mitos +mitos +DTT
DTT
D
mock +mitos +GSH +GSSG +mitos +GSSG
GSH or GSSG
E
mock +Cys +mitos +mitos +Cys
Cys
F
mock +NAC +mitos +mitos +NAC
NAC
G
mock +β-ME +mitos +mitos +β-ME
β-ME
log10(tS/mC)
H
m
Δ log10(tS/mC) min-1
I
Δ1
J
Δ2
mock DTT GSH Cys NAC GSSG

Figure 34: *Ex situ* monitoring of mitochondrial NADH oxidation in response to malate and different reducing agents.
(**A**) Schematic representation of the plate reader-based experimental approach to monitor NADH consumption of mitochondria. **Left box**: purification of intact mitochondria from 16-d-old wild-type Arabidopsis seedlings, re-suspended in basic incubation buffer, 500 µM NAD^+ and 0.5 µM recombinantly purified Peredox-mCherry. T-Sapphire (tS) and mCherry (mC) emission from Peredox-mCherry was recorded using a plate reader. tS excitation: 400 ± 10 nm, tS emission: 515 ± 7.5 nm, mC excitation: 570 ± 10 nm, mC emission: 610 ± 5 nm. **Centre box**: manipulations during running assay. i: re-suspended, respiratory-inactive mitochondria (mitos) with NAD^+ and Peredox-mCherry. ii: addition of malate to produce NADH via malate dehydrogenases released from mitochondria ruptured during purification or assay. Over time, mitochondria respire off malate-derived reductant and deplete NADH. iii: addition of reductant to compete with NADH as respiratory substrate for mitochondrial electron transport chain (ETC), delaying NADH depletion. **Right box**: NAD redox dynamics in mitochondrial suspension medium *ex situ* monitored by Peredox-mCherry in response to manipulations (i–iii) described in centre box. Scheme additionally indicates parameters extracted from traces for statistical analyses. *m*: slope of initial linear phase after reductant addition. Δ_1 and Δ_2: substrate-induced NAD redox state differences (difference between state 15 or 90 min after compared directly before reductant addition). (**B**) NAD redox dynamics in mitochondrial suspension medium in response to the addition of different amounts of malate (mal). Increase or decrease of tS/mC ratio indicates more reduced or more oxidised NAD pool, respectively. $n = 4$, mean + SD Black bar at the bottom of the graph indicates the addition of malate. (**C**), (**D**), (**E**), (**F**) and (**G**) NAD redox dynamics in mitochondrial suspension medium in response to the addition of 1.5 mM mal and different reducing agents or controls indicated by the black bars at the bottom of the graphs (β-ME: 10 mM β-mercaptoethanol, Cys: 10 mM cysteine, DTT: 10 mM dithiothreitol, GSH: 10 mM glutathione, GSSG: 5 mM oxidised glutathione, NAC: 10 mM N-acetyl-cysteine). Dots without borders: without mitochondria, dots with borders: mitochondria added prior start of recordings. Note that mock and +mitos traces are identical and serve as reference. $n = 4$, mean + SD. (**H**), (**J**) and (**I**) Dot plots depicting quantification of *m*, Δ_1 and Δ_2, as described in (A), from traces with mitochondria shown in (C–F). (G) was omitted from analysis due to interference of β-ME with sensor. $n = 4$, black lines: mean ± SD. Significant differences between mitochondria in the absence and presence of reductant according to one-way ANOVA with Dunnett's multiple comparisons test ($^*P < 0.05$, $^{**}P < 0.01$, $^{****}P < 0.0001$).

of the electrons were redirected into reducing the NAD pool rather than directly into the mitochondrial ETC. β-ME was excluded from any further interpretation due to its technical interference with the Peredox-mCherry sensor (Figure 34G). Oxidised glutathione, GSSG, was added as negative control (Figure 31D). Notably, the addition of GSSG elicited a significantly faster NAD oxidation than in the mock treatment (Figure 34D, H–J), potentially constituting a competing metabolic reductant sink and thereby indirectly supporting NADH oxidation.

3.5.6 Discussion

The different orthogonal approaches pinpoint a novel electron transfer pathway from thiol-based reductant to the mitochondrial ETC. The applied concentrations of reducing agents (10 mM) in the *in organello* assays were relatively high, but drawing preliminary conclusions about the *in vivo* relevance of the observations appears legitimate nevertheless. The exposure of mitochondria to DTT or NAC does not aim to constitute physiological conditions, but serves as a proof of principle that electrons from thiols can be passed to the mitochondrial ETC. In the case of GSH, cellular concentrations ranging from 3–5 mM were observed (Meyer et al., 2001; Krueger et al., 2009; Queval et al., 2011). Analyses of the subcellular GSH distribution via immunocytochemical approaches discovered the highest GSH concentrations in mitochondria, being more than two-fold higher than the concentration in the cytosol (Zechmann et al., 2008; Queval et al., 2011). Thus, mitochondrial GSH levels realistically approach concentrations of 10 mM and also cytosolic levels are likely to fall into the mM range.

3.5.6.1 Different thiol-based reducing agents lead to different responses

The addition of the different thiol-based reducing agents to mitochondria induced clearly detectable changes in most, but not all, cases. Different amplitudes of the effects might originate from different chemical and steric properties or/and different pathways of the electrons from the reducing agents to the mitochondrial ETC. The reducing agent β-ME consistently failed to indicate ETC activity, but was the only reducing agent directly interfering with the Peredox-mCherry sensor (Figure 34). The difference between β-ME and the other reducing agents might originate different structural backbones.

For human cells, it was recently shown that NAC-derived Cys is desulfurated to produce hydrogen sulfide (H_2S), which is subsequently oxidised to sulfane sulfur species (Ezeriņa et al., 2018). Oxidation of H_2S was found to be directly coupled to the ETC via the sulfide:quinone oxidoreductase in the mitochondrial matrix (Libiad et al., 2014). In contrast to animals, sulfide:quinone oxidoreductase is absent in Arabidopsis mitochondria, however, an alternative pathway allowing the oxidation of H_2S coupled to the ETC has not been reported so far. Another striking feature of Cys was the biphasic response on mitochondrial matrix pH (Figure 31) and $\Delta\Psi$ dynamics (Figure 32). After an initial boost, the mitochondrial ETC activity appeared to drop considerably. It is well known that

increased concentrations of H_2S inhibit the mitochondrial ETC complex IV (Dorman et al., 2002). Mitochondrial Cys catabolism is insufficiently understood, but it is tempting to speculate that plant mitochondria, similar to animals, desulfurate Cys and produce H_2S, which may inhibit the mitochondrial ETC.

3.5.6.2 Candidate pathways for the transfer of electrons from thiols to the mitochondrial ETC

The identification of the exact electron route(s) from the thiols to the mitochondrial ETC is beyond the scope of this work and remains to be investigated in the future. It is conceivable that several pathways act in parallel. For instance, *ex situ* monitoring of the NAD redox state with the Peredox-mCherry indicated that a significant extent of electrons was supplied into the NAD pool (Figure 34). From there, electrons could enter the mitochondrial ETC via Complex I as well as the alternative NAD(P)H dehydrogenases (Rasmusson et al., 2008). Electron transfer between the thiol/disulfide and the NAD pool is biochemically possible, for instance, via an interaction of lipoic acid and thioredoxins (TRX): Lipoic acid is an organosulfur compound (8-carbon fatty acid containing a thiolane ring with a disulfide joining carbons 6 and 8) which serves as a cofactor in different enzyme complexes, such as the pyruvate dehydrogenase complex and the 2-oxoglutarate dehydrogenase complex (Cronan, 2014). Lipoic acid is known to interact with the NAD pool, but was also shown *in vitro* to equilibrate with TRX (Holmgren, 1979); TRX in turn can be directly reduced by DTT (Laloi et al., 2001). Accordingly, DTT could reduce NAD via TRX and lipoic acid. Alternatively, reduced TRX could redox-equilibrate with the NADP pool via the NADPH-dependent thioredoxin reductase (NTR). NADPH can in turn be oxidised at the alternative NAD(P)H dehydrogenases and supply electrons to the mitochondrial ETC (Rasmusson et al., 2008), or redox-equilibrated with the NAD pool. Although plants, unlike animals and bacteria, possess no gene encoding a *bona fide* transhydrogenase (Clarke and Bragg, 1985; Olausson et al., 1995; Arkblad et al., 2002), equilibration is possible via transhydrogenase activity as provided by metabolic shuttling. For instance, forward and reverse reactions with the mitochondrial $NADP^+$- and NAD^+-dependent isocitrate dehydrogenases allow exchange of electrons between the NAD and NADP pools, depending on the metabolic situation (Igamberdiev and Gardeström, 2003). The mitochondrial NAD-malic enzyme and the

NAD-malate dehydrogenase have also been shown to utilise both NAD(H) and NADP(H) as substrates (Møller and Rasmusson, 1998). Although these enzymes are usually localised in the mitochondrial matrix, the fraction of ruptured mitochondria releases a proportion of enzymatic activity as indicated by the *ex situ* NAD measurements (Figure 34).

Another candidate pathway is the mitochondrial disulfide relay system in the IMS. The system, composed of the oxidoreductase MIA40 and the sulfhydryl oxidase ERV1, mediates the formation of structural disulfide bonds during oxidative protein folding (Böttinger et al., 2012; Peleh et al., 2017). Recent *in vitro* experiments showed that DTT can reduce *At*ERV1, which subsequently reduces Cytochrome *c* and thereby supplies electrons to the mitochondrial ETC directly upstream of complex IV (Bihlmaier et al., 2007; Peleh et al., 2017). Evidence from *in organello* experiments suggests that both DTT and GSH can pass the OMM and freely access the redox relay system (Mesecke et al., 2005; Kojer et al., 2012; Bragoszewski et al., 2015). The effective abolishment of the mitochondrial ETC activity in response to the inhibition at complex III and AOX (Figure 31), which is upstream of Cytochrome *c*, however, argues against this pathway as a major route for DTT- and GSH-derived electrons.

Notably, the inhibition of the mitochondrial ETC at complex III and AOX revealed no effect on mitochondria supplemented with Cys (Figure 31). This points towards an electron entry downstream of complex III and would be compatible with the IMS disulfide relay system. The different responses to the ETC inhibitors suggest that the pathways of the electrons to the mitochondrial ETC differ, despite the structural similarities of the thiol-based reducing agents.

3.5.6.3 Why was the link between thiol oxidation and the mitochondrial ETC not detected before?

A forward electron transfer route from the thiol/disulfide redox pool to the mitochondrial ETC has not been reported in literature, despite the plethora of studies undertaken in the redox and mitochondrial field. The absence of such an observation may be explained by the comparatively small magnitudes of the effects, *e.g.* the DTT-triggered increase of mitochondrial oxygen consumption (Figure 30). Furthermore, increased oxygen consumption upon DTT addition, that has likely been observed, may have been interpreted as the result of uncatalysed DTT-mediated reduction of O_2 to H_2O_2. Such an

effect was indeed observed is this work as evidenced by an increased oxygen consumption rate in the absence of mitochondria (Figure 30D). Mitochondrial ETC linked activity may have been overlooked as a result.

Changes in mitochondrial matrix pH (Figure 31) and ΔΨ (Figure 32) were considerably smaller for reducing agents than for tricarboxylic acid (TCA) cycle intermediates. It is noteworthy that the monitored changes in pH and ΔΨ result from the relative differences in proton translocation rate by the mitochondrial ETC and the re-translocation rate (Brand et al., 2005; Klingenberg, 2008). Low mitochondrial ETC proton-pumping activities are often obscured by significant re-translocation proton-fluxes, resulting in unchanged net pH and ΔΨ values. Conversely, the detected changes were the result of mitochondrial ETC-mediated activities which outcompeted the re-translocation proton-flux, suggesting that the addition of reducing agents resulted in substantial respiratory electron transport rates. This is consistent with the results from the orthogonal *ex situ* NAD redox state monitoring, in which the addition of reducing agents including the 'mild' reducing agent NAC all exhibited significant effects on the substrate depletion rates (Figure 34).

3.6 *In vivo* analysis of sub-mitochondrial architecture and physiology

3.6.1 Introduction

Compared to the emerging insights in the field of mammalian mitochondria, analyses of the *in vivo* sub- or potentially microcompartmentation are largely lacking for plant mitochondria (section 1.4.3). The overall bioenergetic characteristics of mitochondrial ETC functions are largely conserved between mitochondria of animals and plants, even though individual components can differ markedly (Millar et al., 2011; Schertl and Braun, 2014). In contrast, electron microscopy and tomographic reconstructions revealed remarkably variable morphologies and ultrastructures of mitochondria between and within the plant and animal kingdoms (Parsons et al., 1965; Lea and Hollenberg, 1989; Brandt et al., 2017). Considering an intimate interconnection between shape and function of mitochondria, it is unclear to what extent findings from the animal field regarding submitochondrial pH compartmentation can be applied to plant mitochondria. Experiments in the following section aim to shed light on submitochondrial pH as a key bioenergetic parameter of mitochondrial energy metabolism in plants.

3.6.2 Reporter proteins can be targeted to different mitochondrial subcompartments

A major advantage of genetically encoded sensors over conventional dyes lies in their targetability to specific cellular subcompartments and the absence of destructive interference with cellular physiology. This potential was exploited in the next step by targeting the circularly permuted Yellow Fluorescent Protein (cpYFP, Figure 7; Schwarzländer et al., 2011, 2014) pH biosensor to different mitochondrial locations.

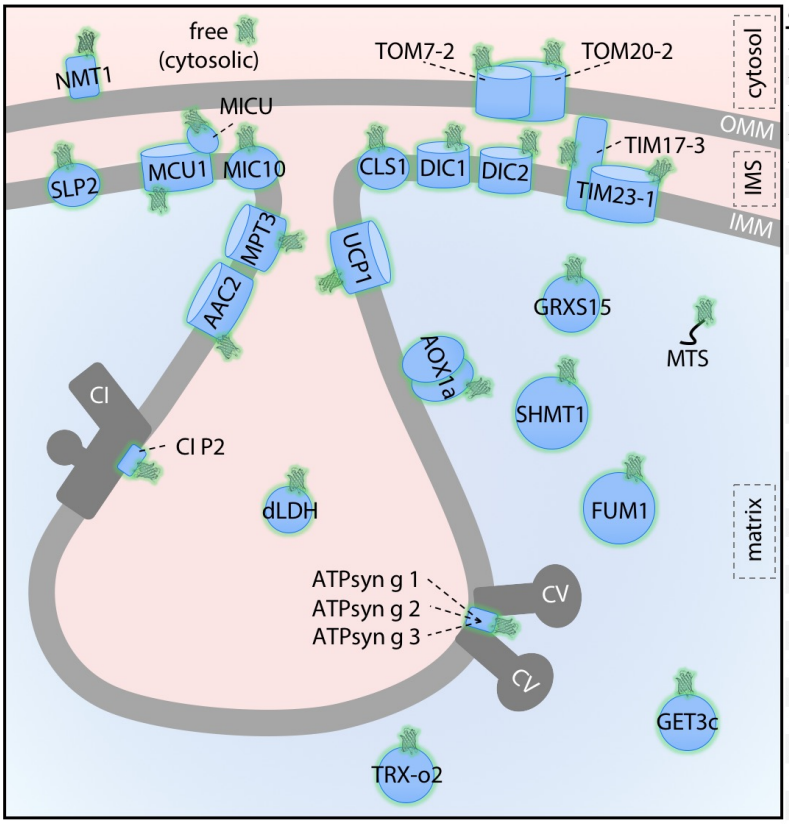

Gene	identifier	topo
AAC2	*AT5G13490*	IMS
AOX1a	*AT3G22370*	matrix
ATPsyn g 1	*AT2G19680*	matrix
ATPsyn g 2	*AT4G26210*	matrix
ATPsyn g 3	*AT4G29480*	matrix
CI P2	*AT2G27730*	IMS
CLS1	*AT4G04870*	IMS
none	none	cytosol
DIC1	*AT2G22500*	IMS
DIC2	*AT4G24570*	IMS
dLDH1	*AT5G06580*	IMS
FUM1	*AT2G47510*	matrix
GET3C	*AT5G60730*	matrix
GRXS15	*AT3G15660*	matrix
MCU1	*AT1G09575*	matrix
MIC10	*AT1G22520*	IMS
MICU1	*AT4G32060*	IMS
MPT3	*AT5G14040*	IMS
MTS	none	matrix
NMT1	*AT5G22350*	cytosol
SHMT1	*AT4G37930*	matrix
SLP2	*AT1G18480*	IMS
TIM17-3	*AT5G11690*	IMS
TIM23-1	*AT1G17530*	IMS
TOM20-2	*AT1G27390*	cytosol
TOM7-2	*AT1G64220*	cytosol
TRX-o2	*AT1G31020*	matrix
UCP1	*AT3G54110*	IMS

Figure 35: Overview of Arabidopsis lines generated to express mitochondrial proteins fused to the cpYFP pH biosensor.

Graphical scheme (left) indicates the hypothetical spatial arrangement of different mitochondrial proteins which were fused to cpYFP and stably expressed in Arabidopsis wild-type plants. Lines are only shown for which reasonable fluorescent signal-to-noise ratio was confirmed. Note that for several proteins, the available knowledge on topology and subcompartmental localisation is scarce or contradictory. Green β-barrel proteins indicate the hypothetical topology of the fused cpYFP. Grey: larger protein complexes of which subunits were fused to cpYFP. OMM: outer mitochondrial membrane, IMS: intermembrane space, IMM: inner mitochondrial membrane. Table (right) summarises corresponding mitochondrial proteins fused to cpYFP and lists associated gene identifier and predicted subcompartmental topology of cpYFP.

Recent studies have considerably advanced our understanding of mitochondrial protein import (Stojanovski et al., 2012; Murcha et al., 2014). Nevertheless, knowledge about the motifs and mechanisms responsible for sorting proteins into microcompartments is limited and the very existence of microcompartments is still debated. To better define localisation and topology of candidate proteins endogenous full-length sequences of mitochondrially targeted proteins were fused to the N- or C-terminus of cpYFP (depending on the import mechanism to minimise the risk of masking of critical motives). Although empirical data about precise sublocalisation for most plant

mitochondrial proteins are missing, some proteins have been assigned to specific locations using for instance immunogold labelling, super-resolution microscopy or mitochondrial subfractionation (Sweetlove et al., 2001; Jans et al., 2013; Haindrich et al., 2017). A selection of such proteins was employed as marker proteins to target cpYFP to the different corresponding mitochondrial compartments (Figure 35) (Supplemental Table 1). In total, 48 vectors with cpYFP fused to different candidate genes under the control of the CaMV35S promoter were successfully cloned and used for transformation of Arabidopsis to give rise to stable lines (Table 19). Resistance marker-mediated selection allowed recovery of transformants in all instances and for 26 of the constructs the transformants revealed good cpYFP signal-to-noise ratios as judged by confocal imaging (Figure 36). Those lines were propagated for the experiments. Previously characterised lines expressing cpYFP in the mitochondrial matrix (mts-cpYFP; Schwarzländer et al., 2011) or the cytosol (cyt-cpYFP; unpublished line from M. Schwarzländer) served as controls. The lines from the transformation with the remaining 22 cpYFP fusion constructs were not further investigated either due to their insufficient signal-to-noise ratio or due to ambiguous (dual) targeting of the fluorescence (NDPK3-cpYFP; Supplemental Figure 3).

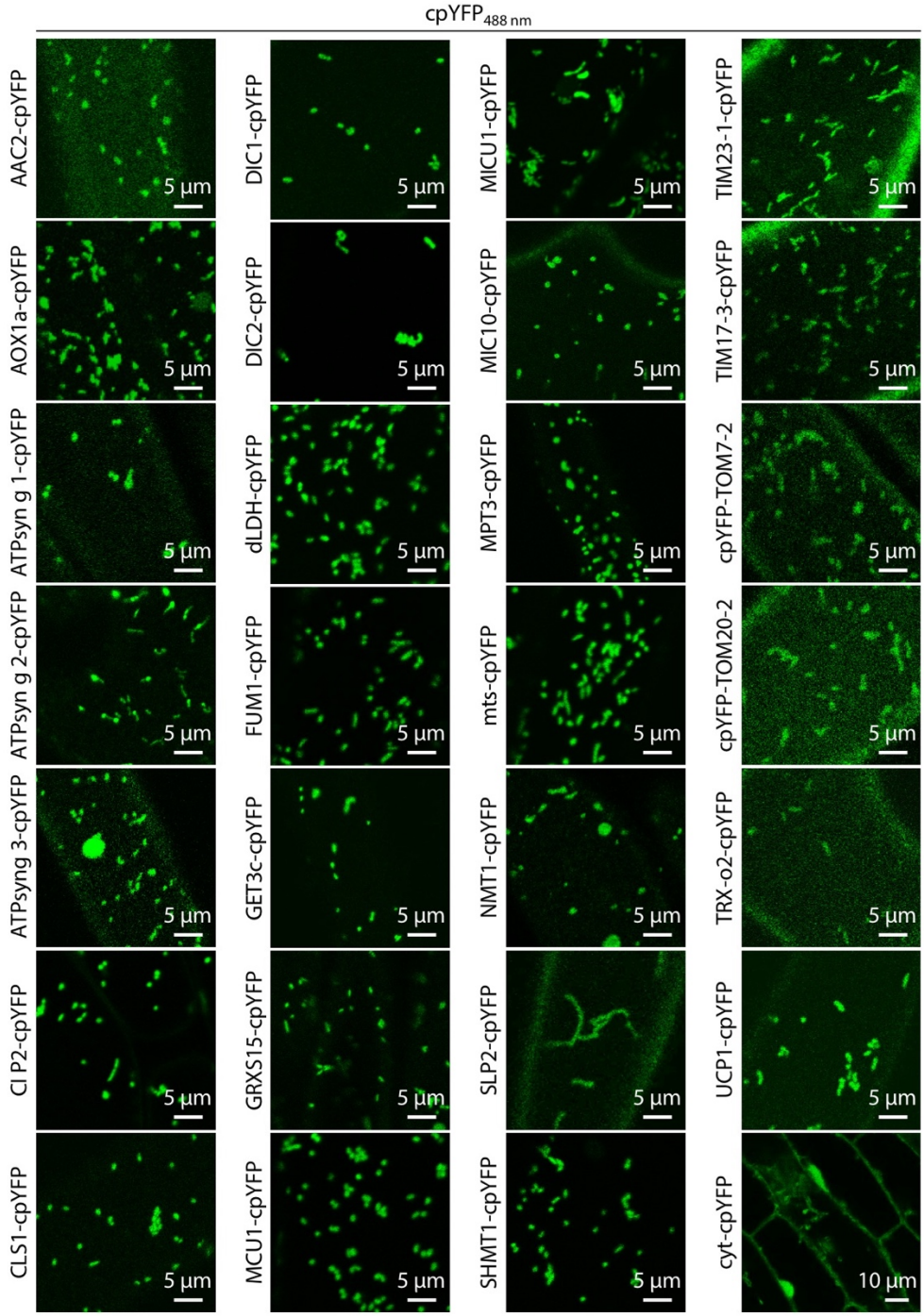

Figure 36: Representative CLSM images of hypocotyl epidermal cells from Arabidopsis seedlings expressing mitochondrial proteins fused to the cpYFP pH biosensor.

Representative CLSM images of hypocotyl cells from 5-d-old Arabidopsis seedlings stably transformed expressing the indicated candidate protein fused to the circularly permuted Yellow Fluorescent Protein (cpYFP) pH sensor (for sublocalisation see Figure 36). For clarity reasons, only the images from cpYFP emission channel excited at 488 nm are shown. Candidate protein-cpYFP or cpYFP-candidate protein indicate fusion to N- or C-terminus of cpYFP, respectively.

3.6.3 Mitochondrial proteins targeted to different subcompartments reveal distinct bioenergetic pH dynamics

Selected sensor-fusion lines were examined using plate reader-based fluorimetry. Although confocal images of all selected lines indicated mitochondrial targeting of the cpYFP-fusion constructs, they did not provide any clear information about the targeted mitochondrial subcompartment. As shown above (Figure 31), resumption of proton pumping in isolated mitochondria leads to an alkalinisation in the mitochondrial matrix (Schwarzländer et al., 2011). It was reasoned that proton-pumping activity should result in the qualitatively opposite effect for the IMS, *i.e.* in an acidification. However, quantitative effects are hard to predict as they are strongly influenced by the pH buffering potential of the respective compartment. To test this, fluorimetric *in organello* cpYFP measurements (Figure 37A) were conducted analogously to the substrate feeding assays in section 3.5.3. To validate the method, mitochondria from the reference line mts-cpYFP were investigated first. Addition of succinate, a respiratory substrate of complex II of the mitochondrial ETC, elicited a pronounced increase of the cpYFP ratio, which indicated an alkalinisation of the cpYFP environment. The cpYFP ratio was restored to the baseline by the addition of chemical uncouplers (Figure 37B). The dynamics were in line with the observations for the addition of pyruvate/malate to mts-cpYFP mitochondria (Figure 31). The same assay was then performed with mitochondria isolated from seedlings expressing Network1/ELM1 (*NMT1*; Figure 37C), F_0F_1 ATP synthase subunit g 1 *(ATPsyn g 1*; Figure 37D) or d-Lactate Dehydrogenase (*dLHD*; Figure 37E) fused with cpYFP. The marker proteins NMT1, ATPsyn g 1 and dLDH had been reported to localise to the OMM (exposed to cytosol; Arimura et al., 2008; Duncan et al., 2011), the IMM (exposed to matrix; van Lis et al., 2007; Hahn et al., 2016) and the IMS (Engqvist et al., 2009), respectively. Mitochondria isolated from ATPsyn g 1-cpYFP revealed matrix-typical pH dynamics as observed before for mts-cpYFP (Figure 37D). In contrast, cpYFP ratio in mitochondria from dLDH-cpYFP decreased in response to succinate and increased again at subsequent uncoupler addition (Figure 37E). The absence of an alkalinisation is in agreement with the hypothesised IMS localisation of dLDH (Engqvist et al., 2009). The observed decrease of cpYFP ratio suggested a slight decrease in pH, which was also noted for mitochondria isolated from

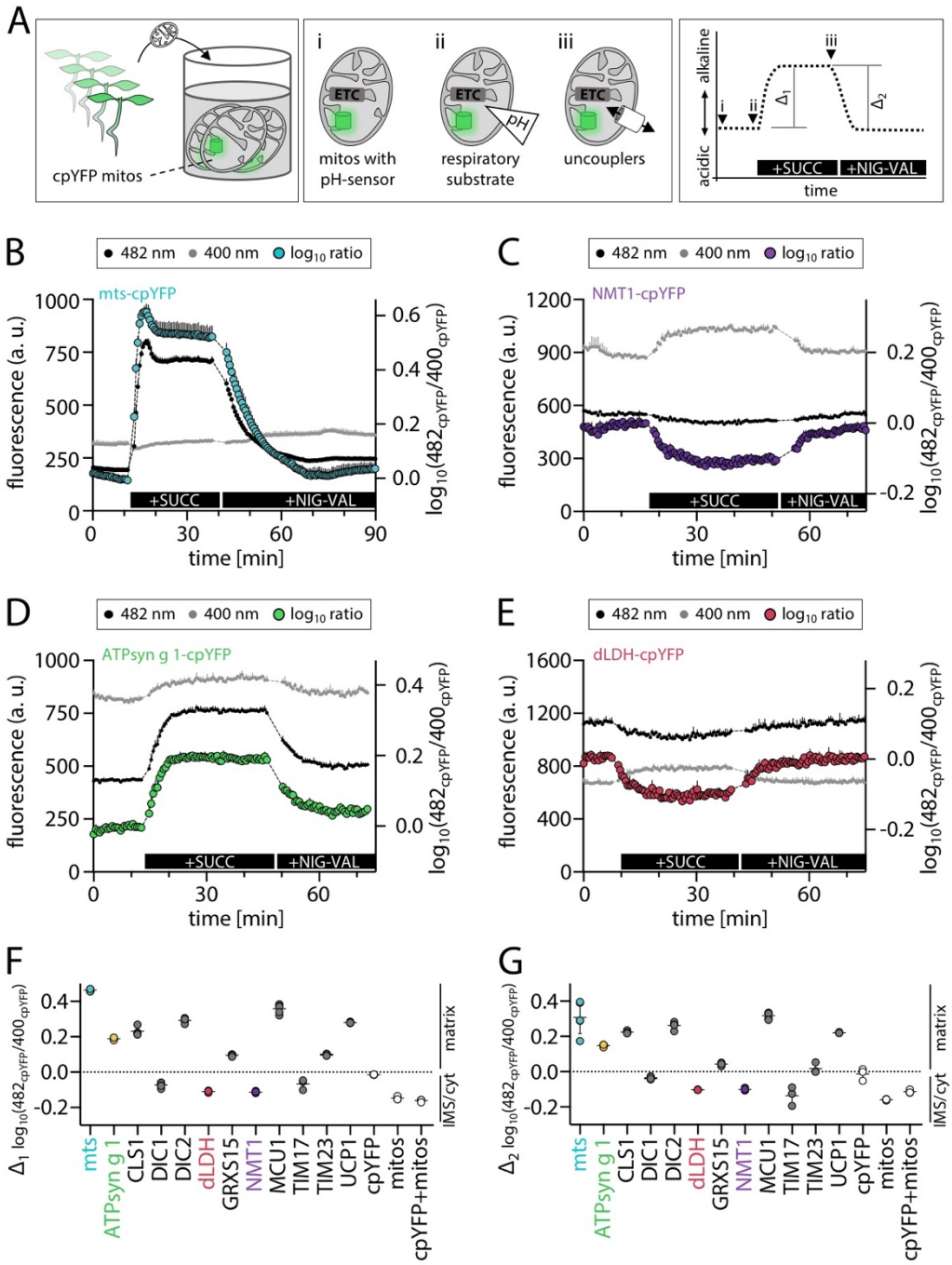

Figure 37: *In organello* monitoring of pH dynamics from different mitochondrial protein-cpYFP fusions. **(A)** Schematic representation of the cpYFP-based sublocalisation assay of mitochondrial proteins. **Left box**: purification of intact mitochondria from 16-d-old Arabidopsis seedlings stably expressing mitochondrial proteins fused to circularly permuted Yellow Fluorescent Protein (cpYFP). Isolated mitochondria were re-suspended in basic incubation buffer and added to wells of a 96-well plate. cpYFP emission was recorded at 520 ± 5 nm in two separate tracks with excitation at 400 ± 5 nm and 482 ± 8 nm using a plate reader. **Centre box**: manipulations during running assay. i: re-suspended, respiratory-inactive mitochondria. ii: addition of respiratory substrate to restore electron transport chain (ETC) activity and establish pH gradient (ΔpH) across inner mitochondrial membrane. iii: addition of uncouplers to dissipate ΔpH. *(continued on next page)*

(Figure 37 continued)
Right box: exemplary pH dynamics reported by mitochondrial matrix-residing cpYFP in response to manipulations i–iii. Scheme additionally indicates parameters extracted from traces for statistical analyses. Δ_1: cpYFP ratio differences between state directly before compared to plateau after succ addition, Δ_2: cpYFP ratio differences between state plateau after compared to state directly before uncoupler addition. (**B**), (**C**), (**D**) and (**E**) Assays as described in (A) with mitochondria isolated from Arabidopsis seedlings stably expressing different cpYFP fusions (see Figure 36 and Supplemental Table 1 for details about proteins). Left y-axis: fluorescence emission intensities while exciting at 400 nm (grey) or 482 nm (black). Right y-axis: $\log_{10}$ ratios (482 nm/400 nm). Increase or decrease of ratio indicates more alkaline or more acidic pH, respectively. $n \geq 3$, mean + SD. Black bars at the bottom of the graphs indicate addition of 10 mM succinate + 250 µM ATP (succ) or 50 µM nigericin and 10 µM valinomycin (nig-val). Note that emission gainment was adjusted between experiments and fluorescence intensities (left y-axes) are not directly comparable. (**F**) and (**G**) Dot plots depicting quantification of Δ_1 and Δ_2 (succinate and uncoupler-induced pH differences) from (B–E) as described in (A). $n \geq 3$, black lines: mean ± SD. Dots in grey: quantifications from traces shown in Figure 39. For details about proteins-cpYFP fusions see Figure 36 and Supplemental Table 1. Dots in white: controls with recombinant cpYFP without mitochondria (cpYFP), wild-type mitochondria without cpYFP (mitos) and recombinant cpYFP + mitochondria (cpYFP+mitos; see Figure 39 for details). Dotted lines indicate expected value if addition of succinate or uncouplers had no impact on cpYFP value, respectively. Values above and below dotted line represent cpYFP ratio differences typical associated to matrix or IMS/cytosolic cpYFP exposure, respectively.

NMT1-cpYFP (Figure 37C). Similar pH dynamics observed for the IMS (dLHD) and cytosolic face of the OMM (NMT1) might imply that either dLDH or NMT1 mis-localised to end up in the same mitochondrial subcompartment or that proton extrusion out of the mitochondrial matrix led to a similar acidification in the IMS as at the cytosolic surface of the mitochondrial OMM. To test the latter hypothesis, mitochondria from WT seedlings without any sensor expression were isolated and resuspended together with recombinantly purified cpYFP for pH measurements in the medium. Conducting the same experimental regime (Figure 37A), the cpYFP ratios exhibited a slight decrease which was reverted by uncoupling (Figure 38C) as observed before for dLDH and NMT1. This suggests a general acidification of the extra-matrix spaces in response to mitochondrial ETC activity. Importantly it needs pointing out that control assays with sensor-free mitochondria showed a similar ratio decrease upon succinate addition (Figure 38B), originating mainly from the increased emission collected in the 400-nm-excitation channel. A relatively high autofluorescence of biological samples at excitation around 400 nm and its increase upon mitochondrial energisation results in a low signal-to-noise ratio. Thus, distinguishing between an exposure to the IMS or cytosol is difficult based on changes in the 400-nm-excitation channel.

In contrast, the dynamics between protein fusions with cpYFP exposure to the mitochondrial matrix and exposure to compartments other than the mitochondrial matrix were clearly distinct. To further assess the potential and robustness of the assay, mitochondria from additional lines were investigated applying the same assay routine. The addition of succinate followed by uncoupling revealed overall two different patterns of cpYFP dynamics (Figure 37F, G). The first pattern included mitochondria from mts-cpYFP (Figure 37 B), ATPsyn g 1-cpYFP (Figure 37D) and from the lines expressing cpYFP fused to Uncoupling Protein 1 (*UCP1*; Figure 39A), Cardiolipin Synthase 1 (*CLS1*; Figure 39C), Translocase of the Inner mitochondrial Membrane 23-1 (TIM23-1; Figure 39D), Mitochondrial Calcium Uniporter 1 (*MCU1*; Figure 39F), Dicarboxylate Carrier 2 (*DIC2*; Figure 39G) or Glutaredoxin S15 (*GRXS15*; Figure 39H). The corresponding mitochondria exhibited an increase of the cpYFP ratio upon energisation, marked by changes predominately occurring in the 482-nm-channel. The cpYFP linked to those proteins appears to be exposed to the mitochondrial matrix. The second pattern showed unchanged or slightly decreasing cpYFP ratios in response to succinate addition (Figure 37F), indicating localisation outside of the mitochondrial matrix. This pattern was observed for the mitochondria from NMT1-cpYFP (Figure 37C) and dLDH-cpYFP (Figure 37E) and from the lines expressing cpYFP fused to Dicarboxylate Carrier 1 (*DIC1*; Figure 39E) or Translocase of the Inner mitochondrial Membrane 17-3 (*TIM17-3*; Figure 39B). Comparing the behaviour of the different protein cpYFP fusions with the predicted exposure of cpYFP (Figure 35, Supplemental Table 1), the results indicate different topologies for CLS1-cpYFP, DIC2-cpYFP and UCP1-cpYFP. The reasons for those discrepancies are unclear and will require analyses by orthogonal methods. Independent data to validate the topology of these proteins in plant mitochondria is currently lacking.

Taken together, the cpYFP response in mitochondria at IMM energisation using succinate followed by uncoupling indicated that the approach provides a valuable new tool to assess submitochondrial protein topology, at least for a clear discrimination between the matrix and extra-matrix subcompartments. In contrast, differentiation between IMS and exposure to the cytosol has proven technically difficult with the current approach.

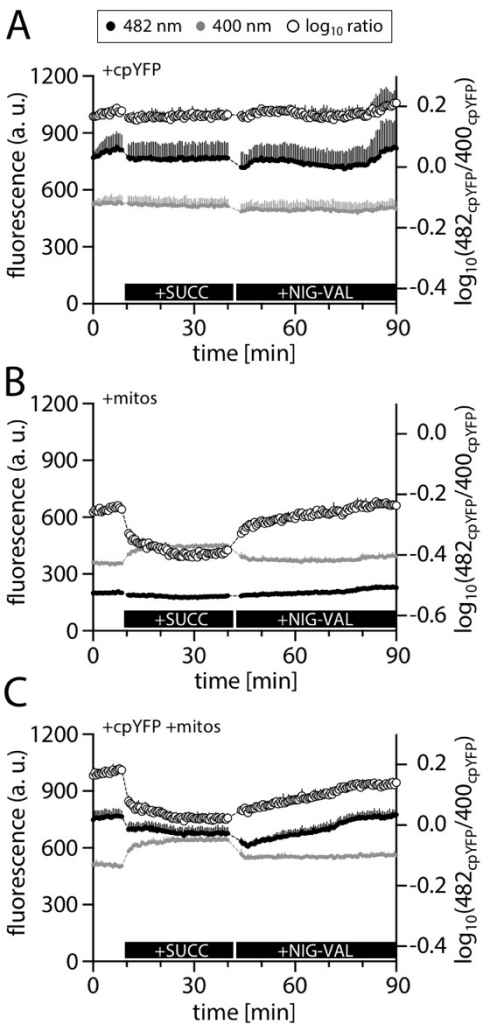

Figure 38: Control experiments with purified cpYFP sensor protein and isolated wild-type mitochondria. Control runs of cpYFP mitochondria-based protein sublocalisation assays with identical methodology as described in Figure 38 except for substitution of cpYFP-carrying mitochondria with WT mitochondria expressing no sensor. (**A**), (**B**) and (**C**) Emission fluorescence recordings in response to excitation at 400 or 482 nm of wells containing isolated cpYFP-free mitochondria (+mitos), recombinant cpYFP (+cpYFP) or both (+cpYFP +mitos). Left y-axis: emission fluorescence intensities. Right y-axis: corresponding $\log_{10}$ ratios (482 nm/400 nm). Increase or decrease of ratio values indicate more alkaline or more acidic pH, respectively. For quantification see Figure 38. All traces: $n \geq 3$, mean + SD. Black bars at the bottom of the graphs indicate addition of 10 mM succinate + 250 µM ATP (succ) or 50 µM nigericin + 10 µM valinomycin (nig-val).

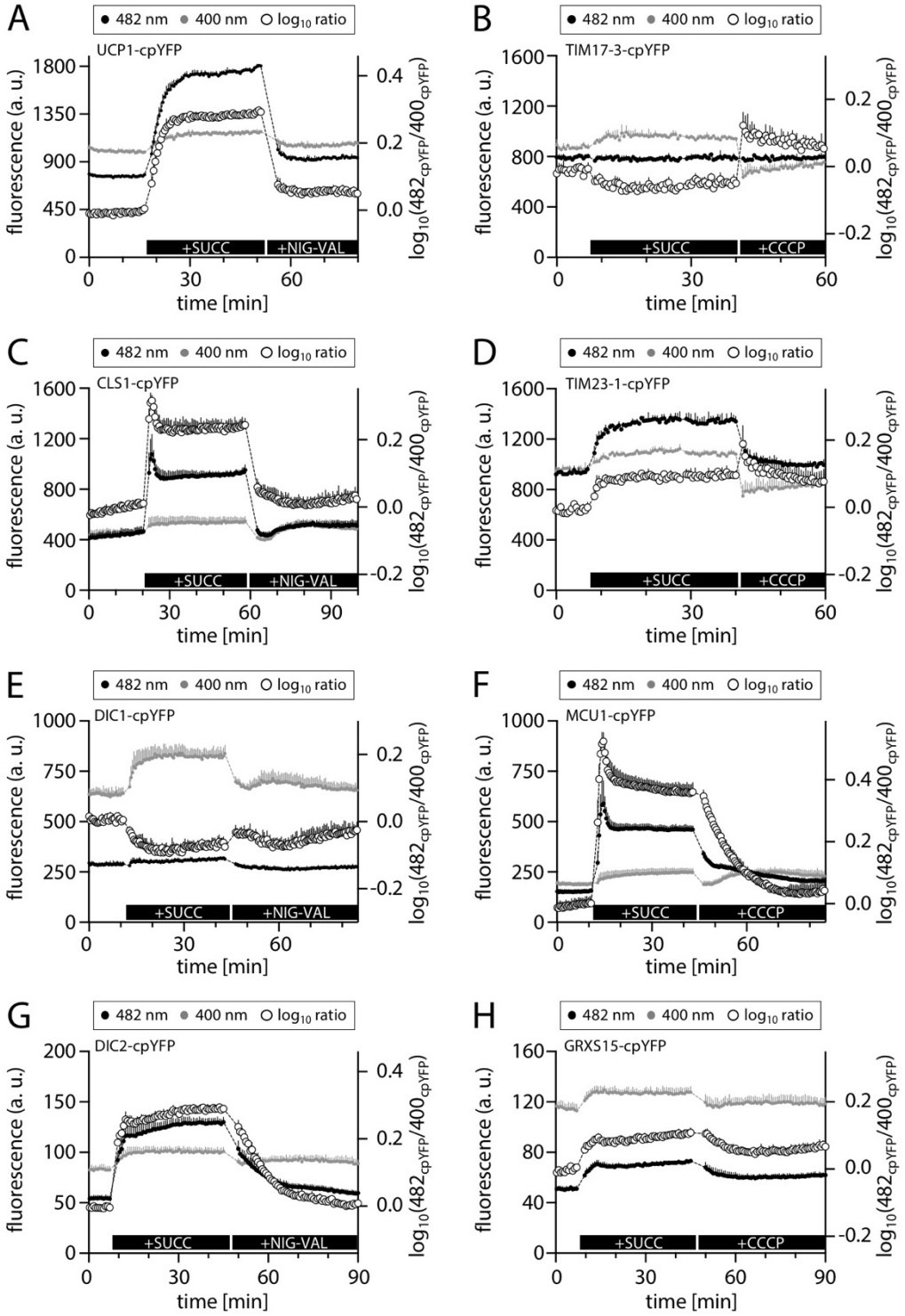

Figure 39: Additional *in organello* monitoring of pH dynamics from different mitochondrial protein-cpYFP fusions. *(continued on next page)*

(Figure 39 continued)
(**A**–**H**) CpYFP mitochondria-based protein sublocalisation assays monitoring pH dynamics in mitochondria isolated from wild-type Arabidopsis plants stably expressing different mitochondrial proteins fused to cpYFP. Left y-axis: fluorescence intensities while exciting at 400 nm (grey dots) or 482 nm (black dots). Right y-axis: normalised $\log_{10}$ ratios (482 nm/400 nm; white dots). Increase or decrease of ratio indicates more alkaline or more acidic pH, respectively. For quantification see Figure 38. All traces: $n \geq 3$, mean + SD. Black bars at the bottom of the graphs indicate addition of 10 mM succinate + 250 µM ATP (succ), 10 µM carbonyl cyanide m-chlorophenylhydrazone (CCCP) or 50 µM nigericin + 10 µM valinomycin (nig-val). Note that emission gain was adjusted between experiments and fluorescence intensities (left-axes) are not directly comparable.

3.6.4 Quantitative CLSM analyses and protease protection assays support IMS localisation for dLDH

The pH-based protein topology approach provided a means to differentiate between matrix and IMS, but failed to provide a clear distinction between IMS and cytosolic side of the OMM. To complement this shortcoming, a combination of quantitative CLSM analysis and protease protection assay was applied on an exemplary set of mitochondrially targeted proteins fused to reporter proteins. dLDH was used as a candidate protein to obtain proof-of-principle for the approach. To enhance the signal-to-noise ratio which was not ideal for cpYFP outside the matrix, dLDH was fused to the reporter protein roGFP2 (here simply used as fluorescent marker; referred to as dLDH-GFP). Consistent with the observations for dLDH-cpYFP (Figure 36), the fluorescence consistently labelled small, round–elongated subcellular structures. Co-localisation with MitoTracker Orange confirmed mitochondrial localisation but exhibited obvious differences in shape compared to the GFP signal. MitoTracker Orange revealed a typical spot-like signal with highest intensities in the centre, whereas GFP exhibited halo-like structures (Figure 40A). To quantitatively assess the different fluorescent shapes, a recently developed method to quantify averaged fluorescence distributions across individual mitochondria was employed (Wagner et al., 2015a). Magnified confocal images of MitoTracker stained mitochondria from different lines were recorded for that purpose (Figure 40B). In a next step, averaged MitoTracker and GFP signal intensity distributions across mitochondria were captured and quantified. The comparison of dLDH-GFP to the reference lines mts-GFP (mitochondrial matrix) and NMT1-GFP (OMM facing cytosol) revealed comparable MitoTracker signals, indicating that expression of dLDH-GFP did not alter mitochondrial shape in any obvious manner (Figure 40B). Conversely, the GFP signals differed among the

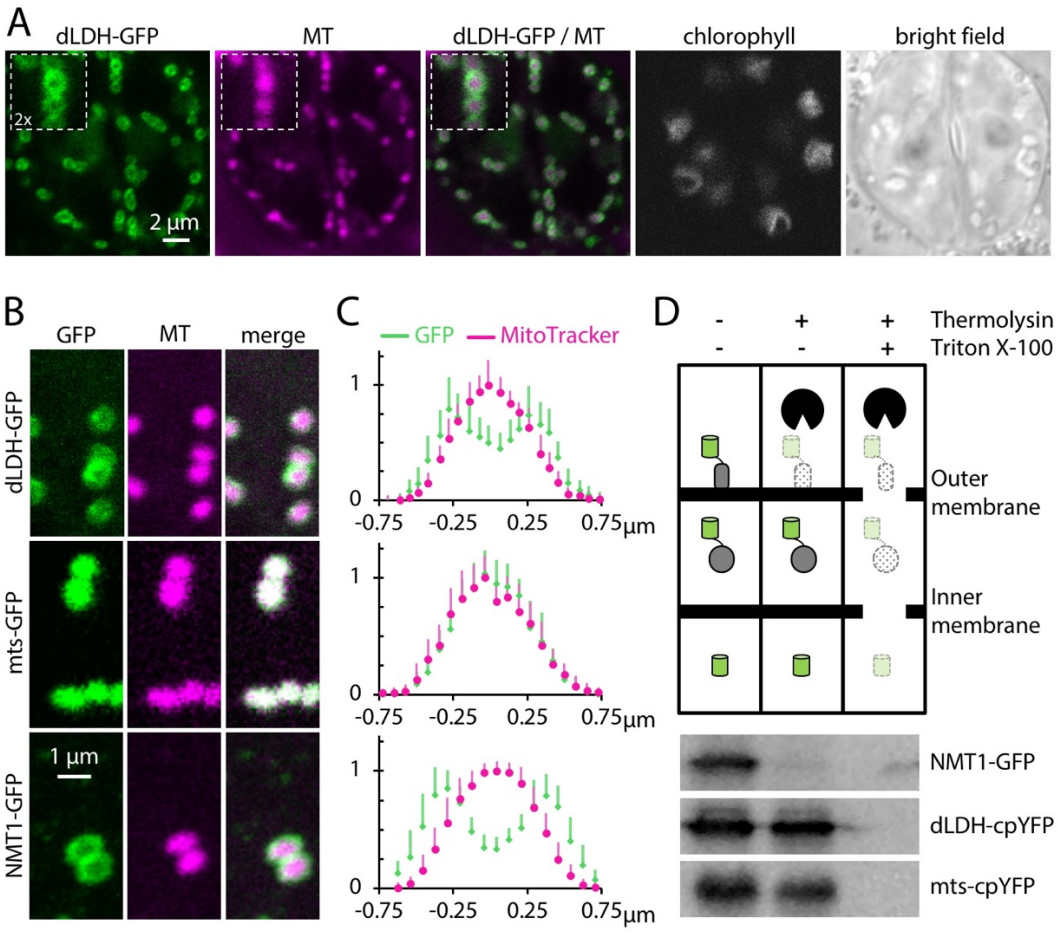

Figure 40: Quantitative analysis of submitochondrial localisation of Arabidopsis dLDH.
Modified figure published in Welchen et al., 2016.
(**A**) Arabidopsis seedlings stably expressing D-Lactate dehydrogenase fused to N-terminus of GFP (LDH-GFP) and stained with MitoTracker Orange were imaged by CLSM. Representative images are shown for two guard cells of an Arabidopsis leaf. GFP: green, MitoTracker (MT): magenta, chlorophyll: white. Insets: 2-fold magnification from centre top part of images. (**B**) CLSM images from Arabidopsis seedlings stably expressing dLDH-GFP (top row), *Nicotiana plumbaginifolia* β-ATPase mitochondrial presequence fused to GFP (mts-GFP; middle row) and Network1/ELM1 fused to GFP (NMT1-GFP; bottom row) and stained with MitoTracker Orange. mts-GFP and NMT1-GFP were used as markers for the mitochondrial matrix and outer mitochondrial membrane, respectively. GFP: green, MitoTracker: magenta. (**C**) Normalised pixel intensity distributions in the GFP and MitoTracker channels plotted centrally across, and averaged over, individual mitochondria. $n \geq 15$, mean + SD. (**D**) Protease protection analysis by GFP immunodetection after thermolysin treatment of intact, purified mitochondria expressing GFP or YFP fusions of the proteins used in (B) and (C) in the absence and presence of 0.1% (v/v) Triton X-100 to disrupt mitochondrial membranes. The experiment was repeated three times with consistent results.

lines. dLDH exhibited an intermediate GFP distribution signature to those observed for mts-GFP and NMT1-GFP, suggesting localisation to the IMS rather than to the OMM. The exclusion of the OMM localisation was independently verified using a protease protection assay. Freshly purified mitochondria were subjected to different protease treatments. Subsequently, degradation of the protein of interest fused to the fluorescent reporter protein was analysed by Western blotting using a GFP antibody. The addition of thermolysin to intact mitochondria (> 90% according to Cytochrome *c* latency assays; performed according to Sweetlove et al., 2002) degraded NMT1-GFP, whereas dLDH-cpYFP and mts-cpYFP were unaffected by the treatment (Figure 40D). In contrast, addition of thermolysin supplemented with triton to disrupt the mitochondrial membranes resulted in the degradation of the fluorescent proteins in all cases. Recapitulating the findings, quantitative CLSM image analysis and the protease protection assay conclusively argue against a localisation of dLDH to the cytosolic side of the OMM. The *in organello* plate reader-based fluorimetry data on dLDH further evidence localisation outside of the mitochondrial matrix. Accordingly, dLDH is most likely targeted to the IMS of mitochondria, which is supported by biochemical evidence from interaction assays demonstrating that dLDH can function as a substrate of Cytochrome *c* (Engqvist et al., 2009).

3.6.5 CLSM-based measurements reveal an *in vivo* pH gradient of 0.4 units across the inner mitochondrial membrane

The connection between mitochondrial energy metabolism and pH as a component of the Δp is evident. Yet, relatively little is known about *in vivo* plant mitochondrial pH gradients, and the current understanding is almost exclusively based on isolated organelles. Thus, the successful targeting of the cpYFP pH sensor to the IMS was exploited to investigate *in vivo* plant submitochondrial pH gradients.

Seedlings of the Arabidopsis cpYFP pH sensor lines mts-cpYFP (matrix), dLDH-cpYFP (IMS) and cyt-cpYFP (cytosol) were grown in parallel for 7 days on standard agar plates. When subjected to confocal microscopy, notably different cpYFP fluorescence intensities and signal-to-noise ratios were observed for the three selected lines (Figure 41 and Figure 37) (signal-to-noise ratios: mts-cpYFP > cyt-cpYFP > dLDH-cpYFP). Although cpYFP is ratiometric, which facilitates the comparison of different lines, low or strongly

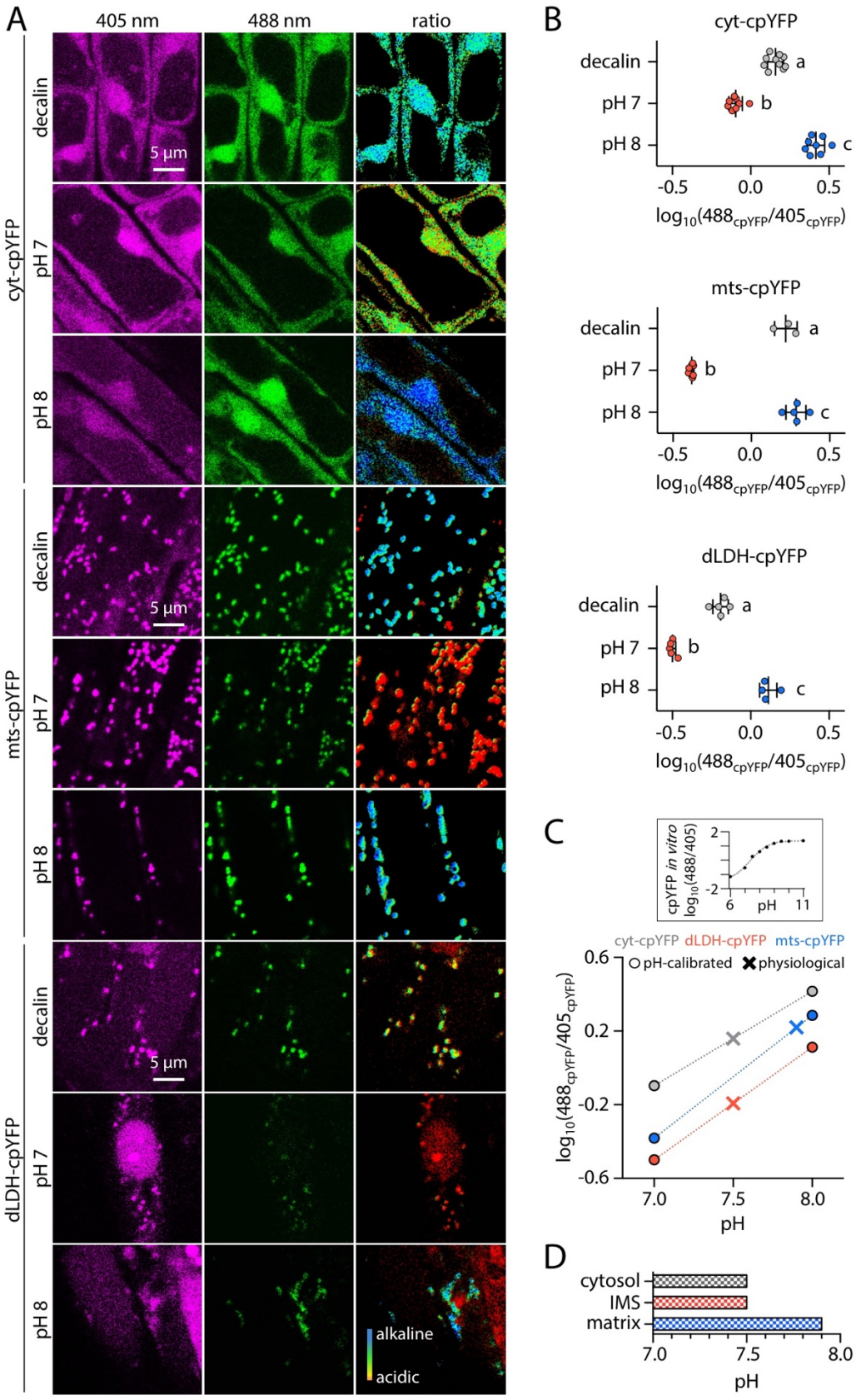
A
405 nm
488 nm
ratio
cyt-cpYFP
mts-cpYFP
dLDH-cpYFP
decalin
pH 7
pH 8
5 µm
alkaline
acidic
B
cyt-cpYFP
mts-cpYFP
dLDH-cpYFP
a
b
c
-0.5
0.0
0.5
log10(488cpYFP/405cpYFP)
C
cpYFP in vitro log10(488/405)
pH
cyt-cpYFP dLDH-cpYFP mts-cpYFP
pH-calibrated
physiological
log10(488cpYFP/405cpYFP)
7.0
7.5
8.0
D
cytosol
IMS
matrix

Figure 41: CLSM-based i*n vivo* measurements of mitochondrial matrix, intermembrane space and cytosol pH in Arabidopsis seedlings using the cpYFP pH biosensor.
(**A**) Representative CLSM images of root tips of 7-d-old Arabidopsis seedlings expressing cpYFP in the mitochondrial matrix (mts-cpYFP), intermembrane space (dLDH-cpYFP) or in the cytosol (cyt-cpYFP). Seedlings were incubated 30 min in pH-adjusted (pH 7 or 8) assay medium (10 mM MES pH 5.8, 5 mM KCl, 10 mM $MgCl_2$, 10 mM $CaCl_2$) supplemented with 100 µM CCCP for pH calibration prior mounting on microscope. For physiological measurements, untreated seedlings were mounted directly in perfluorodecalin (decalin). Magenta: cpYFP excited at 405 nm, green: cpYFP excited at 488 nm. False-colour images (ratio) depict the cpYFP emission intensity ratio. High cpYFP ratios indicate more alkaline pH and are shown in blue whereas low ratios are shown in red. (**B**) Quantification of cpYFP ratio for lines and treatments described in (A). Higher and lower ratios indicate more alkaline or more acidic pH, respectively. $n \geq 3$ biological replicates. Different letters indicate significant differences according to one-way ANOVA with Tukey's multiple comparisons test ($P < 0.01$). (**C**) Mean $\log_{10}$ cpYFP ratio values from (B) with linear curve fitted between pH 7 and 8 for individual Arabidopsis lines. Inset on the top: $\log_{10}$-transformed cpYFP ratios in dependence of ambient pH (retrieved from Schwarzländer et al., 2011). (**D**) Summary of apparent pH for individual subcompartments after correction with pH calibration and curve fitting described in (C).

varying signal-to-noise ratios might restrict the direct comparability between lines. To account for potential artefacts resulting from this, the lines were two-step pH calibrated. The seedlings were incubated in assay medium with pH adjusted to 7.0 or 8.0 for 30 min. To remove interfering subcellular proton gradients, the incubation media were additionally supplemented with 100 µM of the ionophore carbonyl cyanide m-chlorophenyl hydrazone (CCCP). The seedlings were mounted in the corresponding incubation medium and confocal images of the root tips of the seedlings recorded (Figure 41A). For the non-pH equilibrated, physiological measurements, images were acquired with identical settings of root tips of seedlings mounted in perfluorodecalin, a non-fluorescent, chemically and biologically inert imaging fluid (Littlejohn et al., 2014). Subsequent ratiometric image analysis demonstrated different cpYFP ratio values among the pH-equilibrated lines (Figure 41B), indicating that the lines cannot be directly compared. Thus, cpYFP values recorded under physiological conditions were corrected based on the pH equilibration. *In vitro* cpYFP ratio changes of recombinant cpYFP exhibited a largely linear response of the ($\log_{10}$) cpYFP ratio in the pH range of 7.0–8.0 (Figure 41C) (Schwarzländer et al., 2014). Therefore, a linear function seemed a reasonable approximation to interpolate cpYFP ratios for pH values within this range. The mean values from the physiological cpYFP measurements were inserted into the linear function equations derived from the pH calibrations (Figure 41C). The correspondingly estimated pH values were 7.9 for the

mitochondrial matrix, 7.5 for the IMS and 7.5 for the cytosol, suggesting a pH difference of 0.4 units across the IMM (Figure 41D).

3.6.6 Discussion

The *in organello* plate reader-based fluorimetry assay and the quantitative CLSM and/or protease protection analyses (Figure 40) together constitute a novel approach to pinpoint subcellular localisations of mitochondrial proteins fused to cpYFP. Specifically, the combination of the different experimental approaches provided strong evidence for the IMS sublocalisation of dLDH (Figure 38, Figure 41), which was exploited in the subsequent step to quantify in Arabidopsis seedlings *in vivo* the pH in the mitochondrial matrix, the IMS and the cytosol (Figure 42). Based on the pH calibrations, a pH difference of 0.4 units was calculated between the IMS and the more alkaline mitochondrial matrix. This represent the first report to describe *in planta* measurements of the IMS pH and is concordant to previous estimation deduced from isolated mitochondria (Moore et al., 1978).

3.6.6.1 Sublocalising mitochondrial proteins with cpYFP

In theory, fusion of a protein to cpYFP and conductance of the here presented sublocalisation experiments should allow to assign the submitochondrial localisation of any given mitochondrial protein. The preliminary data indicate limitations which restrict this approach (1) to the ability to successfully fuse, transform and express the protein of interest, (2) and by the need to control for potential miss-targeting:

(1) About 50% of the attempted candidate-protein fusions revealed insufficient or no cpYFP fluorescence upon stable transformation into Arabidopsis (Supplemental Figure 2). Several possible reasons are conceivable, such as a deleterious effect due to overexpression of a catalytically active protein or failure of import caused by the masking of import signature and subsequent proteasomal degradation. It is interesting that fusions of cpYFP to small IMS proteins, such as Adenylate Kinase 1 (AK1), Cytochrome *c* 1 or 2 (CYT*c*1), (CYT*c*2) or Translocase of the Inner mitochondrial Membrane 9 (TIM9) (all < 13 kDa), all failed to report detectable cpYFP fluorescence (Supplemental Figure 2). Possibly, fusions of cpYFP (27.7 kDa) to the tail of these comparatively small proteins might interfere with plant mitochondrial IMS targeting.

(2) The fusion of cpYFP might lead to mistargeting or incomplete membrane integration of the endogenous protein. In contradiction to the IMS prediction, the C-terminally fused cpYFP of CLS1 and the mitochondrial carrier proteins DIC2 and UCP1 appeared matrix exposed (Figure 40). The extent to which this implies mistargeting remains difficult to assess, mainly due to the lack of robust empirical data on the mitochondrial sublocalisation of the aforementioned proteins in Arabidopsis. CLS1 was reported to localise to the IMM in cucumber, mung beans and Arabidopsis (Douce et al., 1972; Frentzen and Griebau, 1994; Pan et al., 2014), but the topology has not been conclusively addressed yet. The C-terminus of DIC2 and UCP1 was predicted to be exposed to the IMS according to sequence homologies to the bovine ADP/ATP carrier sequence (Pebay-Peyroula et al., 2003; Palmieri et al., 2008; Haferkamp and Schmitz-Esser, 2012; Crichton et al., 2017), but have not yet been empirically investigated in plants. Thus, the evaluation of mistargeting remains challenging and requires additional, orthogonal techniques (*e.g.* immunogold labelling) to verify the robustness of sublocalisation determination by this assay.

3.6.6.2 pH gradients across the inner mitochondrial membrane

The observed ΔpH of 0.4 across the IMM (Figure 42) is similar to findings in two independent studies measuring *in vivo* pH gradients in mitochondria of human HeLa cells. Comparison of pH values in the mitochondrial matrix and cytosol with the pH biosensor EYFP revealed a pH gradient of 0.5 units (Llopis et al., 1998). In the second study, the pH in the mitochondrial matrix and the cytosol was monitored in parallel employing the biosensor SypHer and the pH-sensitive dye SNARF, respectively. The combination revealed a pH difference of 0.45 units between the two compartments (Poburko et al., 2011). Furthermore, the ΔpH between the mitochondrial matrix and the IMS observed in this study is in line with *in vitro* measurements on plant mitochondria, reporting a ΔpH of 0.40 and 0.35 for purified mung bean and arum spadix mitochondria (Moore et al., 1978). The consistency between the *in organello* and *in vivo* observations is noteworthily high, even though it was shown that the composition of the incubation medium has a direct influence on ΔpH (Schwarzländer et al., 2012). The here presented data suggest that the *in organello* studies represented *in planta* conditions reasonably well.

3.6.6.3 Additional pH differences between and within mitochondrial compartments

In contrast to the ΔpH across the IMM, the proton concentration in the IMS equalled that of the cytosol. This is in line with the general assumption that the OMM does not constitute a diffusional barrier to protons. However, this is contradicted by the measurements in human ECV304 cells with the EYFP pH sensors, suggesting a ΔpH of 0.7 across the OMM (Porcelli et al., 2005). The discrepancy might indicate (1) a genuine ΔpH across the OMM that might be dependent on the specific conditions and cell types or/and (2) that EYFP was specifically targeted to IMS subcompartments with lower pH differences, *i.e.* cristal IMS, which would then be interpreted as a ΔpH across the OMM.

(1) The presence of a ΔpH across the OMM seems counterintuitive given the extremely high abundance of voltage-dependent anion channels (VDACs) (Figure 3), which render the OMM permeable to solutes smaller than ~5000 Da (Werkheiser and Bartley, 1957; Colombini, 1980) (section 1.4.1). The VDAC permeability depends on the assumed functional state of the pore. Membrane voltage and additional post-translational modifications were shown to affect VDAC selectivity and conductance, which can vary between anion-selective to cation-selective and from open to half-open, respectively (Moran et al., 1992; Bera and Ghosh, 2001; Pavlov et al., 2005). Hypothetically, the motion of charged substrates combined with pore selectivity and mitochondrial metabolism could result in a notable potential. Further speculating, such a potential should be balanced by the highly mobile protons and could result in a small pH gradient across the OMM. As a note on the side, such a ΔΨ for the OMM would be compatible with the *in vitro* observed ΔΨ-dependent activity of VDACs (Colombini, 2004). Investigations on the IMS pH from isolated rat liver mitochondria support this hypothesis. For rat mitochondria in the condensed form (large IMS), the pH of the IMS was reported to amount to 0.4–0.5 units more negative than the pH of the resuspension medium. Conversely, the pH was similar in the IMS and resuspension medium for mitochondria in the orthodox state (small IMS) (Cortese et al., 1992). The extent to which such a ΔpH across the OMM is transferable to *in vivo* situations is unclear. The findings from Porcelli et al. (2005) suggest this gradient might also exist *in vivo*, but it has not been further investigated nor addressed in plant mitochondria.

(2) Different pH values could also be accounted for by differences between the peripheral and cristal IMS. As introduced earlier, both membrane architecture and

heterogeneous distribution of mitochondrial ETC complexes are hypothesised to restrict proton diffusion and to give rise to pH microcompartments, which indeed have been observed *in vivo* (Rieger et al., 2014). It should be noted that evidences supporting microcompartmentation have exclusively been generated based on animal mitochondria (Gilkerson et al., 2003; Strauss et al., 2008; Rieger et al., 2014). In contrast to the often tubular or shelf-like mitochondrial cristae frequently observed in animal tissues (Lea and Hollenberg, 1989; Picard et al., 2015; Brandt et al., 2017), plant mitochondrial cristae appear generally more saccular and less regularly shaped (Parsons et al., 1965). Whether plant mitochondrial ultrastructure allows pH microcompartmentation to a similar degree or whether it favours a more homogenous pH within the IMS remains an open question. It will be exciting to compare lines with cpYFP targeted to different IMS compartments, *e.g.* cpYFP attached to subunit of complex I (CI P2-cpYFP) representing the cristal IMS *versus* cpYFP attached to the translocase apparatus (TIM17-3) representing the peripheral IMS to address this matter.

4 DISCUSSION

4.1 The electron pathway between thiols and the mitochondrial ETC

The exposure of uncoupling mutants to the unspecific thiol-reductant, DTT, led to strong phenotypic impairments of root growth (Figure 26–Figure 28). This was unexpected since there is no known pathway supporting suitable fluxes to connect thiol redox biochemistry and mitochondrial ETC redox biochemistry. An exception to this is the above discussed MIA40-ERV1 disulfide relay system located in the mitochondrial IMS (section 3.5.6.2), which has been shown *in vitro* to supply at low flux electrons to Cytochrome *c* (Bihlmaier et al., 2007; Peleh et al., 2017). In contrast to an electron pathway from thiol molecules to the mitochondrial ETC, an oxidising influence on the thiol redox homeostasis has typically been ascribed to the mitochondrial ETC through its ability to generate reactive oxygen species (ROS) (Miwa and Brand, 2003; Dröse et al., 2014; Bleier et al., 2015). The rate of ROS production in the form of single electron reduction of molecular oxygen to superoxide increases with membrane potential and limitation of electron transport rate (Murphy, 2009). Vice versa, a minor decrease of the Δp by mild uncoupling was shown to dramatically reduce the mitochondrial ETC-mediated ROS production (Miwa and Brand, 2003). Disrupting the uncoupling capacity in plants by genetically interfering with UCP and AOX was also suggested to increase ROS production, in particular under stress (Giraud et al., 2008; Smith et al., 2004, 2009; Barreto et al., 2014, 2017). In that context DTT may be expected to provide additional reducing power to the ROS scavenging systems, such as the thiol-based peroxidases, to restore the redox balance in the uncoupling mutants. In contrast with this hypothesis, the growth of mutants restricted in mitochondrial uncoupling was strongly inhibited in presence of DTT (Figure 27, Figure 28), suggesting the requirement of active uncoupling to combat DTT-induced reductive stress. The ability of mitochondria to use DTT-derived electrons as respiratory substrate is strongly supported by the *in organello* experiments (section 3.5), which clearly showed electron flux from DTT to oxygen via the ETC.

Those observations point to a novel pathway that enables mitochondria to respire on thiol-based reductant (Figure 42). Under reductant excess, flexible engagement of mitochondrial uncoupling then serves to avoid thiol redox-mediated dysregulation and

malfunctioning. When uncoupling capacity is restricted, dissipation of excess reductant remains inefficient and gives rise to cellular over-reduction and consequentially to the disruption of essential processes in which maintenance of thiol oxidation is critical. A potential candidate for such a process is oxidative protein folding in the ER. Cellular over-reduction due to restricted uncoupling may disturb the oxidising environment in the ER and block the oxidative formation of disulfide bonds, analogously to the well-described induction of reductive ER-stress by DTT (Martínez and Chrispeels, 2003; Iwata et al., 2008; Pérez-Martín et al., 2014). This results in the accumulation of un- and misfolded proteins in the ER and triggers downstream mechanisms — commonly referred to as unfolded protein response (UPR) — to reinstall homeostasis of protein synthesis. Sustained ER-stress may damage the ER, but also other organelles and under extreme conditions lead to cell death (Howell, 2013; Wan and Jiang, 2016).

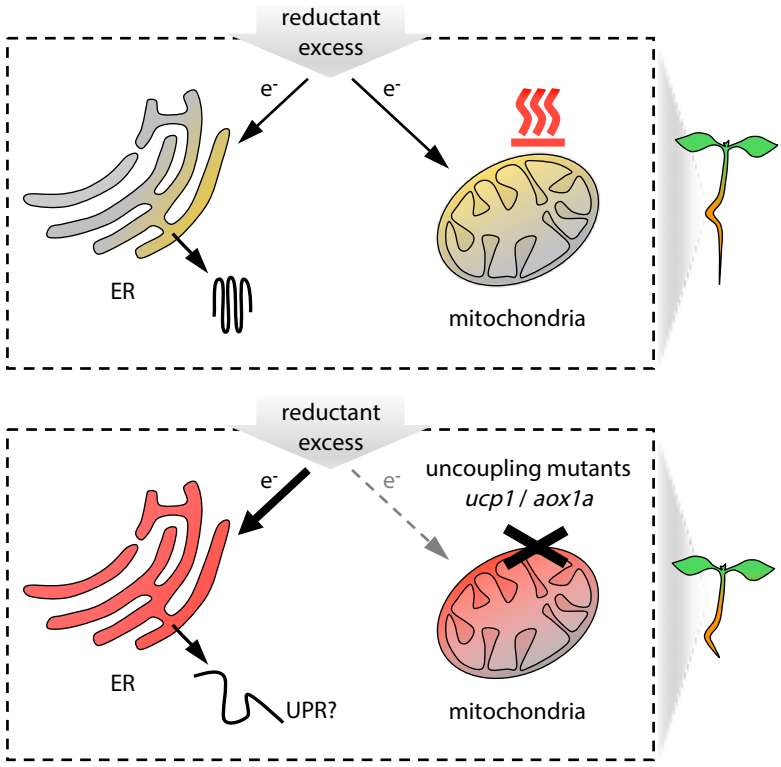

Figure 42: Hypothetical model of how mitochondrial uncoupling may prevent reductive stress and counteract reductive ER-stress.
Top panel: reductant excess is actively dissipated in mitochondria by flexible uncoupling of respiration from oxidative phosphorylation in wild-type (see section 1.5 for details). Bottom panel: decreased mitochondrial uncoupling capacity, *e.g.* lack of functional UCP1 or AOX1a, disables efficient dissipation of excess reductant, leading to reducing ER-stress and unfolded protein response (UPR).

Conceptually the here presented model (Figure 42) expands the current view of mitochondria as cellular safe-guards against stress-induced metabolic over-reduction (*e.g.* balancing photosynthesis-associated reductant excess), by a link to thiol redox metabolism, potentially associated with ER function.

4.2 The effects of restricted uncoupling capacity on shoot and root

Light energy absorbed by the photosynthetic machinery needs to be carefully balanced to meet, but not to exceed, the cellular demand of metabolic reductant. Decreasing demands due to restricted carbon assimilation rates under drought and sustained irradiance require swift metabolic adjustments to avoid photoinhibition and damage arising from over-reduction (section 1.2). In line with previous reports, the triple mutant *ucp1 ucp3 aox1a* showed decreased tolerance to combined treatment of drought and moderate light stress (Figure 16) (Sweetlove et al., 2006; Giraud et al., 2008; Kühn et al., 2015), however, the changes were relatively minor compared to the reported response of *aox1a* to the same treatment (Giraud et al., 2008; Kühn et al., 2015). The absence of a more pronounced phenotypic response to the treatments points towards a high resilience of the redox network in leaves (section 1.2) (Scheibe et al., 2005; Kramer and Evans, 2011; Taniguchi and Miyake, 2012) and indicates that limitations of those systems occur under very specific conditions only.

Interestingly it was previously observed that the DTT-treatment of leaf discs from WT plants elicits a highly similar gene expression pattern to that observed for leaves of *aox1a* plants exposed to the treatment of combined drought and moderate light stress. Although this correlation had been lacking any mechanistic explanation, it is in line with the findings of this work, suggesting that DTT can be used to mimic the reductive stress effect of the combined drought and light stress treatment (Kolbe et al., 2006; Giraud et al., 2008, 2012). The exposure of *aox1a* to the combined drought and moderate light stress treatment induced increased anthocyanin accumulation compared to the WT plants (Giraud et al., 2008; Kühn et al., 2015), which was not observed, however, for *aox1a* plants exposed to DTT on plates (Figure 27, Figure 28). The fact that shoots of WT and uncoupling mutant seedlings were indistinguishable under DTT is in line with a robust redox network in leaves. That contrasts with the roots, where the inhibitory effect of DTT-treatment impacts strongly on growth (Figure 27, Figure 28).

What might be the reason for the tissue-specific role of mitochondrial uncoupling in DTT-based reductive stress tolerance? It should be considered that roots are more directly exposed to DTT in the agar plate-based phenotyping assays (Figure 26–Figure 28). However, the replacement of DTT with tunicamycin strongly impairs not only root but also shoot growth (Figure 29), indicating that the absence of shoot impairments under DTT may be accounted for by additional aspects. A major difference between roots and shoots lies in the absence or presence of chloroplasts, respectively. The additional presence of chloroplasts extends the cellular metabolic flexibility in two ways: Chloroplasts are equipped with endogenous energy dissipating systems and might, in parallel to mitochondria, contribute to the removal of excess reductant. Although the *in organello* assays focussed on mitochondria, it is tempting to speculate that thiol-based reducing agents might also transfer electrons to the chloroplast. For instance, thiol-based reducing agents might pass electrons via an unknown mechanism to the plastoquinone pool. Plastoquinol can then be oxidised by the plastoquinol oxidase, dissipating the redox potential as heat by transferring electrons onto molecular oxygen in an analogous manner to the function of AOX in the mitochondrial ETC (Houille-Vernes et al., 2011; Fu et al., 2012; Laureau et al., 2013). It would be interesting to conduct cpYFP-based pH gradient measurements on isolated chloroplasts using the same approach as for mitochondria (Figure 31) to investigate whether thiol-based reductant can also relay electrons to the photosynthetic ETC. Interestingly, treatment of oleander leaves with DTT led to a strong decrease of photon-use efficiency whilst the capacity of photosynthetic O_2 evolution was little affected (Winter and Königer, 1989). This indicates that the photosynthetic apparatus was not *per se* impaired, but that the activity of chloroplast and cellular reductant dissipating systems were increased. Apart from dissipating energy directly, chloroplasts may also improve resilience towards reductive stress by improving metabolic redox buffering, reshuffling and dissipating excess reductant (Scheibe and Dietz, 2012; Tikkanen and Aro, 2014).

In plants, reductive stress is commonly associated to photosynthetically active tissues. This may be met by more resilient mechanisms of dissipating excess reductant, which is in line with the higher DTT tolerance of shoot compared to root tissues. Although roots might not be naturally exposed to reductive stress of the extent as reached by the DTT treatments in this study, they offer an excellent system to dissect redox homeostasis *in*

planta. The decreased complexity due to the absence of chloroplasts, and the clearly quantifiable growth response render roots an effective experimental model to assess the impact of mitochondria on cellular redox homeostasis. Furthermore, the low autofluorescence and high cell permeability makes the root outer tissue layers favourable for fluorescent biosensor-based imaging and efficient pharmaceutical manipulations (Figure 41). For instance, roGFP-based monitoring of E_{GSH} is a promising approach to investigate the role of mitochondria in balancing cellular redox homeostasis. It will be interesting to compare re-oxidation rates of E_{GSH} upon DTT treatment in WT against uncoupling mutants or in plants subjected to mitochondrial ETC inhibitors to assess the redox-balancing role of mitochondria. Those measurements are planned as a follow-up experiment.

4.3 The impact of reductive stress on roots

The *in organello* assays demonstrated a mitochondrial oxidation of thiol-based reducing agents coupled to the ETC (section 3.5). Thus, mitochondrial uncoupling in seedlings presumably allowed the dissipation of excess DTT reductant and counteracted toxicity by over-reduction of endogenous thiol redox systems (Figure 42). Conversely, restricted uncoupling in the mutants led to more severe reductive stress which likely includes the ER as a key site of DTT stress, due to the relatively oxidised steady state of the thiol redox systems in this compartment. Support for ER-stress as the cause of reduced root growth comes from tunicamycin treated seedlings, which also show a reduced primary growth similar to that observed for the uncoupling mutants when exposed to DTT (Supplemental Figure 2) (Ruberti and Brandizzi, 2018) In contrast to the DTT-treatment, uncoupling mutants are phenotypically indistinguishable from WT plants under tunicamycin treatments, supporting the hypothesis that mitochondria are working upstream to protect from reductive ER-stress (Figure 42). Tissue-specific occurrence of ER-stress is supported by the expression pattern of Binding Protein 3 (BiP3), a well-established ER-stress marker (Cho and Kanehara, 2017). The authors used fluorescent reporter lines and immunofluorescence analyses, which revealed that tunicamycin treatments induce expression of BiP3 specifically in root tips, in the outer cell layer of the maturation and in the inner cell layer of the mature zone in roots. Notably, the spatial induction of BiP3 expression overlaps with the location of the apical meristem and also the pericycle cells,

which can initiate lateral root formation (De Smet et al., 2007). Noteworthy, gene expression of UCP1 and AOX1a is generally higher in these tissues compared to other parts of the roots (Brady et al., 2007). The reductive stress treatment might impair root growth by causing ER-stress across tissues and specifically in the areas of active primary and lateral root growth. It will be interesting to compare the degree of ER stress and unfolded protein response induced by DTT in the WT and uncoupling mutant seedlings to investigate whether the level of induction correlates with the observed phenotypes.

Another speculative mechanism by which DTT exposure might influence root growth is by reducing the quiescent centre. Quiescent centre cells were reported to be comparatively oxidised and metabolically inactive relative to active cells (Jiang et al., 2003, 2006). It was reasoned that the development of the root apical meristem is under redox control and oxidation was reported to slow down cell cycles of quiescent centre cells (De Tullio, 2009). In agreement with the concept of oxidised quiescent centre cells, there is particularly high expression of UCP1 and AOX1a in the apical meristem cells (~16-fold higher than in neighbouring cells; Brady et al., 2007), which could contribute to the maintenance of an oxidised environment. If mitochondrial uncoupling capacity is restricted, DTT (or other thiol-based reductants) might not be efficiently oxidised and could lead to a reductive 'over-activation' of the quiescent centre cells. This could rapidly deplete the initial cells and thereby arrest primary root growth. Yet, such a redox regulation of the apical meristem remains to be convincingly shown and does not satisfyingly explain the lack of lateral root formation at high DTT concentrations in the case of *aox1a*.

4.4 Regulation of the oxidation of thiol-based reductant at the ETC

Thiol-based reductant, such as glutathione, can be oxidised and electrons respired via the mitochondrial ETC (Figure 31). Arabidopsis mitochondrial glutathione concentrations are estimated to range in similar concentrations (~6–10 mM; see section 3.5.6 for details) as applied in the *in organello* assays (10 mM) (Meyer et al., 2001; Krueger et al., 2009; Zechmann et al., 2008; Queval et al., 2011). This suggests that GSH oxidation via the ETC can also take place *in vivo*. Accordingly, the question arises on how oxidation might be regulated to prevent excessive electron drain, which would cause oxidation of the thiol pools and potentially oxidative stress. The concept of electron transfer

from thiols to the ETC is newly explored in this thesis and no regulatory mechanism can be pinpointed yet.

At first glance, the oxidation of thiols such as GSH via the ETC seems a wasteful process since it would require a steady input of electrons to re-reduce disulfide bonds to maintain a physiological redox potential. Thus, a tightly controlled pathway would be expected. However, the pathway might be less strictly regulated when taking the following aspects into consideration. Firstly, apart from the observed thiol oxidation (section 3.5), mitochondria are also a major provider of NADPH, which serves as electron source for the redox machinery to reduce thiols. Secondly, transfer of electrons derived from thiols at the ETC can be coupled to proton translocation (Figure 31) and thereby to ATP synthesis. From a thermodynamic perspective, supplying electrons directly to the ETC or via the thiol/disulfide pool detour is indistinguishable. Thus, oxidation of thiols via the ETC might not require strict regulation, but may constitute a steady sink, which is counterbalanced by the input of electrons derived from metabolic reactions. Continuous thiol oxidation by the ETC may offer several advantages. For instance, the ability to flexibly and safely dissipate excess reductant via mitochondrial uncoupling components appears central and is supported by the phenotyping experiments (section 3.4). Consistently diverting a part of the electron flux into the thiol/disulfide pools before eventually ending up at the ETC would also provide an elegant mechanism to synchronise the flux through individual metabolic pathways with the redox properties of a cell compartment. Redox regulation of mitochondrial processes has been proposed several years ago and several mitochondrial proteins have been identified to be subject of redox regulation since (Balmer et al., 2004; Yoshida et al., 2013; Schmidtmann et al., 2014; Daloso et al., 2015). Regulatory disulfides can be reduced via the NADPH-NTR-TRX pathway (Balmer et al., 2004; Daloso et al., 2015), but how exactly re-oxidation of these thiol-switches is achieved and regulated is not fully understood. Thiol oxidation coupled to the ETC offers a potential mechanism. Under conditions of limited metabolic reductant supply, sustained thiol oxidation by mitochondrial ETC activity would dominate over re-reduction, which would trigger increased thiol oxidation and may allow direct adjustment of metabolic fluxes by redox-regulation. An alternative concept has very recently been proposed for the redox-regulation of chloroplast metabolism. It was shown that 2-Cysteine Peroxiredoxin (2-CysPrx) mediates the rapid oxidative inactivation of reductively activated proteins in the chloroplast

stroma and thereby secures efficient regulation of photosynthesis (Vaseghi et al., 2018). Although similar, the proposed 2-CysPrx system in chloroplasts differs in two key aspects from the oxidation coupled to the mitochondrial ETC. Firstly, ETC-coupled oxidation can be used to drive the phosphorylation of ADP, whereas the 2-CysPrx system is non-energy-conserving. Secondly, oxidation at the ETC relies on O_2 as an electron sink, which is usually available in unlimited amounts. In contrast, the 2-CysPrx system was suggested to use H_2O_2 as an electron acceptor (Vaseghi et al., 2018), the concentration of which in the cell is likely to be variable, and potentially even limiting, depending on conditions. Notably, a protein of the Peroxiredoxin family (PRX IIF) is also localised to the mitochondrial matrix, but in contrast to the 2-CysPrx, PRX IIF seems predominantly involved in peroxide reduction (Gama et al., 2007; Barranco-Medina et al., 2008).

Altogether, the ability to oxidise thiols via the ETC can protect from cellular over-reduction by mitochondrial uncoupling and thereby mediate dissipation of excess reductant (Figure 42). Potential regulation/restriction of thiol oxidation by the ETC remains to be addressed in future. Conceptually, the pathway could constitute a mechanism to re-oxidise thiol-switched proteins, and actively synchronise metabolic fluxes with the current reductant status.

4.5 Effects of the ETC on the local redox states

Theoretically, the capability of the mitochondrial ETC to oxidise thiols could give rise to locally distinct redox potentials of subcellular thiol redox pools. However, discriminate oxidation of the IMS compartment is unlikely since the OMM was found to allow rapid equilibration of the IMS with the cytosolic glutathione pool in yeast (Kojer et al., 2012). Nonetheless, redox state gradients on a smaller scale within the IMS cannot be excluded. Redox states measurements in HeLa cells with cytosol-targeted GRX1-roGFP2 or attached to the cytosolic side of intracellular vesicles reported a more oxidised E_{GSH} at the surface of intracellular vesicles (Δ 77 mV) (Hatori et al., 2018). Although the cause for the apparent oxidative influence at the surface of the vesicles is unclear and the observation remains to be independently confirmed, it suggests that even in the absence of bulk phase differences, redox gradients on a nano-scale may exist. It would be interesting to investigate whether the oxidative influence of the ETC, via ROS production (Murphy, 2009) and thiol oxidation as suggested in this work, gives rise to a detectable more oxidised E_{GSH} at the IMM

surface. Corresponding measurements have not been reported and may constitute interesting future research. Fusing the redox-sensor roGFP2 to mitochondrial candidate proteins successfully characterised in section 3.6 could help to address this question. It seems conceivable that mitochondrial microsubcompartments, similar to the observations for pH in HeLa mitochondria (Rieger et al., 2014), might also exist for redox potentials of micropools of glutathione and other thiol compounds. Noteworthy, pH has a relatively large impact on the redox potential of thiols by increasing the standard potential by 5.9 mV per 0.1 pH unit. The findings of the pH difference of 0.4 units across the IMM *in vivo* (Figure 41) imply that the standard potential in the mitochondrial matrix is decreased by about 24 mV for thiol/disulfide redox reactions, which is in line with the more negative *in vivo* E_{GSH} reported for the mitochondrial matrix than the cytosol of Arabidopsis epidermis cells (Schwarzländer et al., 2008). Accordingly, alkalinisation of compartments can give rise to more reactive thiol pools, which conceivably affects redox-regulated enzymes and might also favour the observed thiol oxidation by the mitochondrial ETC (section 3.5). Changes in pH, resulting from alterations of mitochondrial activity, cytosolic pH changes or pulsing of individual mitochondria, that is a transient decrease of membrane potential and a counter-increased pH gradient (Schwarzländer et al., 2012), might constitute a mechanism to fine-tune redox-reactions. The extent by which pH affects redox-reactions in the mitochondria and the degree this is of physiological significance represent exciting questions and open possibilities for the future.

4.6 Conclusion

This thesis provides empirical evidence for a degree of functional redundancy between the proteins of the AOX and UCP families. While plants with restricted mitochondrial uncoupling tolerated the combination of drought and moderate light stress comparatively well, root growth of both *ucp1* and *aox1a* was strongly impaired under reductive stress mediated by DTT. Further investigations reveal a hitherto unknown functional role of small thiol molecules to act as substrate for the mitochondrial ETC. The oxidation can be coupled to the generation of chemiosmotic potential and subsequent ATP synthesis, whereas under conditions of excess reductant uncoupled mitochondrial electron transport allows safe electron disposal to secure cellular redox homeostasis. Furthermore, targeting the cpYFP pH sensor to different mitochondrial compartments enabled *in vivo* measurements of pH gradients and revealed a pH difference of 0.4 units between the mitochondrial matrix and the IMS.

5 REFERENCES

Affourtit, C. and Brand, M.D. (2008). Uncoupling protein-2 contributes significantly to high mitochondrial proton leak in INS-1E insulinoma cells and attenuates glucose-stimulated insulin secretion. Biochem. J. 409: 199–204.

Alberts, B., Johnson, A., Lewis, J., Raff, M., Roberts, K. and Walter, P. (2002). Molecular Biology of the Cell: The mitochondrion (4th ed). New York: Garland Science.

Albrecht, S.C., Sobotta, M.C., Bausewein, D., Aller, I., Hell, R., Dick, T.P. and Meyer, A.J. (2014). Redesign of genetically encoded biosensors for monitoring mitochondrial redox status in a broad range of model eukaryotes. J. Biomol. Screen. 19: 379–386.

Aller, I., Rouhier, N. and Meyer, A.J. (2013). Development of roGFP2-derived redox probes for measurement of the glutathione redox potential in the cytosol of severely glutathione-deficient *rml1* seedlings. Front. Plant Sci. 4: 506.

Andersson, B. and Aro, E.M. (2001). Regulation of photosynthesis: Photodamage and D1 protein turnover in photosystem II. Dordrecht: Springer, 377–393.

Aranda, P.S., LaJoie, D.M. and Jorcyk, C.L. (2012). Bleach gel: a simple agarose gel for analyzing RNA quality. Electrophoresis 33: 366–369.

Araújo, W.L., Nunes-Nesi, A. and Fernie, A.R. (2014). On the role of plant mitochondrial metabolism and its impact on photosynthesis in both optimal and sub-optimal growth conditions. Photosynth. Res. 119: 141–156.

Arimura, S., Fujimoto, M., Doniwa, Y., Kadoya, N., Nakazono, M., Sakamoto, W. and Tsutsumi, N. (2008). Arabidopsis elongated mitochondria 1 is required for localization of dynamin-related protein 3a to mitochondrial fission sites. Plant Cell 20: 1555–1566.

Arkblad, E.L., Egorov, M., Shakhparonov, M., Romanova, L., Polzikov, M. and Rydström, J. (2002). Expression of proton-pumping nicotinamide nucleotide transhydrogenase in mouse, human brain and *C. elegans*. Comp. Biochem. Physiol. Biochem. Mol. Biol. 133: 13–21.

Arsenijevic, D. et al. (2000). Disruption of the uncoupling protein-2 gene in mice reveals a role in immunity and reactive oxygen species production. Nat. Genet. 26: 435–439.

Atkin, O.K. and Macherel, D. (2009). The crucial role of plant mitochondria in orchestrating drought tolerance. Ann. Bot. 103: 581–597.

Attacha, S., Solbach, D., Bela, K., Moseler, A., Wagner, S., Schwarzländer, M., Aller, I., Müller, S.J. and Meyer, A.J. (2017). Glutathione peroxidase-like enzymes cover five distinct cell compartments and membrane surfaces in *Arabidopsis thaliana*. Plant Cell Environ. 40: 1281–1295.

Bailleul, B. et al. (2015). Energetic coupling between plastids and mitochondria drives CO_2 assimilation in diatoms. Nature 524: 366–369.

Balmer, Y., Vensel, W.H., Tanaka, C.K., Hurkman, W.J., Gelhaye, E., Rouhier, N., Jacquot, J.P., Manieri, W., Schürmann, P., Droux, M. and Buchanan, B.B. (2004). Thioredoxin links redox to the regulation of fundamental processes of plant mitochondria. Proc. Natl. Acad. Sci. 101: 2642–2647.

Baracca, A., Sgarbi, G., Solaini, G. and Lenaz, G. (2003). Rhodamine 123 as a probe of mitochondrial membrane potential: evaluation of proton flux through F_0 during ATP synthesis. Biochim. Biophys. Acta 1606: 137–146.

Barranco-Medina, S., Krell, T., Bernier-Villamor, L., Sevilla, F., Lázaro, J.J. and Dietz, K.J. (2008). Hexameric oligomerization of mitochondrial peroxiredoxin PrxIIF and formation of an ultrahigh affinity complex with its electron donor thioredoxin Trx-o. J. Exp. Bot. 59: 3259–3269.

Barratt, D.H.P., Derbyshire, P., Findlay, K., Pike, M., Wellner, N., Lunn, J., Feil, R., Simpson, C., Maule, A.J. and Smith, A.M. (2009). Normal growth of Arabidopsis requires cytosolic invertase but not sucrose synthase. Proc. Natl. Acad. Sci. 106: 13124–13129.

Barreto, P., Okura, V.K., Neshich, I.A.P., Maia, I. G. and Arruda, P. (2014). Overexpression of UCP1 in tobacco induces mitochondrial biogenesis and amplifies a broad stress response. BMC Plant Biol. 14: 144.

Barreto, P., Yassitepe, J.E.C.T., Wilson, Z.A. and Arruda, P. (2017). Mitochondrial uncoupling protein 1 overexpression increases yield in *Nicotiana tabacum* under drought stress by improving source and sink metabolism. Front. Plant Sci. 8: 1836.

Bartoli, C.G., Gomez, F., Gergoff, G., Guiamét, J.J. and Puntarulo, S. (2005). Up-regulation of the mitochondrial alternative oxidase pathway enhances photosynthetic electron transport under drought conditions. J. Exp. Bot. 56: 1269–1276.

Bauwe, H., Hagemann, M. and Fernie, A.R. (2010). Photorespiration: players, partners and origin. Trends Plant Sci. 15: 330–336.

Bayrhuber, M., Meins, T., Habeck, M., Becker, S., Giller, K., Villinger, S., Vonrhein, C., Griesinger, C., Zweckstetter, M. and Zeth, K. (2008). Structure of the human voltage-dependent anion channel. Proc. Natl. Acad. Sci. 105: 15370–15375.

Beardsell, M.F. and Cohen, D. (1975). Relationships between leaf water status, abscisic acid levels, and stomatal resistance in maize and sorghum. Plant Physiol. 56: 207–212.

Begcy, K., Mariano, E.D., Mattiello, L., Nunes, A.V., Mazzafera, P., Maia, I.G. and Menossi, M. (2011). An Arabidopsis mitochondrial uncoupling protein confers tolerance to drought and salt stress in transgenic tobacco plants. PloS One 6: e23776.

Bera, A.K. and Ghosh, S. (2001). Dual mode of gating of voltage-dependent anion channel as revealed by phosphorylation. J. Struct. Biol. 135: 67–72.

Berardi, M.J. and Chou, J.J. (2014). Fatty acid flippase activity of UCP2 is essential for its proton transport in mitochondria. Cell Metab. 20: 541–552.

Bertani, G. (1951). Studies on lysogenesis. The mode of phage liberation by lysogenic *Escherichia coli*. J. Bacteriol. 62: 293–300.

Bieniawska, Z., Paul Barratt, D.H., Garlick, A.P., Thole, V., Kruger, N.J., Martin, C., Zrenner, R. and Smith, A.M. (2007). Analysis of the sucrose synthase gene family in Arabidopsis. Plant J. 49: 810–828.

Bihlmaier, K., Mesecke, N., Terziyska, N., Bien, M., Hell, K. and Herrmann, J.M. (2007). The disulfide relay system of mitochondria is connected to the respiratory chain. J. Cell Biol. 179: 389–395.

Bleier, L., Wittig, I., Heide, H., Steger, M., Brandt, U. and Dröse, S. (2015). Generator-specific targets of mitochondrial reactive oxygen species. Free Radic. Biol. Med. 78: 1–10.

Borecký, J., Maia, I.G., Costa, A.D., Ježek, P., Chaimovich, H., de Andrade, P.B., Vercesi, A.E. and Arruda, P. (2001). Functional reconstitution of *Arabidopsis thaliana* plant uncoupling mitochondrial protein (*At*PUMP1) expressed in *Escherichia coli*. FEBS Lett. 505: 240–244.

Borecký, J., Nogueira, F.T.S., de Oliveira, K.A.P., Maia, I.G., Vercesi, A.E. and Arruda, P. (2006). The plant energy-dissipating mitochondrial systems: depicting the genomic structure and the expression profiles of the gene families of uncoupling protein and alternative oxidase in monocots and dicots. J. Exp. Bot. 57: 849–864.

Borecký, J. and Vercesi, A.E. (2005). Plant uncoupling mitochondrial protein and alternative oxidase: energy metabolism and stress. Biosci. Rep. 25: 271–286.

Böttinger, L., Gornicka, A., Czerwik, T., Bragoszewski, P., Loniewska-Lwowska, A., Schulze-Specking, A., Truscott, K.N., Guiard, B., Milenkovic, D. and Chacinska, A. (2012). *In vivo* evidence for cooperation of Mia40 and Erv1 in the oxidation of mitochondrial proteins. Mol. Biol. Cell 23: 3957–3969.

Bouillaud, F., Weissenbach, J. and Ricquier, D. (1986). Complete cDNA-derived amino acid sequence of rat brown fat uncoupling protein. J. Biol. Chem. 261: 1487–1490.

Boyer, J.S. (2015). Turgor and the transport of CO_2 and water across the cuticle (epidermis) of leaves. J. Exp. Bot. 66: 2625–2633.

Brach, T., Soyk, S., Müller, C., Hinz, G., Hell, R., Brandizzi, F. and Meyer, A.J. (2009). Non-invasive topology analysis of membrane proteins in the secretory pathway. Plant J. 57: 534–541.

Bradford, M.M. (1976). A rapid and sensitive method for the quantitation of microgram quantities of protein utilizing the principle of protein-dye binding. Anal. Biochem. 72: 248–254.

Brady, S.M., Orlando, D.A., Lee, J.Y., Wang, J.Y., Koch, J., Dinneny, J.R., Mace, D., Ohler, U. and Benfey, P.N. (2007). A high-resolution root spatiotemporal map reveals dominant expression patterns. Science 318: 801–806.

Bragoszewski, P., Wasilewski, M., Sakowska, P., Gornicka, A., Böttinger, L., Qiu, J., Wiedemann, N. and Chacinska, A. (2015). Retro-translocation of mitochondrial intermembrane space proteins. Proc. Natl. Acad. Sci. 112: 7713–7718.

Brand, M.D. and Esteves, T.C. (2005). Physiological functions of the mitochondrial uncoupling proteins UCP2 and UCP3. Cell Metab. 2: 85–93.

Brand, M.D., Pakay, J.L., Ocloo, A., Kokoszka, J., Wallace, D.C., Brookes, P.S. and Cornwall, E.J. (2005). The basal proton conductance of mitochondria depends on adenine nucleotide translocase content. Biochem. J. 392: 353–362.

Brandt, T., Mourier, A., Tain, L.S., Partridge, L., Larsson, N.G. and Kühlbrandt, W. (2017). Changes of mitochondrial ultrastructure and function during ageing in mice and Drosophila. eLife 6: e24662.

Braun, H.P. et al. (in preparation). Single organelle function estimated from Arabidopsis mitochondrial proteomics.

Brossa, R., Pintó-Marijuan, M., Jiang, K., Alegre, L. and Feldman, L.J. (2013). Assessing the regulation of leaf redox status under water stress conditions in *Arabidopsis thaliana*. Plant Signal. Behav. 8: e24781.

Brugière, S., Kowalski, S., Ferro, M., Seigneurin-Berny, D., Miras, S., Salvi, D., Ravanel, S., d'Hérin, P., Garin, J., Bourguignon, J., Joyard, J. and Rolland, N. (2004). The hydrophobic proteome of mitochondrial membranes from Arabidopsis cell suspensions. Phytochemistry 65: 1693–1707.

Bustin, S.A., Benes, V., Garson, J.A., Hellemans, J., Huggett, J., Kubista, M., Mueller, R., Nolan, T., Pfaffl, M.W., Shipley, G.L., Vandesompele, J. and Wittwer, C.T. (2009). The MIQE guidelines: minimum information for publication of quantitative real-time PCR experiments. Clin. Chem. 55: 611–622.

Bykova, N.V., Keerberg, O., Pärnik, T., Bauwe, H. and Gardeström, P. (2005). Interaction between photorespiration and respiration in transgenic potato plants with antisense reduction in glycine decarboxylase. Planta 222: 130–140.

Carr, P.D., Verger, D., Ashton, A.R. and Ollis, D.L. (1999). Chloroplast NADP-malate dehydrogenase: structural basis of light-dependent regulation of activity by thiol oxidation and reduction. Structure 7: 461–475.

Chigri, F., Flosdorff, S., Pilz, S., Kölle, E., Dolze, E., Gietl, C. and Vothknecht, U.C. (2012). The Arabidopsis calmodulin-like proteins *At*CML30 and *At*CML3 are targeted to mitochondria and peroxisomes, respectively. Plant Mol. Biol. 78: 211–222.

Cho, Y. and Kanehara, K. (2017). Endoplasmic reticulum stress response in Arabidopsis roots. Front. Plant Sci. 8: 144.

Chrobok, D. et al. (2016). Dissecting the metabolic role of mitochondria during developmental leaf senescence. Plant Physiol. 172: 2132–2153.

Claeys, H., Van Landeghem, S., Dubois, M., Maleux, K. and Inzé, D. (2014). What is stress? Dose-response effects in commonly used *in vitro* stress assays. Plant Physiol. 165: 519–527.

Clark, R.T., Famoso, A.N., Zhao, K., Shaff, J.E., Craft, E.J., Bustamante, C.D., Mccouch, S.R., Aneshansley, D.J. and Kochian, L.V. (2013). High-throughput two-dimensional root system phenotyping platform facilitates genetic analysis of root growth and development. Plant Cell Environ. 36: 454–466.

Clarke, D.M. and Bragg, P.D. (1985). Cloning and expression of the transhydrogenase gene of *Escherichia coli*. J. Bacteriol. 162: 367–373.

Clarkson, A.B., Bienen, E.J., Pollakis, G. and Grady, R.W. (1989). Respiration of bloodstream forms of the parasite *Trypanosoma brucei brucei* is dependent on a plant-like alternative oxidase. J. Biol. Chem. 264: 17770–17776.

Clifton, R., Lister, R., Parker, K.L., Sappl, P.G., Elhafez, D., Millar, A.H., Day, D.A. and Whelan, J. (2005). Stress-induced co-expression of alternative respiratory chain components in *Arabidopsis thaliana*. Plant Mol. Biol. 58: 193–212.

Clifton, R., Millar, A.H. and Whelan, J. (2006). Alternative oxidases in Arabidopsis: a comparative analysis of differential expression in the gene family provides new insights into function of non-phosphorylating bypasses. Biochim. Biophys. Acta 1757: 730–741.

Clough, S.J. and Bent, A.F. (1998). Floral dip: a simplified method for *Agrobacterium*-mediated transformation of *Arabidopsis thaliana*. Plant J. 16: 735–743.

Colombini, M. (1980). Structure and mode of action of a voltage dependent anion-selective channel (VDAC) located in the outer mitochondrial membrane. Ann. N. Y. Acad. Sci. 341: 552–563.

Colombini, M. (2004). VDAC: the channel at the interface between mitochondria and the cytosol. Mol. Cell. Biochem. 256–257: 107–115.

Considine, M.J., Goodman, M., Echtay, K.S., Laloi, M., Whelan, J., Brand, M.D. and Sweetlove, L.J. (2003). Superoxide stimulates a proton leak in potato mitochondria that is related to the activity of uncoupling protein. J. Biol. Chem. 278: 22298–22302.

Considine, M.J., Holtzapffel, R.C., Day, D.A., Whelan, J. and Millar, A.H. (2002). Molecular distinction between alternative oxidase from monocots and dicots. Plant Physiol. 129: 949–953.

Cornic, G. and Fresneau, C. (2002). Photosynthetic carbon reduction and carbon oxidation cycles are the main electron sinks for photosystem II activity during a mild drought. Ann. Bot. 89: 887–894.

Cortese, J.D., Voglino, A.L. and Hackenbrock, C.R. (1995). Persistence of cytochrome *c* binding to membranes at physiological mitochondrial intermembrane space ionic strength. Biochim. Biophys. Acta 1228: 216–228.

Cortese, J.D., Voglino, A.L. and Hackenbrock, C.R. (1992). The ionic strength of the intermembrane space of intact mitochondria is not affected by the pH or volume of the intermembrane space. Biochim. Biophys. Acta 1100: 189–197.

Costa, J.H., McDonald, A.E., Arnholdt-Schmitt, B. and Fernandes de Melo, D. (2014). A classification scheme for alternative oxidases reveals the taxonomic distribution and evolutionary history of the enzyme in angiosperms. Mitochondrion 19: 172–183.

Crichton, P.G., Lee, Y. and Kunji, E.R.S. (2017). The molecular features of uncoupling protein 1 support a conventional mitochondrial carrier-like mechanism. Biochimie 134: 35–50.

Cronan, J.E. (2014). Biotin and lipoic acid: synthesis, attachment and regulation. EcoSal Plus 6.

Czechowski, T., Stitt, M., Altmann, T., Udvardi, M.K. and Scheible, W.R. (2005). Genome-wide identification and testing of superior reference genes for transcript normalization in Arabidopsis. Plant Physiol. 139: 5–17.

Dai, A. (2013). Increasing drought under global warming in observations and models. Nat. Clim. Change 3: 52–58.

Daloso, D.M. et al. (2015). Thioredoxin, a master regulator of the tricarboxylic acid cycle in plant mitochondria. Proc. Natl. Acad. Sci. 112: 1392–1400.

Davies, K.M., Anselmi, C., Wittig, I., Faraldo-Gómez, J.D. and Kühlbrandt, W. (2012). Structure of the yeast F_1F_0-ATP synthase dimer and its role in shaping the mitochondrial cristae. Proc. Natl. Acad. Sci. 109: 13602–13607.

De Col, V. et al. (2017). ATP sensing in living plant cells reveals tissue gradients and stress dynamics of energy physiology. eLife 6: e26770.

De Smet, I. et al. (2007). Auxin-dependent regulation of lateral root positioning in the basal meristem of Arabidopsis. Development 134: 681–690.

De Smet, I. et al. (2008). Receptor-like kinase ACR4 restricts formative cell divisions in the Arabidopsis root. Science 322: 594–597.

De Tullio, M.C., Jiang, K. and Feldman, L.J. (2010). Redox regulation of root apical meristem organization: connecting root development to its environment. Plant Physiol. Biochem. 48: 328–336.

Deblaere, R., Bytebier, B., De Greve, H., Deboeck, F., Schell, J., Van Montagu, M. and Leemans, J. (1985). Efficient octopine Ti plasmid-derived vectors for *Agrobacterium*-mediated gene transfer to plants. Nucleic Acids Res. 13: 4777–4788.

Dietz, K.J. and Heber, U. (1983). Carbon dioxide gas exchange and the energy status of leaves of *Primula palinuri* under water stress. Planta 158: 349–356.

Dixon, D.P., Skipsey, M., Grundy, N.M. and Edwards, R. (2005). Stress-induced protein S-glutathionylation in Arabidopsis. Plant Physiol. 138: 2233–2244.

Dooley, C.T., Dore, T.M., Hanson, G.T., Jackson, W.C., Remington, S.J. and Tsien, R.Y. (2004). Imaging dynamic redox changes in mammalian cells with green fluorescent protein indicators. J. Biol. Chem. 279: 22284–22293.

Dorman, D.C., Moulin, F.J.M., McManus, B.E., Mahle, K.C., James, R.A. and Struve, M.F. (2002). Cytochrome oxidase inhibition induced by acute hydrogen sulfide inhalation: correlation with tissue sulfide concentrations in the rat brain, liver, lung, and nasal epithelium. Toxicol. Sci. Off. J. Soc. Toxicol. 65: 18–25.

Douce, R., Mannella, C.A. and Bonner, W.D. (1972). Site of the biosynthesis of CDP-diglyceride in plant mitochondria. Biochem. Biophys. Res. Commun. 49: 1504–1509.

Dröse, S., Brandt, U. and Wittig, I. (2014). Mitochondrial respiratory chain complexes as sources and targets of thiol-based redox-regulation. Biochim. Biophys. Acta 1844: 1344–1354.

Dubreuil-Maurizi, C., Vitecek, J., Marty, L., Branciard, L., Frettinger, P., Wendehenne, D., Meyer, A.J., Mauch, F. and Poinssot, B. (2011). Glutathione deficiency of the Arabidopsis mutant *pad2-1* affects oxidative stress-related events, defense gene expression, and the hypersensitive response. Plant Physiol. 157: 2000–2012.

Duncan, O., Taylor, N.L., Carrie, C., Eubel, H., Kubiszewski-Jakubiak, S., Zhang, B., Narsai, R., Millar, A.H. and Whelan, J. (2011). Multiple lines of evidence localize signaling, morphology, and lipid biosynthesis machinery to the mitochondrial outer membrane of Arabidopsis. Plant Physiol. 157: 1093–1113.

Edgar, R.C. (2004). MUSCLE: multiple sequence alignment with high accuracy and high throughput. Nucleic Acids Res. 32: 1792–1797.

Edwards, K., Johnstone, C. and Thompson, C. (1991). A simple and rapid method for the preparation of plant genomic DNA for PCR analysis. Nucleic Acids Res. 19: 1349.

El Zawily, A.M. et al. (2014). FRIENDLY regulates mitochondrial distribution, fusion, and quality control in Arabidopsis. Plant Physiol. 166: 808–828.

Elhafez, D., Murcha, M.W., Clifton, R., Soole, K.L., Day, D.A. and Whelan, J. (2006). Characterization of mitochondrial alternative NAD(P)H dehydrogenases in Arabidopsis: intraorganelle location and expression. Plant Cell Physiol. 47: 43–54.

Emaus, R.K., Grunwald, R. and Lemasters, J.J. (1986). Rhodamine 123 as a probe of transmembrane potential in isolated rat-liver mitochondria: spectral and metabolic properties. Biochim. Biophys. Acta 850: 436–448.

Enerbäck, S., Jacobsson, A., Simpson, E.M., Guerra, C., Yamashita, H., Harper, M.E. and Kozak, L.P. (1997). Mice lacking mitochondrial uncoupling protein are cold-sensitive but not obese. Nature 387: 90–94.

Engqvist, M., Drincovich, M.F., Flügge, U.I. and Maurino, V.G. (2009). Two D-2-hydroxy-acid dehydrogenases in *Arabidopsis thaliana* with catalytic capacities to participate in the last reactions of the methylglyoxal and beta-oxidation pathways. J. Biol. Chem. 284: 25026–25037.

Escobar, M.A., Geisler, D.A. and Rasmusson, A.G. (2006). Reorganization of the alternative pathways of the Arabidopsis respiratory chain by nitrogen supply: opposing effects of ammonium and nitrate. Plant J. 45: 775–788.

Estabrook, R.W. (1967). Methods in enzymology: Mitochondrial respiratory control and the polarographic measurement of ADP:O ratios. Academic press, 41–47.

Ezeriņa, D., Takano, Y., Hanaoka, K., Urano, Y. and Dick, T.P. (2018). N-acetyl cysteine functions as a fast-acting antioxidant by triggering intracellular H_2S and sulfane sulfur production. Cell Chem. Biol. 25: 447-459.

Fiorani, F., Umbach, A.L. and Siedow, J.N. (2005). The alternative oxidase of plant mitochondria is involved in the acclimation of shoot growth at low temperature. A study of Arabidopsis AOX1a transgenic plants. Plant Physiol. 139: 1795–1805.

Flexas, J., Bota, J., Loreto, F., Cornic, G. and Sharkey, T.D. (2004). Diffusive and metabolic limitations to photosynthesis under drought and salinity in C_3 plants. Plant Biol. 6: 269–279.

Frentzen, M. and Griebau, R. (1994). Biosynthesis of cardiolipin in plant mitochondria. Plant Physiol. 106: 1527–1532.

Friedrich, T., Steinmüller, K. and Weiss, H. (1995). The proton-pumping respiratory complex I of bacteria and mitochondria and its homologue in chloroplasts. FEBS Lett. 367: 107–111.

Fu, A., Liu, H., Yu, F., Kambakam, S., Luan, S. and Rodermel, S. (2012). Alternative oxidases (AOX1a and AOX2) can functionally substitute for plastid terminal oxidase in Arabidopsis chloroplasts. Plant Cell 24: 1579–1595.

Gama, F., Keech, O., Eymery, F., Finkemeier, I., Gelhaye, E., Gardeström, P., Dietz, K.J., Rey, P., Jacquot, J.P. and Rouhier, N. (2007). The mitochondrial type II peroxiredoxin from poplar. Physiol. Plant. 129: 196–206.

Gandin, A., Duffes, C., Day, D.A. and Cousins, A.B. (2012). The absence of alternative oxidase AOX1A results in altered response of photosynthetic carbon assimilation to increasing CO_2 in *Arabidopsis thaliana*. Plant Cell Physiol. 53: 1627–1637.

Gautheron, D.C. (1984). Mitochondrial oxidative phosphorylation and respiratory chain. J. Inherit. Metab. Dis. 7: 57–61.

Geisler, D.A., Broselid, C., Hederstedt, L. and Rasmusson, A.G. (2007). Ca^{2+}-binding and Ca^{2+}-independent respiratory NADH and NADPH dehydrogenases of *Arabidopsis thaliana*. J. Biol. Chem. 282: 28455–28464.

Gilkerson, R.W., Selker, J.M.L. and Capaldi, R.A. (2003). The cristal membrane of mitochondria is the principal site of oxidative phosphorylation. FEBS Lett. 546: 355–358.

Giraud, E., Ho, L.H.M., Clifton, R., Carroll, A., Estavillo, G., Tan, Y.F., Howell, K.A., Ivanova, A., Pogson, B.J., Millar, A.H. and Whelan, J. (2008). The absence of Alternative Oxidase 1a in *Arabidopsis thaliana* results in acute sensitivity to combined light and drought stress. Plant Physiol. 147: 595–610.

Giraud, E., Van Aken, O., Uggalla, V. and Whelan, J. (2012). REDOX regulation of mitochondrial function in plants. Plant Cell Environ. 35: 271–280.

Golozoubova, V., Hohtola, E., Matthias, A., Jacobsson, A., Cannon, B. and Nedergaard, J. (2001). Only UCP1 can mediate adaptive nonshivering thermogenesis in the cold. FASEB J. Off. Publ. Fed. Am. Soc. Exp. Biol. 15: 2048–2050.

Grabelnych, O.I., Borovik, O.A., Tauson, E.L., Pobezhimova, T.P., Katyshev, A.I., Pavlovskaya, N.S., Koroleva, N.A., Lyubushkina, I.V., Bashmakov, V.Y., Popov, V.N., Borovskii, G.B. and Voinikov, V.K. (2014). Mitochondrial energy-dissipating systems (alternative oxidase, uncoupling proteins, and external NADH dehydrogenase) are involved in development of frost-resistance of winter wheat seedlings. Biochem. 79: 506–519.

Grefen, C., Donald, N., Hashimoto, K., Kudla, J., Schumacher, K. and Blatt, M.R. (2010). A ubiquitin-10 promoter-based vector set for fluorescent protein tagging facilitates temporal stability and native protein distribution in transient and stable expression studies. Plant J. 64: 355–365.

Gupte, S., Wu, E.S., Hoechli, L., Hoechli, M., Jacobson, K., Sowers, A.E. and Hackenbrock, C.R. (1984). Relationship between lateral diffusion, collision frequency, and electron transfer of mitochondrial inner membrane oxidation-reduction components. Proc. Natl. Acad. Sci. 81: 2606–2610.

Hackenbrock, C.R. (1966). Ultrastructural bases for metabolically linked mechanical activity in mitochondria. Reversible ultrastructural changes with change in metabolic steady state in isolated liver mitochondria. J. Cell Biol. 30: 269–297.

Haferkamp, I. and Schmitz-Esser, S. (2012). The plant mitochondrial carrier family: functional and evolutionary aspects. Front. Plant Sci. 3: 2.

Hahn, A., Parey, K., Bublitz, M., Mills, D.J., Zickermann, V., Vonck, J., Kühlbrandt, W. and Meier, T. (2016). Structure of a complete ATP synthase dimer reveals the molecular basis of inner mitochondrial membrane morphology. Mol. Cell 63: 445–456.

Haindrich, A.C., Boudová, M., Vancová, M., Diaz, P.P., Horáková, E. and Lukeš, J. (2017). The intermembrane space protein Erv1 of *Trypanosoma brucei* is essential for mitochondrial Fe-S cluster assembly and operates alone. Mol. Biochem. Parasitol. 214: 47–51.

Hallermayer, G. and Neupert, W. (1974). Lipid composition of mitochondrial outer and inner membranes of *Neurospora crassa*. Hoppe-Seyler's Zeitschr. Physiol. Chem. 355: 279–288.

Hanahan, D. (1983). Studies on transformation of *Escherichia coli* with plasmids. J. Mol. Biol. 166: 557–580.

Hanson, G.T., Aggeler, R., Oglesbee, D., Cannon, M., Capaldi, R.A., Tsien, R.Y. and Remington, S.J. (2004). Investigating mitochondrial redox potential with redox-sensitive green fluorescent protein indicators. J. Biol. Chem. 279: 13044–13053.

Hao, M.S., Jensen, A.M., Boquist, A.S., Liu, Y.J. and Rasmusson, A.G. (2015). The Ca^{2+}-regulation of the mitochondrial external NADPH dehydrogenase in plants is controlled by cytosolic pH. PLoS One 10: e0139224.

Harrison, S.J., Mott, E.K., Parsley, K., Aspinall, S., Gray, J.C. and Cottage, A. (2006). A rapid and robust method of identifying transformed *Arabidopsis thaliana* seedlings following floral dip transformation. Plant Methods 2: 19.

Hartmann, S.K., Stockdreher, Y., Wandrey, G., Hosseinpour Tehrani, H., Zambanini, T., Meyer, A.J., Büchs, J., Blank, L.M., Schwarzländer, M. and Wierckx, N. (2018). Online *in vivo* monitoring of cytosolic NAD redox dynamics in *Ustilago maydis*. Biochim. Biophys. Acta. 1859: 1015–1024.

Heazlewood, J.L., Tonti-Filippini, J.S., Gout, A.M., Day, D.A., Whelan, J. and Millar, A.H. (2004). Experimental analysis of the Arabidopsis mitochondrial proteome highlights signaling and regulatory components, provides assessment of targeting prediction programs, and indicates plant-specific mitochondrial proteins. Plant Cell 16: 241–256.

Hebbelmann, I. et al. (2012). Multiple strategies to prevent oxidative stress in Arabidopsis plants lacking the malate valve enzyme NADP-malate dehydrogenase. J. Exp. Bot. 63: 1445–1459.

Heber, U. (1974). Metabolite exchange between chloroplasts and cytoplasm. Annu. Rev. Plant Physiol. 25: 393–421.

Heber, U., Bligny, R., Streb, P. and Douce, R. (1996). Photorespiration is essential for the protection of the photosynthetic apparatus of C_3 plants against photoinactivation under sunlight. Bot. Acta 109: 307–315.

Hilleary, R., Choi, W.G., Kim, S.H., Lim, S.D. and Gilroy, S. (2018). Sense and sensibility: the use of fluorescent protein-based genetically encoded biosensors in plants. Curr. Opin. Plant Biol. 46: 32–38.

Hodge, T. and Colombini, M. (1997). Regulation of metabolite flux through voltage-gating of VDAC channels. J. Membr. Biol. 157: 271–279.

Holmgren, A. (1979). Thioredoxin catalyzes the reduction of insulin disulfides by dithiothreitol and dihydrolipoamide. J. Biol. Chem. 254: 9627–9632.

Houille-Vernes, L., Rappaport, F., Wollman, F.A., Alric, J. and Johnson, X. (2011). Plastid terminal oxidase 2 (PTOX2) is the major oxidase involved in chlororespiration in *Chlamydomonas*. Proc. Natl. Acad. Sci. 108: 20820–20825.

Howell, S.H. (2013). Endoplasmic reticulum stress responses in plants. Annu. Rev. Plant Biol. 64: 477–499.

Hruz, T., Laule, O., Szabo, G., Wessendorp, F., Bleuler, S., Oertle, L., Widmayer, P., Gruissem, W. and Zimmermann, P. (2008). Genevestigator v3: a reference expression database for the meta-analysis of transcriptomes. Adv. Bioinforma. 2008: 420747.

Huelsenbeck, J.P. and Ronquist, F. (2001). MRBAYES: Bayesian inference of phylogenetic trees. Bioinforma. Oxf. Engl. 17: 754–755.

Hung, Y.P., Albeck, J.G., Tantama, M. and Yellen, G. (2011). Imaging cytosolic NADH-NAD^+ redox state with a genetically encoded fluorescent biosensor. Cell Metab. 14: 545–554.

Hung, Y.P. and Yellen, G. (2014). Live cell imaging of cytosolic NADH-NAD^+ redox state using a genetically encoded fluorescent biosensor. Methods Mol. Biol. 1071: 83–95.

Hurd, T.R., Collins, Y., Abakumova, I., Chouchani, E.T., Baranowski, B., Fearnley, I.M., Prime, T.A., Murphy, M.P. and James, A.M. (2012). Inactivation of pyruvate dehydrogenase kinase 2 by mitochondrial reactive oxygen species. J. Biol. Chem. 287: 35153–35160.

Igamberdiev, A.U., Bykova, N.V. and Gardeström, P. (1997). Involvement of cyanide-resistant and rotenone-insensitive pathways of mitochondrial electron transport during oxidation of glycine in higher plants. FEBS Lett. 412: 265–269.

Igamberdiev, A.U., Bykova, N.V., Lea, P.J. and Gardeström, P. (2001). The role of photorespiration in redox and energy balance of photosynthetic plant cells: a study with a barley mutant deficient in glycine decarboxylase. Physiol. Plant. 111: 427–438.

Igamberdiev, A.U. and Gardeström, P. (2003). Regulation of NAD- and NADP-dependent isocitrate dehydrogenases by reduction levels of pyridine nucleotides in mitochondria and cytosol of pea leaves. Biochim. Biophys. Acta 1606: 117–125.

Imamura, H., Huynh Nhat, K.P., Togawa, H., Saito, K., Iino, R., Kato-Yamada, Y., Nagai, T. and Noji, H. (2009). Visualization of ATP levels inside single living cells with fluorescence resonance energy transfer-based genetically encoded indicators. Proc. Natl. Acad. Sci. 106: 15651–15656.

Ivanova, A., Law, S.R., Narsai, R., Duncan, O., Lee, J.H., Zhang, B., Van Aken, O., Radomiljac, J.D., van der Merwe, M., Yi, K. and Whelan, J. (2014). A functional antagonistic relationship between auxin and mitochondrial retrograde signaling regulates *Alternative Oxidase1a* expression in Arabidopsis. Plant Physiol. 165: 1233–1254.

Iwata, Y., Fedoroff, N.V. and Koizumi, N. (2008). Arabidopsis bZIP60 is a proteolysis-activated transcription factor involved in the endoplasmic reticulum stress response. Plant Cell 20: 3107–3121.

Jans, D.C., Wurm, C.A., Riedel, D., Wenzel, D., Stagge, F., Deckers, M., Rehling, P. and Jakobs, S. (2013). STED super-resolution microscopy reveals an array of MINOS clusters along human mitochondria. Proc. Natl. Acad. Sci. 110: 8936–8941.

Jarmuszkiewicz, W., Almeida, A.M., Sluse-Goffart, C.M., Sluse, F.E. and Vercesi, A.E. (1998). Linoleic acid-induced activity of plant uncoupling mitochondrial protein in purified tomato fruit mitochondria during resting, phosphorylating, and progressively uncoupled respiration. J. Biol. Chem. 273: 34882–34886.

Ježek, P., Costa, A.D.T. and Vercesi, A.E. (1996). Evidence for anion-translocating plant uncoupling mitochondrial protein in potato mitochondria. J. Biol. Chem. 271: 32743–32748.

Jiang, K., Ballinger, T., Li, D., Zhang, S. and Feldman, L. (2006). A role for mitochondria in the establishment and maintenance of the maize root quiescent center. Plant Physiol. 140: 1118–1125.

Jiang, K., Meng, Y.L. and Feldman, L.J. (2003). Quiescent center formation in maize roots is associated with an auxin-regulated oxidizing environment. Dev. Camb. Engl. 130: 1429–1438.

Joseph-Horne, T., Hollomon, D.W. and Wood, P.M. (2001). Fungal respiration: a fusion of standard and alternative components. Biochim. Biophys. Acta 1504: 179–195.

Jubany-Mari, T., Alegre-Batlle, L., Jiang, K. and Feldman, L.J. (2010). Use of a redox-sensing GFP (c-roGFP1) for real-time monitoring of cytosol redox status in *Arabidopsis thaliana* water-stressed plants. FEBS Lett. 584: 889–897.

Kinoshita, H., Nagasaki, J., Yoshikawa, N., Yamamoto, A., Takito, S., Kawasaki, M., Sugiyama, T., Miyake, H., Weber, A.P.M. and Taniguchi, M. (2011). The chloroplastic 2-oxoglutarate/malate transporter has dual function as the malate valve and in carbon/nitrogen metabolism. Plant J. 65: 15–26.

Klingenberg, M. (2008). The ADP and ATP transport in mitochondria and its carrier. Biochim. Biophys. Acta 1778: 1978–2021.

Klodmann, J., Senkler, M., Rode, C. and Braun, H.P. (2011). Defining the protein complex proteome of plant mitochondria. Plant Physiol. 157: 587–598.

Knöpfel, T. (2012). Genetically encoded optical indicators for the analysis of neuronal circuits. Nat. Rev. Neurosci. 13: 687–700.

Kojer, K., Bien, M., Gangel, H., Morgan, B., Dick, T.P. and Riemer, J. (2012). Glutathione redox potential in the mitochondrial intermembrane space is linked to the cytosol and impacts the Mia40 redox state. EMBO J. 31: 3169–3182.

Kolbe, A., Oliver, S.N., Fernie, A.R., Stitt, M., van Dongen, J.T. and Geigenberger, P. (2006). Combined transcript and metabolite profiling of Arabidopsis leaves reveals fundamental effects of the thiol-disulfide status on plant metabolism. Plant Physiol. 141: 412–422.

Kotera, I., Iwasaki, T., Imamura, H., Noji, H. and Nagai, T. (2010). Reversible dimerization of *Aequorea victoria* fluorescent proteins increases the dynamic range of FRET-based indicators. ACS Chem. Biol. 5: 215–222.

Kozaki, A. and Takeba, G. (1996). Photorespiration protects C_3 plants from photooxidation. Nature 384: 557–560.

Kramer, D.M. and Evans, J.R. (2011). The importance of energy balance in improving photosynthetic productivity. Plant Physiol. 155: 70–78.

Krauss, S., Zhang, C.Y. and Lowell, B.B. (2002). A significant portion of mitochondrial proton leak in intact thymocytes depends on expression of UCP2. Proc. Natl. Acad. Sci. 99: 118–122.

Krömer, S. and Heldt, H.W. (1991). On the role of mitochondrial oxidative phosphorylation in photosynthesis metabolism as studied by the effect of oligomycin on photosynthesis in protoplasts and leaves of barley (*Hordeum vulgare*). Plant Physiol. 95: 1270–1276.

Krueger, S., Niehl, A., Lopez Martin, M.C., Steinhauser, D., Donath, A., Hildebrandt, T., Romero, L.C., Hoefgen, R., Gotor, C. and Hesse, H. (2009). Analysis of cytosolic and plastidic serine acetyltransferase mutants and subcellular metabolite distributions suggests interplay of the cellular compartments for cysteine biosynthesis in Arabidopsis. Plant Cell Environ. 32: 349–367.

Kühn, K., Yin, G., Duncan, O., Law, S.R., Kubiszewski-Jakubiak, S., Kaur, P., Meyer, E., Wang, Y., Small, C.C., Giraud, E., Narsai, R. and Whelan, J. (2015). Decreasing electron flux through the cytochrome and/or alternative respiratory pathways triggers common and distinct cellular responses dependent on growth conditions. Plant Physiol. 167: 228–250.

Kwok, K.H.H., Ho, P.W.L., Chu, A.C.Y., Ho, J.W.M., Liu, H.F., Yiu, D.C.W., Chan, K.H., Kung, M.H.W., Ramsden, D.B. and Ho, S.L. (2010). Mitochondrial UCP5 is neuroprotective by preserving mitochondrial membrane potential, ATP levels, and reducing oxidative stress in MPP^+ and dopamine toxicity. Free Radic. Biol. Med. 49: 1023–1035.

Laemmli, U.K. (1970). Cleavage of structural proteins during the assembly of the head of bacteriophage T4. Nature 227: 680–685.

Laloi, C., Rayapuram, N., Chartier, Y., Grienenberger, J.M., Bonnard, G. and Meyer, Y. (2001). Identification and characterization of a mitochondrial thioredoxin system in plants. Proc. Natl. Acad. Sci. 98: 14144–14149.

Laloi, M., Klein, M., Riesmeier, J.W., Müller-Röber, B., Fleury, C., Bouillaud, F. and Ricquier, D. (1997). A plant cold-induced uncoupling protein. Nature 389: 135–136.

Lambers, H., Chapin III, F.S. and Pons, T.L. (2008). Plant Physiological Ecology: Photosynthesis (2nd ed). New York: Springer, 11–99.

Larosa, V., Meneghesso, A., Rocca, N.L., Steinbeck, J., Hippler, M., Szabo, I. and Morosinotto, T. (2018). Mitochondria affects photosynthetic electron transport and photo-sensitivity in a green alga. Plant Physiol. pp.01249.2017.

Laureau, C., Paepe, R.D., Latouche, G., Moreno-Chacón, M., Finazzi, G., Kuntz, M., Cornic, G. and Streb, P. (2013). Plastid terminal oxidase (PTOX) has the potential to act as a safety valve for excess excitation energy in the alpine plant species *Ranunculus glacialis* L. Plant Cell Environ. 36: 1296–1310.

Lawlor, D.W. and Cornic, G. (2002). Photosynthetic carbon assimilation and associated metabolism in relation to water deficits in higher plants. Plant Cell Environ. 25: 275–294.

Lazo, G.R., Stein, P.A. and Ludwig, R.A. (1991). A DNA transformation-competent Arabidopsis genomic library in *Agrobacterium*. Biotechnol. Nat. Publ. Co. 9: 963–967.

Lea, P.J. and Hollenberg, M.J. (1989). Mitochondrial structure revealed by high-resolution scanning electron microscopy. Am. J. Anat. 184: 245–257.

Lesk, C., Rowhani, P. and Ramankutty, N. (2016). Influence of extreme weather disasters on global crop production. Nature 529: 84–87.

Levitan, A., Danon, A. and Lisowsky, T. (2004). Unique features of plant mitochondrial sulfhydryl oxidase. J. Biol. Chem. 279: 20002–20008.

Libiad, M., Yadav, P.K., Vitvitsky, V., Martinov, M. and Banerjee, R. (2014). Organization of the human mitochondrial hydrogen sulfide oxidation pathway. J. Biol. Chem. 289: 30901–30910.

van Lis, R., Mendoza-Hernández, G., Groth, G. and Atteia, A. (2007). New insights into the unique structure of the F_0F_1-ATP synthase from the Chlamydomonad algae *Polytomella* sp. and *Chlamydomonas reinhardtii*. Plant Physiol. 144: 1190–1199.

Lister, R., Chew, O., Lee, M.N., Heazlewood, J.L., Clifton, R., Parker, K.L., Millar, A.H. and Whelan, J. (2004). A transcriptomic and proteomic characterization of the Arabidopsis mitochondrial protein import apparatus and its response to mitochondrial dysfunction. Plant Physiol. 134: 777–789.

Lister, R., Mowday, B., Whelan, J. and Millar, A.H. (2002). Zinc-dependent intermembrane space proteins stimulate import of carrier proteins into plant mitochondria. Plant J. 30: 555–566.

Littlejohn, G.R., Mansfield, J.C., Christmas, J.T., Witterick, E., Fricker, M.D., Grant, M.R., Smirnoff, N., Everson, R.M., Moger, J. and Love, J. (2014). An update: improvements in imaging perfluorocarbon-mounted plant leaves with implications for studies of plant pathology, physiology, development and cell biology. Front. Plant Sci. 5: 140.

Liu, J.X., Srivastava, R., Che, P. and Howell, S.H. (2007). An endoplasmic reticulum stress response in Arabidopsis is mediated by proteolytic processing and nuclear relocation of a membrane-associated transcription factor, bZIP28. Plant Cell 19: 4111–4119.

Llopis, J., McCaffery, J.M., Miyawaki, A., Farquhar, M.G. and Tsien, R.Y. (1998). Measurement of cytosolic, mitochondrial, and Golgi pH in single living cells with green fluorescent proteins. Proc. Natl. Acad. Sci. 95: 6803–6808.

Luévano-Martínez, L.A. (2012). Uncoupling proteins (UCP) in unicellular eukaryotes: true UCPs or UCP1-like acting proteins? FEBS Lett. 586: 1073–1078.

Maia, I.G., Benedetti, C.E., Leite, A., Turcinelli, S.R., Vercesi, A.E. and Arruda, P. (1998). *AtPUMP*: an Arabidopsis gene encoding a plant uncoupling mitochondrial protein. FEBS Lett. 429: 403–406.

Mannella, C.A. and Bonner, W.D. (1975). X-ray diffraction from oriented outer mitochondrial membranes: detection of in-plane subunit structure. Biochim. Biophys. Acta 413: 226–233.

Martínez, I.M. and Chrispeels, M.J. (2003). Genomic analysis of the unfolded protein response in Arabidopsis shows its connection to important cellular processes. Plant Cell 15: 561–576.

Marty, L., Siala, W., Schwarzländer, M., Fricker, M.D., Wirtz, M., Sweetlove, L.J., Meyer, Y., Meyer, A.J., Reichheld, J.P. and Hell, R. (2009). The NADPH-dependent thioredoxin system constitutes a functional backup for cytosolic glutathione reductase in Arabidopsis. Proc. Natl. Acad. Sci. 106: 9109–9114.

Marty, N.J., Teresinski, H.J., Hwang, Y.T., Clendening, E.A., Gidda, S.K., Sliwinska, E., Zhang, D., Miernyk, J.A., Brito, G.C. Andrews, D.W., Dyer, J.M. and Mullen, R.T. (2014). New insights into the targeting of a subset of tail-anchored proteins to the outer mitochondrial membrane. Front. Plant Sci. 5: 426.

Matthias, A., Ohlson, K.B., Fredriksson, J.M., Jacobsson, A., Nedergaard, J. and Cannon, B. (2000). Thermogenic responses in brown fat cells are fully UCP1-dependent. UCP2 or UCP3 do not substitute for UCP1 in adrenergically or fatty scid-induced thermogenesis. J. Biol. Chem. 275: 25073–25081.

Maxwell, D.P., Wang, Y. and McIntosh, L. (1999). The alternative oxidase lowers mitochondrial reactive oxygen production in plant cells. Proc. Natl. Acad. Sci. 96: 8271–8276.

McAdam, S.A.M., Manzi, M., Ross, J.J., Brodribb, T.J. and Gómez-Cadenas, A. (2016). Uprooting an abscisic acid paradigm: shoots are the primary source. Plant Signal. Behav. 11: e1169359.

Meng, L., Wong, J.H., Feldman, L.J., Lemaux, P.G. and Buchanan, B.B. (2010). A membrane-associated thioredoxin required for plant growth moves from cell to cell, suggestive of a role in intercellular communication. Proc. Natl. Acad. Sci. 107: 3900–3905.

Mesecke, N., Terziyska, N., Kozany, C., Baumann, F., Neupert, W., Hell, K. and Herrmann, J.M. (2005). A disulfide relay system in the intermembrane space of mitochondria that mediates protein import. Cell 121: 1059–1069.

Meyer, A.J., Brach, T., Marty, L., Kreye, S., Rouhier, N., Jacquot, J.P. and Hell, R. (2007). Redox-sensitive GFP in *Arabidopsis thaliana* is a quantitative biosensor for the redox potential of the cellular glutathione redox buffer. Plant J. 52: 973–986.

Meyer, A.J. and Dick, T.P. (2010). Fluorescent protein-based redox probes. Antioxid. Redox Signal. 13: 621–650.

Meyer, A.J., May, M.J. and Fricker, M. (2001). Quantitative *in vivo* measurement of glutathione in Arabidopsis cells. Plant J. 27: 67–78.

Meyer, E.H. (2012). Proteomic investigations of complex I composition: how to define a subunit? Front. Plant Sci. 3: 106.

Michalecka, A.M., Svensson, Å.S., Johansson, F.I., Agius, S.C., Johanson, U., Brennicke, A., Binder, S. and Rasmusson, A.G. (2003). Arabidopsis genes encoding mitochondrial type II NAD(P)H dehydrogenases have different evolutionary origin and show distinct responses to light. Plant Physiol. 133: 642–652.

Michaud, M. et al. (2016). *At*Mic60 is involved in plant mitochondria lipid trafficking and is part of a large complex. Curr. Biol. CB 26: 627–639.

Millar, A.H., Carrie, C., Pogson, B. and Whelan, J. (2009). Exploring the function-location nexus: using multiple lines of evidence in defining the subcellular location of plant proteins. Plant Cell 21: 1625–1631.

Millar, A.H. and Heazlewood, J.L. (2003). Genomic and proteomic analysis of mitochondrial carrier proteins in Arabidopsis. Plant Physiol. 131: 443–453.

Millar, A.H., Whelan, J., Soole, K.L. and Day, D.A. (2011). Organization and regulation of mitochondrial respiration in plants. Annu. Rev. Plant Biol. 62: 79–104.

Millar, A.H., Wiskich, J.T., Whelan, J. and Day, D.A. (1993). Organic acid activation of the alternative oxidase of plant mitochondria. FEBS Lett. 329: 259–262.

Minagawa, N., Koga, S., Nakano, M., Sakajo, S. and Yoshimoto, A. (1992). Possible involvement of superoxide anion in the induction of cyanide-resistant respiration in *Hansenula anomala*. FEBS Lett. 302: 217–219.

Mitchell, P. (2011). Chemiosmotic coupling in oxidative and photosynthetic phosphorylation. Biochim. Biophys. Acta 1807: 1507–1538.

Mitchell, P. (1961). Coupling of phosphorylation to electron and hydrogen transfer by a chemi-osmotic type of mechanism. Nature 191: 144–148.

Miwa, S. and Brand, M.D. (2003). Mitochondrial matrix reactive oxygen species production is very sensitive to mild uncoupling. Biochem. Soc. Trans. 31: 1300–1301.

Mlayeh, L., Chatkaew, S., Léonetti, M. and Homblé, F. (2010). Modulation of plant mitochondrial VDAC by phytosterols. Biophys. J. 99: 2097–2106.

Møller, I.M. and Rasmusson, A.G. (1998). The role of NADP in the mitochondrial matrix. Trends Plant Sci. 3: 21–27.

Monné, M., Daddabbo, L., Gagneul, D., Obata, T., Hielscher, B., Palmieri, L., Miniero, D.V., Fernie, A.R., Weber, A.P.M. and Palmieri, F. (2018). Uncoupling proteins 1 and 2 (UCP1 and UCP2) from *Arabidopsis thaliana* are mitochondrial transporters of aspartate, glutamate, and dicarboxylates. J. Biol. Chem. 293: 4213–4227.

Moore, A.L., Bonner, W.D. and Rich, P.R. (1978). The determination of the proton-motive force during cyanide-insensitive respiration in plant mitochondria. Arch. Biochem. Biophys. 186: 298–306.

Moran, O., Sciancalepore, M., Sandri, G., Panfili, E., Bassi, R., Ballarin, C. and Sorgato, M.C. (1992). Ionic permeability of the mitochondrial outer membrane. Eur. Biophys. J. 20: 311–319.

Moseler, A., Aller, I., Wagner, S., Nietzel, T., Przybyla-Toscano, J., Mühlenhoff, U., Lill, R., Berndt, C., Rouhier, N., Schwarzländer, M. and Meyer, A.J. (2015). The mitochondrial monothiol glutaredoxin S15 is essential for iron-sulfur protein maturation in *Arabidopsis thaliana*. Proc. Natl. Acad. Sci. 112: 13735–13740.

Munemasa, S., Hauser, F., Park, J., Waadt, R., Brandt, B. and Schroeder, J.I. (2015). Mechanisms of abscisic acid-mediated control of stomatal aperture. Curr. Opin. Plant Biol. 28: 154–162.

Murashige, T. and Skoog, F. (1962). A revised medium for rapid growth and bio assays with tobacco tissue cultures. Physiol. Plant. 15: 473–497.

Murcha, M.W., Elhafez, D., Lister, R., Tonti-Filippini, J., Baumgartner, M., Philippar, K., Carrie, C., Mokranjac, D., Soll, J. and Whelan, J. (2007). Characterization of the preprotein and amino acid transporter gene family in Arabidopsis. Plant Physiol. 143: 199–212.

Murcha, M.W., Wang, Y., Narsai, R. and Whelan, J. (2014). The plant mitochondrial protein import apparatus — the differences make it interesting. Biochim. Biophys. Acta 1840: 1233–1245.

Murchie, E.H. and Niyogi, K.K. (2011). Manipulation of photoprotection to improve plant photosynthesis. Plant Physiol. 155: 86–92

Murphy, M.P. (2009). How mitochondria produce reactive oxygen species. Biochem. J. 417: 1–13.

Nagai, T., Sawano, A., Park, E.S. and Miyawaki, A. (2001). Circularly permuted green fluorescent proteins engineered to sense Ca^{2+}. Proc. Natl. Acad. Sci. 98: 3197–3202.

Nakabayashi, K., Okamoto, M., Koshiba, T., Kamiya, Y. and Nambara, E. (2005). Genome-wide profiling of stored mRNA in *Arabidopsis thaliana* seed germination: epigenetic and genetic regulation of transcription in seed. Plant J. 41: 697–709.

Nedergaard, J., Golozoubova, V., Matthias, A., Asadi, A., Jacobsson, A. and Cannon, B. (2001). UCP1: the only protein able to mediate adaptive non-shivering thermogenesis and metabolic inefficiency. Biochim. Biophys. Acta 1504: 82–106.

Negroni, Y.L. (2017). Characterization of a re-engineered fluorescent protein sensor for NAD redox monitoring in living plant cells. Master Thesis.

Nie, S., Yue, H., Zhou, J. and Xing, D. (2015). Mitochondrial-derived reactive oxygen species play a vital role in the salicylic acid signaling pathway in *Arabidopsis thaliana*. PloS One 10: e0119853.

Nietzel, T. (2017). Mitochondrial regulation through thiol-switching in plants. Doctoral thesis.

Nisbet, E.G., Grassineau, N.V., Howe, C.J., Abell, P.I., Regelous, M. and Nisbet, R.E.R. (2007). The age of Rubisco: the evolution of oxygenic photosynthesis. Geobiology 5: 311–335.

Nogueira, F.T.S., Sassaki, F.T. and Maia, I.G. (2011). *Arabidopsis thaliana* uncoupling proteins (*AtUCP*s): insights into gene expression during development and stress response and epigenetic regulation. J. Bioenerg. Biomembr. 43: 71–79.

Norman, C., Howell, K.A., Millar, A.H., Whelan, J.M. and Day, D.A. (2004). Salicylic acid is an uncoupler and inhibitor of mitochondrial electron transport. Plant Physiol. 134: 492–501.

Olausson, T., Fjellström, O., Meuller, J. and Rydström, J. (1995). Molecular biology of nicotinamide nucleotide transhydrogenase — a unique proton pump. Biochim. Biophys. Acta 1231: 1–19.

Ordon, J., Gantner, J., Kemna, J., Schwalgun, L., Reschke, M., Streubel, J., Boch, J. and Stuttmann, J. (2017). Generation of chromosomal deletions in dicotyledonous plants employing a user-friendly genome editing toolkit. Plant J. 89: 155–168.

Palmieri, F., Pierri, C.L., De Grassi, A., Nunes-Nesi, A. and Fernie, A.R. (2011). Evolution, structure and function of mitochondrial carriers: a review with new insights. Plant J. 66: 161–181.

Palmieri, L., Picault, N., Arrigoni, R., Besin, E., Palmieri, F. and Hodges, M. (2008). Molecular identification of three *Arabidopsis thaliana* mitochondrial dicarboxylate carrier isoforms: organ distribution, bacterial expression, reconstitution into liposomes and functional characterization. Biochem. J. 410: 621–629.

Pan, R., Jones, A.D. and Hu, J. (2014). Cardiolipin-mediated mitochondrial dynamics and stress response in Arabidopsis. Plant Cell 26: 391–409.

Parsons, D.F., Bonner Jr., W.D. and Verboon, J.G. (1965). Electron microscopy of isolated plant mitochondria and plastids using both the thin-section and negative-staining techniques. Can. J. Bot. 43: 647–655.

Parsons, H.T. et al. (2012). Isolation and proteomic characterization of the Arabidopsis Golgi defines functional and novel components involved in plant cell wall biosynthesis. Plant Physiol. 159: 12–26.

Pastore, D., Di Pede, S. and Passarella, S. (2003). Isolated durum wheat and potato cell mitochondria oxidize externally added NADH mostly via the malate/oxaloacetate shuttle with a rate that depends on the carrier-mediated transport. Plant Physiol. 133: 2029–2039.

Pavlov, E., Grigoriev, S.M., Dejean, L.M., Zweihorn, C.L., Mannella, C.A. and Kinnally, K.W. (2005). The mitochondrial channel VDAC has a cation-selective open state. Biochim. Biophys. Acta 1710: 96–102.

Pebay-Peyroula, E., Dahout-Gonzalez, C., Kahn, R., Trézéguet, V., Lauquin, G.J.M. and Brandolin, G. (2003). Structure of mitochondrial ADP/ATP carrier in complex with carboxyatractyloside. Nature 426: 39–44.

Peleh, V., Zannini, F., Backes, S., Rouhier, N. and Herrmann, J.M. (2017). Erv1 of *Arabidopsis thaliana* can directly oxidize mitochondrial intermembrane space proteins in the absence of redox-active Mia40. BMC Biol. 15: 106.

Pennisi, R., Salvi, D., Brandi, V., Angelini, R., Ascenzi, P. and Polticelli, F. (2016). Molecular evolution of alternative oxidase proteins: a phylogenetic and structure modeling approach. J. Mol. Evol. 82: 207–218.

Pérez-Martín, M., Pérez-Pérez, M.E., Lemaire, S.D. and Crespo, J.L. (2014). Oxidative stress contributes to autophagy induction in response to endoplasmic reticulum stress in *Chlamydomonas reinhardtii*. Plant Physiol. 166: 997–1008.

Peterhänsel, C., Horst, I., Niessen, M., Blume, C., Kebeish, R., Kürkcüoglu, S. and Kreuzaler, F. (2010). Photorespiration. Arab. Book. Am. Soc. Plant Biol. 8.

Picard, M., McManus, M.J., Csordás, G., Várnai, P., Ii, G.W.D., Williams, D., Hajnóczky, G. and Wallace, D.C. (2015). Trans-mitochondrial coordination of cristae at regulated membrane junctions. Nat. Commun. 6: 6259.

Poburko, D., Santo-Domingo, J. and Demaurex, N. (2011). Dynamic regulation of the mitochondrial proton gradient during cytosolic calcium elevations. J. Biol. Chem. 286: 11672–11684.

Porcelli, A.M., Ghelli, A., Zanna, C., Pinton, P., Rizzuto, R. and Rugolo, M. (2005). pH difference across the outer mitochondrial membrane measured with a green fluorescent protein mutant. Biochem. Biophys. Res. Commun. 326: 799–804.

Pracharoenwattana, I., Zhou, W., Keech, O., Francisco, P.B., Udomchalothorn, T., Tschoep, H., Stitt, M., Gibon, Y. and Smith, S.M. (2010). Arabidopsis has a cytosolic fumarase required for the massive allocation of photosynthate into fumaric acid and for rapid plant growth on high nitrogen. Plant J. 62: 785–795.

Queval, G., Jaillard, D., Zechmann, B. and Noctor, G. (2011). Increased intracellular H_2O_2 availability preferentially drives glutathione accumulation in vacuoles and chloroplasts. Plant Cell Environ. 34: 21–32.

Quick, W.P., Chaves, M.M., Wendler, R., David, M., Rodrigues, M.L., Passaharinho, J.A., Pereira, J.S., Adcock, M.D., Leegood, R.C. and Stitt, M. (1992). The effect of water stress on photosynthetic carbon metabolism in four species grown under field conditions. Plant Cell Environ. 15: 25–35.

Raghavendra, A.S. and Padmasree, K. (2003). Beneficial interactions of mitochondrial metabolism with photosynthetic carbon assimilation. Trends Plant Sci. 8: 546–553.

Raghavendra, A.S., Padmasree, K. and Saradadevi, K. (1994). Interdependence of photosynthesis and respiration in plant cells: interactions between chloroplasts and mitochondria. Plant Sci. 97: 1–14.

Rasmusson, A.G., Geisler, D.A. and Møller, I.M. (2008). The multiplicity of dehydrogenases in the electron transport chain of plant mitochondria. Mitochondrion 8: 47–60.

Rasmusson, A.G. and Møller, I.M. (1991). NAD(P)H dehydrogenases on the inner surface of the inner mitochondrial membrane studied using inside-out submitochondrial particles. Physiol. Plant. 83: 357–365.

Rasmusson, A.G., Svensson, A.S., Knoop, V., Grohmann, L. and Brennicke, A. (1999). Homologues of yeast and bacterial rotenone-insensitive NADH dehydrogenases in higher eukaryotes: two enzymes are present in potato mitochondria. Plant J. 20: 79–87.

Rhoads, D.M., Umbach, A.L., Sweet, C.R., Lennon, A.M., Rauch, G.S. and Siedow, J.N. (1998). Regulation of the cyanide-resistant alternative oxidase of plant mitochondria identification of the cysteine residue involved in α-keto acid stimulation and intersubunit disulfide bond formation. J. Biol. Chem. 273: 30750–30756.

Rieger, B., Junge, W. and Busch, K.B. (2014). Lateral pH gradient between OXPHOS complex IV and F_0F_1 ATP-synthase in folded mitochondrial membranes. Nat. Commun. 5: 3103.

Roach, T. and Krieger-Liszkay, A.K. (2014). Regulation of photosynthetic electron transport and photoinhibition. Curr. Protein Pept. Sci. 15: 351–362.

Ruberti, C. and Brandizzi, F. (2018). Unfolded protein response in Arabidopsis. Methods Mol. Biol. 1691: 231–238.

Rueden, C.T., Schindelin, J., Hiner, M.C., DeZonia, B.E., Walter, A.E., Arena, E.T. and Eliceiri, K.W. (2017). ImageJ2: ImageJ for the next generation of scientific image data. BMC Bioinformatics 18: 529.

Saisho, D., Nambara, E., Naito, S., Tsutsumi, N., Hirai, A. and Nakazono, M. (1997). Characterization of the gene family for alternative oxidase from *Arabidopsis thaliana*. Plant Mol. Biol. 35: 585–596.

Sanford, L. and Palmer, A. (2017). Recent advances in development of genetically encoded fluorescent sensors. Methods Enzymol. 589: 1–49.

Santelia, D. and Lawson, T. (2016). Rethinking guard cell metabolism. Plant Physiol. 172: 1371–1392.

Scheibe, R. (2004). Malate valves to balance cellular energy supply. Physiol. Plant. 120: 21–26.

Scheibe, R., Backhausen, J.E., Emmerlich, V. and Holtgrefe, S. (2005). Strategies to maintain redox homeostasis during photosynthesis under changing conditions. J. Exp. Bot. 56: 1481–1489.

Scheibe, R. and Beck, E. (1979). On the mechanism of activation by light of the NADP-dependent malate dehydrogenase in spinach chloroplasts. Plant Physiol. 64: 744–748.

Scheibe, R. and Dietz, K.J. (2012). Reduction–oxidation network for flexible adjustment of cellular metabolism in photoautotrophic cells. Plant Cell Environ. 35: 202–216.

Schertl, P. and Braun, H.P. (2014). Respiratory electron transfer pathways in plant mitochondria. Front. Plant Sci. 5.

Schindelin, J. et al. (2012). Fiji: an open-source platform for biological-image analysis. Nat. Methods 9: 676–682.

Schmidtmann, E., König, A.C., Orwat, A., Leister, D., Hartl, M. and Finkemeier, I. (2014). Redox regulation of Arabidopsis mitochondrial citrate synthase. Mol. Plant 7: 156–169.

Schwarzländer, M. et al. (2014). The 'mitoflash' probe cpYFP does not respond to superoxide. Nature 514: E12–E14.

Schwarzländer, M., Dick, T.P., Meyer, A.J. and Morgan, B. (2016). Dissecting redox biology using fluorescent protein sensors. Antioxid. Redox Signal. 24: 680–712.

Schwarzländer, M., Fricker, M.D., Müller, C., Marty, L., Brach, T., Novak, J., Sweetlove, L.J., Hell, R. and Meyer, A.J. (2008). Confocal imaging of glutathione redox potential in living plant cells. J. Microsc. 231: 299–316.

Schwarzländer, M. and Fuchs, P. (2017). Plant mitochondrial membranes: adding structure and new functions to respiratory physiology. Curr. Opin. Plant Biol. 40: 147–157.

Schwarzländer, M., Logan, D.C., Fricker, M.D. and Sweetlove, L.J. (2011). The circularly permuted yellow fluorescent protein cpYFP that has been used as a superoxide probe is highly responsive to pH but not superoxide in mitochondria: implications for the existence of superoxide 'flashes.' Biochem. J. 437: 381–387.

Schwarzländer, M., Logan, D.C., Johnston, I.G., Jones, N.S., Meyer, A.J., Fricker, M.D. and Sweetlove, L.J. (2012). Pulsing of membrane potential in individual mitochondria: a stress-induced mechanism to regulate respiratory bioenergetics in Arabidopsis. Plant Cell 24: 1188–1201.

Selinski, J., Hartmann, A., Deckers-Hebestreit, G., Day, D.A., Whelan, J. and Scheibe, R. (2018). Alternative oxidase isoforms are differentially activated by tricarboxylic acid cycle intermediates. Plant Physiol. 176: 1423–1432.

Senkler, J., Senkler, M., Eubel, H., Hildebrandt, T., Lengwenus, C., Schertl, P., Schwarzländer, M., Wagner, S., Wittig, I. and Braun, H.P. (2017). The mitochondrial complexome of *Arabidopsis thaliana*. Plant J. 89: 1079–1092.

Sharkey, T.D. (1988). Estimating the rate of photorespiration in leaves. Physiol. Plant. 73: 147–152.

Slater, E.C. (1967). An evaluation of the Mitchell hypothesis of chemiosmotic coupling in oxidative and photosynthetic phosphorylation. Eur. J. Biochem. 1: 317–326.

Smith, A.M.O., Ratcliffe, R.G. and Sweetlove, L.J. (2004). Activation and function of mitochondrial uncoupling protein in plants. J. Biol. Chem. 279: 51944–51952.

Smith, C.A., Melino, V.J., Sweetman, C. and Soole, K.L. (2009). Manipulation of alternative oxidase can influence salt tolerance in *Arabidopsis thaliana*. Physiol. Plant. 137: 459–472.

Stefano, G., Renna, L. and Brandizzi, F. (2014). The endoplasmic reticulum exerts control over organelle streaming during cell expansion. J. Cell Sci. 127: 947–953.

Stojanovski, D., Bohnert, M., Pfanner, N. and van der Laan, M. (2012). Mechanisms of protein sorting in mitochondria. Cold Spring Harb. Perspect. Biol. 4: a011320.

Strauss, M., Hofhaus, G., Schröder, R.R. and Kühlbrandt, W. (2008). Dimer ribbons of ATP synthase shape the inner mitochondrial membrane. EMBO J. 27: 1154–1160.

Strodtkötter, I. et al. (2009). Induction of the AOX1D isoform of alternative oxidase in *A. thaliana* T-DNA insertion lines lacking isoform AOX1A is insufficient to optimize photosynthesis when treated with antimycin A. Mol. Plant 2: 284–297.

Stuart, J.A., Harper, J.A., Brindle, K.M. and Brand, M.D. (1999). Uncoupling protein 2 from carp and zebrafish, ectothermic vertebrates. Biochim. Biophys. Acta 1413: 50–54.

Studier, F.W. and Moffatt, B.A. (1986). Use of bacteriophage T7 RNA polymerase to direct selective high-level expression of cloned genes. J. Mol. Biol. 189: 113–130.

Sweetlove, L.J., Heazlewood, J.L., Herald, V., Holtzapffel, R., Day, D.A., Leaver, C.J. and Millar, A.H. (2002). The impact of oxidative stress on Arabidopsis mitochondria. Plant J. 32: 891–904.

Sweetlove, L.J., Lytovchenko, A., Morgan, M., Nunes-Nesi, A., Taylor, N.L., Baxter, C.J., Eickmeier, I. and Fernie, A.R. (2006). Mitochondrial uncoupling protein is required for efficient photosynthesis. Proc. Natl. Acad. Sci. 103: 19587–19592.

Sweetlove, L.J., Mowday, B., Hebestreit, H.F., Leaver, C.J. and Millar, A.H. (2001). Nucleoside diphosphate kinase III is localized to the inter-membrane space in plant mitochondria. FEBS Lett. 508: 272–276.

Sweetlove, L.J., Taylor, N.L. and Leaver, C.J. (2007). Isolation of intact, functional mitochondria from the model plant *Arabidopsis thaliana*. Methods Mol. Biol. 372: 125–136.

Takahashi, S. and Badger, M.R. (2011). Photoprotection in plants: a new light on photosystem II damage. Trends Plant Sci. 16: 53–60.

Tamura, K., Stecher, G., Peterson, D., Filipski, A. and Kumar, S. (2013). MEGA6: molecular evolutionary genetics analysis version 6.0. Mol. Biol. Evol. 30: 2725–2729.

Taniguchi, M. and Miyake, H. (2012). Redox-shuttling between chloroplast and cytosol: integration of intra-chloroplast and extra-chloroplast metabolism. Curr. Opin. Plant Biol. 15: 252–260.

Teardo, E. et al. (2017). Physiological characterization of a plant mitochondrial calcium uniporter *in vitro* and *in vivo*. Plant Physiol. 173: 1355–1370.

Tezara, W., Mitchell, V.J., Driscoll, S.D. and Lawlor, D.W. (1999). Water stress inhibits plant photosynthesis by decreasing coupling factor and ATP. Nature 401: 914–917.

Tikkanen, M. and Aro, E.M. (2014). Integrative regulatory network of plant thylakoid energy transduction. Trends Plant Sci. 19: 10–17.

Trono, D., Flagella, Z., Laus, M.N., Di Fonzo, N. and Pastore, D. (2004). The uncoupling protein and the potassium channel are activated by hyperosmotic stress in mitochondria from durum wheat seedlings. Plant Cell Environ. 27: 437–448.

Udvardi, M.K., Czechowski, T. and Scheible, W.R. (2008). Eleven golden rules of quantitative RT-PCR. Plant Cell 20: 1736–1737.

Uhrig, R.G., Labandera, A.M., Tang, L.Y., Sieben, N.A., Goudreault, M., Yeung, E., Gingras, A.C., Samuel, M.A. and Moorhead, G.B.G. (2017). Activation of mitochondrial protein phosphatase SLP2 by MIA40 regulates seed germination. Plant Physiol. 173: 956–969.

Umbach, A.L., Ng, V.S. and Siedow, J.N. (2006). Regulation of plant alternative oxidase activity: a tale of two cysteines. Biochim. Biophys. Acta 1757: 135–142.

Umbach, A.L. and Siedow, J.N. (1993). Covalent and noncovalent dimers of the cyanide-resistant alternative oxidase protein in higher plant mitochondria and their relationship to enzyme activity. Plant Physiol. 103: 845–854.

Urban, J., Ingwers, M.W., McGuire, M.A. and Teskey, R.O. (2017). Increase in leaf temperature opens stomata and decouples net photosynthesis from stomatal conductance in *Pinus taeda* and *Populus deltoides x nigra*. J. Exp. Bot. 68: 1757–1767.

Vanlerberghe, G.C., Cvetkovska, M. and Wang, J. (2009). Is the maintenance of homeostatic mitochondrial signaling during stress a physiological role for alternative oxidase? Physiol. Plant. 137: 392–406.

Vanlerberghe, G.C. and McIntosh, L. (1996). Signals regulating the expression of the nuclear gene encoding alternative oxidase of plant mitochondria. Plant Physiol. 111: 589–595.

Vanlerberghe, G.C. and Ordog, S.H. (2002). Photosynthetic nitrogen assimilation and associated carbon and respiratory metabolism: Alternative oxidase: integrating carbon metabolism and electron transport in plant respiration. Dordrecht: Springer, 173–191.

Vanlerberghe, G.C., Yip, J.Y.H. and Parsons, H.L. (1999). *In organello* and *in vivo* evidence of the importance of the regulatory sulfhydryl/disulfide system and pyruvate for alternative oxidase activity in tobacco. Plant Physiol. 121: 793–803.

Vaseghi, M.J., Chibani, K., Telman, W., Liebthal, M.F., Gerken, M., Mueller, S.M. and Dietz, K.J. (2018). The chloroplast 2-cysteine peroxiredoxin functions as thioredoxin oxidase in redox regulation of chloroplast metabolism. bioRxiv: 317107.

Vercesi, A.E., Borecký, J., Maia, I.G., Arruda, P., Cuccovia, I.M. and Chaimovich, H. (2006). Plant uncoupling mitochondrial proteins. Annu. Rev. Plant Biol. 57: 383–404.

Vercesi, A.E., Martins, I.S., Silva, M.A.P., Leite, H.M.F., Cuccovia, I.M. and Chaimovich, H. (1995). PUMPing plants. Nature 375: 24.

Vishwakarma, A., Tetali, S.D., Selinski, J., Scheibe, R. and Padmasree, K. (2015). Importance of the alternative oxidase (AOX) pathway in regulating cellular redox and ROS homeostasis to optimize photosynthesis during restriction of the cytochrome oxidase pathway in *Arabidopsis thaliana*. Ann. Bot. 116: 555–569.

Wagner, S. et al. (2015a). The EF-hand Ca^{2+} binding protein MICU choreographs mitochondrial Ca^{2+} dynamics in Arabidopsis. Plant Cell 27: 3190–3212.

Wagner, S., Nietzel, T., Aller, I., Costa, A., Fricker, M.D., Meyer, A.J. and Schwarzländer, M. (2015b). Analysis of plant mitochondrial function using fluorescent protein sensors. Methods Mol. Biol. 1305: 241–252.

Walia, A., Waadt, R. and Jones, A.M. (2018). Genetically encoded biosensors in plants: pathways to discovery. Annu. Rev. Plant Biol. 69: 497–524.

Wan, S. and Jiang, L. (2016). Endoplasmic reticulum (ER) stress and the unfolded protein response (UPR) in plants. Protoplasma 253: 753–764.

Watanabe, A., Nakazono, M., Tsutsumi, N. and Hirai, A. (1999). *At*UCP2: a novel isoform of the mitochondrial uncoupling protein of *Arabidopsis thaliana*. Plant Cell Physiol. 40: 1160–1166.

Watanabe, C.K., Hachiya, T., Terashima, I. and Noguchi, K. (2008). The lack of alternative oxidase at low temperature leads to a disruption of the balance in carbon and nitrogen metabolism, and to an up-regulation of antioxidant defence systems in *Arabidopsis thaliana* leaves. Plant Cell Environ. 31: 1190–1202.

Weger, H.G., Chadderton, A.R., Lin, M., Guy, R.D. and Turpin, D.H. (1990). Cytochrome and alternative pathway respiration during transient ammonium assimilation by N-limited *Chlamydomonas reinhardtii*. Plant Physiol. 94: 1131–1136.

Weigle, D.S., Selfridge, L.E., Schwartz, M.W., Seeley, R.J., Cummings, D.E., Havel, P.J., Kuijper, J.L. and BeltrandelRio, H. (1998). Elevated free fatty acids induce uncoupling protein 3 expression in muscle: a potential explanation for the effect of fasting. Diabetes 47: 298–302.

Welchen, E., Schmitz, J., Fuchs, P., García, L., Wagner, S., Wienstroer, J., Schertl, P., Braun, H.P., Schwarzländer, M., Gonzalez, D.H. and Maurino, V.G. (2016). D-lactate dehydrogenase links methylglyoxal degradation and electron transport through cytochrome *c*. Plant Physiol. 172: 901–912.

Werkheiser, W.C. and Bartley, W. (1957). The study of steady-state concentrations of internal solutes of mitochondria by rapid centrifugal transfer to a fixation medium. Biochem. J. 66: 79–91.

Wigge, B., Krömer, S. and Gardeström, P. (1993). The redox levels and subcellular distribution of pyridine nucleotides in illuminated barley leaf protoplasts studied by rapid fractionation. Physiol. Plant. 88: 10–18.

Wilkins, O., Bräutigam, K. and Campbell, M.M. (2010). Time of day shapes Arabidopsis drought transcriptomes. Plant J. 63: 715–727.

Wilkinson, S. and Davies, W.J. (1997). Xylem sap pH increase: a drought signal received at the apoplastic face of the guard cell that involves the suppression of saturable abscisic acid uptake by the epidermal symplast. Plant Physiol. 113: 559–573.

Williams, D.E. and Reisfeld, R.A. (1964). Disc electrophoresis in polyacrylamide gels: extension to new conditions of pH and buffer. Ann. N. Y. Acad. Sci. 121: 373–381.

Wingler, A., Quick, W.P., Bungard, R.A., Bailey, K.J., Lea, P.J. and Leegood, R.C. (1999). The role of photorespiration during drought stress: an analysis utilizing barley mutants with reduced activities of photorespiratory enzymes. Plant Cell Environ. 22: 361–373.

Winter, D., Vinegar, B., Nahal, H., Ammar, R., Wilson, G.V. and Provart, N.J. (2007). An "electronic fluorescent pictograph" browser for exploring and analyzing large-scale biological data sets. PLoS One 2: e718.

Winter, K. and Königer, M. (1989). Dithiothreitol, an inhibitor of violaxanthin de-epoxidation, increases the susceptibility of leaves of *Nerium oleander* L. to photoinhibition of photosynthesis. Planta 180: 24–31.

Wu, J., Neimanis, S. and Heber, U. (1991). Photorespiration is more effective than the Mehler reaction in protecting the photosynthetic apparatus against photoinhibition. Bot. Acta 104: 283–291.

Xing, S., Mehlhorn, D.G., Wallmeroth, N., Asseck, L.Y., Kar, R., Voss, A., Denninger, P., Schmidt, V.A.F., Schwarzländer, M., Stierhof, Y.D., Grossmann, G. and Grefen, C. (2017). Loss of GET pathway orthologs in *Arabidopsis thaliana* causes root hair growth defects and affects SNARE abundance. Proc. Natl. Acad. Sci. 114: E1544–E1553.

Yoshida, K., Noguchi, K., Motohashi, K. and Hisabori, T. (2013). Systematic exploration of thioredoxin target proteins in plant mitochondria. Plant Cell Physiol. 54: 875–892.

Yoshida, K., Terashima, I. and Noguchi, K. (2007). Up-regulation of mitochondrial alternative oxidase concomitant with chloroplast over-reduction by excess light. Plant Cell Physiol. 48: 606–614.

Yukioka, H., Inagaki, S., Tanaka, R., Katoh, K., Miki, N., Mizutani, A. and Masuko, M. (1998). Transcriptional activation of the alternative oxidase gene of the fungus *Magnaporthe grisea* by a respiratory-inhibiting fungicide and hydrogen peroxide. Biochim. Biophys. Acta 1442: 161–169.

Zechmann, B., Mauch, F., Sticher, L. and Müller, M. (2008). Subcellular immunocytochemical analysis detects the highest concentrations of glutathione in mitochondria and not in plastids. J. Exp. Bot. 59: 4017–4027.

Zhang, H., Zhang, L., Gao, B., Fan, H., Jin, J., Botella, M.A., Jiang, L. and Lin, J. (2011). Golgi apparatus-localized synaptotagmin 2 is required for unconventional secretion in Arabidopsis. PLoS One 6: e26477.

Zhang, X., Zhang, L., Dong, F., Gao, J., Galbraith, D.W. and Song, C.P. (2001). Hydrogen peroxide is involved in abscisic acid-induced stomatal closure in *Vicia faba*. Plant Physiol. 126: 1438–1448.

Zhang, Z.S., Liu, M.J., Scheibe, R., Selinski, J., Zhang, L.T., Yang, C., Meng, X.L. and Gao, H.Y. (2017). Contribution of the alternative respiratory pathway to PSII photoprotection in C_3 and C_4 Plants. Mol. Plant 10: 131–142.

Zhou, H., Zhao, J., Yang, Y., Chen, C., Liu, Y., Jin, X., Chen, L., Li, X., Deng, X.W., Schumaker, K.S. and Guo, Y. (2012). Ubiquitin-specific protease 16 modulates salt tolerance in Arabidopsis by regulating Na^+/H^+ antiport activity and serine hydroxymethyltransferase stability. Plant Cell 24: 5106–5122.

Zizi, M., Forte, M., Blachly-Dyson, E. and Colombini, M. (1994). NADH regulates the gating of VDAC, the mitochondrial outer membrane channel. J. Biol. Chem. 269: 1614–1616.

Zoglowek, C., Krömer, S. and Heldt, H.W. (1988). Oxaloacetate and malate transport by plant mitochondria. Plant Physiol. 87: 109–115.

APPENDIX

I. Supplemental figures and tables

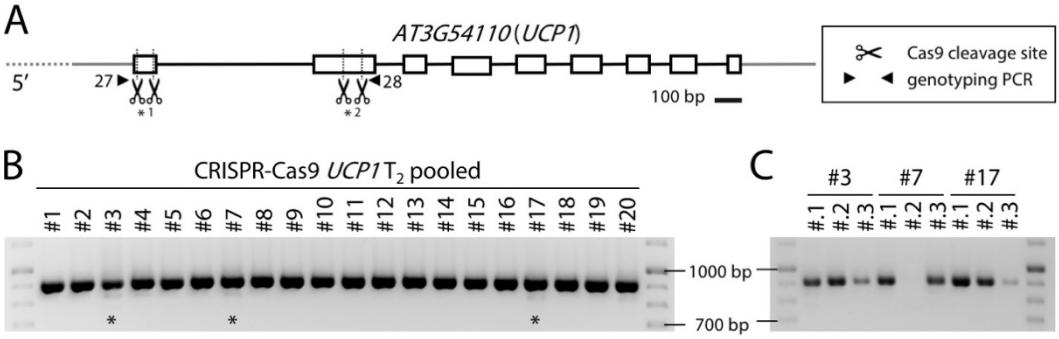

Supplemental Figure 1: Screening of CRISPR-Cas9 genome editing-induced chromosomal deletions in *UCP1*.

(**A**) Gene models of Arabidopsis *Uncoupling Protein1* (*UCP1*) with expected CRISPR-Cas9 genome editing sites. Black boxes: exons, black lines in-between: introns, grey lines at 5' and 3' end: UTRs, black arrow heads: genotyping PCR primers used in (B) and (C) for genome editing assessments, scissors: expected double-strand breaks by Cas9 cleavage eliciting chromosomal deletions in exon 1 (*1) and/or in exon 2 (*2).

(**B**) Representative PCR and gel electrophoresis-based screen of putatively edited T_2 plants. Three lines were pooled for gDNA isolation and the genomic fragments harbouring both putative deletion sites PCR amplified with primers described in (A). Successful editing (deletion) events were expected to result in ~75-bp (single deletion event) or ~150-bp (double deletion event) band shifts. Asterisks: faint bands detected underneath main bands. (**C**) Follow-up examination by repeating PCR and gel electrophoresis on individual lines from asterisks-marked pooled lines in (B).

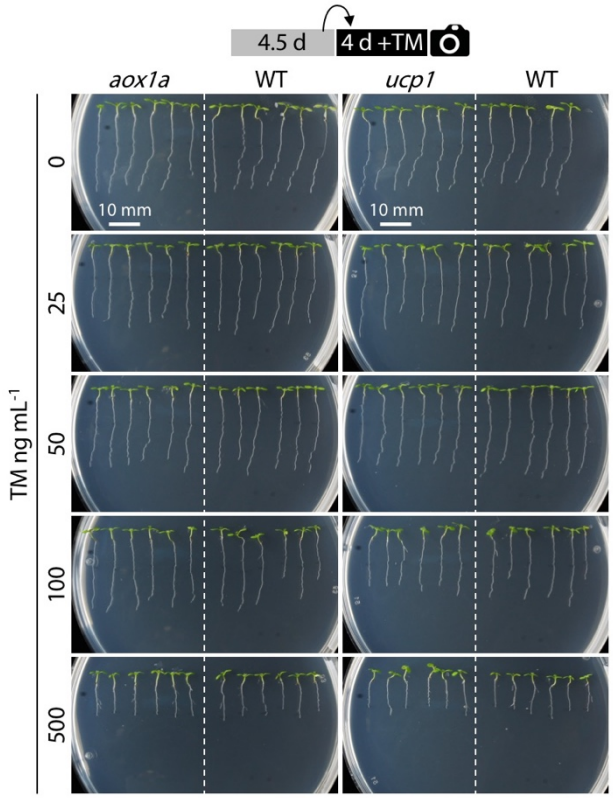

Supplemental Figure 2: Root growth analysis of Arabidopsis wild-type and uncoupling mutant seedlings under different concentrations of tunicamycin.

Representative images of 8.5-d-old Arabidopsis seedlings germinated and grown for 4.5 d on standard agar plates before transferred and grown for 4 d on agar plates supplemented with 0–500 ng mL^{-1} tunicamycin (TM).

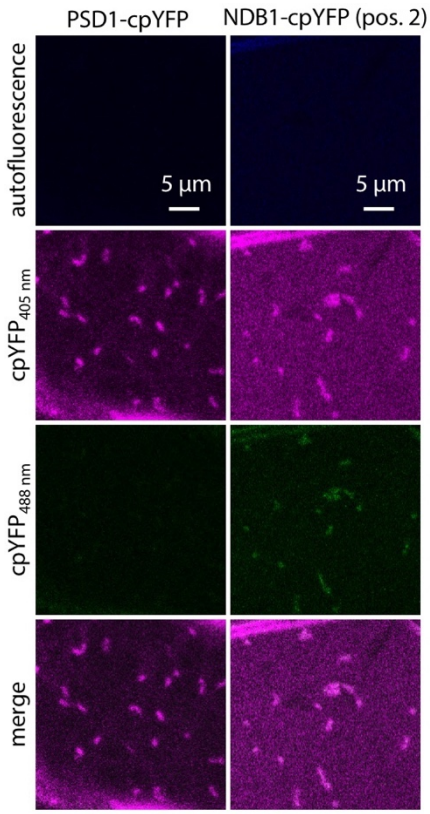

Gene	Identifier	Topo	Fusion
AAC1	*AT3G08580*	IMS	C
AK1	*AT5G63400*	IMS	C
ATPsyn 1	*AT2G19680*	IMS	N
ATPsyn g 2	*AT4G26210*	IMS	N
ATPsyn g 3	*AT4G29480*	IMS	N
CRK21-1	*AT4G23290*	IMS?	C
CYTC1	*AT1G22840*	IMS	C
CYTC2	*AT4G10040*	IMS	C
ERV1	*AT1G49880*	IMS	C
MIRO1	*AT5G27540*	cytosol	N
NDB1	*AT4G28220*	IMS	pos. 1
NDB1	*AT4G28220*	IMS	pos. 2
NDB1	*AT4G28220*	IMS	C
NDPK3	*AT4G11010*	IMS	C
TIM9	*AT3G46560*	IMS	C
TOM40-1	*AT3G20000*	cytosol	N
TOM9-2	*AT5G43970*	cytosol	N
TRX-h2	*AT5G39950*	matrix	C
UCP2	*AT5G58970*	Golgi	C
UCP3	*AT1G14140*	IMS	C
VDAC1	*AT3G01280*	cytosol	C
VDAC3	*AT5G15090*	cytosol	C

Supplemental Figure 3: Overview of mitochondrial proteins fused to cpYFP pH biosensor with insufficient fluorescent signal-to-noise ratio upon stable expression in Arabidopsis plants.

Left: Representative CLSM images from hypocotyl cells of 5-d-old Arabidopsis seedlings stably transformed expressing indicated candidate protein fused to cpYFP. PSD1-cpYFP and NDB1-cpYFP (pos. 2) lines exemplify criteria defined as poor signal-to-noise ratio of cpYFP fluorescence in response to excitation at 405 or/and 488 nm. Top down: 405 nm-induced autofluorescence: blue, cpYFP excited at 405 nm: magenta, cpYFP excited at 488 nm: green. **Right**: Table summarising fusions of mitochondrial proteins with cpYFP which reported insufficiently high fluorescence signal-to-noise ratio upon stable expression in Arabidopsis. Identifier: associated gene identifier, topo: predicted mitochondrial subcompartmental exposure of cpYFP, fusion: C- or N-terminal fusion of cpYFP to candidate protein sequence. Exceptions are NDB1 lines with cpYFP inserted into alpha helices at 44K–45E (pos. 1) or 307S–308G (pos. 2).

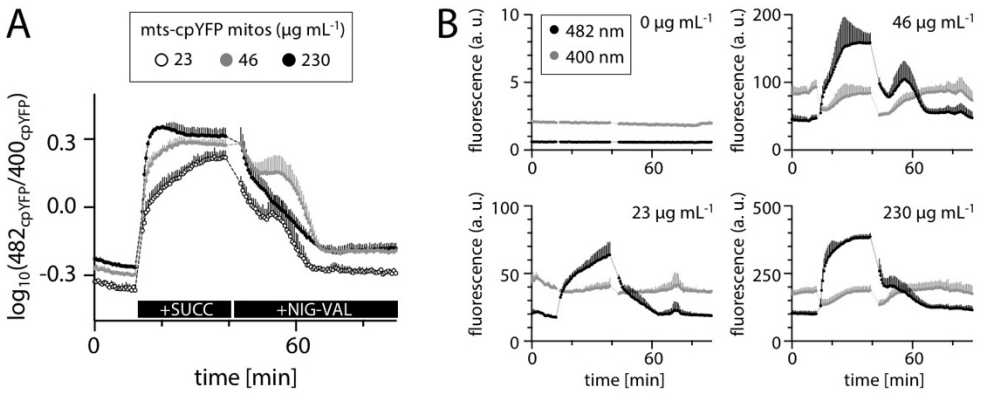

Supplemental Figure 4: Monitoring pH dynamics in dilution series of mts-cpYFP mitochondria.
(A) CpYFP mitochondria assays monitoring pH dynamics in mitochondria purified from wild-type Arabidopsis plants stably expressing *Nicotiana plumbaginifolia* β-ATPase mitochondrial presequence fused to cpYFP (mts-cpYFP). Y-axis: ratio of fluorescence in response to excitation at 482 and 400 nm measured from wells containing different concentrations of mts-cpYFP mitochondria (µg total mitochondrial protein mL^{-1}). Increase or decrease of ratio indicates more alkaline or more acidic pH, respectively. $n \geq 3$, mean + SD. Black bars at the bottom of the graph indicate addition of 10 mM succinate + 250 µM ATP (succ) or 50 µM nigericin + 10 µM valinomycin (nig-val). (**B**) Emission intensities from excitation at 400 and 482 nm from measurements shown in (A). 0 µg mL^{-1}: background fluorescence intensities of mock without mitochondria. Note adjusted y-axis range.

Supplemental Table 1: References used to predict cpYFP exposure upon fusion to mitochondrial candidate protein.

Candidate protein-cpYFP or cpYFP-candidate protein indicate fusion to N- or C-terminus of cpYFP, respectively. Reference: studies reporting on the (sub)localisation of the mitochondrial candidate protein.

Gene identifier	Candidate protein cpYFP fusion	Reference
AT3G08580	AAC1-cpYFP	Brugière et al. 2004
AT5G13490	AAC2-cpYFP	Brugière et al. 2004
AT5G63400	AK1-cpYFP	Brugière et al. 2004
AT3G22370	AOX1a-cpYFP	Brugière et al. 2004
AT2G19680	ATPsyn g 1-cpYFP	van Lis et al. 2007; Hahn et al. 2016
AT4G26210	ATPsyn g 2-cpYFP	van Lis et al. 2007; Hahn et al. 2016
AT4G29480	ATPsyn g 3-cpYFP	van Lis et al. 2007; Hahn et al. 2016
AT2G27730	CI P2-cpYFP	Klodmann et al. 2011; Meyer, 2012
AT4G04870	CLS1-cpYFP	Douce et al. 1972; Pan et al. 2014
AT2G15680	CML30-cpYFP	Chigri et al. 2012
AT4G23290	CRK21-1-cpYFP	Heazlewood et al. 2004
AT1G22840	CYTC1-cpYFP	Cortese et al. 1995
AT4G10040	CYTC2-cpYFP	Cortese et al. 1995
AT2G22500	DIC1-cpYFP	Millar and Heazlewood, 2003
AT4G24570	DIC2-cpYFP	Millar and Heazlewood, 2003
AT5G06580	dLDH1-cpYFP	Engqvist et al. 2009; Welchen et al. 2016
AT1G49880	ERV1-cpYFP	Levitan et al. 2004
AT2G47510	FUM1-cpYFP	Pracharoenwattana et al. 2010
AT5G60730	GET3c-cpYFP	Xing et al. 2017
AT3G15660	GRXS15-cpYFP	Moseler et al. 2015
AT1G09575	MCU1-cpYFP	Teardo et al. 2017
AT1G22520	MIC10-cpYFP	Michaud et al. 2016
AT1G09575	MICU-cpYFP	Wagner et al. 2015a
AT5G27540	cpYFP-MIRO1	Duncan et al. 2011; Marty et al. 2014
AT5G14040	MPT3-cpYFP	Millar and Heazlewood, 2003
AT4G28220	NDB1-cpYFP	Elhafez et al. 2006
AT4G11010	NDPK3-cpYFP	Sweetlove et al. 2006
AT5G22350	NMT1-cpYFP	Arimura et al. 2008; Duncan et al. 2011
AT4G37930	SHMT1-cpYFP	Zhou et al. 2012
AT1G18480	SLP2-cpYFP	Uhrig et al. 2017
AT3G46560	TIM9-cpYFP	Lister et al. 2002, 2004
AT5G11690	TIM17-3-cpYFP	Murcha et al. 2007
AT1G17530	TIM23-1-cpYFP	Murcha et al. 2007
AT1G64220	cpYFP-TOM7-2	Duncan et al. 2011; Marty et al. 2014
AT1G27390	cpYFP-TOM20-2	Duncan et al. 2011; Marty et al. 2014
AT3G20000	TOM40-1-cpYFP	Duncan et al. 2011; Marty et al. 2014
AT5G39950	TRX-h2-cpYFP	Meng et al. 2010b
AT1G31020	TRX-o2-cpYFP	Laloi et al. 2001
AT3G54110	UCP1-cpYFP	Sweetlove et al. 2006; Monné et al. 2018
AT5G58970	UCP2-cpYFP	Parsons et al. 2012; Monné et al. 2018
AT1G14140	UCP3-cpYFP	Klodmann et al. 2011; Senkler et al. 2017
AT3G01280	VDAC1-cpYFP	Bayrhuber et al. 2008; Duncan et al. 2011
AT5G15090	VDAC3-cpYFP	Bayrhuber et al. 2008; Duncan et al. 2011

LIST OF FIGURES

LIST OF TABLES

ABBREVIATIONS

2PG	2-phosphoglycolate
A.U.	arbitrary unit
ABA	abscisic acid
ADP	adenosine diphosphate
ANOVA	analysis of variance
AOX	alternative oxidase
ATP	adenosine triphosphate
BiP3	immunoglobulin-binding protein 3
BSA	bovine serum albumin
CCCP	carbonyl cyanide m-chlorophenyl hydrazone
cDNA	complementary DNA
CLSM	confocal laser scanning microscopy
Col-0	Arabidopsis thaliana ecotype Columbia 0 (wildtype)
cpYFP	circular permutated Yellow Fluorescent Protein
Cys	cysteine
Cyt *c*	cytochrome *c*
DCMU	3-(3,4-dichlorophenyl)-1,1-dimethylurea
DTT	dithiothreitol
EGFP	enhanced Green Fluorescent Protein
E_{GSH}	glutathione redox-potential
ER	endoplasmic reticulum
ETC	electron transport chain
FRET	Förster resonance energy transfer
g	multiples of the earth`s gravitational acceleration
GRX	glutaredoxin
GSH	glutathione (reduced)
GSSG	glutathione disulfide (oxidised)
H^+	hydrogen proton
H_2O_2	hydrogen peroxide
IMM	inner mitochondrial membrane
IMS	intermembrane space
kDa	kilodalton
K_m	Michaelis constant
LB-medium	Lysogeny broth-medium
m	slope
mts	mitochondrial targeting sequence
n	sample size
N.A.	numerical aperture

NAC	N-actyl-cysteine
NAD+	nicotinamide adenine dinucleotide (oxidised)
NADH	nicotinamide adenine dinucleotide (reduced)
NADP+	nicotinamide adenine dinucleotide phosphate (oxidised)
NADPH	nicotinamide adenine dinucleotide phosphate (reduced)
ND	NAD(P)H-dehydrogenase
ns	not significant
NTR	NADPH thioredoxin reductase
OD	optical density
OMM	outer mitochondrial membrane
P	probability value
PMSF	phenylmethane sulfonyl fluoride
PSII	photosystem II
PVDF	polyvinylidene difluoride
PVP	polyvinyl-pyrrolidone
qRT	quantitative real-time
RGB	red-green-blue colours
roGFP2	redox-sensitive Green Fluorescent Protein 2
ROS	reactive oxygen species
rpm	rounds per minute
Rubisco	ribulose bisphosphate carboxylase/oxygenase
SD	standard deviation
sgRNA	single guide RNA
SHAM	salicylhydroxamic acid
SOC	super optimal broth with catabolite repression
suc	sucrose
succ	succinate
T-DNA	transfer DNA
TCA	tricarboxylic acid
TIM	translocase of the inner membrane
TOM	translocase of the outer membrane
Trx	thioredoxin
UCP	uncoupling protein
UTR	untranslated region
v/v	volume per volume
VDAC	voltage-dependent anion channel
w/v	weight per volume
WT	wild-type
β-ME	β-mercaptoethanol
Δp	proton motive force
$\Delta\Psi$	(membrane) potential

PUBLICATIONS

Following articles were published during the doctoral studies:

De Col, V., **Fuchs, P**., Nietzel, T., Elsässer, M., Voon, C.P., Candeo, A., Seeliger, I., Fricker, M.D., Grefen, C., Møller, I.M., Bassi, A., Lim, B.L., Zancani, M., Meyer, A.J., Costa A., Wagner, S. and Schwarzländer, M. (2017). ATP sensing in living plant cells reveals tissue gradients and stress dynamics of energy physiology. eLife 6: e26770.

Schwarzländer, M. and **Fuchs, P.** (2017). Plant mitochondrial membranes: adding structure and new functions to respiratory physiology. Curr. Opin. Plant Biol. 40, 147–157.

Teardo, E., Carraretto, L., Wagner, S., Formentin, E., Behera, S., De Bortoli, S., Larosa, V., **Fuchs, P.**, Lo Schiavo, F., Raffaello, A., Rizzuto, R., Costa, A., Schwarzländer, M. and Szabò, I. (2017). Physiological characterization of a plant mitochondrial calcium uniporter *in vitro* and *in vivo*. Plant Physiol. 173, 1355–1370.

Welchen, E., Schmitz, J., **Fuchs, P.**, García, L., Wagner, S., Wienstroer, J., Schertl, P., Braun, H.-P., Schwarzländer, M., Gonzalez, D.H., and Maurino, V.G. (2016). D-lactate dehydrogenase links methylglyoxal degradation and electron transport through cytochrome *c*. Plant Physiol. 172, 901–912.

Following articles were submitted or are in preparation:

Braun, H.-P., Carrie, C., Elsässer, M., Eubel, H., Finkemeier, I., **Fuchs, P.**, Giese, J., Hildebrandt, T., Klodmann, J., Kühn, K., Maurino, V.G., Meyer, E., Moratti, F.G., Müller-Schüssele, S., Ruberti, C., Rugen, N., Schallenberg-Rüdinger, M., Schwarzländer, M. and Steinbeck, J. (in preparation). Single organelle function estimated from Arabidopsis mitochondrial proteomics.

Nietzel, T., Elsässer, M., Ruberti, C., Steinbeck, J., Ugalde, J.M., **Fuchs, P.**, Wagner, S., Ostermann, L., Moseler, A., Lemke, P., Fricker, M., Müller-Schüssele, S., Moerschbacher, B., Costa, A., Meyer, A.J. and Schwarzländer, M. (submitted). The fluorescent protein sensor roGFP2-Orp1 monitors *in vivo* H_2O_2 and thiol redox integration and elucidates intracellular H_2O_2 dynamics at elicitor-induced oxidative burst in Arabidopsis. New Phytol.

GENERAL STATEMENT

I hereby affirm that I am the sole author of this submitted dissertation. I have prepared the thesis self-dependently, and without the use of any other tools apart from those indicated. All parts of the text, having been taken over verbatim or analogously from published or not published sources, are indicated as such. I declare that the thesis has not been submitted in the same or similar form, or in extracts within the context of another examination. I also affirm that I did not apply, neither previously nor now, to enter the examination procedure at any other institution.

Bonn, Tuesday, 26 February 2019

_____

Philippe Fuchs